

Research Paper

Innovation of Flux Switching Machine: Design Variation Review

Roshada Ismail^{1a}, Erwan Sulaiman^{1b}, Mahyuzie Jenal^{1c}, Irfan Ali Soomro^{2d}¹D Research Centre for Applied Electromagnetics, Faculty of Electrical and Electronic Engineering, Universiti Tun Hussein Onn Malaysia²Department of Electrical Engineering Quaid-e-Awam University of Engineering Science and Technology Nawabshah, Pakistan

roshadaismail98@gmail.com.my

DOI : 10.31202/ecjse.1372835

Received: 09.01.2024 Accepted: 02.09.2024

How to cite this article:

Ismail R, Sulaiman E, Jenal M, Soomro IA, " Innovation of Flux Switching Machine: Design Variation Review ", El-Cezeri Journal of Science and Engineering, Vol: 12, Iss: 2, (2025), pp.(86-101).

ORCID: ^a0000-0003-4863-9137; ^b0000-0003-0303-6191; ^c0000-0002-0957-7784; ^d0000-0003-4009-8498.

Abstract : Flux switching machines (FSM) have advantages, including high torque density, low acoustic pollution, minimal vibration and high-speed potential. In addition, due to the PM's placement on the stator, the configuration also provides advantageous thermal management. However, it has been discovered that this machine tends to generate significant cogging torque, exhibit high leakage current, and possess a complex design for flux weakening capability. Numerous research efforts are dedicated to addressing these limitations, but there is a lack of comprehensive reviews specifically focused on the design variations of this type of machine. The objective of this study is to conduct a thorough analysis of the Permanent Magnet Flux Switching Machines (PMFSM), Field Excitation Flux Switching Machines (FEFSM), and Hybrid Excitation Flux Switching Machines (HEFSM), which employ field excitation in addition to permanent magnet operation. Subsequently, the review encompasses a variety of stator structures, rotor structures, and unique structures that employ distinct methodologies to mitigate the limitations of conventional FSM. This evaluation aims to pinpoint the prospective research topics and deficiencies the FSM should prioritize, particularly in industrial applications and transportation. Conclusively, the literature study indicates that PMFSM accounts for around 71% of the attention, whereas FEFSM and HEFSM each account for 14%.

Keywords: Field excitation, Electromagnetics, Flux switching machine, Finite element, Permanent magnet

1. Introduction

The Flux Switching Machine (FSM) provides numerous benefits over its competitors, including high torque density, low acoustic pollution, minimal vibration, ease of control and high-speed potential. Additionally, the FSM can function as a mechanical rotator, auxiliary power supply, or wind turbine [1-3]. Due to its stator excitation and absence of an active rotor component, this motor configuration is considered abhorrent for propulsion in electric vehicles. Compared to the Double Salient Permanent Magnet Motor (DPSM), the FSM exhibited a significant advantage in phase flux-linkage [4]. The inductor alternator with the switching reluctance motor is combined to create the FSM. In 1999, the beginning of the Permanent Magnet Flux Switching Machine (PMFSM) motor was presented to simplify motor design and power electronics control while achieving flux weakening capability, high torque density, and easy thermal management [5-6]. The automobile industry opted for switched reluctance motors, induction motors, and brushless DC motors to replace mechanically driven auxiliaries with electrically powered equipment in various applications such as heating, ventilation, steering systems, water pumps, and air conditioning. However, these motors require power electronic motor drives, which are comparatively costly [7].

In recent years, several novel FSM machine configurations have been created. These configurations offer sinusoidal back-electromotive force (EMF) and low speed at maximum torque, making them well-suited for demanding operating environments like aerospace, automotive, marine, and wind power implementations [8-12]. According to the source of their excitation, these machines have three types [13-17]: Hybrid Excitation Flux Switching Machine Permanent (HEFSM), Permanent Magnet Flux Switching Machines (PMFSM) and Field Excitation Flux Switching Machines (FEFSM) or Wound Field. This paper review primarily focuses on the latest advancements in

the design of PMFSM, FEFSM, and HEFSM. This review delves into different facets, including slot-rotor poles, stator structure, rotor structure, and unique configurations. The main goal of this review is to pinpoint areas in which the PMFSM necessitates additional investigation and to implement successful techniques employed in one configuration to improve the performance of the PMFSM across different setups.

2. Permanent Magnet Flux Switching Machine

2.1. Ration stator slot-rotor pole

Analyzing the quantity of rotor poles and stator slots in a machine's design is crucial for enhancing performance. A recent study [18] examined the number of rotor-pole's impact on single-phase motor's properties. The findings revealed that the 4S-8P PMFSM configuration exhibited the most significant initial output torque of 2.47 Nm, exceptional alternative designs like 2S-8P, 8S-12P and 10S-15P achieved the torque values of 1.45 Nm, 1.66 Nm, and 1.72 Nm respectively. Another investigation [19] compared the straight rotor configuration of PMFSM of 6S-10P with the rotor structure PMFSM of 6S-8P, and it was found that the straight rotor structure produced higher magnetizing flux concentration.

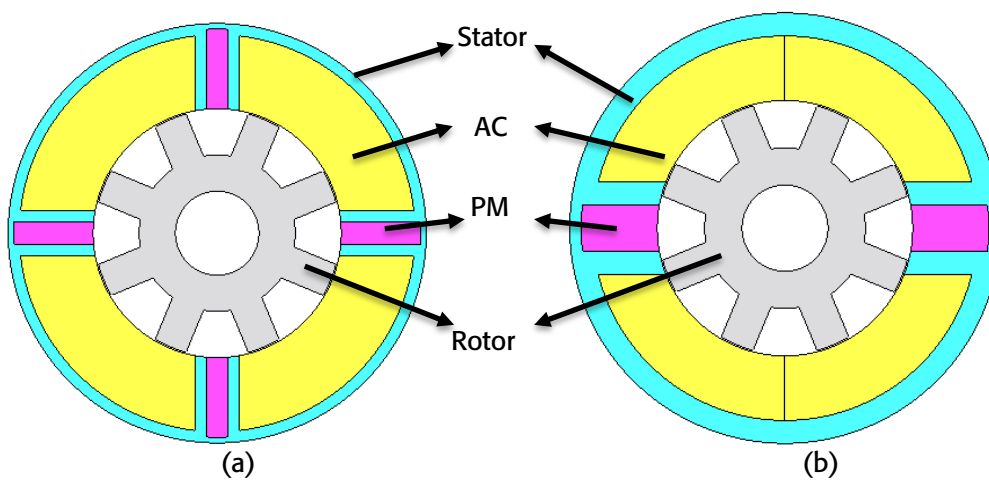


Figure 1. Configuration of PMFSM (a) 4S/8P (b) 2S/8P

In multiple articles, various additional stator-rotor combination topologies have also been presented [20-22]. Interestingly, odd numbers of rotors may reach torque capability and higher back emf compared to the 12S-10P configuration, but they have the disadvantage of unstable magnetic force [23]. Figure 1 displays the cross-sectional perspective of 4S/8P and 4S/8P configurations.

2.2. Configuration of the Rotor

In the past few years, there has been an increasing trend towards using wheel motors in the context of electric vehicles (EVs) due to their ability to offer more space and direct wheel control. The outer-rotor configuration for permanent magnet flux switching motors (PMFSM) was created in 2010 [24]. Since then, more studies have been conducted on this structure's working principle and performance with different stator slot rotor pole ratios and sizes, using finite element software and laboratory experiments [25-29]. Nevertheless, despite its notable characteristics, the assembly of the outer rotor structure can pose challenges due to the need for substantial adjustments to the control mechanisms. For example, in [30], forced oil cooling is extensively employed to augment the heat transfer generated by the rotor. Cooling a rotor is typically more challenging than cooling a stator, particularly in vacuum settings, due to the air gap surrounding the rotor acting as an insulating medium. The stator and rotor immersion in oil effectively cools the motor. Next, [31] discussed the cooling system using the hollow shaft method. Its benefit is that it effectively cools the permanent magnet synchronous machine's (PMSM) rotor at high speed. Findings indicate that this approach effectively mitigates the rise in rotor temperature even when rotor losses occur. Additionally, the outer rotor bearing holds greater importance compared to the inner rotor, resulting in an increased friction area and presenting difficulties in effectively cooling the machine's

internal components. Conversely, dual-rotor structures have also been studied [31-33], where several topologies have been reported, but to date, research has been restricted to both rotors rotating identically in orientation. Generally, the dual-rotor configuration improves PM utilization and efficiency, and more advanced structures employ an axial field, resulting in a shorter axial length, greater torque density and improved heat released [34-35]. However, to achieve rotation in the opposite direction, it might be necessary to use a separate stator. Recent studies propose using a double rotor configuration in co-axial magnetic gear applications[36-38]. Figures 2 and 3 visually depict the dual-rotor configuration of PMFSM from a cross-sectional perspective.

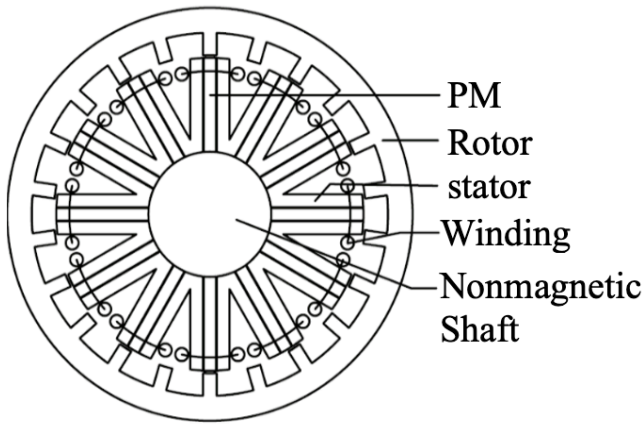


Figure 2. Outer-rotor PMFSM

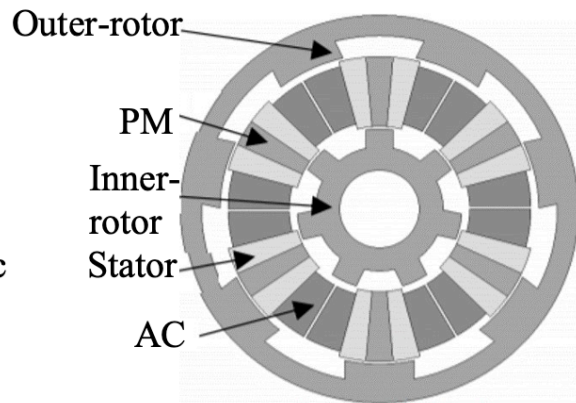


Figure 3. Dual rotor structure PMFSM.

2.3. Configuration of the Stator

It has been found that the Partitioned Stator (PS) PMFSM, also called a dual-stator machine, has been discovered to possess improved torque density because it effectively uses the available space by incorporating two stators [39]. Conversely, the Permanent Magnet (PM) is typically positioned inside the stator [39-42]. Table 1 compares the partitioned stator flux-switching permanent magnet (PA-FSPM), partitioned stator flux-switching hybrid excitation (PS-FSHE) and flux adjuster. The vast space within the inner stator allows for using a ferrite magnet with equivalent flux performance, replacing the need for rare earth magnets. However, the larger size of the motor limits its application in smaller spaces and increases manufacturing costs. Moreover, the losses of the stator core are also heightened in the PSPMFSM. Figure 4 depicts the partial structure of the PSPMFSM.

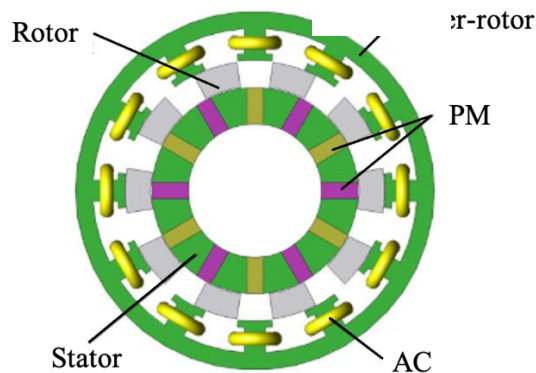


Figure 4. Dual-stator structure of PMFSM

References [43] and [44] explain the advantages of a segmented stator, including its ability to endure various stator winding faults. The segmented stator permanent magnet flux switching motor's construction from separate stator parts, with non-magnetic material replacing the gap between sections at an angle α . If an electrical problem exists in a particular stator section, the electric motor is expected to operate, but the torque value is reduced.

Table 1: Comparison of the partitioned stator

Item	PS-FSPM	PS-FSHE	FA-PS-FSPM	Prius
Cost-effectiveness	Medium	Low	Medium	High
Power- torque density	High	Low	Medium	Medium
Operating range	Narrow	Medium	High	Narrow
Flux-regulation	Low	Medium	High	Low
Thermal dissipation	Good	Medium	Good	Poor
Efficiency	High	Medium	High	High

2.4. Summary of PMFSM

Table 2 shows the performance comparison of different PMFSMs. All the performance is extracted from the reference discussed in the PMFSM section.

Table 2: Comparison of the various PMFSM

Types of motor	12S-12P	12S-8P	12S-22P	8S-12P	10S-15P	6S-10P	6S-8P	PS-FSHE 12S-10P	FA-PS-FSPM 12S-10P
Year	2015		2016	2016		2017		2019	
Author	M.Jenal and E.Sulaiman		Z.Xiang, L.Quan and X.Zhu	M.Jenal, E.Sulaiman, H.A.Soomro, S.M.N. Syed Naufal		R.Kumar, E.Sulaiman, H.A.Soomro, S.H.A Musavi, G.Kumar, I.A.Sohu		SM.N.S.Othman, N.Lassim, E.I.Mbadiwe, M.F.Omar, E.Sulaiman	
Rotor structure	segmental	Salient	salient	Straight rotor	Spanned rotor	Salient		Salient	
Stator structure	Salient		Partitioned	salient		V-shape		Segmental	
Rotor	Inner		Outer	Inner		Outer		Inner	
Stator diameter (mm)	150		269	150		80		132	
Rotor diameter (mm)	89.7		193.4	89.7		100		92.4	
Stack length (mm)	70		83.56	70		20		80	
Flux linkage (Wb)	21.04	15.25	0.09	0.06	1.88	7.8	9.0	N/a	0.034
Cogging torque (Nm)	13.33	21.11	3.2	1.12	3.00	1.75	4.94	27.5	231
Back-emf(V)	35.68	23.93	205.2	5.20	18.40	13.6	1.52	N/a	65.98
Torque (Nm)	9.50	25.54	19.39	1.5	1.65	6.22	0.22	342	222.30
Power (W)	2.93	8.11	4.13k	312.40	402.7	N/a	N/a	377	243.63
Speed (rpm)	N/a	N/a	2406.55	1805.4	2327.4	N/a	N/a	N/a	N/a
Efficiency (%)	N/a	N/a	94.08	N/a	N/a	N/a	N/a	87	N/a

3. Field Excitation Flux Switching Machine (FEFSM)

Recently, Neodymium (Nd) and Dysprosium (Dy) prices, necessary rare-earth materials used in PMSM and IPMSM, have experienced a significant increase due to yearly consumption and cost factors. This price surge has resulted in supply shortages and security concerns [45]. One possible way to tackle this issue is to substitute the permanent magnet (PM) excitation in traditional PMSM and IPMSM rotors with field excitation coils (FEC). This creates the field excitation-flux-switching machine (FEFSM) motor. The fundamental concept of the FEFSM is to alter the orientation of the magnetic flux linked to the armature winding based on the rotor's location. FEFSMs offer several benefits, including simple construction, the absence of permanent magnets, and a straightforward controller circuit. Numerous topologies of FEFSM have been extensively researched and printed [45-47].

Figures 5,6 and 7 display several three-phase FEFSMs with various combinations of winding arrangement and slot-poles. Based on the figures, different rotor structures and coil winding techniques have been developed to achieve optimal performance of FEFSMs. There are two types of three-phases FEFSM rotor structures: salient and segmental. The coil winding configuration is divided into overlap and non-overlap [48-51]. The three-phase Field Excitation Flux Switching Machine (FEFSM) is introduced, with different FEFSM designs utilizing overlap windings with both even and odd rotor pole numbers. Various designs of even rotor-pole number three-phase fractional-slot concentrated winding permanent magnet synchronous machines (FEFSMs) and overlapping windings have been suggested and recorded [52-55].

In 2012, Sulaiman et al. proposed 24S-10P for hybrid electric vehicle (HEV) applications [56]. The motor depicted in Figure 5(a) comprises 24 stator slots, with 12 slots dedicated to FEC coils and another 12 slots for armature coils. Additionally, there are 10 salient poles positioned on the inner part of the motor. Figure 5(b) illustrates the

stator core assembly, which consists of 200 units of 35H210 electromagnetic steels with a stack length of 70 mm. In addition, Figure 5(c) displays the windings of armature coils and FECs overlapping in the 24 stator slots. Figure 5(d) illustrates that the entire assembly comprises a rotor core. The structural constraints and restrictions of the 24S-10P FEFSM were readily available, as were the anticipated value of the IPMSM [57]. From the results, at the based speed of 5,585 rpm, torque of 210.4 Nm is achieved, while the corresponding power is 123 kW. In open circuit conditions, the proposed motor has produced back-emf and torque ripple of 295 V and 6.4%, respectively. The motor efficiency at the highest torque operating point is achieved at 93%, and when high-speed operating, efficiency is slightly degraded to 91.5% owing to the escalation in iron loss [57]. However, the 24S-10P FEFSM has a low torque density because of the high volume of stator and rotor, thus resulting in high motor weight.

To achieve an additional enhancement in the torque density of a 24S-10P, the 12S-5P and 9S-5P FEFSMs with an odd number of rotor poles were proposed by Zhou [58]. Both 12S-5P and 9S-5P FEFSMs maintain a 90 mm outer stator diameter, but 9S-5P has much shorter end windings and less weight. Therefore, the 9S-5P motor has produced better efficiency and torque density performances. Figure 6(a) illustrates the 9S-5P FEFSM three-phase motor configuration, which features a prominent rotor and overlapping windings. The diagram illustrates that the 9S-5P FEFSM has an outer rotor diameter of 49.5 mm and a stack length of 25 mm. The torque and power output were quantified as 0.9 Nm and 37.7 W, respectively. Nevertheless, the motor under consideration has produced a substantial cogging torque of 0.2 Nm, which accounts for 22.2% of the average torque. Additionally, a significant torque ripple of 20% requires development.

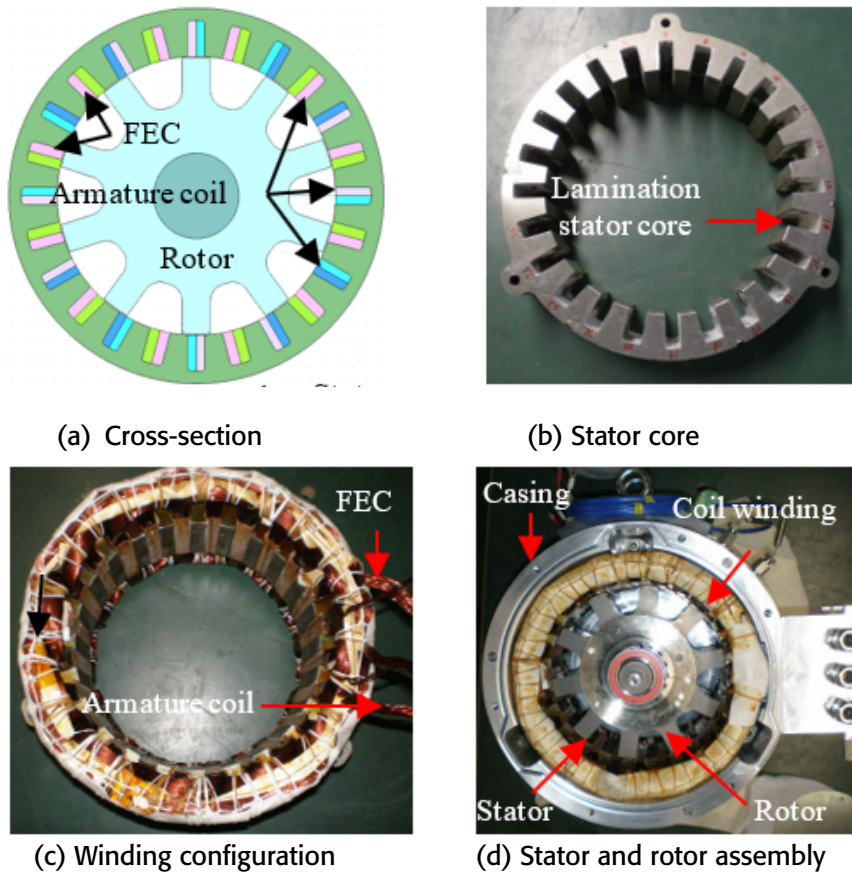


Figure 5. 24S-10 configuration of salient rotor FEFSM [56]

Nguyen et al. have presented three-phase outer-rotor 12S-7P salient rotor FEFSM and overlap windings for electric scooters [59]. The author alleged that outer-rotor FEFSM with odd rotor poles and 12 stator-slots combination can deliver high performance. Figure 6(b) displays the part of the projected motor. The diagram shows 6 armature stator slots and stator slots for FEC coils, respectively. The coil windings are wound over 2 stator teeth. The highest current density of 20 A/mm² and a speed of 500 rpm create a back-emf of 55 V and a flux

linkage of 0.15 Wb for the FEC. At the same time, the outer rotor of 12S-7P can produce 18.75 Nm torque with the corresponding power of 981.7 W. In addition, FSMs that use odd rotor poles suffer from the disadvantages of noise and vibrations, which will shorten the bearing's life [60-62].

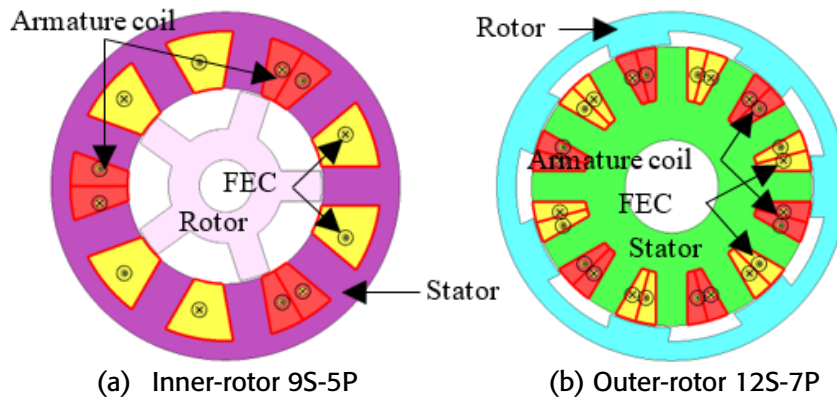


Figure 6. Three-phase, overlap windings with odd rotor poles FEFSM [56].

The study of three-phase FEFSM not only focused on an overlapping winding's inner rotor, but research has also been conducted and presented on the non-overlap winding of outer-rotor FEFSM and odd rotor pole [63]. Furthermore, the outer-rotor three-phase FEFSM with concentrated windings and even rotor poles were studied by Othman et al. [64]. Figure 7(a) illustrates the innovative configuration of a segmented FEFSM with concentrated windings presented by Galea et al. in 2012 [65]. The motor design consists of 36 stator slots and 21 segmental rotors with a dovetail shape, as shown in Figure 7(b). The author states that the segmental rotor, depicted in Figure 7(a), possesses favorable mechanical characteristics and yields exceptional motor performance. The machine being described has a diameter of 600 mm for its outer rotor and a length of 130 mm for its stack. The outer-rotor 36S-21P FEFSM has achieved the most considerable torque output of 2.81k Nm and a low torque ripple of 5.7%, as indicated by the findings. Furthermore, the maximum power output of 8.14 kW is achieved at a rotational speed of 28.6 rpm. Despite the motor's favorable torque and power capabilities, the drawbacks arise from its intricate design, which involves many slot-pole combinations and outer-rotor configurations. These challenges need to be addressed.

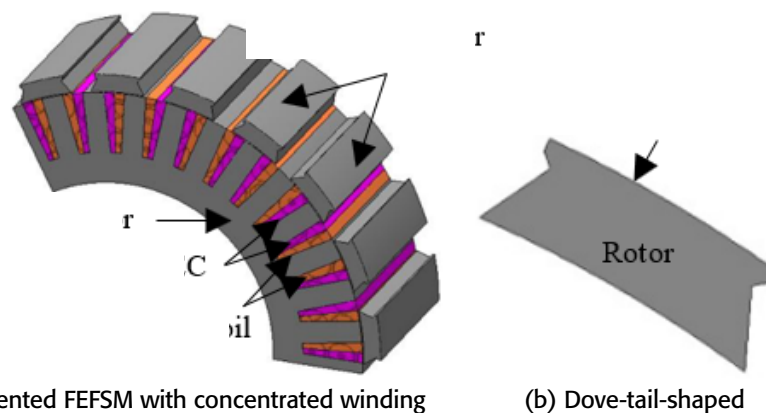


Figure 7. Odd rotor pole, three-phase outer rotor 36S-21P (a) non-overlap windings FEFSM, (b) Dove-tail-shaped [64]

3.1. Summary of FEFSM

Table 3 shows the performance comparison of different FEFSM. All the performance is extracted from the reference discussed in the FEFSM section.

Table 3: Comparison of the various FEFSM

Types of motor	12S-8P	24S-10P	12S-14P	12S-6P	12S-9P	8S-4P	8S-6P	8S-10P
----------------	--------	---------	---------	--------	--------	-------	-------	--------

Year	2013		2014		2018		2019	
Author	E.Sulaiman, F.Khan, M.Z. Ahmad, M.Jenal, S.A.Zulkifli and A.A.Bakar		Z.A.Husin, E.Sulaiman, F.Khan and M.F.Omar		M.F1.Omar, E.Sulaiman, H.A. Soomro, L.I.Jusoh and F.Amin		B.Khan, F.Khan, N.Ahymad, G.Faraz, R.Ahmad and K.Naveed	
Rotor structure	Segmental		Salient		Segmental		Salient	
Stator structure	Salient		Salient		Salient		Salient	
Rotor	Inner		Inner		Inner		Inner	
Stator diameter (mm)	150		264		75		N/a	
Rotor diameter (mm)	90.6		N/a		44.5		N/a	
Stack length (mm)	N/a		70		N/a		N/a	
Flux linkage (Wb)	2.76	31.5	0.04	0.0412	0.031	0.32	0.12	0.1
Cogging torque (Nm)	N/a		18.5		3.4		1.03	
Back-emf(V)	N/a		N/a		12.7		7.5	
Torque (Nm)	0.31	21	43.04	0.77	0.55	1.6	1.3	1.1
Power (W)	N/a		5.41		0.26		0.23	
Speed (rpm)	N/a		N/a		N/a		N/a	
Efficiency (%)	N/a		N/a		N/a		N/a	

4. Hybrid Excitation Flux Switching Machine (HEFSM)

HEFSMs, also acknowledged as Hybrid Excitation Flux Switching Machines as advertised in Figure 8 [65-66], utilize two distinct sources of excitation flux. These machines have undergone thorough research and analysis over a considerable period and can deliver significant torque and power density. Additionally, they exhibit high efficiency and offer the flexibility of adjusting the flux as needed [67-70].

A 6S-4P arrangement of a HEFSM with three layers of PM, field winding, and armature winding inside the stator is depicted in Figure 8(a) [71]. Nevertheless, the extended end windings of this configuration result in heightened copper loss and diminished efficiency. Due to the low permeability of the PM, the field excitation coil (FEC) and PM are also connected in series, which limits the capacity to alter flux. A new 12S-10P HEFSM was proposed to address these issues in [66]. In this design, the permanent magnet (PM) is strategically placed near the center of the stator segments, allowing for ample space to accommodate a DC field excitation coil-(FEC), as illustrated in Figure 8(b). The DC FEC produces the presence of the flux path that can reduce the primary flux produced by the PM for higher torque generation.

Adding the concentrated field and armature depicted in Figure 8(c) produced a new extension of an E-Core HEFSM [67]. The armature winding and the field excitation coil (FEC) occupied the same slot area and had an equivalent number of turns. On the contrary, the PM was situated on the external top of the stator in this particular configuration. Consequently, the PM that produces flux acts as leakage flux and does not contribute to torque generation. Recently, a three-phase E-core HEFSM was analysed in [69] featuring non-overlapping windings, illustrated in Figure 8(d). The power-speed curve, torque, and flux capability were examined to assess the proposed motor's efficacy. The machine offers advantages such as lower cost and reduced copper usage. Nevertheless, the torque density might experience a decline as a result of the diminished PM volume.

HEFSMs equipped with active components on the stator face certain drawbacks, such as the challenging manufacturing and assembly process due to the segmented stator core. The presence of a salient rotor structure also results in increased rotor weight. Moreover, compared to PMFSMs, HEFSMs that utilize two excitation flux sources necessitate a complex control circuit for regulating the magnetic flux linkages in the Field Excitation Coil (FEC) and armature coil. Furthermore, the FEC and armature coil might reduce overall motor efficiency due to higher copper losses.

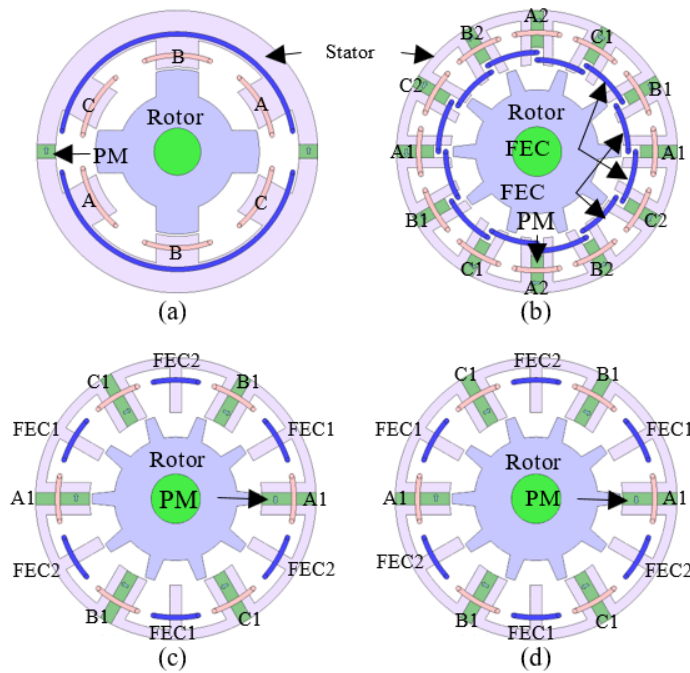


Fig. 8. HEFSM three-phase, (a) 6S 4P, (b) C-core 12S-10P, (c) E core 12S-10P, and (d) E-core 6S-8P E core [65-69].

4.1. Design Extension and Customization

This portion of the text discusses how design can be customized and expanded for specific reasons. Using a segmented rotor has been proven effective in reducing the magnetic path length, as stated in reference [72]. Flux in the armature teeth and magnetic connections in the winding's armature can be generated using a segmented rotor in a single operation cycle. This design is commonly used in dissimilar types of machines [73-77]. The angle of each segment is established by the most minor separation required to avoid substantial flux transfer between adjacent segments. The number of segments employed determines the segment pitch. Figure 9 shows a partial view of a 6-pole and an 8-pole segmental rotor.

Most modern electrical machines use an anisotropic and circumferential flux distribution, with permanent magnets (PMs) placed tangential to the shaft, as seen in FSMs. Modifying the configuration of permanent magnets (PMs) around the stator circumference can alter the magnetic flux pattern. Various studies, referenced as [42], [78], [79], have explored the utilization of radial and circumferential flux. Recent advancements, cited in references [80-82], have significantly progressed the design of axial flux machines. These improvements entail the application of a dual rotor or dual stator arrangement in which magnetic flux is directed perpendicular to the stator and rotor's surface. However, designing and analyzing axial flux devices is more time-consuming due to the need for three-dimensional modelling. Additionally, as the complexity of the design increases, manufacturing the machine can become more challenging. Figure 10(a) illustrates a partial depiction of the design of magnets in an outspread and circumferential configuration. However, Figure 10(b) displays a three-dimensional depiction of an axial flux machine that showcases a dual stator. The flux path in an axial flux machine is unidirectional, and grain-oriented magnetic steels are used to achieve maximum efficiency.

Before this stage, the design's magnets were positioned directly from the inner to outer stator or along the inside of the stator diameter. A recent development has involved modifying the shape of the magnets to resemble the letter "V" to maximize output torque and improve magnet utilization. In conventional configuration, a pair of permanent magnets (PMs) are positioned within the stator [83]. When the machine has an outer-rotor arrangement, the V-shaped permanent magnet is visible on the outside of the machine [59]. A multi-tooth machine, known as another inventive stator core arrangement, was developed to enhance the torque value of the V-shaped permanent magnet. The multi-tooth machine demonstrates a higher average torque, lower inductance, and significantly less imbalanced magnetic force. It does so at the expense of a marginally increased cogging

torque and undesirable total harmonic distortion [84]. In reference [85], a permanent magnet flux-switching synchronous machine (PMFSM) with radial segmentation was presented.

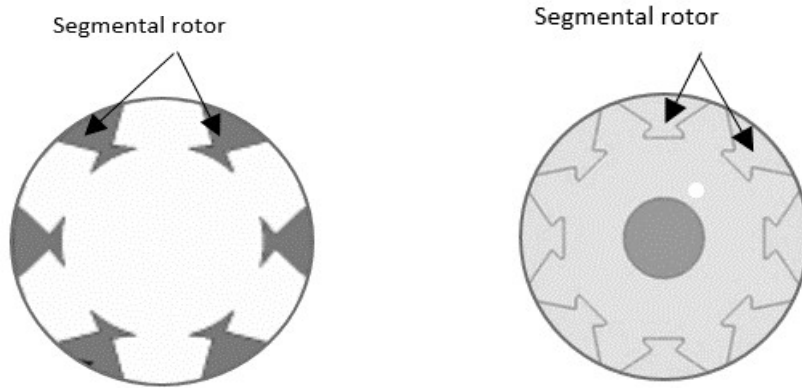


Figure 9. Segmental rotor (a) 6-rotor pole (b) 8-rotor pole

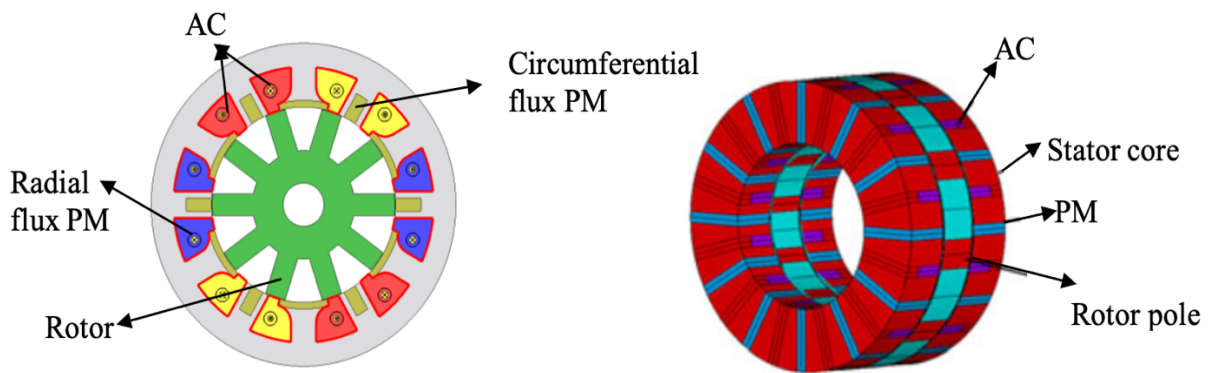


Figure 10. (a) Circumferential arrangement of the magnet (b) Double stator axial flux machine

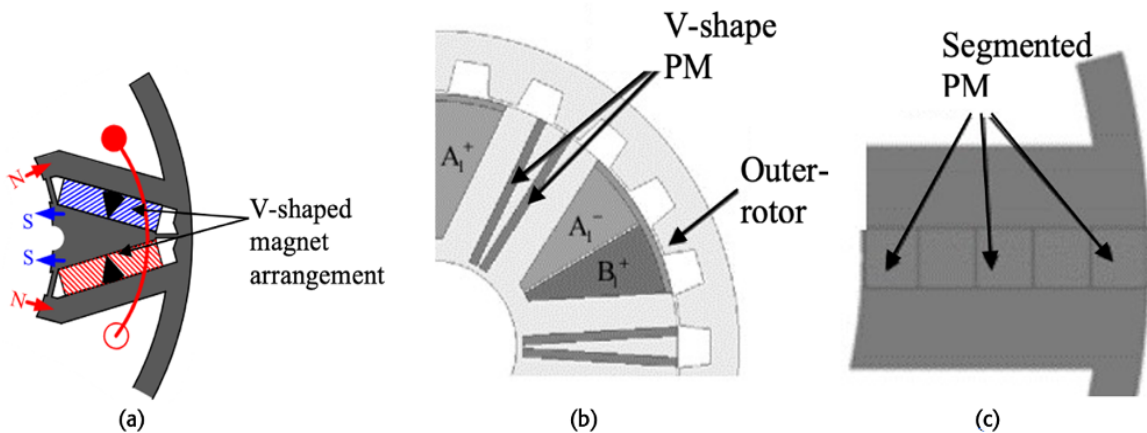


Figure 11. Magnet-V-shaped (a) rotor inner, (b) rotor-outer, (c) magnet-segmented

Researchers found dividing a rectangular magnet into five segments leads to a slight increase in torque production and a higher volume ratio of torque-to-magnet. In this design, smaller permanent magnets (PM) segments are positioned in the higher flux density region near the air gap. In comparison, more significant PM segments are suggested to be closer to the outer surface as the PM placement progresses. Figure 11 displays the V-shaped magnet design [86] and a cross-sectional representation of the segmented magnet. Moreover, Figure 12 depicts the multi-toothed machine.

The flux barrier (FB) method decreases the flux that escapes from the stator, specifically in C-type stators. There are six ways to arrange flux bridges on stator teeth, and the C2, C3, and C5 arrangements [87-88], which are positioned arrangements in the rotor at a greater distance from the stator teeth, produce superior maximum torque outcomes compared to alternative configurations. In addition to reducing flux leakage, FB can also lessen cogging torque and slightly reduce PM length, although it may also slightly lower the machine's average torque [89].

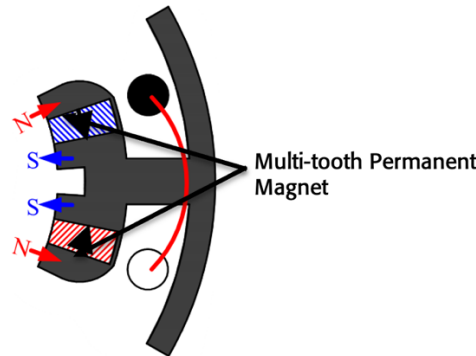


Figure 12. Cross-sectional view of multi-toothed machine

Table 4: Summary of design variation

Design extension and customization	Design variation			Motivation
	PMFSM	FEFSM	HEFSM	
Segmental rotor	/	/	/	Flux path
Modular rotor	/	/	/	Flux path
Segmental stator	/	/	/	Fault-tolerant
Stator E, U, C shape	/	/	/	Magnetic circuit arrangement
Multi-tooth	/	/	/	Advancement of V-shape
Segment magnet	/	/	/	Reducing flux leakage
Flux-bridge	/	/	/	Flux weakening
Mechanical flux adjuster	/	/	/	Flux weakening
Flux adjuster	/	/	/	Flux weakening

A movable flux adjuster (FA) placed on the stator's outer cover can enhance the flux weakening capability, but it also increases the motor's size [90-91]. To tackle this problem, The FA is integrated into the interior stator of the PMFSM partitioned stator machine in order to address this issue. This arrangement enables the FA to occupy the same space as the PM, thereby decreasing the size of the machine while enhancing its power and torque densities. Another design improvement involves inserting an FB in the rotor yoke and teeth to reduce eddy-current loss and minimize eddy-current harmonics [92]. The cylindrical rotor structure, borrowed from the SRM and features ribs linking each rotor pole, is utilized to reduce loss in high-speed operation [93-95]. This loss reduces efficiency in SRM's high-speed and low-power sectors [96]. While the cylindrical rotor structure is rarely utilized in PMFSM, a comprehensive investigation was undertaken regarding HEFSM, which uses two distinct varieties of cylindrical rotor structures. The study found that the cylindrical rotor structure reduces windage loss by 35.4% compared to the salient rotor type, with a minor disadvantage in the highest torque [97-98]. Table 4 summarizes the design variation of PMFSM, HEFSM and FEFSM. Although most publications have focused on inner rotor designs, only a few have explored outer rotors.

4.2 Manufacturing Challenges

Its design often determines the intricacy of the manufacturing process for a Flux Switching Machine (FSM). It is essential to consider the rotor's manufacture to reduce the number of rotor losses. The more sophisticated and unique a design, the more complexity the manufacturer must deal with. Three points need to be highlighted here. Firstly, rotor structure. Frankly, the salient rotor structure is better than the segmented rotor structure. Based on Figure 10(a) and in [98], the salient rotor tooth has a rectangular shape, while the segmented rotor tooth produces various shapes. The segmented rotor has many shaped sides, complicating the design manufacturing process. On the other hand, the salient rotor has only one slot pole, even though it has many teeth. However, one tooth equals

one slot pole for the segmented rotor, making manufacturing more expensive. However, the segmented rotors outperform the salient rotors in terms of flux linkage, torque, and power.

Apart from that, the positioning of permanent magnets also affects the manufacturing challenges. Essentially, this machine can be categorised into two main types: surface-mounted permanent (SPM) machines and internally mounted permanent-magnet (IPM) machines. In the context of Integrated Permanent Magnet (IPM) systems, the reluctance route experiences specific torque loads, which necessitates a reduction in the mass of the magnet in order to achieve the desired torque [99]. Additionally, when calculating the mass of the PM, the stator volume will change depending on the volume of PM needed. The manufacturer complexity will appear here due to the various sizes and shapes of the stator following the PM restriction. In addition, placing any non-passive components on the rotor could lead to challenges in effectively managing heat and thermal concerns [100]. Regarding sandwich PM shape, the machine is more complex than others. Usually, the sandwich PM shape comes with a double rotor or double stator. So, the cost of manufacturing will increase along with the difficulty of design.

Next, the last point that needs to be considered is the machine's winding. It is essential to consider the manufacturing process for the stator core and windings early on in the design of the machine. The method used determines the teeth geometry of the machine and whether it has tips or not. The various manufacturing procedures are given and further analysed in [101]. [102] provides a concise overview of the techniques employed in producing the stator core and windings for a Permanent Magnet Synchronous Motor (PMSM) with concentrated windings. Next, an appropriate number of winding layers should be selected after carefully considering the manufacturing process. The selection of the layers primarily depends on their application. Besides that, from the mechanical side, the machine also faced manufacturing challenges regarding the bearing, inner shaft, end coil and casing.

5. Conclusions

This research addresses this deficiency by examining the most recent design modifications in three Finite State Machines (FSMs) categories: the FEFSM, PMFSM and HEFSM, which combines permanent magnet and field excitation. The review encompasses the analysis of various armature slots, rotor poles, stator structures, rotor structures, and unique structures that employ different approaches to mitigate the drawbacks of conventional FSMs. The main objective of this analysis is to pinpoint possible research topics and gaps that necessitate greater attention in the development of FSM, specifically for industrial applications and transportation. Additionally, the paper emphasizes the design possibilities of incorporating different structures into one another to enhance the performance of FSMs. In conclusion, the literature review reveals that approximately 71% of the research on FSMs is focused on PMFSMs, while FEFSMs and HEFSMs each account for 14%. This highlights the dominant research emphasis on PMFSMs.

Acknowledgments

This research was supported by Universiti Tun Hussein Onn Malaysia (UTHM) through Geran Penyelidikan Pascasiswazah (GPPS) (Vot Q583).

Authors' Contributions

Therefore, each author contributed to the study's design conception, optimization, and analysis. All authors reviewed the results and approved the final version of the manuscript.

Competing Interests

The authors declare that they have no competing interests.

References

- [1] M. Lehr, D. Dietz, and A. Binder, "Electromagnetic design of a permanent magnet Flux-Switching-Machine as a direct-driven 3 MW wind power generator," IEEE International Conference on Industrial Technology (ICIT), Darmstadt, Germany, 2018, pp. 383–388.
- [2] Essam E. Mohamed, "Novel partitioned stator Switched Flux PM machines for wind generator applications," International Conference on Innovative Trends in Computer Engineering (ITCE), Egypt, 2018, pp. 427–434.
- [3] W. I. Gabr et al., "Design and Analysis of a Brushless Three Phase Flux Switching Generator for Aircraft Auxiliary Power Unit," Twentieth International Middle East Power Systems Conference (MEPCON), Cairo University, Egypt, 2018, pp. 198–202.
- [4] W. Hua, Z. Q. Zhu, M. Cheng, Y. Pang, and D. Howe, "Comparison of flux-switching and doubly-salient permanent magnet brushless machines," Proceedings of the Eighth International Conference on Electrical Machines and Systems (ICEMS), 2005, pp. 165–17.
- [5] C. Pollock and M. Wallace, "Flux switching motor, a DC motor without magnets or brushes," Conference Record – IAS Annual Meeting (IEEE Industry Applications Society), 1999, pp. 1980–1987,
- [6] N. Fernando, I. U. Nutkani, S. Saha, and M. Niakinezhad, "Flux switching machines: A review on design and applications," 20th International Conference on Electrical Machines and Systems, ICEMS, 2017.
- [7] C. Pollock et al., "Flux-switching motors for automotive applications," IEEE Transaction on Industry Application, vol. 42, no. 5, pp. 1177–1184, 2006.
- [8] S. Amin, S. Khan, S. Sabir, and H. Bukhari, "A comprehensive review on Axial Flux Machines and Its Applications," 2nd International Conference on Computing, Mathematics and Engineering Technologies (iCoMET), 2019, pp. 1–7.
- [9] Z. Q. Zhu, "Switched flux permanent magnet machines – Innovation continues," International Conference on Electrical Machines and Systems (ICEMS), 2011, pp. 1–10,
- [10] G. Verez, G. Barakat, and Y. Amara, "Influence of slots and rotor poles combinations on noise and vibrations of magnetic origins in 'U'-core flux-switching permanent magnet machines," Progress In Electromagnetics Research B, vol. 61, no. 1, pp. 149–168, 2015.
- [11] M. Sharma, P. Nijhawan, and A. Sinha, "Role of battery energy storage system in modern electric distribution networks - A review," International Journal of Advanced Trends in Computer Science and Engineering, vol. 8, no. 3, pp. 443–450, 2019.
- [12] M. K. Singla, A. S. Oberoi, and P. Nijhawan, "Trends so far in hydrogen fuel cell technology: State of the art," International Journal of Advanced Trends in Computer Science and Engineering, vol. 8, no. 4, pp. 1146–1155, 2019.
- [13] F. Khan, E. Sulaiman, and M. Z. Ahmad, "Review of Switched Flux Wound-Field Machines Technology," IETE Technical Review (Institution of Electronics and Telecommunication Engineers, India), vol. 34, no. 4, pp. 343–352, 2017.
- [14] L. I. Jusoh, E. Sulaiman, and S. M. N. S. Othman, "Comparative study of single phase FE, PM and HE flux switching motors," IEEE Student Conference on Research and Development, SCOReD, 2015, pp. 583–588.
- [15] J. A. Rani, E. Sulaiman, M. F. Omar, M. Z. Ahmad, and F. Khan, "Computational method of rotor stress analysis for various flux switching machine using J-MAG," IEEE Student Conference on Research and Development, SCOReD, 2015, pp. 721–726.
- [16] M. Jenal, S. A. Hamzah, F. Khan, H. A. Soomro, and E. Sulaiman, "Performance investigations of flux switching machines for lightweight electric vehicles," IEEE Conference on Energy Conversion, CENCON, 2015, pp. 78–83.
- [17] E. Sulaiman, T. Kosaka, and N. Matsui, "Design and analysis of high-power/high-torque density dual excitation switched-flux machine for traction drive in HEVs," Renewable and Sustainable Energy Reviews, vol. 34, pp. 517–524, 2014.
- [18] L. I. Jusoh, E. Sulaiman, R. Kumar, F. S. Bahrim, and M. F. Omar, "Preliminary studies of various rotor pole number for permanent magnet flux switching machines (PMFSM)," International Journal of Applied Engineering Research, vol. 12, no. 7, pp. 1377–1382, 2017.
- [19] M. Jenal, E. Sulaiman, H. A. Soomro, and S. M. N. Syed Othman, "Primary study of a new permanent magnet flux switching machine over straight and spanned rotor configurations," World Journal of Engineering, vol. 13, no. 5, pp. 441–446, 2016.
- [20] Y. Yao and C. Liu, "An efficient nine-phase PM flux-switching machine with high torque density and low torque ripple," Asia-Pacific Magnetic Recording Conference, APMRC, USST China, 2018, pp. 1–2.

- [21] L. Q. J. Xq et al., "A New 12 / 11-pole Dual Three-Phase Flux-Switching Permanent Magnet Machine," International Conference on Electrical Machines and Systems (ICEMS), Pattaya, Thailand, 2015, pp.1502-1507.
- [22] W. Xu, J. Zhu, Y. Zhang, Y. Guo, and G. Lei, "New axial laminated-structure flux-switching permanent magnet machine with 6/7 poles," IEEE Transaction on Magnetic, vol. 47, no. 10, pp. 2823–2826, 2011.
- [23] J. H. Kim, Y. Li, D. Bobba, and B. Sarlioglu, "New perspective to understand winding configurations of even and odd numbers of pole flux-switching permanent magnet machine," IEEE Transportation Electrification Conference and Expo, ITEC, 2016, no. 1, pp. 1–6.
- [24] H. Zhang and W. Hua, "A novel outer-rotor-permanent magnet flux-switching machine for in-wheel light traction," IECON Proceedings (Industrial Electronics Conference), 2016, vol. 0, no. 2, pp. 6633–6638.
- [25] R. Kumar, E. Sulaiman, H. A. Soomro, S. H. A. Musavi, G. Kumar, and I. A. Sohu, "Electromagnetic analysis of outer rotor permanent magnet flux switching machine for downhole application," ICIEECT 2017 – International Conference on Innovations in Electrical Engineering and Computational Technologies 2017, Proceedings, pp. 4–9, 2017, doi: 10.1109/ICIEECT.2017.7916555.
- [26] E. Sulaiman, G. M. Romalan, and N. W. A. Ghani, "Design improvement of flux switching permanent magnet using the combined local and global method," ICCEREC 2016 – International Conference on Control, Electronics, Renewable Energy, and Communications 2016, Conference Proceedings, 2017, vol. 1, pp. 214–219.
- [27] M. Z. Ahmad, E. Sulaiman, Z. A. Haron, F. Khan, and M. A. Mazlan, "Analysis of a New Dual Excitation Flux Switching Machine with Outer-Rotor Configuration for Direct Drive EV," Applied Mechanics and Materials, vol. 695, pp. 787–791, 2014.
- [28] E. Bin Sulaiman and A. M. Arab, "Fundamental study of outer-rotor hybrid excitation flux switching generator for grid-connected wind turbine applications," 2015 IEEE Student Conference on Research and Development, SCORed, 2015, pp. 716–720.
- [29] E. I. Mbadiwe and E. Sulaiman, "Improved design of outer rotor machine in PM technology for motorbike drive application," ISCAIE 2018 – 2018 IEEE Symposium on Computer Applications and Industrial Electronics, 2018, pp. 167–172.
- [30] M. R. Khowja, G. Vakil, C. Gerada, and P. Electronics, "Characteristics for Surface Mounted PM Machines," Annual Conference of the IEEE Industrial Electronics Society, 2019, vol. 1, pp. 758–763.
- [31] E. Sulaiman, M. F. Omar, and L. M. Ishak, "Design of a Hybrid Permanent Magnetic Flux Switching Machinewith compound rotor configuration," International Conference on Control, Electronics, Renewable Energy, and Communications 2016, Conference Proceedings, 2017, pp. 208–213.
- [32] M. K. Hassan, E. Sulaiman, G. M. Romalan, M. F. Omar, and M. Jenal, "12Slot-14pole Dual Rotor Hybrid Excitation Flux Switching Machine (DR-HEFSM) load analysis,"IEEE Student Conference on Research and Development, SCORed, 2015, vol. 10, no. 16, pp. 245–249.
- [33] Z. Xiang, L. Quan, and X. Zhu, "A New Partitioned-Rotor Flux-Switching Permanent Magnet Motor with High Torque Density and Improved Magnet Utilization," IEEE Transactions on Applied Superconductivity, vol. 26, no. 4, pp. 1–5, 2016.
- [34] W. Zhao, T. A. Lipo, and B. Il Kwon, "A novel dual-rotor, axial field, fault-tolerant flux-switching permanent magnet machine with high-torque performance," IEEE Transaction Industry on Magnetic, vol. 51, no. 11, pp. 1–4, 2015.
- [35] J. Rahmani Fard and M. Ardebili, "Optimal Design and Analysis of the Novel Low Cogging Torque Axial Flux-Switching Permanent-Magnet Motor," Electric Power Components and Systems, vol. 46, no. 11–12, pp. 1330–1339, 2018.
- [36] Z. Q. Zhu, "Overview of novel magnetically geared machines with partitioned stators," IET Electric Power Applications, vol. 12, no. 5. Institution of Engineering and Technology, pp. 595–604, 2018.
- [37] Y. J. Ge, C. Y. Nie, and Q. Xin, "A three-dimensional analytical calculation of the air-gap magnetic field and torque of coaxial magnetic gears," Progress in Electromagnetics Research, vol. 131, no. September, pp. 391–407, 2012.
- [38] C. Liu and K. T. Chau, "Electromagnetic design and analysis of double-rotor flux-modulated permanent magnet machines," Progress in Electromagnetics Research, vol. 131, no: September, pp. 81–97, 2012.
- [39] D. J. Evans, Z. Q. Zhu, H. L. Zhan, Z. Z. Wu, and X. Ge, "Flux-Weakening Control Performance of Partitioned Stator-Switched Flux PM Machines," IEEE Transaction on Industrial Application, vol. 52, no. 3, pp. 2350–2359, 2016.

- [40] C. C. Awah, Z. Q. Zhu, Z. Z. Wu, J. T. Shi, and D. Wu, "Comparison of partitioned stator switched flux permanent magnet machines having single- and double-layer windings," *International Conference on Ecological Vehicles and Renewable Energies, EVER*, 2015, pp. 0–4.
- [41] C. H. T. Lee, J. L. Kirtley, and M. Angle, "A Partitioned-Stator Flux-Switching Permanent-Magnet Machine with Mechanical Flux Adjusters for Hybrid Electric Vehicles," *IEEE Transaction Industry on Magnetic*, vol. 53, no. 11, 2017.
- [42] X. Ma et al., "Comparative analysis of flux switching machines between toothed rotor with permanent magnet excitation and segmented rotor with field coil excitation," *IECON Proceedings (Industrial Electronics Conference)*, 2016, no. 1, pp. 1610–1615.
- [43] S. M. N. S. Othman, N. Lassim, E. I. Mbadiwe, M. F. Omar, and E. Sulaiman, "Segmental Stator as a Fault Tolerant for 2Slot-12Pole Switched Flux Permanent Magnet Machine," *ICSGRC 2019, IEEE 10th Control and System Graduate Research Colloquium, Proceeding*, 2019, pp. 32–35, 2019.
- [44] S. M. N. B. S. Othman, H. A. Soomro, E. I. Mbadiwe, M. F. Bin Omar, and E. Bin Sulaiman, "Design Optimisation of SegSta 12S-12P Permanent Magnet Flux Switching Machine," *2019 IEEE International Conference on Automatic Control and Intelligent Systems, I2CACIS*, 2019, pp. 135–138.
- [45] M. Jenal and E. Sulaiman, "Comparative study on a new permanent magnet flux switching machine configuration over segmental and salient rotor structure," *ARNP Journal of Engineering and Applied Sciences*, vol. 10, no. 19, pp. 8846–8852, 2015.
- [46] E. I. Mbadiwe, E. Sulaiman, and F. Khan, "Consideration of permanent magnet flux switching motor in segmented rotor for in-wheel vehicle propulsion," *International Conference on Computing, Mathematics and Engineering Technologies: Invent, Innovate and Integrate for Socioeconomic Development, iCoMET*, 2018, pp. 1–6, 2018,
- [47] M. F. Omar, E. Sulaiman, H. A. Soomro, L. I. Jusoh, and F. Amin, "Slot Pole Study of Field Excitation Flux Switching Machines Using Segmental Rotor and Non-Overlap Windings," *International Journal of Engineering & Technology*, vol. 7, no. 2.23, p. 459, 2018.
- [48] M. F. Omar, E. Sulaiman, M. Ahmad, M. Jenal, and G. M. Romalan, "Magnetic flux analysis of a new Field Excitation Flux Switching Motor with segmental rotor," *IEEE International Magnetics Conference, INTERMAG*, 2017, vol. 53, no. 11, pp. 10–13.
- [49] S. M. K. Sangdehi, S. E. Abdollahi, and S. A. Gholamian, "A segmented rotor hybrid excited flux switching machine for electric vehicle application," *8th Power Electronics, Drive Systems and Technologies Conference, PEDSTC*, 2017, pp. 347–352.
- [50] Z. Xu, D. H. Lee, and J. W. Ahn, "Design and Operation Characteristics of a Novel Switched Reluctance Motor with a Segmental Rotor," *IEEE Transaction Industry on Application*, vol. 52, no. 3, pp. 2564–2572, 2016.
- [51] A. R. Dehghanzadeh, V. Behjat, and M. R. Banaei, "Dynamic modelling of wind turbine based axial flux permanent magnetic synchronous generator connected to the grid with switch reduced converter," *Ain Shams Engineering Journal*, vol. 9, no. 1, pp. 125–135, 2018.
- [52] Q. A. S. Syed and I. Hahn, "Analysis of flux focusing double stator and single rotor axial flux permanent magnet motor," *IEEE International Conference on Power Electronics, Drives and Energy Systems, PEDES*, 2016, no. 1, pp. 1–5.
- [53] W. Zhang, X. Liang, and M. Lin, "Analysis and Comparison of Axial Field Flux-Switching Permanent Magnet Machines with Three Different Stator Cores," *IEEE Transactions on Applied Superconductivity*, vol. 26, no. 7, pp. 1–6, 2016.
- [54] Y. J. Zhou and Z. Q. Zhu, "Torque density and magnet usage efficiency enhancement of sandwiched switched flux permanent magnet machines using V-shaped magnets," *IEEE Trans Magn*, vol. 49, no. 7, pp. 3834–3837, 2013.
- [55] X. Zhu, Z. Shu, L. Quan, Z. Xiang, and X. Pan, "Multi-Objective Optimization of an Outer-Rotor V-Shaped Permanent Magnet Flux Switching Motor Based on Multi-Level Design Method," *IEEE Trans Magn*, vol. 52, no. 10, pp. 1–8, 2016.
- [56] G. Zhao and W. Hua, "Comparative Study between a Novel Multi-Tooth and a V-Shaped Flux-Switching Permanent Magnet Machines," *IEEE Trans Magn*, vol. 55, no. 7, pp. 1–8, 2019.
- [57] M. M. J. Al-Ani and M. L. Jupp, "Switched flux permanent magnet machine with segmented magnets," *IET Conference Publications*, vol. 2016, no. CP684, 2016.
- [58] Y. J. Zhou and Z. Q. Zhu, "Comparison of low-cost single-phase wound-field switched-flux machines," *Proceedings of the 2013 IEEE International Electric Machines and Drives Conference, IEMDC*, 2013, vol. 5, pp. 1275–1282.

- [59] H. Q. Nguyen, J. Y. Jiang, and S. M. Yang, "Design of a 12-slot 7-pole wound-field flux switching motor for traction applications," *Proceedings of the IEEE International Conference on Industrial Technology*, 2016, pp. 1275–1280.
- [60] C. Gan, J. Wu, M. Shen, W. Kong, Y. Hu, and W. Cao, "Investigation of Short Permanent Magnet and Stator Flux Bridge Effects on Cogging Torque Mitigation in FSPM Machines," *IEEE Transactions on Energy Conversion*, vol. 33, no. 2, pp. 845–855, 2018.
- [61] R. P. Deodhar, A. Pride, S. Iwasaki, and J. J. Bremner, "Performance improvement in flux-switching PM machines using flux diverters," *IEEE Trans Ind Appl*, vol. 50, no. 2, pp. 973–978, 2014.
- [62] Z. Q. Zhu, M. M. J. Al-Ani, X. Liu, and B. Lee, "A Mechanical Flux Weakening Method for Switched Flux Permanent Magnet Machines," *IEEE Transactions on Energy Conversion*, vol. 30, no. 2, pp. 806–815, 2015.
- [63] J. Luo, J. Ji, and Y. Zhang, "Reduction of eddy current loss in flux-switching permanent-magnet machines using rotor magnetic flux barriers," *2017 IEEE International Magnetics Conference, INTERMAG, 2017*, vol. 53, no. 11.
- [64] J.-W. Ahn and G. F. Lukman, "Switched reluctance motor: Research trends and overview," *CES Transactions on Electrical Machines and Systems*, vol. 2, no. 4, pp. 339–347, 2019.
- [65] S. H. Won, J. Choi, and J. Lee, "Windage Loss Reduction of High-Speed SRM Using Rotor Magnetic Saturation," *IEEE Trans Magn*, vol. 44, no. 11, pp. 4147–4150, 2008.
- [66] K. Kiyota, T. Kakishima, and A. Chiba, "Cylindrical rotor design for acoustic noise and windage loss reduction in switched reluctance motor for HEV applications," *2014 IEEE Energy Conversion Congress and Exposition, ECCE 2014*, pp. 1814–1821, 2014.
- [67] J. Wang, W. Wang, K. Atallah, and D. Howe, "Design considerations for tubular flux-switching permanent magnet machines," *IEEE Trans Magn*, vol. 44, no. 11 PART 2, pp. 4026–4032, 2008.
- [68] Y. Okada, T. Kosaka, and N. Matsui, "Windage loss reduction for hybrid excitation flux switching motors based on rotor structure design," *2017 IEEE International Electric Machines and Drives Conference, IEMDC, 2017*, pp. 1–8.
- [69] E. Sulaiman, F. Khan, M. Z. Ahmad, M. Jenal, S. A. Zulkifli, and A. A. Bakar, "Investigation of field excitation switched flux motor with segmental rotor," *2013 IEEE Conference on Clean Energy and Technology (CEAT), 2013*, pp. 317–322.
- [70] Z. A. Husin, E. Sulaiman, F. Khan, and M. F. Omar, "Performances comparison of 12S-14P field excitation flux switching motor with overlap and non-overlap windings for hybrid electric vehicles," *2014 IEEE Student Conference on Research and Development, SCOREd, 2014*, vol. 2, no. c, pp. 1–6.
- [71] S. D. Chishko, Y. Tang, J. J. H. Paulides, and E. A. Lomonova, "DC excited flux-switching motor: Rotor structural optimisation," *2014 17th International Conference on Electrical Machines and Systems, ICEMS, 2014*, pp. 2867–2871.
- [72] R. Cao, Y. Jin, Y. Zhang, and W. Huang, "A new general design method of segmented-rotor wound field flux-switching motors with complementary magnet circuit," *2015 IEEE International Magnetics Conference, INTERMAG, 2015*, vol. 59, no. 10, p. 1.
- [73] B. Khan, F. Khan, N. Ahmad, G. Faraz, R. Ahmad, and K. Naveed, "Preliminary study of a new octane modular stator field excited flux switching motor for high-speed applications," *2019 2nd International Conference on Computing, Mathematics and Engineering Technologies, iCoMET, 2019*, pp. 1–5.
- [74] G. Zhao, W. Hua, and J. Qi, "Comparative study of wound-field flux-switching machines and switched reluctance machines," *IEEE Trans Ind Appl*, vol. 55, no. 3, pp. 2581–2591, 2019.
- [75] D. Wang, X. Du, and X. Wang, "Force ripple reduction of a linear flux switching motor with segmented secondary," *20th International Conference on Electrical Machines and Systems, ICEMS, 2017*, vol. 977, pp. 8–12.
- [76] E. Sulaiman, M. F. M. Teridi, Z. A. Husin, M. Z. Ahmad, and T. Kosaka, "Performance comparison of 24S-10P and 24S-14P field excitation flux switching machine with single DC-Coil polarity," *Proceedings of the 2013 IEEE 7th International Power Engineering and Optimization Conference, PEOCO, 2013*, vol. 1, no. June, pp. 46–51.
- [77] U. B. Akuru and M. J. Kamper, "Performance comparison of optimum wound-field and ferrite PM flux switching machines for wind energy applications," *22nd International Conference on Electrical Machines, ICEM, 2016*, pp. 2478–2485.
- [78] Z. Z. Wu, Z. Q. Zhu, J. C. Mipo, and P. Farah, "Design and analysis of a partitioned stator wound field switched flux machine for an electric vehicle," *19th International Conference on Electrical Machines and Systems, ICEMS, 2016*, pp. 1–6.

- [79] R. Cao, X. Yuan, Y. Jin, and Z. Zhang, "MW-Class Stator Wound Field Flux-Switching Motor for Semidirect Drive Wind Power Generation System," *IEEE Transactions on Industrial Electronics*, vol. 66, no. 1, pp. 795–805, 2019.
- [80] E. Sulaiman, T. Kosaka, and N. Matsui, "A new structure of 12Slot-10Pole field-excitation flux switching synchronous machine for hybrid electric vehicles," *Proceedings of the 2011 14th European Conference on Power Electronics and Applications, (EPE)*, 2011, no. Dc, pp. 1–10.
- [81] K. M. Rahman, B. Fahimi, G. Suresh, A. V. Rajarathnam, and M. Ehsani, "Advantages of switched reluctance motor applications to EV and HEV: design and control issues," *IEEE Trans Ind Appl*, vol. 36, no. 1, pp. 111–121, 2000.
- [82] E. Bin Sulaiman, T. Kosaka, and N. Matsui, "Design study and experimental analysis of wound field flux switching motor for HEV applications," *Proceedings - 2012 20th International Conference on Electrical Machines, (ICEM)*, 2012, pp. 1269–1275.
- [83] S. Ishaq, F. Khan, N. Ahmad, L. U. Rahman, and T. Zaman, "Performance comparison of single phase wound field flux switching machines," *5th International Multi-Topic ICT Conference: Technologies For Future Generations, (IMTIC)*, 2018, pp. 1–6.
- [84] L. J. Wu, Z. Q. Zhu, J. T. Chen, and Z. P. Xia, "An analytical model of unbalanced magnetic force in fractional-slot surface-mounted permanent magnet machines," *IEEE Trans Magn*, vol. 46, no. 7, pp. 2686–2700, 2010.
- [85] J. T. Chen and Z. Q. Zhu, "Comparison of all- and alternate-poles-wound flux-switching pm machines having different stator and rotor pole numbers," *IEEE Trans Ind Appl*, vol. 46, no. 4, pp. 1406–1415, 2010.
- [86] L. J. Wu, Z. Q. Zhu, and M. L. Mohd Jamil, "Unbalanced magnetic force in permanent magnet machines having asymmetric windings and static/ rotating eccentricities," *2013 International Conference on Electrical Machines and Systems, (ICEMS) 2013*, pp. 937–942.
- [87] N. Ahmad, F. Khan, A. Rashid, K. Ayaz, and E. Sulaiman, "Rotor pole study of outer rotor wound field flux switching motor for in-wheel drive," *2018 International Conference on Computing, Mathematics and Engineering Technologies: Invent, Innovate and Integrate for Socioeconomic Development, (iCoMET)*, 2018, vol. 2018-Janua, pp. 1–5.
- [88] S. M. N. S. Othman, L. I. B. Jusoh, M. K. Hassan, G. M. Romalan, and E. Sulaiman, "Rotor pole analysis for 12slot outer-rotor field excitation flux switching motor (ORFEFSM) for an electric vehicle," *2015 IEEE Student Conference on Research and Development, (SCORED)*, 2015, no. 2, pp. 511–516.
- [89] M. Galea, C. Gerada, and T. Hamiti, "Design considerations for an outer rotor, field wound, flux switching machine," *20th International Conference on Electrical Machines (ICEM)*, 2012, pp. 171–176.
- [90] A. Chen, N. Rotevatn, R. Nilssen, and A. Nysveen, "Characteristic investigations of a new three-phase flux-switching permanent magnet machine by FEM simulations and experimental verification," *The 12th International Conference on Electrical Machines and Systems (ICEMS)*, 2009.
- [91] E. Hoang, M. Lecrivain, and M. Gabsi, "A new structure of a switching flux synchronous polyphase machine with hybrid excitation," *European Conference on Power Electronics and Applications (EPE)*, 2007, no. 33, pp. 1–8.
- [92] R. L. Owen, Z. Q. Zhu, and G. W. Jewell, "Hybrid-excited flux-switching permanent-magnet machines with iron flux bridges," *IEEE Trans Magn*, vol. 46, no. 6, pp. 1726–1729, 2010.
- [93] J. T. Chen, Z. Q. Zhu, S. Iwasaki, and R. P. Deodhar, "A novel hybrid-excited switched-flux brushless AC machine for EV/HEV applications," *IEEE Trans Veh Technol*, vol. 60, no. 4, pp. 1365–1373, 2011.
- [94] Y. Yang, X. Yang, P. Chen, and X. Wang, "Electromagnetic performance analysis of hybrid excited segmental rotor flux switching machine," *IEEE Trans Magn*, vol. 54, no. 11, pp. 1–5, 2018.
- [95] Y. Yang, J. Chen, B. Yan, C. Zhu, and X. Wang, "Analytical magnetic field prediction of flux switching machine with segmental rotor," *IET Electr Power Appl*, vol. 13, no. 1, pp. 91–100, 2019.
- [96] H. Ali, E. Sulaiman, Z. Omar, M. F. Omar, F. Amin, and S. Khalidah Rahimi, "Preliminary design investigation of dual stator HEFSM using segmental rotor," *International Journal of Engineering and Technology (UAE)*, vol. 7, no. 2, pp. 77–82, 2018.
- [97] A. Z. dan D. Yusri, "Nonlinear Magnetic Circuit Analysis For a Novel Stator-Doubly-Fed Doubly-Slaint Machine," *Jurnal Ilmu Pendidikan*, vol. 7, no. 2, pp. 809–820, 2020.
- [98] S. N. U. Zakaria and E. Sulaiman, "Magnetic flux analysis of E-Core hybrid excitation flux switching motor with various topologies," *2014 IEEE Asia-Pacific Conference on Applied Electromagnetics (APACE)*, 2015 pp. 95–98.

-
- [99] M. Jenal and E. Sulaiman, "Comparative study on a new permanent magnet flux switching machine configuration over segmental and salient rotor structure," *ARPJ Journal of Engineering and Applied Sciences*, vol. 10, no. 19, pp. 8846–8852, 2015.
- [100] Mohd Fairoz Omar, Erwan Sulaiman, Faisal Khan, Gadafi M Romalan, and Muhammad Kamaluddin Hassan, "Performances Comparison of Various Design Slot Pole of Field Excitation Flux Switching Machines with Segmental Rotor," in *IEEE Conference on Energy Conversion (CENCON): 2015, Johor Bahru*, pp. 320–324.
- [101] F. Meier, *Permanent-Magnet Synchronous Machines with NonOverlapping Concentrated Windings for Low-speed direct-drive applications*. 2008.
- [102] F. Meier and J. Soulard, "PMSMs with Non-Overlapping Concentrated Windings: Design Guidelines and Model References," *Ecological Vehicles and Renewable Energies (EVER)*, 2009, no. September, pp. 26–29.

Review Paper

Hybrid Offshore Wind and Hydrogen Energy Risk Analysis

Ayşe Nuray Canat^{1a}, Coşkun Özkan^{2b}¹Industrial Engineering Department, Faculty of Engineering and Natural Sciences, Istanbul Sabahattin Zaim University, Istanbul, Türkiye²Industrial Engineering Department, Faculty of Mechanical Engineering, Yıldız Technical University, Istanbul, Türkiye

ayse.canat@izu.edu.tr

DOI : 10.31202/ecjse.1420397

Received: 15.01.2024 Accepted: 01.09.2024

How to cite this article:

Ayşe Nuray Canat, Coşkun Özkan, "Hybrid Offshore Wind and Hydrogen Energy Risk Analysis", El-Cezeri Journal of Science and Engineering, Vol: 12, Iss: 2, (2025), pp.(xx-xx).

ORCID: ^a0000-0002-8527-550X; ^b0000-0002-0318-8614.

Abstract : The importance of clean energy is gradually increasing for the depletion of fossil fuels, preventing global warming, and livable and sustainable life. The renewable energies used to achieve this are very diverse. Wind energy and hydrogen energy, which are among these sources, are the subject of this study. In wind energy, it is possible to produce higher power energy by installing wind turbines on the sea, due to the stronger and uninterrupted wind blowing in the seas. There is no continuity of wind energy, it is important to store renewable energy to ensure the continuity of the energy to be supplied to the grid and to create the electricity supply and demand balance. In this study, hydrogen storage energy was preferred in terms of having different usage areas and not harming the environment during energy storage. There are various hazards and associated risks during the installation, transportation, production, and storage of energy production facilities. These risks need to be identified, analyzed, and prevented. In this study, the risks that may be encountered in the offshore wind and hydrogen hybrid power generation and storage facility will be analyzed through a literature review, and evaluations for prevention will be made.

Keywords: Offshore wind energy, hydrogen storage, risk assessment, hazard, hybrid energy.

1. Introduction

The world is facing problems such as global warming, depletion of fossil resources and energy shortages. The Paris Lesson was signed in 2015 to put a stop to this wrong course, to use resources efficiently and to produce environmentally friendly green energy. According to this agreement, taking the necessary measures against the negative effects of climate change will be possible with the right investments in the energy of the countries themselves. To achieve this, countries have given importance to investing in renewable energy sources. With a rapidly increasing momentum, the production of electrical energy is tried to be provided with these resources. One of the sources used for this is offshore wind energy. The fact that the wind blows more strongly in the seas and that there is no obstacle to block the wind, and its continuity has increased the orientation to offshore wind energy. In addition, there is a tendency towards offshore wind farms, since the large turbine to be located does not cause any visual problems and can produce higher energy. However, energy from nature is not continuous and this can lead to problems in meeting energy demand. For this, it is important to provide energy storage in renewable energy sources. In this way, stored energy can be utilized during periods of high energy demand. Energy storage technologies are a field that has been studied extensively in recent years. It has been pointed out in the literature that energy storage technology plays an important role in line congestion management, ensuring power quality, increasing power supply reliability, and absorbing highly renewable energy. [1] Among these technologies, hydrogen energy is preferred because it is both green and has many usage areas in the following years. Comparative studies among energy storage technologies have shown that hydrogen storage energies will play a leading role for future decarbonization targets, while being economically comparable [2]–[4]. The analysis of hydrogen storage and transportation for various forms of hydrogen (compressed hydrogen gas, liquid hydrogen, pipeline hydrogen, liquid organic hydrogen carriers) shows that hydrogen storage and transportation is economical [5]. Hydrogen energy can be obtained in many ways, but electrolysis is the easiest method. There are many reasons why hydrogen is preferred. The first of these is that it can be integrated with renewable energy. Renewable energy sources are utilized for the electrolysis process in the production of green hydrogen. There are many articles in the literature on hydrogen production from renewable energy sources such as solar [6]–[11], geothermal [12]–

[14], biomass [15]–[17], wind [18]–[20] and wave energy [21]–[24]. Obtaining hydrogen by electrolysis alone is more expensive than fossil sources in terms of cost. With the development of technology, it is predicted that prices will be more affordable and supply will become easier [25].

In this study, offshore wind energy and hydrogen energy, among the renewable energy types, which are an important factor of the green energy society, are mentioned and evaluations are made on what the risks are in these branches and how they can be eliminated to ensure the sustainability of development. For a better understanding of the components of the hybrid energy system in this study, a graphical representation of the hybrid energy system is given in Figure 1. Even though both energy types have been produced before, studies have shown that risk assessment has not yet been made at sufficient maturity. When the literature was scanned, specific regions in the energy production part were discussed, and the whole framework was not examined. The novelty of this study is to hybridize these energies, which are two different types of energy, with each other and to analyze this hybrid energy under the headings of hazard, risk, and risk assessment.

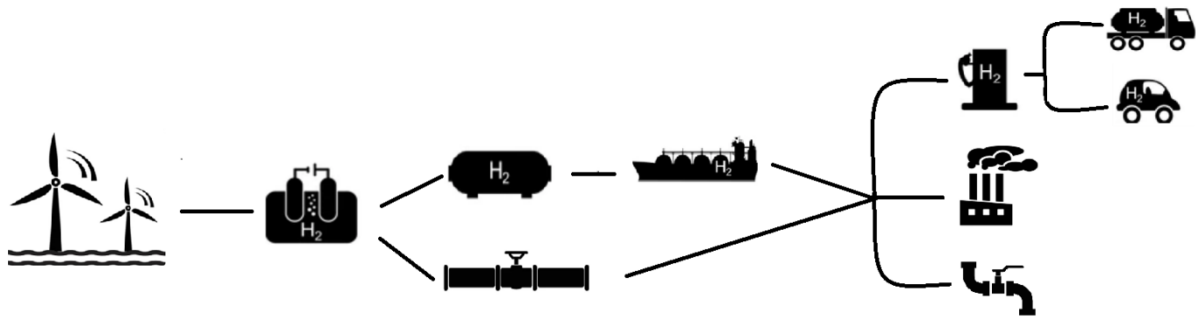


Figure 1. Graphical representation of a hybrid energy system

2. Research Methods

Searches were made with the keyword phrases "offshore wind energy, risk assessment, hazard, risk analysis, risk evaluation, hydrogen energy, energy storage" in article search engines such as WOS (Web of Science), IEEE (Institute of Electrical and Electronics Engineers), and Scopus.

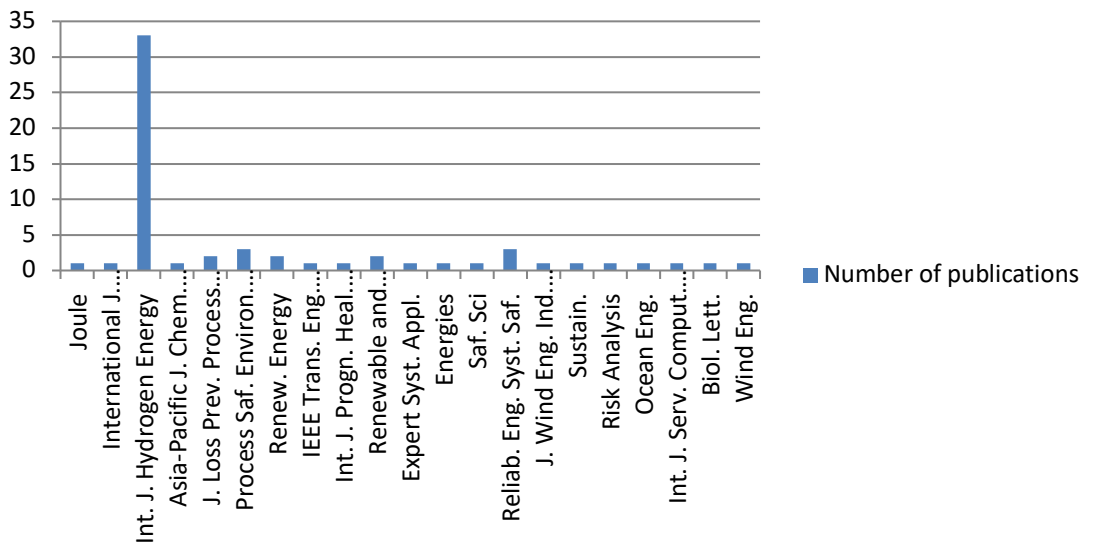


Figure 2. Name of the journals in which the articles were published and the number of articles

The studies found were evaluated from the perspective of risk analysis. As a result of the searches made in search engines, the pie chart of the journals in which the articles on the subject were published and the number of articles is shown in Figure 2. In addition, the percentage of publication of the relevant articles according to journals is shown in Figure 3. The journal in which the most articles related to the subject were published is the International Journal of Hydrogen Energy with a percentage of 55%. In addition, when the research on offshore wind energy and hydrogen energy and storage used as a hybrid was evaluated from the perspective of risk analysis, no article was found that conducted such a study. In the majority of studies on hydrogen energy, it has been observed that there are answers to the questions of what dangers can occur when hydrogen is used as a fuel and how these dangers can be eliminated. In most of the studies on this subject, the dangers of hydrogen filling stations and the precautions to be taken to eliminate these hazards are mentioned. The studies on this subject have been completed with the methods used and the explanations of these methods. Offshore wind energy is one of the topics that has been studied extensively in the literature in recent years. When this issue is narrowed down to hazards, risks and the assessment of these risks, it has been determined that there are not many studies and no detailed examination has been made. The studies carried out are on the accidents that may occur in installation and maintenance-repair and they are few.

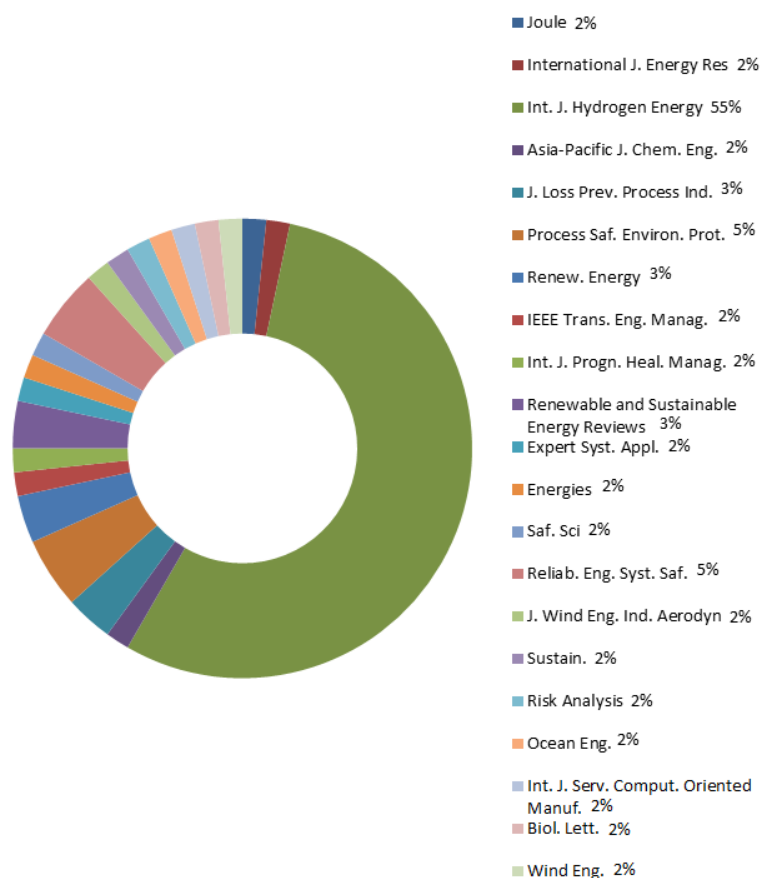


Figure 3. Percentage of related articles published according to journals

3. Risk Analysis and Assessment Studies Related to Hydrogen Energy

The increase in population, the development of technology, and the increasing energy need have increased the search for new energy sources. One of these energy sources is hydrogen energy. Hydrogen energy is seen by the International Energy Agency as one of the energy providers of the future [26]. Hydrogen is an ambitious candidate for green and clean energy when properly produced. But not only the right production method is enough, it is also necessary to ensure safety. For the production, transportation, storage, and use of hydrogen as a fuel, it is necessary to identify the hazards and ensure safety. In Najjar's study on hydrogen energy, these issues were addressed and general information was provided [27]. To achieve net zero emissions by 2050, carbon-free production of hydrogen energy must be achieved. One of the most suitable ways for this is the electrolysis way.

Although electrolysis is an old technology, it is still very new to separate water and use it for hydrogen energy production. There are studies on this, but it is still in its infancy. This is because hydrogen production from fossil sources is currently more cost-effective.

There are studies on the production of hydrogen by electrolysis, but these studies can be evaluated within the field of chemistry. There are only a few studies in which hydrogen is obtained by electrolysis and its risk analysis is done. In this study, 133 possible accident scenarios were evaluated for the system. The effectiveness of the security measures was analyzed and the risks that may arise as a result of the hazards were evaluated with risk matrixes [28]. Another study in which hydrogen production was done by electrolysis method and risk analysis was carried out by Zarei et al. [29]. In the study, uncertainties in hydrogen release scenarios in hydrogen systems are handled holistically and dynamically. The created model was applied to the electrolysis system and a clearer understanding of the accident scenarios related to uncertainty was provided. In the studies on risk analysis and evaluation in hydrogen energy, hazards in hydrogen filling facilities take the first place. Next, come studies examining the risks associated with transporting hydrogen to storage areas. Hydrogen has a lower boiling density due to its structure. In addition, the burning velocity is high with low ignition energy. It can be deflagration-to-detonation-transition. For these reasons, fires pose a great danger to hydrogen plants. It is necessary to take precautions to eliminate this danger.

There are several purposes for assessing risks. The first is to have detailed information about the activities and processes in the system under study and to systematize uncertainties. The other is to assess and identify which of these uncertainties are tolerable and which are not as a result of the analysis. Finally, it is determined what options can be designed in the face of these uncertainties and what applications can be made to reduce the risk. There are inherent uncertainties associated with most risk analysis, especially for complex systems and emerging technologies. The hazard identification process is particularly challenging for industries where there is no framework for systematic reporting of accidents and near misses. There is often insufficient data to estimate exact and current expectation values for event frequencies. Finally, there is significant uncertainty often associated with predicted outcomes. Therefore, the result depends not only on the choice of methodology, data, and tools but also on the experience and competence of the personnel involved. Due to the lack of experience in relatively new technologies and facilities such as hydrogen energy, all possible dangers should be taken into account. The consequences of these dangers should be analyzed in advance so that the necessary measures can be taken.

In technologies up to nuclear energy, risk assessment was not seen as essential for energy production, but rather the hazards were combated by trial and error. After nuclear power, risk research and assessment and making appropriate arrangements have become a priority to prevent potential accidents. Along with the changing energy sources, risk assessment methods applied to these technologies have also developed. The same is true for hydrogen energy production. For this purpose, the HIAD (Hydrogen Incident and Accident Database) was created. In this database, there is information about the accidents that occur in the supply chain from the production process of hydrogen until it reaches the end user. The purpose of keeping this information is to guide future accidents [30]. Various project frameworks were established for this study, in which academics and industry representatives specializing in hydrogen energy sought to provide a basis that would allow the removal of safety-related barriers to the application of hydrogen as an energy carrier.

In some of the studies on hydrogen safety, the hydrogen risk assessment model software toolkit called HyRAM (Hydrogen Risk Assessment Models) is mentioned. In this model, a standard methodology is established, working with relevant quantitative risk assessment and independent outcome analysis, to assess the safety of hydrogen refueling and storage infrastructure [31]. The HyRAM toolkit integrates deterministic and probabilistic models to quantify accident scenarios, predict physical effects, and characterize the impact of hydrogen hazards on people and structures. The main purpose of the paper by Skjold et al. is to demonstrate the use of three-dimensional risk management in the prototype of a hypothetical hydrogen filling station. It also addresses critical knowledge gaps in understanding flame propagation, including the transition from flash to detonation. In the study, a scenario that can be observed as a result of 672 gas emissions was created. While calculating the scenarios, the probability of occurrence was calculated by multiplying the probabilities for the frequency of occurrence, the direction of the leakage of the relevant leakage frequency, the wind condition, sudden (fire) - delayed (burning) ignition, and ignition location [32]. There are similar studies in the literature on this subject, and one of them is the article by the authors Groth and Hecht, in which the current situation and vision of Hyram is discussed. In this article, it is

emphasized that certain points should be considered to improve the system. It is mentioned that various hazard scenarios for using hydrogen infrastructure should include the possibility of progressing with the latest available data, what are the characteristics of physical phenomena in hydrogen releases, what latest data are available to predict the results in ignition events that may cause, and how modeling is done. In addition, subjects such as observable physical values such as injuries and death numbers required to create systemic codes, comparison of risks and facilitating the taking of necessary precautions as a result of this, and obtaining graphics that provide convenience to the end user are emphasized [31].

In the article where HyRAM is explained in the most detailed way, it is stated that this platform was developed by Sandia National Laboratories (SNL) for the Fuel Cell Technologies Office (FCTO) of the US Department of Energy's Energy Efficiency and Renewable Energy Office (EERE). The use of a standardized platform to conduct a Hydrogen Quantitative Risk Assessment (QRA) mentions that it was created to enable various industry stakeholders to produce repeatable, verifiable results. The hydrogen gas emission and jet flame models used in the HyRAM platform were validated against the available experimental and computational data for hydrogen in the parameter range of interest for hydrogen transport systems. Probability data encoded in HyRAM was developed concerning hydrogen data. This report provides technical documentation of algorithms, models, and data included in HyRAM 1.1 [33]. One of the databases containing hydrogen events is the Hydrogen Event Reporting Database, abbreviated as HIRD. In the study, 32 hydrogen processing events selected from HIRD were analyzed to find out their root causes. As a result of the study, a checklist with statistical values about their effects, causes and consequences has been developed to avoid these events. Support for risk assessment is mainly directed towards the analysis of weak points and system optimization. Extending incident analysis and documentation to support various aspects of risk analysis is among the recommendations of this study [34].

It is undoubtedly important to benefit from databases and platforms when assessing risk for hydrogen production, which is considered to be the technology of the future. When talking about hydrogen energy, it should not be seen only as an energy source. Hydrogen is also used as a fuel in new technology vehicles. With the use of hydrogen as a fuel in vehicles, new risk situations have emerged for hydrogen. Both the hazards that may occur when hydrogen is used as a fuel and the hazards during the transportation and storage of the hydrogen to be used for fuel should be carefully analyzed and analyses should be made for the risks that will occur. There are also studies related to this. One of them is the work, which serves as a template for the implementation of a performance-based design method for an outdoor hydrogen refueling station. Performance-based design refers to the specification of a working procedure based on the Society of Fire Protection Engineers (SFPE) Engineering Guidelines for Performance-Based Fire Protection Analysis and Design of Buildings. Code-based requirements are based on the National Fire Protection Association's (NFPA) Hydrogen Technologies Code. Prescriptive requirements are followed whenever possible and used as a point of comparison with performance-based design to create a risk-equivalent design. Many prescriptive requirements in NFPA 2 are based on a quantitative risk assessment process, but requirements such as bulk liquefied hydrogen separation distances have not been updated as such. The SFPE Guidelines define a Fire Protection Engineering Design Brief that documents the early parts of the design and serves as a record of all stakeholder agreements for the methods and performance criteria to be used in evaluating trial designs [35]. Several countries are incentivizing the use of hydrogen (H₂) fuel cell vehicles, thereby increasing the number of hydrogen refueling stations (HRSs), particularly in urban areas with high population density and heavy traffic. Therefore, it is necessary to assess the risks of gaseous hydrogen refueling stations (GHRs) and liquefied hydrogen refueling stations (LHRs). This study aimed to perform a quantitative risk assessment (QRA) of GHRs and LHRs. LHRs present lower hazard risk than GHRs. However, both station types require additional safety barrier devices for risk reduction, such as detachable couplings, hydrogen detection sensors, and automatic and manual emergency shutdown systems, which are required for risk acceptance [36].

The lack of reliable data for on-site bulk liquid hydrogen (LH₂) storage systems at gas stations limits the use of QRAs. This hinders the ability to develop the necessary security codes and standards that enable the worldwide distribution of these stations. This study focuses on identifying relevant scenario and probability data currently available and identifying future data collection requirements regarding risks specific to liquid hydrogen releases, through QRA-based analysis of an LH₂ storage system. The developed work consists of an analysis of a general bulk LH₂ storage system design in a hydrogen fuel station. Based on this analysis, scenario, and reliability data needs are identified to add LH₂-related components to the QRA to improve the future safety and risk assessment

of these systems [37]. There are many quantitative risk assessment studies for hydrogen refueling stations. However, there is no study stating the general framework for all stations. In the study of Honselaar et al., the quantitative risk assessment applied to hydrogen fuel stations in the Netherlands was examined and compared. It has been determined what are the deficiencies and the aspects that need improvement [38]. Another study on liquid hydrogen is on the liquefaction, transport, and storage of hydrogen. In the study conducted by Lowesmith et al., it was stated that hydrogen transport as liquid is more advantageous than gas. The accidents that occurred during the production, transportation, and storage of liquid hydrogen were compiled and the causes of the accident were determined. Statistical evaluations were made on the results of the hazards [39]. Many articles have been written about the dangers of leakage in hydrogen filling stations. Over the years, it has been possible to gain more experience on the subject and to eliminate the dangers with the developing technology. Suzuki et al. conducted a recent quantitative risk assessment on Japanese hydrogen filling stations [40]. Pu et al. studied the leakage of liquid hydrogen in fuel filling stations and public vehicles. In the study, research was conducted on the smoke distribution behavior and what causes it. Relevant hazards were identified and numerical research was carried out [41]. Another risk analysis study related to leakage in hydrogen production plants was done by Chang et al. In this study, a Dynamic Bayesian Network approach methodology is proposed for the risk of hydrogen leakage. Recommendations that can be taken to reduce the risk of leakage of the hydrogen generation unit are presented as critical events. When the relevant evaluations are made, it has been reported that the risk of accidents will be significantly reduced when equipment maintenance and repair are planned and controlled [42]. In another study on the gas hydrogen refueling station, the people affected by the gas leak were categorized. Personnel working at the station were classified as first-degree affected, refueling customers second-degree, and passers-by and those living nearby were classified as third-degree affected. How they were affected by the risk was evaluated [43]. In a similar study, the same categorization was used, but only the results of the compressor's effects were discussed when making the evaluation [44].

Hadef et al. carried out risk analysis and evaluation studies on the hydrogen production system EGA-9000. In the study, process safety analysis was applied with functional and non-functional methods. As a result of the analysis, it was decided that additional security measures should be taken [45]. One of the comprehensive studies on hydrogen safety is the statistical analysis of 120 events based on historical data. Based on the results of this analysis, key issues related to hydrogen safety including hydrogen leakage and diffusion, hydrogen ignition, and explosion are reviewed. The source of the hazards, the reason why they occur, and the solution method are stated [46].

One of the resources used in the hydrogen production process is the natural gas reforming method. The study describing the generation of hydrogen by the natural gas reforming process was done by Jafari et al. In this study, hazard definitions related to the process were made and scenario frequency was estimated using literature data. Quantitative risk methods were used in the study [47]. In the reliability risk model for a hydrogen production facility in an oil refinery, a comprehensive risk analysis framework was created by analyzing major accidents [48]. He drew attention to the importance of using a risk simulator because of the large amount of data used in the study. The explosion risk analysis (ERA) method can be used to investigate potential accidents that may occur in hydrogen production facilities. Using this method alone suffers from significant parametric uncertainty. Thousands of Computational Fluid Dynamics (CFD) scenarios need to be calculated to better understand the uncertainty. These calculations create high costs. A stochastic procedure integrating Bayesian Regulatory Artificial Neural Network (BRANN) methodology with ERA to effectively manage uncertainty and reduce stimulus intensity is presented in this study. With the BRANN method, a lot of data about hydrogen distribution and explosion are generated. The generated data is used to develop scenario-based probability models [49].

Another study on hydrogen infrastructure is on which phase of hydrogen use and transport poses less risk. An attempt was made to determine the estimated hazard distance for each phase, as well as the frequency assessments of risk screening for release, dispersal, fire, and explosion. An optimum design approach has been demonstrated [50]. A comprehensive results analysis of liquid hydrogen boiling liquid expanding vapor explosions (BLEVE) for both small and medium-sized tests has been carried out by evaluating hazard consequences such as pressure waves and fireballs in liquid hydrogen vessels. Theoretical and analytical models were compared with the experimental results and deficiencies were observed [51].

The hazards in the hydrogen production and storage phase should not be identified as only leakage and explosion. When the results of the accident are examined, there are other consequences arising from the fire. These results can be personnel injuries and deaths due to plant/equipment failures caused by high temperature, radiant heat flow, and explosion. A harm criterion is used to translate the consequences of an accident into the probability of harming people, structures, or components. The article by LaChance et al. presents a survey of the different methods that can be used to determine hazard criteria and makes recommendations on criteria that should be used for hydrogen-related hazards [52]. Another study for fire and explosion events at hydrogen refueling stations involved mapping the hydrogen refueling station surroundings with a grid-based risk map. In the study, the region is divided into small parts so that it can be scanned more effectively and in detail. A risk analysis is made for each small piece of settlement, then a collective risk map display is created [53].

A different methodology was used in the study by Kim et al., from the studies on hydrogen infrastructure (production, distribution, and storage). This methodology is a convenient index-based risk assessment model. In the model, the relative risk ranking of hydrogen activities was made and the hydrogen infrastructure was evaluated using the relative impact levels of the different regions where the study was conducted [54].

Hydrogen is stored for different purposes. The first is to reuse hydrogen in power generation when needed. Another is for fuel use by gaseous or liquefying hydrogen. The development of hydrogen storage technologies is as important as producing hydrogen. Because energy can be stored in this era, which creates significant advantages in energy choice. In the study of Moradi and Groth, developments in hydrogen storage technologies were evaluated in terms of safety and reliability [55]. Proton exchange membrane fuel cells are used for hydrogen storage and transport. In this study by Spada et al., a comparative risk assessment of energy-related accidents was conducted by focusing on the hydrogen energy chain and selected fuel cell systems such as proton exchange membrane (PEM), phosphoric acid (PAFC), alkaline (AFC) and molten carbonate (MCFC). Also in the study, the framework created by PSI (Paul Scherrer Institut) for comparative risk assessment is used to comprehensively assess accident risks for hydrogen energy chain and fuel cell systems in the EU28 and compare them with fossil, hydro, and new renewable Technologies [56]. One of the most widely used methods for hydrogen production today is methane steam reforming. Li et al. conducted a study to evaluate the dangers and possible risks of this production method. A new methodology consisting of TOPSIS (Technique for Order Preference by Similarity to Ideal Solution) and Fuzzy DEMATEL (The Decision Making Trial and Evaluation Laboratory) is presented in this study to make a comprehensive risk assessment of the hydrogen production unit [57].

Simulation studies are also carried out to develop strategies to reduce problems in hydrogen safety. Computational fluid dynamics (CFD) methods were used to analyze hydrogen leakage in a semi-enclosed ventilation plant. In the first step, the technological risks of hydrogen were identified and characterized to create a so-called hydrogen energy chain. Later, historical accidents related to the hydrogen chain were collected and added to PSI (Paul Scherrer Institut)'s ENSAD (Energy-related Severe Accident Database) as a separate subsection. Different combinations of hydrogen release pressure and leak hole size were considered in the study. The effectiveness of forced ventilation in semi-enclosed spaces was also investigated. The hydrogen distribution in the aeration plant was studied through experimental research and CFD simulation results were verified [58]. Another article examining studies using the CFD technique was written by Abohamzeh et al. In the study, the works aiming to ensure safety in hydrogen storage, transmission, and application processes has been examined, and mainly CFD studies have been emphasized [46].

Making large-scale deployment and use of hydrogen successfully will require adequate risk control. Despite many years of experience, in general, methods to determine risk lack still robustness: results are highly dependent on choices made by the analyst due to uncertainties, lack of data, and divergent views. This can be disappointing among people depending on the results. A paper talked about current methodological weaknesses and make recommendations for improving quality. Scenario generation will leverage historical incident data and newer methods such as Bayesian belief networks and will cover the entire hydrogen delivery system, not just garages and refueling stations; analyses should more clearly present the confidence intervals for the results. Information gaps will be identified and filled [59]. One of the first studies on the use of Bayesian networks in hydrogen safety applications is the paper by Haugom and Friis-Hansen. In the content of this article, the advantages of using the Bayesian network compared to fault trees and event trees are explained, and this superiority is proven over the virtual hydrogen refueling station [60]. It has been chosen as the subject of another article about what the risk

factors are in hydrogen logistics and how they affect it. While examining this subject, it has been evaluated from the perspective of the network modeling approach. For the study, historical accident databases in hydrogen logistics were examined and related event chains were created. Relevant dependencies have been identified [61]. Hydrogen energy can be transported via pipelines, just like natural gas. Pipeline transportation of hydrogen is mostly similar to natural gas. The different chemical properties of the transported gases and their different reactions to the effects reveal that a separate risk analysis and evaluation process should be performed. Related to this, Lins and Almeida conducted a multidimensional risk analysis of hydrogen pipelines in their study [62]. In another study on the risk analysis of hydrogen transport in natural gas pipelines, many failure events that may occur along the pipeline are discussed. Individual risks in the event of hydrogen jet fire have been evaluated for different scenarios [63]. Many studies have conducted risk assessment studies for the distribution and storage of hydrogen. Moonis et al.'s work is about identifying the data we need to do this risk assessment, finding missing hazard definitions to develop quantitative methodology, and what the gaps are in modeling and frequency assessment. It determines the effects of using ammonia as a hydrogen carrier, and its regulatory applications on hydrogen refueling or landfills [64].

The efficiency of the gas mixture obtained with hydrogen mixed with natural gas is higher than natural gas. This has commercial benefits. This will reduce both installation costs and end-user downtime. However, before hydrogen can provide domestic heat, the 'risk' of its distribution in direct comparison to natural gas needs to be assessed. Quantitative risk assessment has also been carried out for studies where hydrogen is mixed with natural gas and given to the local network. Here, a comprehensive and versatile quantitative risk assessment tool has been developed to assess the 'risk' difference between existing natural gas distribution networks and potential conversion to a hydrogen-based system [65]. In another article examining hydrogen and hydrogen-containing fuel gases, it was mentioned what their dangers could be. In this study, the explosion intervals of hydrogen and hydrogen natural gas mixtures are shown. The dependence of the explosion limits of the mixtures on pressure and temperature was investigated. Maximum experimental safety gaps have been determined for the classification and assignment of mixtures made with hydrogen gas to explosion groups [66]. Other work on injecting hydrogen into natural gas was done by Messaoudani et al. This study does not mention the safe transportation of hydrogen mixed with natural gas, but it is mentioned that there is enough theoretical knowledge on this subject, but the vastness of the experimental data gap [67].

When the studies are examined, there are several existing QRA tools including models developed and approved for use in small-scale hydrogen applications. However, in the last few years, significant progress has been made in the development and validation of deterministic physical and engineering models for hydrogen dispersion, ignition, and flame behavior. In parallel, progress has been made in developing defensible probability models for the occurrence of events such as hydrogen release and ignition. While models and data are available, using this knowledge is difficult due to the lack of ready-made tools to integrate deterministic and probabilistic components into a single analysis framework. This article written by Groth and Tchouvelev discusses the first steps of creating an integrated toolkit to perform QRA on hydrogen transport technologies and proposes guidelines for expanding the toolkit [68].

Many studies have conducted risk assessment studies for the distribution and storage of hydrogen. The work of Moonis et al. is about identifying the data needed to conduct this risk assessment, finding the missing hazard definitions to develop a quantitative methodology, and identifying what the gaps are in modeling and frequency assessment. It determines the effects of using ammonia as a hydrogen carrier, and its regulatory applications on hydrogen refueling or landfills [64].

The comparison tables of the studies we have mentioned regarding the risks in hydrogen energy are given in Table 1. Table 2 shows the usage area of hydrogen and the structural form of hydrogen in the hydrogen energy studies examined.

4. Risk Analysis and Assessment Studies Related to Offshore Wind Energy

Offshore wind farms have a relatively new technology compared to other renewable energy types. For wind turbines to operate with maximum efficiency, the wind must be continuous and the wind speed must be high. Since the seas do not have any blockage compared to the land, they can offer more uninterrupted wind. In

addition, the fact that more offshore wind turbines are larger than onshore wind turbines does not cause any environmental and visual problems. They can have higher energy power. But there are big gaps in where, how, and under what conditions the turbine should be installed. For this, various disciplines come together and try to achieve the optimum result. The location, installation, construction, maintenance, and repair of offshore wind power plants and the formation of energy transmission lines contain many dangers. It is necessary to benefit from various databases, simulations, and analyses to predict the risks that may occur. However, data on offshore power plants and the challenges they face are difficult to find. Since offshore gas and oil fields are based on an older history, a database has been created on these subjects. There are similarities between offshore wind farms and other offshore gas and oil power plants in terms of environmental, logistics, and accessibility. There are only major differences in operational terms. For these reasons and more, it is necessary to establish a database on this subject [72].

Table 1. Comparison table on hydrogen energy risk studies

Reference	Method																						
	FDEMATEL	BTM	DNT	BWM	DBN	CFD	FA	QRA	FEA	HAZID	FAST	HAZOP	RM	ETA	PRA	ERA	BN	GRMM	FMEA	RIM	TOPSIS	NA	
[28]													✓										
[69]		✓	✓	✓	✓																		
[32]						✓	✓	✓	✓														
[33]								✓															
[35]								✓															
[36]								✓															
[37]								✓															
[70]								✓															
[39]									✓														
[40]								✓															
[41]						✓																	
[42]					✓																		
[43]								✓															
[44]								✓															
[45]											✓	✓											
[46]						✓																	
[47]								✓															
[48]								✓															
[49]												✓		✓	✓								
[50]						✓																	
[52]								✓															
[53]																	✓	✓					
[71]																		✓	✓				
[57]	✓																						
[58]						✓																	✓
[59]						✓																	
[60]																	✓						
[61]																							✓
[63]								✓															
[64]										✓			✓										
[65]																							
[66]								✓															
[68]								✓															

Abbreviation: Risk Matrix (RM), Bow-tie method (BTM), D Numbers Theory (DNT), Best-Worst Method (BWM), Dynamic Bayesian Network (DBN), Computational fluid dynamics (CFD), Frequency analysis (FA), Quantitative risk assessment (QRA), Finite element analysis (FEA), HAZID, Functional Analysis System Technique (FAST), HAZOP (HAZard and Operability), Preliminary Risk Analysis (PRA), Event Tree Analysis (ETA), Explosion risk analysis (ERA), Bayesian network (BN), Grid-based risk mapping method (GRMM), Failure mode and effects analysis (FMEA), Risk index method (RIM), Fuzzy DEMATEL (FDEMATEL), TOPSIS, Network Analysis (NA).

In this study, a limited number of articles on offshore wind turbines and power plants have been compiled within the risk framework. Some of the articles are related to maintenance and repair, some to the main part of the turbine and some to the supply chain of wind turbines.

The study by Mogre et al. is about the measures that can be taken to reduce the risks that may occur in the supply chain network in the offshore wind industry. In the study, the relevant literature was scanned and some gaps (such as probability estimation, choice of measure, and assessment of interdependence of risks and precautions) were identified. It is stated that these gaps will be covered with the new decision support methodology to be created [73]. In the study by Dinmohammadi and Shafiee, a different methodological perspective was brought to the risk assessment approach applied to offshore wind turbines. In studies using traditional FMEAs (Failure Mode Effect Analysis), fuzzy set theory was used to clarify expert opinions. The Fuzzy FMEA and Gray theory approach were evaluated on the same data and the results were compared [74]. In the study of Leimeister and Kolios, risk

analysis studies on the offshore industry were compiled and separated by various classifications. As a result of the study, it was observed that qualitative methods were predominantly used due to the lack of sufficient and reliable data in this industry branch [75]. Shafiee's work is a fuzzy analytical network process study to reduce the associated risks in offshore wind farms. The risks specified herein as related risks are; Changes in offshore site layout, Improving maintenance services, Upgrading control and monitoring systems, and Changing the design of wind turbine sub-assemblies are the risks that are predicted to be mitigated [76]. In the study by Luengo and Kolios, the failure modes of offshore wind turbines were defined and various scenarios were discussed for offshore wind turbines that completed their working life [77]. Drilling should be done according to the turbine foundation type to be used when constructing offshore wind farms. Khadzad et al used the bow tie and bayesian network approach to analyze the risks in offshore drilling operations. It has been reported that using the Bayesian network method provides more value than using the bow tie method [78].

Table 2. Risk studies related to hydrogen energy, areas where hydrogen is used and the structural form of hydrogen

Reference	Application Area			The form of hydrogen	
	Production	Construction	Operation and maintenance	Gaseous	Liquid
[27]	✓	✓	✓	✓	
[69]				✓	
[32]				✓	
[33]				✓	
[34]				✓	
[39]	✓	✓	✓		✓
[42]	✓			✓	
[44]				✓	
[45]	✓			✓	
[46]		✓	✓		
[47]	✓			✓	
[48]	✓			✓	
[49]	✓			✓	
[51]			✓		✓
[52]	✓			✓	✓
[53]			✓	✓	
[71]	✓	✓	✓	✓	✓
[55]		✓	✓	✓	
[57]	✓			✓	
[58]			✓	✓	
[59]			✓		
[61]		✓		✓	
[62]		✓			
[63]		✓		✓	
[64]		✓	✓	✓	
[65]		✓		✓	
[66]		✓		✓	
[67]		✓		✓	
[68]		✓		✓	

Working in open sea conditions involves different challenges than working on land. It is necessary to analyze these difficulties and the risks posed by these difficulties. These difficulties cause occupational accidents such as slipping, tripping, and falling from height. In the study of Song et al., a dynamic risk assessment was made for the reduction of occupational accidents, which is called STF (slips, trips and falls from height) for short. Bayesian network approach and bow tie method were also preferred in this study [79]. Offshore wind turbines may differ according to their basic structure. Although not very common yet, it is thought that the use of floating offshore wind turbines will increase day by day. Zhang et al. have conducted a study to have the necessary breakdown and maintenance

information for wind turbines with this foundation type. In the study, the system components were examined, the interrelationship network between them was created and the failure modes analysis was made [80].

In the article written by Tafladinis et al., a risk measurement and assessment was made for an offshore wind turbine exposed to extreme wind and wave conditions. In the study, a simulation study was carried out on the probabilistic characterization of uncertainty. Different risk quantifications are discussed [81].

Nielsen and Sorensen's work is also related to the maintenance of offshore wind turbines. In the study, which evaluates the costs for a single-component wind turbine, it is mentioned that maintenance that is not done on time and properly poses a risk. Risk-based maintenance alternatives are emphasized [82].

In the study of Chou et al., the cause of the accidents occurring during the construction and operation phases of the offshore wind power plant is investigated. Risk management practices at the operational stage were examined. It is in a structure that can be used as a predictive guide for the offshore wind farm personnel planned to be built shortly [83].

Staid and Guikema tried to establish a risk analysis framework for the offshore wind turbine, which was planned to be built for the first time in the United States at the time of the study. An answer has been sought to the question of what dangers the power plants to be built may face in ocean conditions. It has been tried to find answers to the questions of how the risks that may arise as a result of these hazards affect the system [84].

Kang et al. chose the floating turbine model as the offshore wind turbine foundation structure and made a risk assessment based on this basis. The floating turbine foundation structure is still under development and unlike other turbines, it is not driven into the ground with solid piles. It floats on the water with its pontoon system. This situation poses different dangers. In this study, different risks that may occur were evaluated and FMEA application was made together with the PNET method, and the results were evaluated [85].

Gkoumas used Hierarchical Holographic Modeling to analyze the risk of offshore wind turbines in his study. Along with this modeling, he created a large number of risk scenarios organized hierarchically into clusters and subsets [86].

Alvarez et al. used genetic algorithms and simulation methods to manage and, if possible, reduce risks in offshore wind farms. Thanks to these methodologies, generation strategies, and plant layout designs were optimized. In addition, experimental results have been obtained by simulation for the piles to be driven into the seabed depending on the turbine foundation structure [87].

Zhou and Yang conducted a risk management study using the AHP (The analytic hierarchy process) method in distributed wind energy. They classified and evaluated the risks as economic, political, social, and technical risks [88].

Another risk factor for offshore wind farms is bird collisions. Migratory birds migrate towards warm regions during certain seasons and do this in flocks. Offshore wind turbines should not be deployed in these areas. However, this environmental factor has not been taken into account in previous studies. Related to this issue, Desholm and Kahlert conducted a study investigating the risk of bird collisions in offshore wind farms in Denmark [89].

Creating a database for offshore wind farms is an extensive, difficult, and costly activity. This is an important task for offshore wind farms with huge energy potential at a time when renewable sources are being turned to provide the energy consumed on their own. As a result of this study, the risks of power plants can be evaluated in an integrated way. In his study, Ram emphasized that offshore wind power plant decision-makers and stakeholders should have an integrated database to be informed [90].

Various risks may occur during the construction of an offshore wind turbine. Various hazards may occur while loading, transporting, and assembling the turbine parts on the crane. Apart from these, there are additional difficulties brought by the working environment. Bai et al. conducted a study to rate and evaluate the risks posed by these hazards [91].

Gatzert and Kosub present a comprehensive study of the risks of onshore and offshore wind parks. Various sector researches were evaluated mutually and the appropriateness of the risks was determined. The main point of the study is whether the current insurance products cover the risks and if so, to what extent [92].

The comparison tables of the studies we have mentioned regarding the risks in offshore wind energy are given in Table 3.

Table 3. Comparison table for offshore wind energy risk analysis and assessment literature review

Authors	Year	Application Area			Method																			
		Supply Chain	Construction	Operation and maintenance	DSS	FMEA	FFMEA	ANP	AHP	FANP	BTM	BN	SS	FTA	DFTA	BPDT	DEMATEL	PNET	PRA	HMM	GA	SM	RPNM	
(Hameed et al.)	2011			✓																				
(Mogre et al.)	2016	✓			✓																			
(Dinmoham madi & Shafiee)	2013			✓		✓	✓																	
(Shafiee)	2015			✓				✓	✓	✓														
(Luengo& Kolios)	2007			✓																				
(Khakzad et al.)	2013		✓								✓	✓												
(Song et al.)	2016	✓	✓	✓							✓	✓												
(Zhang et al.)	2016		✓	✓														✓						
(Taflanidis et al.)	2013			✓														✓						
(Nielsen& Sorensen)	2011			✓															✓					
(Chou et al.)	2021		✓	✓																✓				
(Kang et al.)	2017			✓		✓															✓			
(Gkoumas)	2010		✓																					
(Álvarez et al.)	2018		✓																			✓	✓	
(Zhou & Yang)	2020		✓	✓								✓												
(Ram)	2011		✓	✓																				
(Bai et al.)	2012	✓	✓			✓																		✓

Abbreviation: Decision support systems (DSS), Failure Mode and Effects Analysis (FMEA), Fuzzy FMEA (FFMEA), Analytic Network Process (ANP), Fuzzy ANP (FANP), Analytical Hierarchy Process (AHP), Bow Tie Methodology (BTM), Bayesian Network (BN), Fault Tree Analysis (FTA), Dynamic FTA (DFTA), Stochastic Simulation (SS), Bayesian pre-posterior decision theory (BPDT), Decision-Making Trial and Evaluation Laboratory (DEMATEL), Probability Network Evaluation Technique (PNET), Probabilistic Risk Analysis (PRA), Hierarchical Holographic Modeling (HMM), Genetic algorithm (GA), simulation model (SM), Risk Priority Number Method (RPNM)

5. Discussion

When the studies are examined, it has been observed that risk analysis and evaluation studies on hybrid energy systems have not been carried out. The examined hydrogen energy studies and offshore wind energy studies are very scattered from a risk perspective. As of yet, no developed database for offshore wind energy describes the causes and consequences of past accidents. This is a major disadvantage for researchers who want to do risk analysis and assessment studies. Offshore gas and oil explorations are leading in this regard. There are databases created on hydrogen energy. The usage area of hydrogen energy alone is quite wide. The database is built on a very large area. The hydrogen energy analyzed in this paper is the part that can be used and stored for electrical energy. But in terms of risk, all hydrogen energy studies are mentioned above.

Since hydrogen has the potential to create danger due to its structure, risk studies are carried out intensively. It is necessary to carry out risk mitigation studies such as the fact that the region where hydrogen is located is not located very close to the residential area, the creation of protection barriers for human safety and the strengthening of structures [53]. Studies should be carried out not only to reduce the potential risk, but also to eliminate the factors that pose risk in the first place. The quality assurance process is important for this [30]. The development and selection of an appropriate risk mitigation strategy for offshore wind farms is a very complex and critical task [76]. Effective risk mitigation and prevention tools are needed for the development of this energy sector [74].

While creating this study, it was considered to generate electricity with an offshore wind power plant and supply it to the grid. In renewable energy types, due to their nature, energy should be consumed as soon as it is produced. In case of low electricity demand supplied to the grid, it should be able to be stored and reused whenever required. Thanks to the research and developing technology, electrical energy storage studies are carried out. Hydrogen energy is a good alternative for energy storage as well as generating electrical energy. The excess energy generated

can be used for electrolysis with platforms to be built on the sea. Hydrogen obtained by electrolysis of seawater can be stored in tanks. If desired, the hydrogen stored in the tanks can be used for different purposes – raw materials for different industries, energy sources, and fuel for hydrogen vehicles.

For these power plants to work properly and uninterruptedly, the system should be evaluated as a whole and the situations that would prevent the system from working should be eliminated. For this reason, this study will guide the joint evaluation of risks in hybrid energy systems and find solutions.

6. Conclusion and Policy Implications

When the literature for hydrogen energy is searched by the terms risk, risk analysis and assessment, hazard, safety, and reliability, the articles after 2010 are mentioned above. Most of the articles are about the use of hydrogen as a fuel in new-generation vehicles. Qualitative and quantitative risk analysis methods were applied for the precautions to be taken against the risks of leakage, explosion, and fire during the transportation, storage, and filling of liquid and gaseous hydrogen at hydrogen filling stations and for possible results. In addition, hydrogen is a substance that can be produced by different methods. The risks that may occur according to the production method are different. The risks and effects that may occur for several different production methods are stated in related studies. In some of the studies carried out to predict the hazards related to hydrogen, simulation programs were used and risk assessments were made for possible accidents. In addition, there are many studies describing hydrogen databases, how they work, and how they rank risks.

Although offshore wind power plants are similar to onshore wind power plants, they face different dangers due to their environment. These differences bring along various risks during installation, maintenance repair, and energy transfer. Risk analysis and assessment studies related to offshore wind power plants are not sufficient. If the previous studies are to be classified, they are mainly related to the construction of the wind turbine. Offshore wind turbine basic structures are diverse. Starting from the drilling for the foundation, the logistics of the turbine materials, and the risks that may occur during the construction of the turbine, the majority of the studies are carried out. The risks posed by ships arriving for maintenance-repair, the risks posed by delayed maintenance for the turbine engine room, the risks posed by the impact of migratory birds, and the risks occurring in the working equipment of the turbine due to environmental effects are the subject of other studies.

In this century, when countries with energy resources are stronger, countries want to gain their energy independence. In countries that do not have fossil resources, what needs to be done is to develop the power of renewable energy sources. Ensuring the supply-demand balance in energy with their resources is the most important point that countries take into consideration while executing their energy policies. To ensure this energy policy, energy production must be sustainable. One of the factors that ensure sustainability is to make risk analyses and assessments correctly and to ensure energy production and distribution. The study provides all the necessary information to serve this purpose through a conceptual study.

Acknowledgments

This research was supported by the Council of Higher Education (YÖK) 100/2000 Doctoral Project.

Authors' Contributions

ANC and CO designed the structure. ANC carried out the work, in collaboration with CO, and wrote up the article. CO is the overall supervisor of the project. Both authors read and approved the final manuscript.

Competing Interests

The authors declare that they have no competing interests.

References

- [1] P. Albertus, J. S. Manser, and S. Litzelman, “Long-Duration Electricity Storage Applications, Economics, and Technologies,” *Joule*, vol. 4, no. 1, pp. 21–32, Jan. 2020, doi: 10.1016/J.JOULE.2019.11.009.
- [2] F. Zhang, P. Zhao, M. Niu, and J. Maddy, “The survey of key technologies in hydrogen energy storage,” *Int. J. Hydrogen Energy*, vol. 41, no. 33, pp. 14535–14552, 2016, doi: 10.1016/j.ijhydene.2016.05.293.
- [3] T. Zhang, “Techno-economic analysis of a nuclear-wind hybrid system with hydrogen storage,” *J. Energy Storage*, vol. 46, no. September 2021, p. 103807, 2022, doi: 10.1016/j.est.2021.103807.
- [4] L. Li et al., “Comparative techno-economic analysis of large-scale renewable energy storage technologies,” *Energy AI*, vol. 14, no. June, p. 100282, 2023, doi: 10.1016/j.egyai.2023.100282.
- [5] Y. Rong et al., “Techno-economic analysis of hydrogen storage and transportation from hydrogen plant to terminal refueling station,” *Int. J. Hydrogen Energy*, vol. 52, pp. 547–558, 2024, doi: 10.1016/j.ijhydene.2023.01.187.
- [6] Y. E. Yüksel and M. Öztürk, “Thermodynamic Analysis of an Integrated Solar-based Chemical Reactor System for Hydrogen Production,” *El-Cezerî J. Sci. Eng.*, vol. 2, no. 2, pp. 19–27, 2015.
- [7] M. Ozturk and I. Dincer, “Thermodynamic analysis of a solar-based multi-generation system with hydrogen production,” *Appl. Therm. Eng.*, vol. 51, no. 1–2, pp. 1235–1244, 2013, doi: 10.1016/j.applthermaleng.2012.11.042.
- [8] Y. Bicer and I. Dincer, “Development of a new solar and geothermal based combined system for hydrogen production,” *Sol. Energy*, vol. 127, pp. 269–284, 2016, doi: 10.1016/j.solener.2016.01.031.
- [9] A. S. Joshi, I. Dincer, and B. V. Reddy, “Effects of various parameters on energy and exergy efficiencies of a solar thermal hydrogen production system,” *Int. J. Hydrogen Energy*, vol. 41, no. 19, pp. 7997–8007, 2016, doi: 10.1016/j.ijhydene.2016.01.025.
- [10] K. Saka and A. S. Canbolat, “an Evaluation on Solar Powered Hydrogen Production,” *Int. J. Energy Eng. Sci.*, vol. 3, no. 2, p. 2016, 2018.
- [11] S. Keykha, E. Assareh, R. Moltames, A. Taghipour, and H. Barati, “Thermoeconomic Analysis And Multi-Objective Optimization Of An Integrated Solar System For Hydrogen Production Using Particle Swarm Optimization Algorithm,” *J. Therm. Eng.*, vol. 7, no. 4, pp. 746–760, 2021, doi: 10.18186/thermal.915413.
- [12] M. Ghazvini, M. Sadeghzadeh, M. H. Ahmadi, S. Moosavi, and F. Pourfayaz, “Geothermal energy use in hydrogen production: A review,” *Int. J. Energy Res.*, vol. 43, no. 14, pp. 7823–7851, 2019, doi: 10.1002/er.4778.
- [13] G. K. Karayel, N. Javani, and I. Dincer, “Effective use of geothermal energy for hydrogen production: A comprehensive application,” *Energy*, vol. 249, p. 123597, 2022, doi: 10.1016/j.energy.2022.123597.
- [14] A. Karapekmez and I. Dincer, “Modelling of hydrogen production from hydrogen sulfide in geothermal power plants,” *Int. J. Hydrogen Energy*, vol. 43, no. 23, pp. 10569–10579, 2018, doi: 10.1016/j.ijhydene.2018.02.020.
- [15] Z. Akyürek, A. Ö. Akyüz, and A. Güngör, “Potential of Hydrogen Production from Pepper Waste Gasification,” *El-Cezerî J. Sci. Eng.*, vol. 6, no. 2, pp. 382–387, 2019, doi: 10.31202/ecjse.532770.
- [16] S. Kaya, B. Ozturk, and H. Aykac, “Hydrogen production from renewable source: Biogas,” *Proc. 2013 Int. Conf. Renew. Energy Res. Appl. ICRERA 2013*, no. October 2013, pp. 633–637, 2013, doi: 10.1109/ICRERA.2013.6749832.
- [17] H. Ishaq and D. Ibrahim, “An Efficient Energy Utilization of Biomass Energy-Based System for Renewable Hydrogen Production and Storage,” *J. Energy Resour. Technol.*, vol. 144, no. 1, p. 011701, 2022.
- [18] R. D’Amore-Domenech and T. J. Leo, “Sustainable Hydrogen Production from Offshore Marine

- Renewable Farms: Techno-Energetic Insight on Seawater Electrolysis Technologies,” ACS Sustain. Chem. Eng., vol. 7, no. 9, pp. 8006–8022, 2019.
- [19] J. Chi and H. Yu, “Water electrolysis based on renewable energy for hydrogen production,” Chinese J. Catal., vol. 39, no. 3, pp. 390–394, Mar. 2018, doi: 10.1016/S1872-2067(17)62949-8.
- [20] H. Dagdougui, A. Ouammi, and R. Sacile, “A regional decision support system for onsite renewable hydrogen production from solar and wind energy sources,” Int. J. Hydrogen Energy, vol. 36, no. 22, pp. 14324–14334, Nov. 2011, doi: 10.1016/J.IJHYDENE.2011.08.050.
- [21] Á. Serna and F. Tadeo, “Offshore hydrogen production from wave energy,” Int. J. Hydrogen Energy, vol. 39, no. 3, pp. 1549–1557, 2014, doi: 10.1016/j.ijhydene.2013.04.113.
- [22] A. Colucci et al., “An inertial system for the production of electricity and hydrogen from sea wave energy,” Ocean. 2015 - MTS/IEEE Washing., pp. 1–10, 2016, doi: 10.23919/oceans.2015.7404569.
- [23] T. C. Moralesa, V. R. Olivab, and L. F. Velázquezc, “Hydrogen from renewable energy in Cuba,” Energy Procedia, vol. 57, pp. 867–876, 2014, doi: 10.1016/j.egypro.2014.10.296.
- [24] F. Posso, J. Sánchez, J. L. Espinoza, and J. Siguencia, “Preliminary estimation of electrolytic hydrogen production potential from renewable energies in Ecuador,” Int. J. Hydrogen Energy, vol. 41, no. 4, pp. 2326–2344, 2016, doi: 10.1016/j.ijhydene.2015.11.155.
- [25] N. Norouzi, “An overview on the renewable hydrogen generation market,” -International J. Energy Res., vol. 7513, no. 1, pp. 1–2, 2021.
- [26] J. M. Bermudez and I. Hannula, “Hydrogen,” IEA, 2021. <https://www.iea.org/reports/hydrogen>
- [27] Y. S. H. Najjar, “Hydrogen safety: The road toward green technology,” Int. J. Hydrogen Energy, vol. 38, no. 25, pp. 10716–10728, Aug. 2013, doi: 10.1016/J.IJHYDENE.2013.05.126.
- [28] N. Kasai, Y. Fujimoto, I. Yamashita, and H. Nagaoka, “The qualitative risk assessment of an electrolytic hydrogen generation system,” Int. J. Hydrogen Energy, vol. 41, no. 30, 2016, doi: 10.1016/j.ijhydene.2016.05.231.
- [29] E. Zarei, F. Khan, and M. Yazdi, “A dynamic risk model to analyze hydrogen infrastructure,” Int. J. Hydrogen Energy, vol. 46, no. 5, 2021, doi: 10.1016/j.ijhydene.2020.10.191.
- [30] M. Cristina Galassi et al., “HIAD – hydrogen incident and accident database,” Int. J. Hydrogen Energy, vol. 37, no. 22, pp. 17351–17357, Nov. 2012, doi: 10.1016/J.IJHYDENE.2012.06.018.
- [31] K. M. Groth and E. S. Hecht, “HyRAM: A methodology and toolkit for quantitative risk assessment of hydrogen systems,” Int. J. Hydrogen Energy, vol. 42, no. 11, 2017, doi: 10.1016/j.ijhydene.2016.07.002.
- [32] T. Skjold et al., “3D risk management for hydrogen installations,” Int. J. Hydrogen Energy, vol. 42, no. 11, 2017, doi: 10.1016/j.ijhydene.2016.07.006.
- [33] K. M. Groth, E. S. Hecht, and J. T. Reynolds, “Methodology for assessing the safety of Hydrogen Systems : HyRAM 1 . 0 technical reference manual,” Sandia Rep., no. March, 2015.
- [34] N. R. Mirza, S. Degenkolbe, and W. Witt, “Analysis of hydrogen incidents to support risk assessment,” Int. J. Hydrogen Energy, vol. 36, no. 18, 2011, doi: 10.1016/j.ijhydene.2011.06.080.
- [35] A. C. LaFleur, A. B. Muna, and K. M. Groth, “Application of quantitative risk assessment for performance-based permitting of hydrogen fueling stations,” Int. J. Hydrogen Energy, vol. 42, no. 11, pp. 7529–7535, Mar. 2017, doi: 10.1016/J.IJHYDENE.2016.06.167.
- [36] B. H. Yoo, S. Wilailak, S. H. Bae, H. R. Gye, and C. J. Lee, “Comparative risk assessment of liquefied and gaseous hydrogen refueling stations,” Int. J. Hydrogen Energy, vol. 46, no. 71, pp. 35511–35524, Oct. 2021, doi: 10.1016/j.ijhydene.2021.08.073.
- [37] C. Correa-Jullian and K. M. Groth, “Data requirements for improving the Quantitative Risk Assessment of liquid hydrogen storage systems,” Int. J. Hydrogen Energy, vol. 47, no. 6, 2022, doi: 10.1016/j.ijhydene.2021.10.266.
- [38] M. Honselaar, G. Pasaoglu, and A. Martens, “Hydrogen refuelling stations in the Netherlands: An

- intercomparison of quantitative risk assessments used for permitting,” *Int. J. Hydrogen Energy*, vol. 43, no. 27, pp. 12278–12294, Jul. 2018, doi: 10.1016/J.IJHYDENE.2018.04.111.
- [39] B. J. Lowesmith, G. Hankinson, and S. Chynoweth, “Safety issues of the liquefaction, storage and transportation of liquid hydrogen: An analysis of incidents and HAZIDS,” *Int. J. Hydrogen Energy*, vol. 39, no. 35, pp. 20516–20521, Dec. 2014, doi: 10.1016/J.IJHYDENE.2014.08.002.
- [40] T. Suzuki et al., “Quantitative risk assessment using a Japanese hydrogen refueling station model,” *Int. J. Hydrogen Energy*, vol. 46, no. 11, pp. 8329–8343, Feb. 2021, doi: 10.1016/J.IJHYDENE.2020.12.035.
- [41] L. Pu, X. Shao, S. Zhang, G. Lei, and Y. Li, “Plume dispersion behaviour and hazard identification for large quantities of liquid hydrogen leakage,” *Asia-Pacific J. Chem. Eng.*, vol. 14, no. 2, 2019, doi: 10.1002/apj.2299.
- [42] Y. Chang, C. Zhang, J. Shi, J. Li, S. Zhang, and G. Chen, “Dynamic Bayesian network based approach for risk analysis of hydrogen generation unit leakage,” *Int. J. Hydrogen Energy*, vol. 44, no. 48, 2019, doi: 10.1016/j.ijhydene.2019.08.065.
- [43] L. Zhiyong, P. Xiangmin, and M. Jianxin, “Quantitative risk assessment on 2010 Expo hydrogen station,” *Int. J. Hydrogen Energy*, vol. 36, no. 6, 2011, doi: 10.1016/j.ijhydene.2010.12.068.
- [44] L. Zhiyong, P. Xiangmin, and M. Jianxin, “Quantitative risk assessment on a gaseous hydrogen refueling station in Shanghai,” *Int. J. Hydrogen Energy*, vol. 35, no. 13, 2010, doi: 10.1016/j.ijhydene.2010.04.031.
- [45] H. Hadeif, B. Negrou, T. G. Ayuso, M. Djebabra, and M. Ramadan, “Preliminary hazard identification for risk assessment on a complex system for hydrogen production,” *Int. J. Hydrogen Energy*, vol. 45, no. 20, 2020, doi: 10.1016/j.ijhydene.2019.10.162.
- [46] E. Abohamzeh, F. Salehi, M. Sheikholeslami, R. Abbassi, and F. Khan, “Review of hydrogen safety during storage, transmission, and applications processes,” *J. Loss Prev. Process Ind.*, vol. 72, p. 104569, Sep. 2021, doi: 10.1016/J.JLP.2021.104569.
- [47] M. J. Jafari, E. Zarei, and N. Badri, “The quantitative risk assessment of a hydrogen generation unit,” *Int. J. Hydrogen Energy*, vol. 37, no. 24, 2012, doi: 10.1016/j.ijhydene.2012.09.082.
- [48] I. Mohammadfam and E. Zarei, “Safety risk modeling and major accidents analysis of hydrogen and natural gas releases: A comprehensive risk analysis framework,” *Int. J. Hydrogen Energy*, vol. 40, no. 39, 2015, doi: 10.1016/j.ijhydene.2015.07.117.
- [49] J. Shi et al., “Stochastic explosion risk analysis of hydrogen production facilities,” *Int. J. Hydrogen Energy*, vol. 45, no. 24, 2020, doi: 10.1016/j.ijhydene.2020.03.040.
- [50] O. R. Hansen, “Hydrogen infrastructure—Efficient risk assessment and design optimization approach to ensure safe and practical solutions,” *Process Saf. Environ. Prot.*, vol. 143, pp. 164–176, Nov. 2020, doi: 10.1016/j.psep.2020.06.028.
- [51] F. Ustolin, N. Paltrinieri, and G. Landucci, “An innovative and comprehensive approach for the consequence analysis of liquid hydrogen vessel explosions,” *J. Loss Prev. Process Ind.*, vol. 68, Nov. 2020, doi: 10.1016/j.jlp.2020.104323.
- [52] J. Lachance, A. Tchouvelev, and A. Engebo, “Development of uniform harm criteria for use in quantitative risk analysis of the hydrogen infrastructure,” *Int. J. Hydrogen Energy*, vol. 36, no. 3, 2011, doi: 10.1016/j.ijhydene.2010.03.139.
- [53] Y. Huang and G. Ma, “A grid-based risk screening method for fire and explosion events of hydrogen refuelling stations,” *Int. J. Hydrogen Energy*, vol. 43, no. 1, pp. 442–454, Jan. 2018, doi: 10.1016/J.IJHYDENE.2017.10.153.
- [54] J. Kim, Y. Lee, and I. Moon, “An index-based risk assessment model for hydrogen infrastructure,” *Int. J. Hydrogen Energy*, vol. 36, no. 11, pp. 6387–6398, Jun. 2011, doi: 10.1016/J.IJHYDENE.2011.02.127.
- [55] R. Moradi and K. M. Groth, “Hydrogen storage and delivery: Review of the state of the art

- technologies and risk and reliability analysis,” *Int. J. Hydrogen Energy*, vol. 44, no. 23, pp. 12254–12269, May 2019, doi: 10.1016/J.IJHYDENE.2019.03.041.
- [56] M. Spada, P. Burgherr, and P. Boutinard Rouelle, “Comparative risk assessment with focus on hydrogen and selected fuel cells: Application to Europe,” *Int. J. Hydrogen Energy*, vol. 43, no. 19, pp. 9470–9481, May 2018, doi: 10.1016/j.ijhydene.2018.04.004.
- [57] X. Li, Z. Han, R. Zhang, Y. Zhang, and L. Zhang, “Risk assessment of hydrogen generation unit considering dependencies using integrated DEMATEL and TOPSIS approach,” *Int. J. Hydrogen Energy*, vol. 45, no. 53, pp. 29630–29642, Oct. 2020, doi: 10.1016/j.ijhydene.2020.07.243.
- [58] A. A. Malakhov, A. V. Avdeenkov, M. H. du Toit, and D. G. Bessarabov, “CFD simulation and experimental study of a hydrogen leak in a semi-closed space with the purpose of risk mitigation,” *Int. J. Hydrogen Energy*, vol. 45, no. 15, pp. 9231–9240, Mar. 2020, doi: 10.1016/j.ijhydene.2020.01.035.
- [59] H. J. Pasman, “Challenges to improve confidence level of risk assessment of hydrogen technologies,” *Int. J. Hydrogen Energy*, vol. 36, no. 3, 2011, doi: 10.1016/j.ijhydene.2010.05.019.
- [60] G. P. Haugom and P. Friis-Hansen, “Risk modelling of a hydrogen refuelling station using Bayesian network,” *Int. J. Hydrogen Energy*, vol. 36, no. 3, 2011, doi: 10.1016/j.ijhydene.2010.04.131.
- [61] C. Y. Lam, M. Fuse, and T. Shimizu, “Assessment of risk factors and effects in hydrogen logistics incidents from a network modeling perspective,” *Int. J. Hydrogen Energy*, vol. 44, no. 36, pp. 20572–20586, Jul. 2019, doi: 10.1016/J.IJHYDENE.2019.05.187.
- [62] P. H. C. Lins and A. T. De Almeida, “Multidimensional risk analysis of hydrogen pipelines,” *Int. J. Hydrogen Energy*, vol. 37, no. 18, pp. 13545–13554, Sep. 2012, doi: 10.1016/J.IJHYDENE.2012.06.078.
- [63] H. A. J. Froeling, M. T. Dröge, G. F. Nane, and A. J. M. Van Wijk, “Quantitative risk analysis of a hazardous jet fire event for hydrogen transport in natural gas transmission pipelines,” *Int. J. Hydrogen Energy*, vol. 46, no. 17, pp. 10411–10422, Mar. 2021, doi: 10.1016/j.ijhydene.2020.11.248.
- [64] M. Moonis, A. J. Wilday, and M. J. Wardman, “Semi-quantitative risk assessment of commercial scale supply chain of hydrogen fuel and implications for industry and society,” *Process Saf. Environ. Prot.*, vol. 88, no. 2, 2010, doi: 10.1016/j.psep.2009.11.006.
- [65] J. Mouli-Castillo, S. R. Haszeldine, K. Kinsella, M. Wheeldon, and A. McIntosh, “A quantitative risk assessment of a domestic property connected to a hydrogen distribution network,” *Int. J. Hydrogen Energy*, vol. 46, no. 29, pp. 16217–16231, Apr. 2021, doi: 10.1016/J.IJHYDENE.2021.02.114.
- [66] M. Molnarne and V. Schroeder, “Hazardous properties of hydrogen and hydrogen containing fuel gases,” *Process Saf. Environ. Prot.*, vol. 130, pp. 1–5, Oct. 2019, doi: 10.1016/j.psep.2019.07.012.
- [67] Z. labidine Messaoudani, F. Rigas, M. D. Binti Hamid, and C. R. Che Hassan, “Hazards, safety and knowledge gaps on hydrogen transmission via natural gas grid: A critical review,” *Int. J. Hydrogen Energy*, vol. 41, no. 39, pp. 17511–17525, Oct. 2016, doi: 10.1016/J.IJHYDENE.2016.07.171.
- [68] K. M. Groth and A. V. Tchouvelev, “A toolkit for integrated deterministic and probabilistic risk assessment for hydrogen infrastructure,” 2014.
- [69] E. Zarei, F. Khan, and M. Yazdi, “A dynamic risk model to analyze hydrogen infrastructure,” *Int. J. Hydrogen Energy*, vol. 46, no. 5, pp. 4626–4643, Jan. 2021, doi: 10.1016/J.IJHYDENE.2020.10.191.
- [70] M. Honselaar, G. Pasaoglu, and A. Martens, “Hydrogen refuelling stations in the Netherlands: An intercomparison of quantitative risk assessments used for permitting,” *Int. J. Hydrogen Energy*, vol. 43, no. 27, pp. 12278–12294, 2018, doi: 10.1016/j.ijhydene.2018.04.111.
- [71] J. Kim, Y. Lee, and I. Moon, “An index-based risk assessment model for hydrogen infrastructure,” *Int. J. Hydrogen Energy*, vol. 36, no. 11, 2011, doi: 10.1016/j.ijhydene.2011.02.127.
- [72] Z. Hameed, J. Vatn, and J. Heggset, “Challenges in the reliability and maintainability data collection

- for offshore wind turbines,” *Renew. Energy*, vol. 36, no. 8, pp. 2154–2165, Aug. 2011, doi: 10.1016/J.RENENE.2011.01.008.
- [73] R. Mogre, S. S. Talluri, and F. Damico, “A decision framework to mitigate supply chain risks: An application in the offshore-wind industry,” *IEEE Trans. Eng. Manag.*, vol. 63, no. 3, 2016, doi: 10.1109/TEM.2016.2567539.
- [74] F. Dinmohammadi and M. Shafiee, “A fuzzy-FMEA risk assessment approach for offshore wind turbines,” *Int. J. Progn. Heal. Manag.*, vol. 4, no. SPECIAL ISSUE 2, 2013, doi: 10.36001/ijphm.2013.v4i3.2143.
- [75] M. Leimeister and A. Kolios, “A review of reliability-based methods for risk analysis and their application in the offshore wind industry,” *Renewable and Sustainable Energy Reviews*, vol. 91, 2018. doi: 10.1016/j.rser.2018.04.004.
- [76] M. Shafiee, “A fuzzy analytic network process model to mitigate the risks associated with offshore wind farms,” *Expert Syst. Appl.*, vol. 42, no. 4, pp. 2143–2152, Mar. 2015, doi: 10.1016/J.ESWA.2014.10.019.
- [77] M. M. Luengo and A. Kolios, “Failure Mode Identification and End of Life Scenarios of Offshore Wind Turbines: A Review,” vol. 8, pp. 8339–8354, 2007, doi: 10.3390/en8088339.
- [78] N. Khakzad, F. Khan, and P. Amyotte, “Quantitative risk analysis of offshore drilling operations: A Bayesian approach,” *Saf. Sci.*, vol. 57, 2013, doi: 10.1016/j.ssci.2013.01.022.
- [79] G. Song, F. Khan, H. Wang, S. Leighton, Z. Yuan, and H. Liu, “Dynamic occupational risk model for offshore operations in harsh environments,” *Reliab. Eng. Syst. Saf.*, vol. 150, pp. 58–64, Jun. 2016, doi: 10.1016/J.RESS.2016.01.021.
- [80] X. Zhang, L. Sun, H. Sun, Q. Guo, and X. Bai, “Floating offshore wind turbine reliability analysis based on system grading and dynamic FTA,” *J. Wind Eng. Ind. Aerodyn.*, vol. 154, pp. 21–33, Jul. 2016, doi: 10.1016/J.JWEIA.2016.04.005.
- [81] A. A. Taflanidis, E. Loukogeorgaki, and D. C. Angelides, “Offshore wind turbine risk quantification/evaluation under extreme environmental conditions,” *Reliab. Eng. Syst. Saf.*, vol. 115, 2013, doi: 10.1016/j.res.2013.02.003.
- [82] J. J. Nielsen and J. D. Sørensen, “On risk-based operation and maintenance of offshore wind turbine components,” in *Reliability Engineering and System Safety*, 2011, vol. 96, no. 1. doi: 10.1016/j.res.2010.07.007.
- [83] J. S. Chou, P. C. Liao, and C. Da Yeh, “Risk analysis and management of construction and operations in offshore wind power project,” *Sustain.*, vol. 13, no. 13, 2021, doi: 10.3390/su13137473.
- [84] A. Staid and S. D. Guikema, “Risk Analysis for U.S. Offshore Wind Farms: The Need for an Integrated Approach,” *Risk Analysis*, vol. 35, no. 4, 2015. doi: 10.1111/risa.12324.
- [85] J. Kang, L. Sun, H. Sun, and C. Wu, “Risk assessment of floating offshore wind turbine based on correlation-FMEA,” *Ocean Eng.*, vol. 129, 2017, doi: 10.1016/j.oceaneng.2016.11.048.
- [86] K. Gkoumas, “A risk analysis framework for offshore wind turbines,” 2010. doi: 10.1061/41096(366)179.
- [87] D. C. Álvarez, A. L. Rodríguez, and J. A. M. Dono, “Risk management and design of mitigation plans through discrete events simulation and genetic algorithms in offshore wind processes,” *Int. J. Serv. Comput. Oriented Manuf.*, vol. 3, pp. 274–292, 2018.
- [88] S. Zhou and P. Yang, “Risk management in distributed wind energy implementing Analytic Hierarchy Process,” *Renew. Energy*, vol. 150, 2020, doi: 10.1016/j.renene.2019.12.125.
- [89] M. Desholm and J. Kahlert, “Avian collision risk at an offshore wind farm,” *Biol. Lett.*, vol. 1, no. 3, pp. 296–298, 2005, doi: 10.1098/rsbl.2005.0336.
- [90] B. Ram, “Assessing integrated risks of offshore wind projects: Moving towards gigawatt-scale deployments,” *Wind Eng.*, vol. 35, no. 3, 2011, doi: 10.1260/0309-524X.35.3.247.

- [91] X. Bai, L. Sun, and H. Sun, "Risk assessment of hoisting aboard and installation for offshore wind turbine," in *Proceedings of the International Conference on Offshore Mechanics and Arctic Engineering - OMAE*, 2012, vol. 2, pp. 107–144. doi: 10.1115/OMAE2012-83187.
- [92] N. Gatzert and T. Kosub, "Risks and risk management of renewable energy projects: The case of onshore and offshore wind parks," *Renew. Sustain. Energy Rev.*, vol. 60, pp. 982–998, Jul. 2016, doi: 10.1016/J.RSER.2016.01.103.

Research Article

Synthesis and Biological Activities of Some 1, 3, 4-thiadiazine Derivatives

Serife Kaymakçı Buldu^{1a}, Erdal Kocabaş^{2b}, Deniz Tuğçe Algan^{3c} Ahmet Burak Sarıgüney^{4d}
Fatih Erci^{2e} Ahmet Coşkun^{1f}

¹ Chemistry Department, Necmettin Erbakan University, Konya, Türkiye

² Biotechnology Department, Necmettin Erbakan University, Konya, Türkiye

³ Chemistry Department, Institute of Science, Necmettin Erbakan University, Konya, Türkiye

⁴ Basic Sciences Department, Necmettin Erbakan University, Konya, Türkiye

ekocabas@erbakan.edu.tr

DOI : 10.31202/ecjse.1433362

Received: 22.07.2024 Accepted: 25.11.2024

How to cite this article:

Şerife Kaymakçı Buldu, Erdal Kocabaş, Deniz Tuğçe Algan, Ahmet Burak Sarıgüney, Fatih Erci, Ahmet Coşkun, " Synthesis and Biological Activities of Some 1, 3, 4-thiadiazine Derivatives ", El-Cezeri Journal of Science and Engineering, Vol: 12, Iss: 2, (2025), pp.(121-126).

ORCID: "0000-003-3435-3210; ^b 0000-0002-0980-0984; ^c 0000-0002-0085-4327; ^d 0000-0003-0815-1578; ^e 0000-0002-3044-7374;

^f 0000-0002-8992-3754.

Abstract : In this study, some 1,3,4-thiadiazine derivatives were synthesized by condensation of appropriate acetophenone derivatives and thiosemicarbazides because of their wide range of biological applications. Structures of synthesized compounds characterized by ¹H NMR and FTIR techniques and evaluated as potential antibacterial or antioxidant agents. The activities of the compounds against *Staphylococcus aureus* (*S. aureus*), *Bacillus cereus* (*B. cereus*), *Escherichia coli* (*E. coli*), and *Salmonella typhimurium* (*S. typhimurium*) were evaluated by the Kirby-Bauer disk diffusion method. From the results, it is clear that the compounds (4) and (5) have stronger activity against Gram-positive bacteria but show no inhibition against Gram-negative bacteria. In addition, the DPPH radical scavenging activity of the compounds was determined by microplate assay with various concentrations of the test compounds. Among the synthesized compounds, (4), (5) and (2) showed the highest interactions. The result showed that the DPPH scavenging activity of compounds also appeared to depend on an increase in concentration. The findings of this work have significance in view of the possibility to design new 1, 3, 4-thiadiazine derivatives with improved potency and activity.

Keywords : 1, 3, 4-thiadiazine; antibacterial activity; DPPH radical; ¹H NMR; FTIR.

1 Introduction

Human pathogens can cause a variety of serious infections, and the recent increase in multidrug resistance in pathogens has created an urgent and worrying need for new and potent antimicrobial agents. The World Health Organization (WHO) published a list of antibiotic-resistant bacteria urgently needed for new treatments in the mid-2000s. Strains to be developed in this process are the most effective strategy to counter the rise of multidrug-resistant (MDR) organisms [1]–[3]. Therefore, the new design and synthesis of heterocyclic compounds, including Nitrogen and sulfur, are very important as they have a wide range of biological applications [4], [5]. Among heterocyclic compounds, 1, 3, 4-thiadiazine scaffolds have been found to have good antimicrobial [6], anticancer [7], [8], analgesic, anticandidal [6], anti-inflammatory, antiaggregant, antitumor, and antioxidant activities [9]. In addition, thiadiazine-thione derivatives are also involved in the treatment of atherosclerosis and have antifibrinolytic, cytotoxic and antiepileptic activities. Furthermore, Thiadiazine-thione derivatives have been investigated as potential components of prodrugs for various biological activities [10]. Also, 3-Nitrobenzyl-5-aryl-1,3,4-thiadiazine-2-one and 1,3,4-thiadiazine-2-one derivatives are used for the treatment of tumors and AIDS because of their Phosphodiesterase 4 inhibitory abilities [11].

Thiazole and thiadiazine derivatives, in addition to their antimicrobial, antifungal, antihypertensive, cardiostimulant, antiviral, anti-inflammatory, analgesic, and antioxidant activities, may be good candidates for antidiabetic drug development. Steroidal 1,3,4-thiadiazines exhibit anticancer, antitumor, antimicrobial, and antibacterial properties. Heterocyclic thiadiazole systems, which enhance interactions with biomolecules, show a natural mesoionic structure that offers low toxicity, high in vivo stability, and good cell and tissue permeability [12]–[14]. Since 1,3,4-thiadiazine derivatives have biological and pharmaceutical importance, they can be considered starting points for the production of pharmacologically active substances [15].

In this study, we designed and synthesized a series of 1, 3, and 4-thiadiazine derivatives whose structures were characterized by FTIR and ¹H NMR. The in vitro susceptibilities of the Gram-positive and Gram-negative bacteria to the synthesized thiadiazine

derivatives were analysed using disk diffusion assays. The radical-scavenging capacity of the compounds was evaluated using the DPPH radical-scavenging assay.

2 Experimental Methods

2.1 Materials

All solvents and reagents were analytical grade and purchased from Sigma-Aldrich. An EZ-Melt Automated Melting Point Apparatus was used to determine melting points. Infrared spectra of the compounds were recorded using a Thermo Nicolet IS5 FTIR spectrometer. In addition, ¹H NMR spectra of the compounds were determined using a Varian 400 MHz NMR Spectrometer in DMSO-d₆ by expressing chemical shifts as δ ppm.

2.2 Biologic Materials And Apparatus

Lyophilized Gram-positive and Gram-negative bacteria cultures were purchased from Microbiologics Inc. (Saint Cloud, MN, USA). Bacterial strains were stored in Nutrient Broth with 20 % glycerol at -18 °C. The antioxidant capacity of the compounds was determined by the DPPH (1,1-diphenyl-2-picrylhydrazil) radical-scavenging assay). The experiment was carried out on the 96-well microplate using the Herald method [16].

2.3 Chemistry

Substituted 1,3,4-thiadiazine derivatives synthesized according to the method described in the literature [17]. However, we determined with TLC that our reactions did not occur in 20 minutes at room temperature as stated in the literature. Therefore, unlike the literature, we observed by following our reactions with TLC that they were completed in 6 hours under reflux. Compounds N-ethyl-5-(4-phenoxyphenyl)-6H-1,3,4-thiadiazine-2-amine 1, N-ethyl-5-(3-nitrophenyl)-6H-1,3,4-thiadiazine-2-amine 3, and N-ethyl-5-(4-nitrophenyl)-6H-1,3,4-thiadiazine-2-amine 7 were first synthesized in this study.

2.3.1 General procedure for the synthesis of 1, 3, 4- thiadiazine derivatives

Acetophenone derivative (1 mmol) and thiosemicarbazide (1 mmol) in 5 mL ethanol with a few drops of dil. hydrochloric acid was refluxed for 6 h. The reaction was followed by TLC. After completion of reaction, pH adjusted to 8-9 by adding of Ammonia solution. The precipitate was filtered and crystallized from ethanol to give 1,3,4-thiadiazine derivatives.

2.4 Biological Assay

2.4.1 Antibacterial activity assay

Lyophilized cultures of *B. cereus* (ATCC 11778), *S. aureus* (ATCC 25923), *E. coli* (ATCC 25922), and *S. typhimurium* (ATCC 14028) were obtained from Microbiologics Inc. (Saint Cloud, MN, USA). The antibacterial activity of the compounds was evaluated using the Kirby-Bauer disk diffusion method. Stock solutions of the compounds were prepared using dimethyl sulfoxide (DMSO). Each bacterial strain was separately inoculated into cation-adjusted Mueller Hinton broth (MHB; BD, Auckland, New Zealand) and incubated at 37°C for 24 hours. The bacterial suspensions were then standardized to a 0.5 MacFarland opacity standard (1.5×10^8 colony-forming units (CFU)/mL) and spread onto cation-adjusted Mueller Hinton agar (MHA, Lab M, UK) plates before placing sterile paper disks (6 mm diameter; BD, Auckland, New Zealand) equidistantly on the plate. 10 μ L of the compounds from stock solutions were then added to the disks. The plates were incubated at 37°C for 24h, and the diameter of the zone of inhibition, which indicated the antimicrobial activity of the compounds, was calculated in millimeters using a ruler. Gentamicin (10 μ g discs) was used as a reference antibacterial agent. DMSO alone (20 μ L) was used as a negative control, and experiments were performed in duplicate.

2.4.2 *In vitro* antioxidant study

The DPPH radical-scavenging activity was assessed using a microplate assay based on a modified version of the Herald method. The scavenging potential of the compounds against the DPPH radical was tested at various concentrations (25, 50, 100, 200, and 400 μ g/mL). For the assay, 20 μ L of the diluted sample was mixed with 180 μ L of DPPH solution (150 μ) in a methanol-water mixture (80:20, v/v) and shaken for 60 seconds in a 96-well microtiter plate. Following a 40-minute incubation in the dark at room temperature, absorbance was recorded at 515 nm using a Thermo Scientific Multiskan GO spectrophotometer (ThermoFisher Scientific, MA, USA). Ascorbic acid served as the standard for comparison.

$$\%DPPHScavenging = 100 \times \frac{[(AbsSample + DPPH) - (AbsBlank)]}{[(AbsControl) - (AbsBlank)]} \quad (1)$$

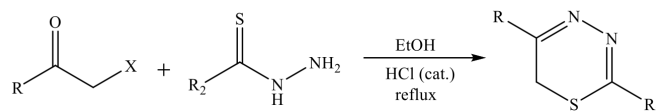
Abs (sample); Absorbance of 20 μ L sample or standard with 180 μ L DPPH solution

Abs (blank); Absorbance of 180 μ L of methanol-water (80 : 20, v/v) and 20 μ L of water

3 Results and Discussion

3.1 Synthesis and Characterization

Substituted 1,3,4-thiadiazine derivatives were prepared via condensation of α -haloketones and thiosemicarbazides as shown in Scheme 1. Structures of synthesized compounds were confirmed by FTIR and ¹H NMR spectroscopic techniques.



	R	X	R ₂
(1)	Ph-O-Ph-	-Cl	-N-Ethyl
(2)	3-NO ₂ -Ph-	-Br	-NH ₂
(3)	3-NO ₂ -Ph-	-Br	-N-Ethyl
(4)	4-Br-Ph-	-Br	-NH ₂
(5)	4-Cl-Ph-	-Br	-NH ₂
(6)	4-NO ₂ -Ph-	-Br	-NH ₂
(7)	4-NO ₂ -Ph-	-Br	-N-Ethyl

	R	X	R ₂
(1)	Ph-O-Ph-	-Cl	-N-Ethyl
(2)	3-NO ₂ -Ph-	-Br	-NH ₂
(3)	3-NO ₂ -Ph-	-Br	-NH ₂
(4)	4-Br-Ph-	-Br	-NH ₂
(5)	4-Cl-Ph-	-Br	-NH ₂
(6)	4-NO ₂ -Ph-	-Br	-NH ₂
(7)	4-NO ₂ -Ph-	-Br	-N-Ethyl

Table 1: Synthetic pathway for synthesis of compounds

N-ethyl-5-(4-phenoxyphenyl)-6H-1,3,4-thiadiazine-2-amine (1): Yellow crystals. Yield 56 %. mp.: 156–158 °C; FTIR (cm⁻¹): 3171, 2968, 1734, 1700, 1636, 1590, 1470, 1412, 1255, 1152, 986, 855, 749, 988; ¹H NMR (400 MHz, DMSO): δ = 7.90 (s, 1H, NH), 6.9-7.19 (m, 9H, Ar-H), 3.35-3.4 (m, 2H, NCH₂), 3.80 (s, 2H, CH₂S), 1.15 (t, 3H, CH₃).

5-(3-nitrophenyl)-6H-1,3,4-thiadiazine-2-amine (2): Green crystals. Yield 89 %. mp.: 149- 153 °C; FTIR (cm⁻¹): 3386, 3366, 3129, 1617, 1507, 1340, 1168, 959, 800, 712, 669; ¹H NMR (400 MHz, DMSO): δ = 9.44 (s, 2H, NH₂), 7.64-7.84 (m, 4H, Ar-H), 4.35 (s, 2H, CH₂S).

N-ethyl-5-(3-nitrophenyl)-6H-1,3,4-thiadiazine-2-amine (3): Yellow crystals. Yield 66 %. mp.: 169- 172 °C; FTIR (cm⁻¹): 3180, 2971, 2862, 1733, 1700, 1653, 1517, 1345, 1258, 1058, 890, 732, 605; ¹H NMR (400 MHz, DMSO): δ = 8.75 (s, 1H, NH), 7.5-8.1 (m, 4H, Ar-H), 3.60 (q, 2H, NCH₂), 3.96 (s, 2H, CH₂S), 1.3 (t, 3H, CH₃).

5-(4-bromophenyl)-6H-1,3,4-thiadiazine-2-amine (4): White crystals. Yield 68 %. mp.: 198- 200 °C; FTIR (cm⁻¹): 3321, 3050, 1660, 1601, 1568, 1478, 1397, 1341, 1283, 1189, 952, 900, 829, 731, 695; ¹H NMR (400 MHz, DMSO): δ = 9.97 (s, 2H, NH₂), 7.61-7.86 (m, 4H, Ar-H), 4.26 (s, 2H, CH₂S).

5-(4-(chlorophenyl)-6H-1,3,4-thiadiazine-2-amine (5): Light brown crystals. Yield 60 %. mp.: 179- 182 °C; FTIR (cm⁻¹): 3370, 3078, 1652, 1491, 1408, 1116, 1011, 830, 756, 595; ¹H NMR (400 MHz, DMSO): δ = 7.52-7.55 (m, 4H, Ar-H), 3.94 (s, 2H, CH₂S).

5-(4-nitrophenyl)-6H-1,3,4-thiadiazine-2-amine (6): Light green crystals. Yield 75 %. mp.: 209- 210 °C; FTIR (cm⁻¹): 3380, 3165, 2888, 1672, 1595, 1513, 1325, 1106, 1005, 854, 750, 666; ¹H NMR (400 MHz, DMSO): δ = 10.1 (s, 2H, NH₂), 8.11-8.17 (m, 4H, Ar-H), 4.33 (s, 2H, CH₂S).

N-ethyl-5-(4-nitrophenyl)-6H-1,3,4-thiadiazine-2-amine (7): Orange crystals. Yield 66 %. mp.: 126- 128 °C; FTIR (cm⁻¹): 3146, 2972, 2799, 1596, 1499, 1465, 1336, 1275, 1218, 1147, 1107, 995, 750, 692, 566; ¹H NMR (400 MHz, DMSO): δ = 8.38 (s, 1H, NH), 8.04 (d, 2H, Ar-H), 7.2-7.5 (m, 2H, Ar-H), 3.37-3.42 (m, 2H, NCH₂), 3.76 (s, 2H, CH₂S), 1.14 (t, 3H, CH₃).

The FTIR spectrum of the thiadiazine derivatives showed peaks at 3050-3386 cm⁻¹; -NH or -NH₂ stretching, 1596-1672 cm⁻¹; -C=N stretching. The ¹H NMR spectrum of synthesized compounds showed δ 3.76-4.35 (-CH₂S-) thiadiazine ring -CH- proton peak. All aromatic protons were assigned between δ 6.9 and 8.17 ppm. The antimicrobial activity of the selected microorganisms against the samples was evaluated using the disk diffusion assay. The diameters of the inhibition zone (mm) around the disks containing the samples are presented in Figures 1 and 2. The findings indicated that samples (4) and (5) exhibited activity against *S. aureus* and *B. cereus* but failed to produce inhibition zones against the Gram-negative bacteria *E. coli* and *S. typhimurium*. Specifically, sample (4) demonstrated inhibition zones of 8.47 \pm 0.45 mm and 8.33 \pm 0.35 mm against *S. aureus* and *B. cereus*, respectively. In contrast, sample (5) exhibited the highest activity, forming inhibition zones of 9.77 \pm 0.47 mm and 10.40 \pm 0.40 mm against *S. aureus* and *B. cereus*, respectively. Other tested compounds showed no antibacterial activity against either bacterial group. The stronger activity of samples (4) and (5) against Gram-positive bacteria, while being ineffective against Gram-negative bacteria, can be attributed to structural differences, such as the presence of an additional outer membrane in

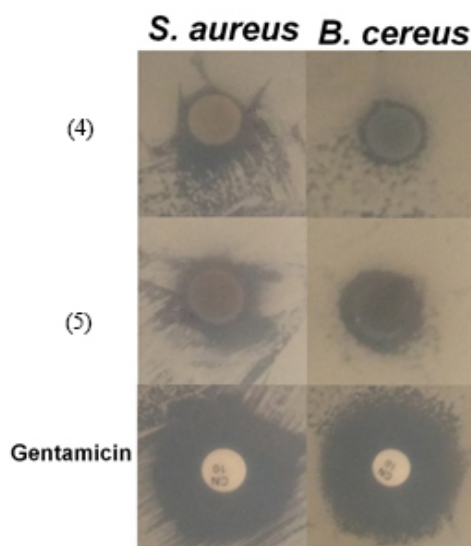


Figure 1: Inhibition zones of the compounds and Gentamicin against tested microorganisms on Muller Hinton agar

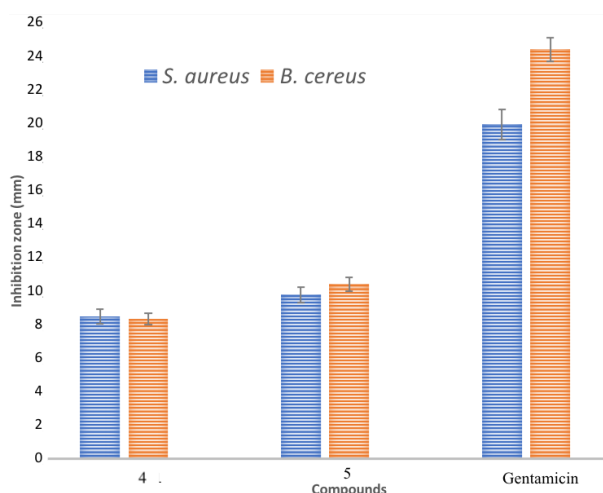


Figure 2: Inhibition zones of the compounds and Gentamicin against tested microorganisms by disc diffusion method

Gram-negative bacteria, which acts as a barrier to many antibacterial agents. [18], [19]. In the evaluation of antioxidant activities in a shorter time, the scavenging activity of the DPPH radical, which can accept an electron or hydrogen radical and thus be converted into a stable diamagnetic molecule, is widely used [20], [21]. We determined the reducing abilities of the synthesized compounds using the 1,1-diphenyl-1-picrylhydrazyl (DPPH) free radical scavenging assay compared to those of the free drug and ascorbic acid.

The DPPH radical scavenging model is a widely used method for assessing antioxidant activity in a shorter time compared to other techniques. DPPH is a stable free radical capable of accepting an electron or hydrogen atom and transforming into a stable, nonmagnetic molecule. The reducing potential of the complexes was determined using the 1,1-diphenyl-1-picrylhydrazyl (DPPH) assay, which reflects their ability to act as reducing agents. The scavenging efficiency of the complexes was evaluated and compared with that of the free drug and ascorbic acid. [22].

According to the results, it was found that not all of the compounds tested interact with the stable free radical DPPH. Among the synthesized compounds, compound 4 showed the highest DPPH scavenging activity because it had fewer electron-withdrawing groups than other compounds. The DPPH radical scavenging activity of all samples was observed to be dependent on the concentration.

4 Conclusion

In this study, we synthesized, characterized, and determined the antibacterial and antioxidant activities of some 1,3,4-thiadiazine derivatives. Among the synthesized compounds, (4) and (5) showed stronger activity against Gram-positive bacteria *S. aureus* and *B. cereus* but did not show any antibacterial activity against Gram-negative bacteria *E. coli* and *S. typhimurium*. In addition,

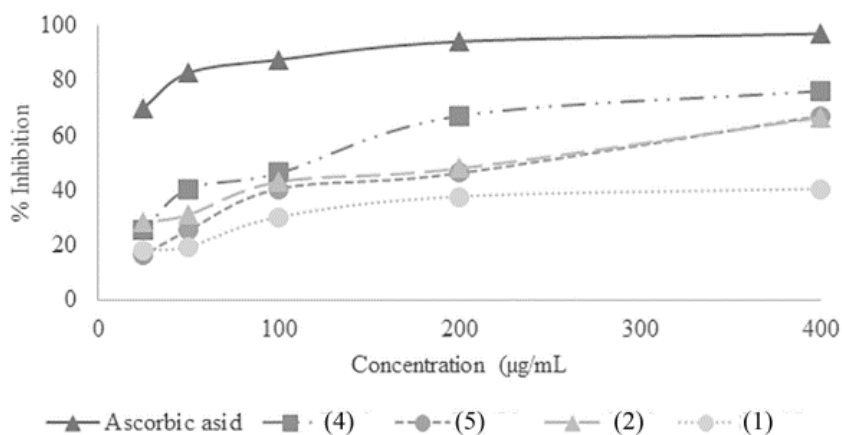


Figure 3: DPPH free radical scavenging activity of the compounds

the results showed that compounds (4), (5), and (2) had the strongest interactions with DPPH. These findings have obvious implications for the possibility of designing new 1,3,4-thiadiazine derivatives with improved potency and activity for use in different applications in various fields.

Acknowledgments

The authors would like to acknowledge the support of Necmettin Erbakan University.

EK and ŞKB designed the synthesis scheme. ŞKB performed the syntheses. AC and EK interpreted the structure characterization of the synthesized compounds. FE performed antimicrobial and antioxidant studies. DTA and ABS wrote the article in collaboration with EK. ABS, EK, and AC read and approved the final version of the manuscript. EK is the corresponding author of the article.

References

- [1] M. Dinarvand and M. Spain, "Identification of bioactive compounds from marine natural products and exploration of structure-activity relationships (sar)," *Antibiotics*, vol. 10, no. 3, p. 337, 2021.
- [2] E. Bentivegna, M. Luciani, L. Arcari, I. Santino, M. Simmaco, and P. Martelletti, "Reduction of multidrug-resistant (mdr) bacterial infections during the covid-19 pandemic: a retrospective study," *International journal of environmental research and public health*, vol. 18, no. 3, p. 1003, 2021.
- [3] T. M. Terreni, Marco and M. Pregnotato, "New antibiotics for multidrug-resistant bacterial strains: latest research developments and future perspectives," *Molecules*, vol. 26, no. 9, p. 2671, 2021.
- [4] P. C. Jilloju, L. Persoons, S. K. Kurapati, D. Schols, S. De Jonghe, D. Daelemans, and R. R. Vedula, "Discovery of (\pm)-3-(1 h-pyrazol-1-yl)-6, 7-dihydro-5 h-[1, 2, 4] triazolo [3, 4-b][1, 3, 4] thiadiazine derivatives with promising in vitro anticoronavirus and antitumoral activity," *Molecular Diversity*, vol. 26, no. 3, pp. 1357–1371, 2022.
- [5] S. Chhabra and K. Shah, "The novel scaffold 1, 2, 4-benzothiadiazine-1, 1-dioxide: a review," *Medicinal Chemistry Research*, vol. 30, pp. 15–30, 2021.
- [6] C. Kamoutsis, M. Fesatidou, A. Petrou, A. Geronikaki, V. Poroikov, M. Ivanov, M. Soković, A. Ćirić, A. Carazo, and P. Mladěnka, "Triazolo based-thiadiazole derivatives. synthesis, biological evaluation and molecular docking studies," *Antibiotics*, vol. 10, no. 7, p. 804, 2021.
- [7] F. Hassanzadeh, E. Jafari, F. Shojaei, and H. Sadeghi-Aliabadi, "Synthesis and cytotoxic activity evaluation of some new 1, 3, 4-oxadiazole, 1, 3, 4-thiadiazole and 1, 2, 4-triazole derivatives attached to phthalimide," *Research in Pharmaceutical Sciences*, vol. 16, no. 6, pp. 634–642, 2021.
- [8] A. M. A. Ouf, H. A. Allam, M. Kamel, F. A. Ragab, and S. A. Abdel-Aziz, "Design, synthesis, cytotoxic and enzyme inhibitory activities of 1, 3, 4-oxadiazole and 1, 3, 4-thiadiazine hybrids against non-small cell lung cancer," *Results in Chemistry*, vol. 4, p. 100373, 2022.
- [9] F. Z. Mohammed, Y. W. Rizzk, I. M. El-Deen, E. M. Gad, M. El Behery, and A. R. Mahdy, "Discovery of 2-amino-4h-1, 3, 4-thiadiazine-5 (6h)-one derivatives and their in vitro antitumor investigation," *ChemistrySelect*, vol. 7, no. 7, p. e202104333, 2022.
- [10] S. Qureshi, G. Ali, M. Idrees, T. Muhammad, I.-K. Kong, M. Abbas, M. I. A. Shah, S. Ahmad, R. D. Sewell, and S. Ullah, "Selected thiadiazine-thione derivatives attenuate neuroinflammation in chronic constriction injury induced neuropathy," *Frontiers in Molecular Neuroscience*, vol. 14, p. 728128, 2021.
- [11] S. Alghamdia and M. Asifb, "phosphodiesterase-iii, iv, and v inhibitors."
- [12] S. Baddi, A. Y. Dang-i, T. Huang, C. Xing, S. Lin, and C.-L. Feng, "Chirality-influenced antibacterial activity of methylthiazole-and thiadiazole-based supramolecular biocompatible hydrogels," *Acta Biomaterialia*, vol. 141, pp. 59–69, 2022.
- [13] M. Alshubramy, M. Asem, and M. Abdel-Motaal, "Efficient synthesis of new fused thiadiazines and their spectroscopic, in silico drug likeness, and adme properties," *Russian Journal of Organic Chemistry*, vol. 58, no. 4, pp. 619–627, 2022.
- [14] A. Maslat, B. Al-Trad, I. Alameen, M. Al-Talib, H. Tashtoush, and B. Ababneh, "The effect of two novel substituted thiazole and thiadiazine derivatives on experimental type-1 diabetes mellitus," *Jordan Journal of Chemistry (JJC)*, vol. 19, no. 1, pp. 41–47, 2024.
- [15] A. De, S. Sarkar, and A. Majee, "Recent advances on heterocyclic compounds with antiviral properties," *Chemistry of Heterocyclic Compounds*, vol. 57, no. 4, pp. 410–416, 2021.
- [16] T. J. Herald, P. Gadgil, and M. Tilley, "High-throughput micro plate assays for screening flavonoid content and dpph-scavenging activity in sorghum bran and flour," *Journal of the Science of Food and Agriculture*, vol. 92, no. 11, pp. 2326–2331, 2012.
- [17] M. Čačić, V. Pavić, M. Molnar, B. Šarkanj, and E. Has-Schon, "Design and synthesis of some new 1, 3, 4-thiadiazines with coumarin moieties and their antioxidative and antifungal activity," *Molecules*, vol. 19, no. 1, pp. 1163–1177, 2014.
- [18] M. T. Madigan, J. M. Martinko, J. Parker et al., *Brock biology of microorganisms*. Prentice hall Upper Saddle River, NJ, 1997, vol. 11.
- [19] G. Guzel Kaya, S. Medaglia, V. Candela-Noguera, M. Á. Tormo-Mas, M. D. Marcos, E. Aznar, H. Deveci, and R. Martínez-Máñez, "Antibacterial activity of linezolid against gram-negative bacteria: Utilization of ϵ -poly-l-lysine capped silica xerogel as an activating carrier," *Pharmaceutics*, vol. 12, no. 11, p. 1126, 2020.

- [20] S. B. Kedare and R. Singh, "Genesis and development of dpph method of antioxidant assay," *Journal of food science and technology*, vol. 48, pp. 412–422, 2011.
- [21] H. Amira, F. Benchikh, H. Benabdallah, W. Mamache, S. Amira *et al.*, "Evaluation of antioxidant activities and total phenolic content of hydro-ethanol extract from *phlomis bovei* de noé areal parts," *Journal of drug delivery and therapeutics*, vol. 10, no. 5, pp. 45–48, 2020.
- [22] K. Jakovljević, M. D. Joksović, B. Botta, L. S. Jovanović, E. Avdović, Z. Marković, V. Mihailović, M. Andrić, S. Trifunović, and V. Marković, "Novel 1, 3, 4-thiadiazole conjugates derived from protocatechuic acid: Synthesis, antioxidant activity, and computational and electrochemical studies," *Comptes Rendus Chimie*, vol. 22, no. 8, pp. 585–598, 2019.

Research Article

Testing and Characterization of FBE+ARO Dual Layer Coatings of Welded Steel Pipes

Erman Ferik^{1a}, Semih Özbey^{1b}, Gökhan Çil^{2c} Mahmut Gel^{2d}

¹ Metallurgical and Materials Engineering Department, Marmara University, Istanbul, Türkiye

² Erciyas Steel Pipe, Design Center, Düzce, Türkiye

erman.ferik@marmara.edu.tr

DOI : 10.31202/ecjse.1445962

Received: 01.03.2024 Accepted: 11.07.2024

How to cite this article:

Erman Ferik, Semih Özbey, Gökhan Çil, Mahmut Gel, “ Testing and Characterization of FBE+ARO Dual Layer Coatings of Welded Steel Pipes”, El-Cezeri Journal of Science and Engineering, Vol: 12, Iss: 2, (2025), pp.(127-133).

ORCID: ^a0000-0002-9694-5732; ^b 0000-0001-5582-9973. ^c 0000-0003-0924-3984; ^d 0000-0002-8384-4932.

Abstract : The demand for extended life and outer surface protective coatings in pipelines is steadily increasing. Several coatings are used to protect pipelines against corrosion, impact, and abrasion. In this study, spiral welded steel pipes were coated with fusion bonded epoxy (FBE) for corrosion protection, followed by an abrasion-resistant coating (ARO) to protect the pipe from impact and abrasion. Various tests and characterization analyses were conducted on the coated pipes under different conditions, and they passed successfully, meeting the relevant standards and specifications.

Keywords : steel pipe, corrosion, abrasion, FBE coating, ARO coating

1 Introduction

Large amounts of crude oil, natural gas, and other resources are delivered efficiently and effectively from production locations to refineries and consumer markets. Pipelines are more cost-effective and safer than roads, rails, and ships for transporting freight across cities, countries, and continents. Every day, thousands of kilometers of steel pipelines are installed around the world for a wide range of civil and industrial purposes, forming a network of pipes similar to a vascular network that transports materials for people's natural resources such as petroleum products, natural gas, water, and air. Natural gas, water, air, and petroleum products are all delivered using steel pipes due to their flexibility and strength. If steel pipes are not covered or coated (galvanizing, plating), they corrode quickly [1]–[4].

Corrosion is simply defined as the deterioration of metal caused by chemical or electrochemical reactions that occur between the metal and its surroundings. A metal's corrosiveness is determined by its kind and surroundings. Corrosion is the second-leading cause of pipeline damage. Corrosion can cause industrial closures, product pollution, soil and groundwater contamination, pipeline breaks that result in significant losses of transported commodities, and even fires. Pipeline coating should always be the primary defense against corrosion, and it needs to be supported by a powerful cathodic protection system [5]–[18].

Nowadays, fusion-bonded epoxy (FBE) is almost usually the preferred alternative for pipeline coatings used around the world. This coating is ideal for pipelines due to its numerous benefits. These include a wide operating temperature range (-40°C to 105°C), strong adhesion to the steel substrate, good flexibility, high chemical resistance, low oxygen permeability, and compatibility with cathodic protection [19], [20].

The primary risk with single-layer FBE coating is shipping and handling damage. The thickness of the coating can be raised to improve impact and abrasion resistance. However, the coating's elasticity decreases with thickness. Steel pipes can also be coated with a secondary coating on top of the anti-corrosion coating to protect against pitting, impact, and abrasion during embedding. The abrasion resistant protective coating (ARO) is a topcoat that protects the steel pipeline's primary corrosion coating against abrasion damage during pipeline construction [2], [21].

2 Experimental Methods

2.1 Materials

This study used a 12m long, Ø762 mm diameter steel pipe made from API X70M PSL2 steel grade material utilizing spiral submerged arc welding (HSAW) with a wall thickness of 12.24 mm, often used in natural gas and oil pipes.

Table 1: Chemical characteristics of X70M PSL2 steel pipe.

Chemical Composition (%)					
C	Si	Mn	P	S	Cr
0.0635	0.221	1.680	0.0100	0.0075	0.136
Mo	Ni	Cu	B	Nb + V + Ti	CEpcm
0.0053	0.0239	0.0387	0.00053	0.0778	0.167

Table 2: Mechanical characteristics of X70M PSL2 steel pipe

Ultimate Tensile Strength (N/mm ²)	Yield Strength (N/mm ²)	Elongation (%)
675	601	27

Electrostatic spray guns were used to apply two-layers of fusion bonded epoxy coating with thermosetting epoxy powders, the first layer (FBE) designed for corrosion protection and the top layer (ARO) designed for high abrasion, followed by two-layers of abrasion resistance coating in accordance with the relevant standard requirements (CSA Z245.20 series 18 - system 2B) using for plant-applied external fusion bond epoxy coating for steel pipe. The chemical and mechanical characteristics of the welded steel pipe are presented in Tables 1 and 2. Table 3 shows the characteristics of both FBE and ARO coatings.

2.2 Method

Before applying the FBE and ARO coatings, the outer surface of the welded steel pipe was blasted in an automatic blasting station using a mixture of grit and shot in equal proportions. The outer surface of the pipe was then treated using phosphoric acid diluted with water, followed by rinsing with distilled water and drying with compressed air. The blasted pipe surface was heated to 215°C with an induction coil before the external surface coating process was applied. Electrostatic spray guns were used to apply powder epoxy materials to the surface of the heated pipe in a single layer for FBE and ARO coating, respectively.

Following the coating procedure, the pipe surface was cooled with water to allow for the gel time of the coatings. To assess the coating’s performance on the coated sample, cross-sectional and interface porosity, interface contamination level, bending, impact, cathodic peeling, and adhesion tests were carried out. The test requirements were determined according to CSA Z245.20 series 18 - system 2B. The coating’s surface was photographed and examined with SEM and EDX methods to ascertain its chemical characterization.

3 Results and Discussion

3.1 Surface Preparation Test and Control Results

Prior to blasting, the ambient conditions, including blasting media, acid, and pure water, were examined and measured. The recorded measurements are shown in Table 4.

Surface preparations before and after coating were carried out in accordance with the CSA-Z245.20 series 18 standard. Surface roughness values ranged from 77µ m to 91µm, meeting the acceptable threshold of 50µm – 100µm [22], [23].

Figure 1 depicts images of the surface roughness test, dust test, acid ratio determination test, and blasting media conductivity test measurements taken following surface preparation.

Table 3: FBE and ARO coating characteristics

Product	FBE	ARO
Colour	Red	Grey
Density (g/L)	1470	1590
Particle size (µm)	% 0.32 > 150 % 0 > 250	% 0.60 > 150 % 0 > 250
Thermal Characteristics (DSC)	T _{g1} : 64.03 °C T _{g2} : 64.03 °C ΔH: 67.41 J/g	T _{g1} : 64.75 °C T _{g2} : 107.82 °C ΔH: 51.54 J/g
Gel Time (s)	17 (at 205 °C)	24 (at 205 °C)
Moisture Content (%)	0.21	0.28

Table 4: Control results prior to blasting

Relative Humidity (%)	72,8
Ambient Temperature (°C)	29,1
Surface Temperature [T ₁] (°C)	72,8
Dew Point [T ₁] (°C)	16,8
ΔT Temperature [T ₁ – T ₂] (°C)	60,2
Pure Water Conductivity (µS/cm)	3,72
Blasting Media Conductivity (µS/cm)	8,95
Phosphoric Acid Percentage (%)	6,8

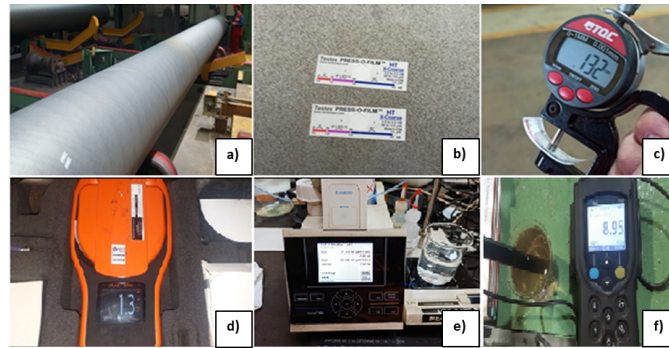


Figure 1: (a) Pipe after sand blasting, (b) roughness tape application on sand blasted pipe, (c) surface roughness measurement, (d) dust test, (e) phosphoric acid ratio determination, (f) blasting media conductivity test

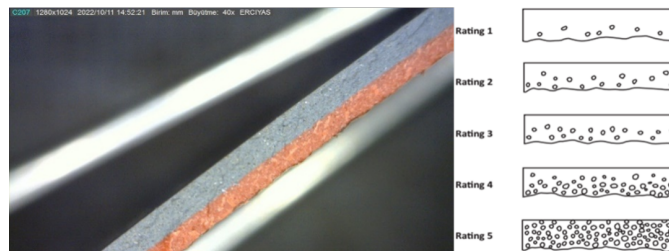


Figure 2: Cross-sectional porosity detection test sample

The blasted surface was examined visually using a comparison catalog in accordance with ISO 8501-1 / SSPC VIS1 standards, and the surface quality was identified as Sa 2.5 / SSPC SP10. The dust level on the blasted surface was measured in accordance with the ISO 8502-3 standard and determined to be the lowest (level 1) [23], [24].

3.2 Physical and Mechanical Test Results

To determine the interface contamination and porosity of the coated pipe, a test sample was cut in the middle and immersed in alcohol at $-30^{\circ}C$ for 1 hour. The test sample was removed from the cooling device and compared with the tables in the CSAZ245.20 series 18 standard using a light microscope at 40X magnification. According to the results of this comparison, the interface and section showed level 1 porosity. The interface pollution determination revealed a contamination level of 21 percent. A cross-sectional porosity detection test sample image is shown in Figure 2.

The interface porosity detection test sample image is shown in Figure 3 and the interface contamination detection test sample image is shown in Figure 4. To examine the adhesive strength of the coatings on the metal surface under cold and stress, test samples of 25x200 mm were extracted from the surface of the coated pipe, a bending test was performed under 1.5° mandrel degree, and crack formation on the coated surfaces was studied. The bending did not cause crack development in the test samples. Table 5 shows the characteristics and results of the bending test samples. Figure 5 depicts an image of the bending test samples.

To determine the impact resistance of the coatings on the metal surface, test samples of 25x200 mm were taken from the surface of the coated pipe and dropped with 1 kg from a height of 15 cm at $-30^{\circ}C$. After dropping 1 kg of weight on the samples, the test temperature was predicted to rise to room temperature. The wet sponge test was carried out with 67.5 volts on test samples whose surface temperature reached room temperature for the control of impact test results. The tested samples were examined and it was found that all of them were suitable, and that following impact with the load, there was no discontinuity

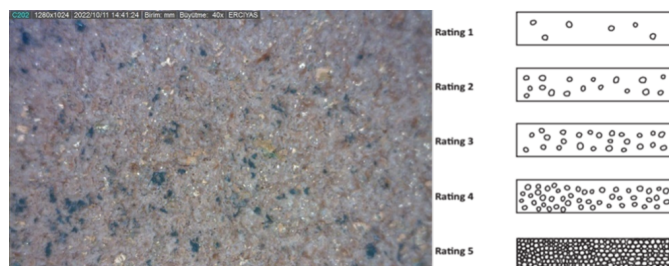


Figure 3: Interfacial porosity detection test sample

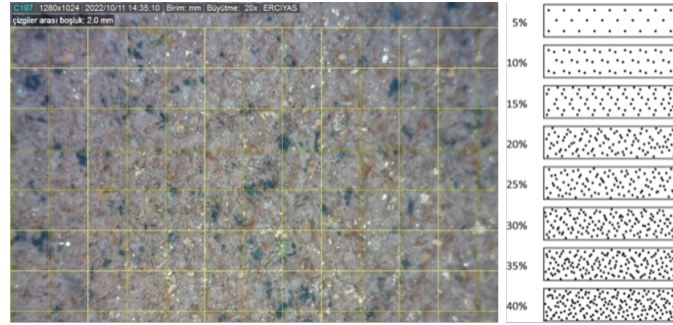


Figure 4: Interfacial contamination detection test sample

Table 5: Bending test sample characteristics and test results

Sample No	Average Dry Film Thickness (µm)	Temperature (°C)	Mandrel Degree (°)	Test Result
1				
2	906,3	-30	1,5	No Crack
3				

that would reach the pipe’s surface and generate a spark. The properties and characteristics of the impact test samples are shown in Table 6. The image of the impact test samples is shown in Figure 6.

3.3 Adhesion Test Results

To determine the adhesion strength of metal on the pipe surface using powder epoxy, 100x100 mm samples were cut and removed from the pipe. These samples were stored at 75⁰C for 24 hours, as shown in Table 7. An hour later, a 30x15 mm rectangle was opened on the coated surface with a knife, and its corners were checked. Adhesion test findings obtained within the scope of the applicable standard were examined and it was concluded that the results were appropriate. Images of adhesion test samples are shown in Figure 7.

3.4 Cathodic Peeling Test Results

After coating the pipe with powder epoxy resin, 100x100 mm test plates were removed and prepared for cathodic peel testing. The parameters utilized in the cathodic peeling tests are listed in Table 8. When the test results from the adhesion test in Figure 8 are examined, it becomes clear that the values in the relevant specifications and standards are within their tolerances [22], [25].

3.5 Characterization of Coatings

Optical and scanning electron microscopes were used to examine coating and microstructure compatibility, as well as morphological findings. Following the metallographic operations of sanding, polishing, and etching with nital solution,



Figure 5: Bending test samples

Table 6: Properties and characteristics of the impact test sample

Sample No	Number of Impact	Temperature (°C)	Test Result
1			
2	5	-30	No discontinuity
3			



Figure 6: Impact test samples

Table 7: Properties and characteristics of the adhesion test sample

Sample No	Temperature (°C)	Time (h)	Adhesion Degree Panel	Acceptance Rating
1	75	24	1 - 1	1 - 3
2				
3				



Figure 7: Adhesion test samples

Table 8: Cathodic peeling test parameters and obtained test results

Sample No	1	2	3
Time (h)		24	
Temperature (°C)		65	
Voltage (V)		-3,5	
Maximum Panel Peeling (mm)		0	
Average Panel Peeling (mm)		0	
Acceptance Rating (mm)	Max. 11,5		



Figure 8: Cathodic peeling test samples

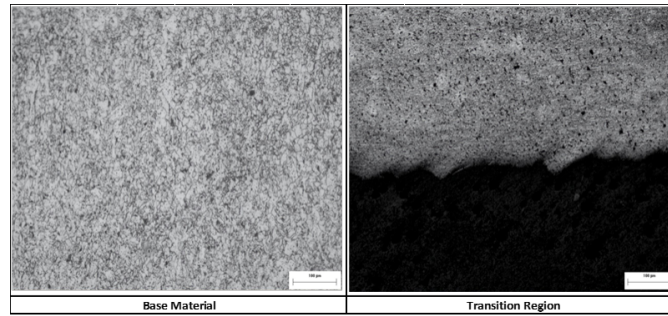


Figure 9: Microstructure of HRC steel after coating at x200 magnification in optical microscope a) base material region, b) steel and coating transition region

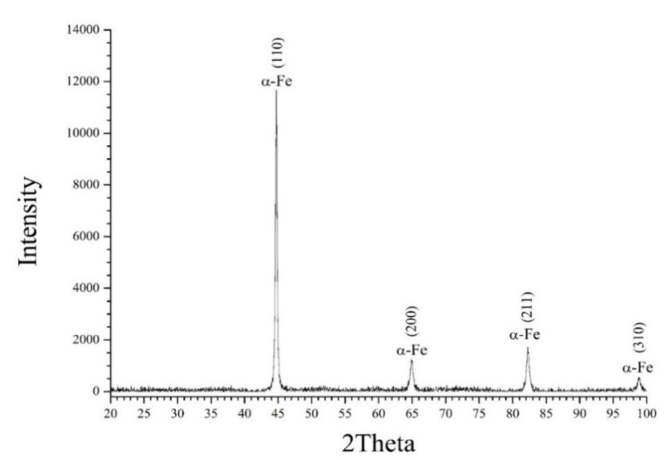


Figure 10: X-Rays diffraction pattern result of HRC steel

respectively, in accordance with the PN-EN ISO 17639:2013-12E standard. The microstructure of HRC steel after the coating process is shown in Figure 9.

The microstructure of HRC steel mainly consists of two phases: polygonal ferrite and granular bainite. It is observed that the microstructure in the transition region has been distorted due to the chemical reaction and heat affect. Thus, polygonal ferrite shape and granular bainite in the main microstructure have disappeared in the transition region. In addition that coated materials have been good compatibility with substrate materials. The effect of void, tear and rupture has been not detected in this region. The coating transitions at the base material-coating interface are smooth [26].

Figure 10 shows the result of the XRD pattern's HRC steel after the coating process due to the high peak intensities of $\alpha - Fe$ phase which has FCC structure, it has dominated in the whole microstructure of HRC Steel. The trace amount of residual austenite could not be detected on the XRD. It was determined by the result of XRD analysis whether there was no phase change or not after the thermal effect and chemical reactions occurring on the surface of the HRC steel during coating. As illustrated in Figure 11, scanning electron microscopy was utilized to distribute these phases [27].

Figure 11 shows the microstructures obtained from the coating and steel interface region from the scanning electron microscope. No adhesion cracks were seen in the coated area. The morphology of the HRC steel more clearly has been seen from the scanning electron microscope. The presence of granular bainite was confirmed at cooling rates below 50°C/s . Granular bainite occurs in steels that are continuously cooled via a mechanism similar to upper bainite (UB). However, due to a more gradual transformation, the beams appear coarse, and carbon enriches the residual austenite during transformation [28]–[31].

4 Conclusions

The feasibility of an FBE+ARO-based coating on steel pipe surfaces was investigated. It was observed that the adhesion and cathodic peeling test, which were used to determine the adhesive and peeling qualities of the coating on the pipe, provided the values in the relevant requirements and standards in tolerances (respectively in accordance with CSA Z245.20-14, TES-CO-FBE-GL standards). In addition, there was no crack and porosity in the coating. The importance of pre-coating and post-coating finishing has been demonstrated in the context of coating characterization. As a result, it has been shown that two-layers of fusion bonded epoxy (FBE+ARO) coating can be used on steel pipe surfaces.

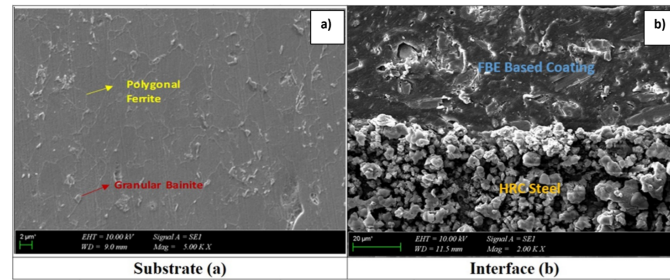


Figure 11: SEM analysis results of HRC steel obtained after coating. (a) HRC steel, (b) coating and steel interface

Authors' Contributions

GÇ and MG performed the coating process and performed physical and mechanical tests. SÖ performed the characterization tests. EF wrote up the article in collaboration with other authors. All authors read and approved the final manuscript.

Competing Interests

The authors declare that they have no competing interests.

References

- [1] H. Liu, *Pipeline engineering*. CRC Press, 2003.
- [2] M. Stewart, "Surface production operations facility piping and pipeline systems: Vol. 3," 2016.
- [3] P. Ellenberger, *Piping and pipeline calculations manual: construction, design fabrication and examination*. Elsevier, 2014.
- [4] A. Dinita and S. Kolisnychenko, *Corrosion. Tube Products and Pipeline Systems*. Trans Tech Publications Ltd, 2021.
- [5] D. Kuang and F. Cheng, "Coating degradation in the presence of alternating current interference," in *NACE CORROSION*. NACE, 2016.
- [6] W. K. Muhlbauer, *Pipeline risk management manual: ideas, techniques, and resources*. Elsevier, 2004.
- [7] E. S. Menon, *Pipeline planning and construction field manual*. Gulf Professional Publishing, 1978.
- [8] Y. Bai and Q. Bai, *Subsea pipeline integrity and risk management*. Gulf Professional Publishing, 2014.
- [9] R. Singh, *Pipeline Integrity: Management and Risk Evaluation*. Gulf Professional Publishing, 2017.
- [10] M. S. Okyere, *Mitigation of Gas Pipeline Integrity Problems*. CRC Press, 2020.
- [11] P. Hopkins, "The skills crisis in the pipeline sector of the oil and gas business," *Journal of Pipeline Engineering*, vol. 7, no. 3, pp. 1–55, 2008.
- [12] D. Alkazraji, *A quick guide to pipeline Engineering*. Elsevier, 2008.
- [13] A. C. Palmer and R. A. King, *Subsea pipeline engineering*. PennWell Books, 2008.
- [14] E. McAllister, *Pipe Line Rules of Thumb Handbook*. Elsevier, 1993.
- [15] J. N. Tiratsoo and J. Tiratsoo, *Pipeline pigging technology*. Gulf Professional Publishing, 1992.
- [16] R. R. Fessler, "Pipeline corrosion," *Report, US Department of Transportation Pipeline and Hazardous Materials Safety Administration, Baker, Evanston, IL*, 2008.
- [17] K. Escoe, *Piping and pipelines assessment guide*. Elsevier, 2006, vol. 1.
- [18] M. Orazem, *Underground pipeline corrosion*. Elsevier, 2014, no. 63.
- [19] M. Mohitpour, A. Murray, M. McManus, and I. Colquhoun, *Pipeline integrity assurance: a practical approach*. ASME Press, 2010.
- [20] E. Altuncu, Ç. Gökhan, and G. Mahmut, "Spiral kaynaklı çelik boruların korozyona karşı fbe kaplamaların test ve karakterizasyonu," *El-Cezeri*, vol. 7, no. 2, pp. 679–689, 2020.
- [21] J. Been and J. Wolodko, "Comparison of the corrosivity of dilbit and conventional crude," *Report of Alberta Innovates Technology Futures*, 2011.
- [22] "Plant-applied external fusion bond epoxy coating for steel pipe (LEFM) approach," Canadian Standards Association, Canada, Standard, 2018.
- [23] "Çelik taban malzeme yüzeylerin hazırlanması (G_{IC} and K_{IC}) Bölüm 1," TSE, Standard, 2008.
- [24] "Çelik yüzeylerin hazırlanması (G_{IC} and K_{IC}) Bölüm 3," TSE, Standard, 2017.
- [25] "External fusion bond epoxy for steel pipe specification (LEFM) approach," Trans Canada Engineering, Specification, 2017.
- [26] A. Roccisano, S. Nafisi, D. Stalheim, and R. Ghomashchi, "Effect of tmcp rolling schedules on the microstructure and performance of x70 steel," *Materials Characterization*, vol. 178, p. 111207, 2021.
- [27] A. Mostafapour, A. Ebrahimpour, and T. Saied, "Identification of retained austenite, ferrite, bainite and martensite in the microstructure of trip steel," *International journal of iron and steel society of Iran*, vol. 13, no. 2, pp. 1–6, 2016.
- [28] K. Kobayashi and K. Takewaka, "Experimental studies on epoxy coated reinforcing steel for corrosion protection," *International Journal of Cement Composites and Lightweight Concrete*, vol. 6, no. 2, pp. 99–116, 1984.
- [29] Z.-X. Gui, K. Wang, Y.-S. Zhang, and B. Zhu, "Cracking and interfacial debonding of the al–si coating in hot stamping of pre-coated boron steel," *Applied surface science*, vol. 316, pp. 595–603, 2014.
- [30] S. Zajac, V. Schwinn, and K. Tacke, "Characterisation and quantification of complex bainitic microstructures in high and ultra-high strength linepipe steels," in *Materials Science Forum*, vol. 500. Trans Tech Publ, 2005, pp. 387–394.
- [31] G. Song, W. G. Sloof, T. Vystavel, and J. T. de Hosson, "Interface microstructure and adhesion of zinc coatings on trip steels," in *Materials science forum*, vol. 539. Trans Tech Publ, 2007, pp. 1104–1109.



Research Paper

Analysis of Boundary Layer Thickness and Temperature Distribution in a Fluidic Stream across a Stretching Sheet with Thermal Nonequilibrium and Viscous Heating Effects

Uchenna Awucha Uka^{1a}, Edwin Esekhaigbe^{2b}, Obi Boniface Inalu^{3c}

¹Basic Sciences Department, School of Science and Technology, Babcock University, Ogun State, Nigeria.

²Mathematics and Computer Science Department, University of Africa, Bayelsa State, Nigeria.

³Mathematics Department, Imo State University, Owerri, Nigeria.

ukau@babcock.edu.ng

DOI : 10.31202/ecjse.1513483

Received: 09.07.2024 Accepted: 28.03.2025

How to cite this article:

Uchenna Awucha Uka, Edwin Esekhaigbe, Obi Boniface Inalu, "Analysis of Boundary Layer Thickness and Temperature Distribution in a Fluidic Stream across a Stretching Sheet with Thermal Nonequilibrium and Viscous Heating Effects", El-Cezeri Journal of Science and Engineering, Vol: 12, Iss: 2, (2025), pp.(134-152).

ORCID: ^a0000-0003-4177-3213; ^b0009-0007-5337-0856, ^c0000-0002-4878-3994.

Abstract : The analysis of a boundary layer thickness and temperature distribution effects in a viscous fluid flow of varying Hartmann intensity and thermal nonequilibrium over an exponentially extending/attenuation sheet is discussed. The fundamental approach to the investigation includes the application of the similarity estimation scheme in the recovery of the ordinary differential equations (ODEs) from the governing partial differential equations (PDEs) of the conservation of momentum, energy, and mass concentration which were modeled from the Navier-Stokes equation. The recovered coupled ordinary differential equations (CODEs) were analytically solved using the series technique and evaluated numerically using the MATHEMATICA scheme. Furthermore, the effect of several physical parameters on the velocity, temperature, and concentration are investigated, presented in graphical forms, and carefully analyzed. Correspondingly, the impact of some parameters on the local Nusselt number and coefficient of skin friction was presented, tabulated, and discussed clearly. Notedly, it is found that as the Hartmann parameter improves, the drag and fluid velocity decrease. Additionally, the enhancement of the thermal nonequilibrium number led to a rise in the temperature. Also, a reduction in skin friction resulted from enhancing the threshold thermal Grashoff number. Equally, the local Nusselt number declines due to the surge in the Prandtl and thermal nonequilibrium parameters, respectively.

Keywords: Heat transfer, Thermal Gradient, Mass diffusivity, Hydromagnetic, Drag.

1. Introduction

Understanding the fluid dynamics past a stretched surface is crucial because of its wide range of applications. For example, sheets of metal and polymer are used in the fabrication of materials in many industrial and manufacturing processes. Its significance also ranges from the cooling of an immeasurable metallic plate in a cooling steam bath to paper manufacturing, glass blowing, steel revolving, and plastic film drawing. Sakiadis [1] explored the effect of the incompressible boundary layer drift of a flat material in motion. The impact of varying fluid characteristics on heat transfer and hydro-magnetic flow across a nonlinearly widening material has been examined by Poply et al. [2]. The problem was solved quantitatively. Prasad et al. [3] investigated the effects of temperature-dependent fluid characteristics on magnetohydrodynamic (MHD) natural stream flow and thermal movement past a nonlinearly strained sheet. They considered the effects of both the magnetic field and Prandtl numbers and used the Keller-Box technique to solve the problem numerically. It was found that the temperature increases as the magnetic strength improves. However, Renuka et al. [4] studied the MHD boundary layer flow influenced by radiation and mass transfer from an exponentially elongating surface due to the heat generation utilizing the Runge-Kuta fourth-order and shooting schemes. The influence of both the magnetic and heat source parameters was discussed. It was found that as the magnetic field intensity increases, the momentum boundary layer thickness shrinks while the temperature and concentration boundary layer thicknesses increase. The slip

effect on the MHD boundary layer stream over an exponentially expanding plate with thermal radiation, suction, and blowing has been examined by Mukhopadhyay [5]. The result indicated that the temperature increases as a result of the enhancement of the thermal radiation and effective thermal diffusivity. The exploration of an MHD boundary layer flow of a viscous incompressible fluid movement across an exponentially enlarged sheet with the thermal radiation effect incorporated into the energy equation has been studied analytically by Mabood et al. [6]. The problem was solved using the homotopy analysis method (HAM). The result showed that the friction factor rises as the magnetic field increases. Poornima and Bhaskar [7] explored the impact of radiation on the MHD nanofluid with natural convective boundary wall drift across a nonlinear stretching sheet using the fourth-order Runge-Kutta and shooting methods. It was noted that the surge in the magnetic strength suppressed the velocity distribution. The non-aligned MHD inactive point flow of a flexible viscous nanofluid across a stretching sheet with radiation influence was presented by Khan et al. [8]. They discovered that as the magnetic constraint rises, the reattached non-alignment point diminishes.

The study of electrically conducting fluid dynamics in an electromagnetic field is known as magnetohydrodynamics (MHD). It is an important aspect of the modern metallurgical and metalworking processes. Thus, the constant dual-dimensional stagnation-point flow of a water-based nanofluid past an exponentially enlarging/lessening material in its plane has been investigated by Bachok et al. [9]. The numerical approach was used to investigate the three different forms of nanoparticles in the water-based fluid containing the Prandtl number. ($Pr = 6.2$), copper (Cu), alumina (Al_2O_3), and titania (TiO_2). It was found that the shrinking sheet solution remains unexceptional. However, the similarity solution of a Casson nanofluid's heat transfer and steady boundary layer flow across a vertical cylinder expanding exponentially in its radial direction with the Prandtl, magnetic, Casson, and mixed convective effects has been explored according to Malik [10]. The equations obtained were solved using the Runge-Kutta Fehlberg approach and the result indicated that as the mixed convective parameter grows, so does the velocity. Eid [11] studied the impact of a chemical reaction on the MHD boundary layer flow of a two-phased nanofluid across an exponentially extending sheet. It was discovered that the source and reaction parameters affected the thermal boundary layer. Similarly, by using the Keller-Box approach, Gangaiah et al. [12] explored the MHD flow of a nanofluid over an exponentially stretched sheet with viscous dissipation and chemical reaction effects. Abel et al. [13] examined the numerical effect of several variables, such as the variable buoyancy, viscosity, and thermal conductivity on the mixed convective thermal transference over an exponentially stretched sheet. The Runge-Kutta Fehlberg and effective shooting methods were deployed in recovering the solution. Yousif et al. [14] utilized the shooting method with the fourth-order Runge-Kutta approach to scrutinize the numerical analysis of the momentum and heat transport of an MHD Carreau nanofluidic across an exponentially strained plate with an internal heat generation/absorption and radiation impact in the absence of the non-thermal equilibrium.

The basic phenomenon behind the dynamics of MHD is that the applied magnetic field drives the current and its effect produces the Lorentz force which impacts the fluid motion dramatically. Meanwhile, several MHD electrically conducting fluids such as plasma, electrolytes, liquid metals, etc., can be mathematically formulated using the Navier-Stokes equations. Hence, the study of MHD fluid remains a subject of significant research due to its vast application to several industrial processes such as the processing of magnetic materials and the generation of MHD electrical power. Additionally, it is useful in the fields of geophysics and astrophysics, radio transmission, solar structure, flow meters, and extraction of geothermal energy. Using the Runge-Kutta and shooting approaches, Ellahi et al. [15] studied the thermally charged MHD bi-phased flow coatings along slippery walls with non-Newtonian nanofluid and hafnium particles. It was observed that the improvement of the Brinkman number led to an increase in the temperature. The unsteady flow and heat transfer of a carbon nanotube-based (CNT) MHD nanofluid with varying viscosity over a permeable shrinking surface has been numerically explored by Ahmed et al. [16] through the application of the Keller-Box approach in the absence of both the Schmidt and Brinkman numbers. The results suggested that an increase in the suction parameter and shrinking magnitude led to an upsurge in the pressure profile. The problem of the tangent hyperbolic liquid stream past an exponentially changing upright cylinder has been reported by Naseer et al. [17]. The Runge-Kutta Fehlberg technique was used in solving the equations. Thus, the result indicated that the heat conductance of the fluid varies with temperature. By deploying the Keller-Box scheme, Rangi and Ahmad [18] examined the flow of a viscous fluid over a stretching cylinder in the presence of a variable thermal conductance. It was concluded that the temperature field is greatly impacted by the varying thermal conductivity. Similarly, Abel and Mathesha [19] studied the effects of temperature-dependent thermal conductivity, non-uniform heating, and thermal radiation on the MHD viscoelastic fluid flow

across a stretched surface. The result affirmed that the temperature profile rises with varying thermal conductivity. However, Öztürk et al. [20] reported the presence of ideal constraints influencing thermal pipes' heating effectiveness via experimentation and the response wall approach with various forms of nanofluids within the heat exchangers. However, four parameters affecting the thermal efficiency were tested at three different levels of the experimental design. The analysis of variance (ANOVA) was used to test the model's accuracy. The ideal parameters were determined to be SiO_2 nanoparticle concentration of 0.32% at the evaporator inlet temperature of 90°C and a condenser Reynolds number of 21600. Öztürk et al. [21] adopted the Taguchi approach to investigate the effective improvement of the factors impacting the thermal efficiency of heated pipes with various types of nanofluids in the heat exchangers. The $L_{27}(3^4)$ orthogonal served as the basis for the experimental design at three levels for four parameters affecting the thermal efficiency with isopropyl alcohol as the basic fluid in the nanofluid suspension. Different quantities of silicon dioxide (SiO_2), titanium dioxide (TiO_2), and aluminum oxide Al_2O_3 were tested at 0.2 to 0.4 at 0.6%. The ideal parameters that were found using the analysis of variance (ANOVA) to assess the model's accuracy were the nanoparticle of the SiO_2 concentration of 0.4, an evaporator inlet temperature of 80°C, and condenser air velocity of 1.2 m/s.

The examination of the boundary layer flow of a viscous incompressible fluid over a nonlinear porous stretching sheet in the presence of a partial slip has been addressed by Mukhopadhyay [22]. The problem was numerically solved via the shooting method. It was observed that the horizontal velocity diminishes as the slip parameter increases. The existence of a dual solution for MHD boundary layer flow over a stretching/shrinking surface in the presence of thermal radiation and porous media was demonstrated by Rizwan et al. [23] through the aid of a KKL nanofluid model and Maple software. The result indicated that the fluid velocity in the upper branch rises as the magnetic parameter M increases while the fluid velocity in the lower branch decreases as M rises. Also, with the rising of the Biot number, the temperature profile improves on both the lower and upper branches. Furthermore, the influence of suction/injection on the local Nusselt number and the upper branch decreased as the magnetic parameter changed. The analysis of a boundary layer of a Jeffrey fluid flow across an expanding or contracting sheet past a porous medium has been examined by Nagaraju et al. [24]. The shooting and Runge-Kutta 4th-order approaches were deployed to derive the numerical solutions. The findings indicated that a rise in the heat source/sink causes a decline in the heat transfer rate. It was also found that an increase in thermal stratification enhances both the fluid temperature and velocity. Additionally, increasing the Jeffrey parameter decreases velocity and thickens the boundary layer. Shree et al. [25] analyzed the MHD boundary layer viscous flow past a stretching sheet by defining suitable non-dimensional parameters governing the boundary layer equations from the Falkner–Skan equations into a dimension-free form using the Legendre wavelet technique. The findings suggested that the thickness of the boundary layer diminishes as the pressure gradient and magnetic field parameters increase. Joseph et al. [26] explored the impact of the Brinkman and magnetic field numbers on a laminar flow in an upright channel. The single-term perturbation series approach was adopted to solve the modified equations. The findings showed that the magnetic field influences the velocity by diminishing turbulence and the Brinkmann number enhances the temperature distribution.

Despite all the aforementioned studies, the MHD boundary layer flow analysis of temperature distribution in a fluid across a stretched/shrunk plate with applied Hartmann, Brinkman, and Schmidt numbers has not received much attention. Inspired by this fact and its numerous significances in the areas of engineering, material science, manufacturing processes, and chemical applications a mathematical model for the boundary layer flow that represents the continuity, and conservation of momentum, energy, and mass equations is formulated. The similarity transformation and series schemes are applied to recover and solve the reformed coupled ordinary differential equations (RCODE) analytically. The results are graphically presented with legends, and the research findings are explained in detail.

However, the MHD effect plays a significant role in altering the boundary layer characteristics of a fluid as it flows over a stretching sheet, particularly in the presence of a magnetic field. The interaction between the motion of the fluid and the magnetic field can lead to changes in the momentum and thermal boundary layers thereby affecting both the momentum and thermal boundary layer thicknesses. Specifically, the impact of MHD tends to increase the boundary layer thickness due to the Lorentz force acting against the flow which counteracts the inertial effects of the fluid motion. As a result of this, the velocity gradient at the surface becomes less steep, leading to a broader region of slower movement of the fluid. Additionally, the presence of a magnetic field can enhance heat transfer mechanisms through the generation of eddies and vortices but may also compound thermal instability, particularly

in higher temperature gradients where the uneven distribution of thermal energy can lead to fluctuations in the boundary layer distributions.

The thermal instability and viscous heating significantly influence the behavior of the boundary layer and temperature distribution. The viscous heating that arises from the internal friction as the fluid flows, tends to increase the fluid temperature thereby modifying the thermal boundary layer. This interaction may exacerbate the thermal stability of the fluid particularly when considering the influence of the thermal non-equilibrium which occurs when the temperatures of the fluid and stretching sheet are not consistent. Thus, this study focuses on these intricate dynamics in addressing how the MHD, thermal instability, and viscous heating collectively influence the boundary layer thickness and temperature distribution in a fluid flow. By incorporating these factors into a comprehensive model, the research fills the critical gap in understanding the interplay of these forces thereby yielding insights into the optimization of cooling rates and heat transfer in engineering applications such as material processing and thermal management in MHD systems. This approach enhances theoretical comprehension and provides practical advantages for improved design and greater efficiency in related industrial processes. This study makes a significant and original contribution by developing a comprehensive analytical and numerical framework to investigate the effects of varying Hartmann intensity and thermal nonequilibrium on viscous fluid flow over an exponentially stretching or attenuating sheet. The ordinary differential equations have been successfully derived through a similarity estimation method which streamlines the examination of the intricacies in fluid dynamics. The findings provide valuable insights into the interplay between fluid velocity, drag, and temperature distribution. It also reveals the critical relationship between the Hartmann and thermal Grashoff numbers. This research does not enhance the theoretical understanding of the boundary layer phenomena under thermal nonequilibrium conditions only but also validates its results with existing literature which illustrates high agreement with established literature.

Significantly, this study contributes to the existing literature by providing a comprehensive mathematical model that elucidates the complex interactions between boundary layer behavior and thermal dynamics in fluid flows over-stretching sheets. By addressing the impacts of thermal nonequilibrium and viscous heating, the research enhances the understanding of heat transfer mechanisms in several areas of applications such as polymer processing and cooling systems where precise thermal control is crucial. This work offers not just a detailed insight into the boundary layer characteristics and temperature distributions but also lays the groundwork for the development of more efficient cooling technologies and materials processing techniques. In a nutshell, this work augments the existing literature by addressing specific phenomena in fluid dynamics by providing new analytical techniques and results that contribute to the theoretical understanding and practical applications of fluid mechanics as well as thermal control. This study addresses a critical knowledge gap in understanding how combined MHD effects, thermal instability, and viscous heating influence the fluid dynamics in the boundary layers. While previous research has explored these phenomena in isolation, the present study integrates them into a comprehensive framework that captures their interdependencies and collective impact on both the boundary layer thickness and temperature distribution. Through the examination of these interactions in the thermal nonequilibrium conditions, the research yields important insights into the complex behavior of fluids and provides a more comprehensive understanding that is crucial in the design and enhancement of several industrial processes such as the thermal management and material processing. This comprehensive method not only enriches theoretical frameworks but also has real-world implications for increasing efficiency in applications to stretching sheets and magnetohydrodynamic systems.

3. Mathematical Formulation and Method

3.1. Materials

A two-dimensional steady incompressible and conducting viscous fluid over a stretched sheet in an applied magnetic field is considered. In the transverse direction to the wall of the stretching sheet, the fluid passes through an even magnetic field intensity B_0 . Meanwhile, the y - axis is normal to the sheet with the sheet positioned along the x - axis at $y = 0$. Since the induced magnetic field is insignificant due to the specified modest magnetic Reynolds number ($Re \ll 1$), the applied magnetic field is being considered. However, both T_s and T_∞ are the wall and ambient temperatures while C_s and C_∞ are the concentrations of the sheet and the immediate vicinity of the sheet. Consequently, the following assumptions have been drawn.

- **Steady State Flow:** The flow is stable which implies that it is independent of time. Therefore, the momentum, conservation of energy, and concentration equations are steady and not functions of time.
- **Boundary Layer Approximation:** Since the problem involves a stretching sheet, it is likely for a boundary layer to be formed along the sheet. This suggests that the flow can be analyzed using the boundary layer theory since the variations in the flow properties are significant only in the vicinity of the sheet and can be neglected far from it.
- **Negligible Induced Magnetic Field:** Given that the magnetic Reynolds number is much less than 1 ($Re \ll 1$), the induced magnetic field due to the motion of the conducting fluid is negligible. This means that the primary magnetic field strength (B_0) applied parallel to the surface of the sheet is considered in the present analysis.
- A constant pressure is incorporated.

Thus, the flow structure is shown below.

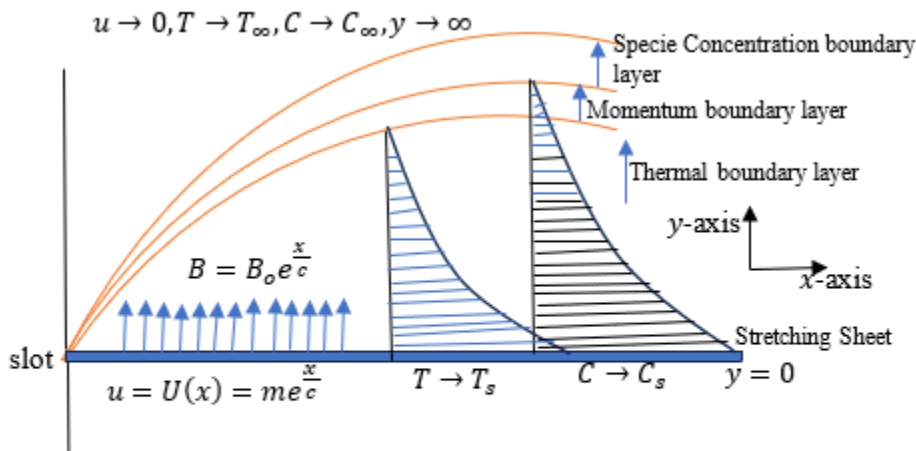


Figure 1. Schematic diagram of the problem

In terms of the modified Buongiorno's model [27], the reformed boundary layer mathematical equations of the flow are expressed as follows:

Continuity Equation

$$\frac{\partial u}{\partial x} + \frac{\partial v}{\partial y} = 0 \tag{1}$$

Momentum Equation

$$\frac{\partial p}{\partial x} + u \frac{\partial u}{\partial x} + v \frac{\partial u}{\partial y} = \mu \frac{\partial^2 u}{\partial y^2} + \frac{\sigma B_0^2 u}{\rho} + g \lambda \frac{T - T_\infty}{Re^2 x} \tag{2}$$

Energy Conservation Equation

$$u \frac{\partial T}{\partial x} + v \frac{\partial T}{\partial y} = \frac{K}{\rho c_p} \frac{\partial^2 T}{\partial y^2} + \frac{\mu}{\rho c_p} \left(\frac{T - T_\infty}{T_s - T_\infty} \right) \tag{3}$$

Mass Conservation Equation

$$u \frac{\partial C}{\partial x} + v \frac{\partial C}{\partial y} = \frac{\partial}{\partial y} (D_c) \frac{\partial C}{\partial y} \tag{4}$$

Subject to the boundary conditions

$$\begin{aligned} u = U_w(x) = m e^{\frac{x}{c}}, v = -v(x), T = T_s, C = C_s & \quad \text{at } y = 0 \\ u \rightarrow 0, T \rightarrow T_\infty, C \rightarrow C_\infty & \quad \text{as } y \rightarrow \infty \end{aligned} \tag{5}$$

With the similarity transformation variables defined as

$$\eta = \sqrt{\frac{m}{2vc}} ye^{\frac{x}{2c}}, \Psi = f(\eta)\sqrt{2vcm} e^{\frac{x}{2c}}, \theta(\eta) = \frac{T-T_\infty}{T_s-T_\infty}, \phi(\eta) = \frac{C-C_\infty}{C_s-C_\infty}, u = me^{\frac{x}{c}}f'(\eta),$$

$$v = -\sqrt{\frac{vm}{2c}} e^{\frac{x}{2c}}(f(\eta) + \eta f'(\eta)) \tag{6}$$

with $m > 0$ indicating a stretching condition and $m < 0$ suggesting a shrinking state. The stream function expressions are given by

$$u = \psi'(y), v = -\psi'(x) \tag{7}$$

Meanwhile, from equations (1) – (4), the following symbols $u, v, p, \mu, \sigma, \rho, g, \lambda, Re, k, c_p,$ and D_c represent the velocities in both x and y axes, constant pressure, dynamic viscosity, electrical conductance, base fluid density, gravitational acceleration, base fluid’s volumetric heat enlargement coefficient, Reynolds number, the thermal conductivity of the fluid, heat at constant pressure, and coefficient of mass diffusivity, respectively. It is vital to note that the additive inverse in equation (5) implies that suction takes place along the path of the stretched surface and the thermal boundary constraint is dependent on the convection transfer process. The primes in equation (6) refer to differentiation concerning the independent variable, η .

3.2. The Regular Approximation Technique

To solve the coupled ordinary differential equation featuring a small parameter ξ , the regular approximation method is applied. The method is particularly valuable when it is challenging or impractical to solve such coupled equations directly probably due to their coupled nature, or complexity. In such a situation, it can be simplified under the assumption that the parameter, $\xi \ll 1$. Thus, the first thing is to ascertain that the differential equations or system of equations governing the problem to be solved have been clearly defined. Thereafter, the equation’s tiny perturbation parameter ξ is determined. To arrange the terms for the perturbation analysis, a scaling analysis is performed to find the typical scales in the problem and to ascertain the terms that dominate in different orders of the small parameter, ξ . The next step in the solution step is to carry out an approximate expansion transformation in terms of the powers of the small parameter. ξ followed by a definition of a sequential solution. Usually, such a solution takes the form of

$$p(\eta) = \sum_{n=0}^{\infty} \xi^n p_n(\eta) \tag{8}$$

where, the functions to be obtained are denoted by $p_n(\eta)$. To generate a series of sequential equations from Equation (8), the proposed solution is used in the original ODEs. Thereafter, the coefficients of similar orders of ξ are equated to create a set of equations involving the following unknown functions $p_0(\eta), p_1(\eta), p_2(\eta),$ etc. These equations are solved to determine the formulas for the unknown functions. After finding the equations for $p_0(\eta), p_1(\eta), p_2(\eta),$ they are substituted into Equation (8) to obtain the approximate solution of $p(\eta)$. Meanwhile, the integration constants in the generated solutions are found by applying the transformed primary boundary conditions. The rationale behind the choice of the adopted method in this study is primarily driven by its simplicity and effectiveness in analytically resolving the coupled ordinary differential equations. The series method offers a straightforward approach to obtaining solutions with clearly defined convergence properties making it particularly suitable for the specific boundary layer problems addressed in this research. However, while the Keller-Box method may provide numerical solutions with good precision, it often involves more complex discretization and stability considerations which may complicate the analytical process. Also, although the Homotopy Analysis Method (HAM) seems appropriate for certain types of non-linear problems, it is associated with higher computational overhead and requires careful selection of auxiliary parameters which may not be necessary for the present study’s objectives. Ultimately, the series method provides a more direct path to achieving the analytical and numerical results and maintains clarity and interpretability of the fluid dynamics involved. The Equation (1) is satisfied as demonstrated below when Equation (7) is introduced into it.

$$\frac{\partial^2 \psi}{\partial x \partial y} + \frac{\partial^2 \psi}{\partial x \partial y} = 0 \tag{9}$$

Progressively, Equations (2) to (5) are transmuted into Equations (10) to (13) through the similarity approximation

process, application of Equation (6), and solved sequentially:

$$f''''(\eta) + f''(\eta)f(\eta) - Htf'(\eta) + \theta(\eta)G_t = 0 \quad (10)$$

$$\theta''(\eta) + P_0f(\eta)\theta'(\eta) + E_0\theta(\eta) = 0 \quad (11)$$

$$\phi''(\eta) + Scf(\eta)\phi'(\eta) \quad (12)$$

$$f(0) = k_0, f'(0) = 1, f'(\infty) = 0, \theta(0) = 1, \theta(\infty) = 0, \phi(0) = 1, \phi(\infty) = 0 \quad (13)$$

Accordingly, the following physical parameters are obtained. $E_0 = \frac{2\mu v l}{k U_w \Delta T}$ is the thermal nonequilibrium (Brinkman) parameter with, $\Delta T = (T_w - T_\infty)$, $Ht = \frac{2l\sigma B_0^2}{\rho U_w}$ refers to the magnetic strength parameter, $G_t = \frac{2g\lambda(T_w - T_\infty)}{U_w^2 R_g^2}$ indicates the threshold thermal Grashoff number, $P_0 = \frac{\mu C_p}{k}$ expresses the Prandtl intensity, and $Sc = \frac{\nu}{D_c}$ specifies the Schmidt factor. In line with [28], let

$$\eta = \Gamma\lambda_0, f(\eta) = \lambda_0 F(\eta), \theta(\eta) = h(\eta), \xi = \frac{1}{\lambda_0^2}, \phi(\eta) = \varphi(\eta) \quad (14)$$

Putting equation (14) and its differentials into equations (10) to (13) produce

$$f''''(\eta) + f''(\eta)f(\eta) - \xi Ht f'(\eta) + \xi^2 h(\eta)G_t = 0 \quad (15)$$

$$h''(\eta) + p_0 f(\eta)h'(\eta) + \xi E_0 h(\eta) = 0 \quad (16)$$

$$\varphi''(\eta) + Sc f(\eta)\varphi'(\eta) = 0 \quad (17)$$

$$F(0) = 1, F'(0) = \delta, F'(\infty) = 0, h(0) = 1, h(\infty) = 0, \varphi(0) = 1, \varphi(\infty) = 0 \quad (18)$$

Since $\delta \ll 1$, we define the solutions of equations (15) to (17) as follows.

$$f(\eta) = 1 + \sum_{z=n=1}^{\infty} z f_n(\eta) \quad (19)$$

$$h(\eta) = \sum_{z=n=1}^{\infty} (\xi)^z h_n(\eta) \quad (20)$$

$$s(\eta) = \sum_{z=n=1}^{\infty} (\xi)^z \varphi_n(\eta) \quad (21)$$

Hence, the following equations are obtained by taking the derivatives of equations (19) thrice, and equations (20) to (21) twice with respect to η . The results are substituted into equations (15) to (18) and simplified. Then, the coefficients of equal powers are equated and the following results are obtained.

$\mathbf{O}(\xi^0)$:

$$h_0''(\eta) + P_0 h_0'(\eta) = 0; h_0(0) = 1, h_0(\infty) = 0 \quad (22)$$

$$\varphi_0''(\eta) + Sc \varphi_0'(\eta) = 0; \varphi_0(0) = 1, \varphi_0(\infty) = 0 \quad (23)$$

$\mathbf{O}(\xi)$:

$$f_1'''(\eta) + f_1''(\eta) = 0; f_1(0) = 0, f_1'(0) = 1, f_1'(\infty) = 0 \quad (24)$$

$$h_1''(\eta) + P h_1'(\eta) + P_0 f_1(\eta)h_0'(\eta) + E_0 h(0) = 0; h_1(0) = 0, h_1(\infty) = 0 \quad (25)$$

$$\varphi_1''(\eta) + Sc \varphi_1'(\eta) + Sc f_1(\eta)\varphi_0'(\eta) = 0; \varphi_1(0) = 0, \varphi_1(\infty) = 0 \quad (26)$$

$\mathbf{O}(\xi^2)$:

$$f_2'''(\eta) + f_2''(\eta) + f_1(\eta)f_1''(\eta) - Ht f_1'(\eta) + h_0(\eta)G_t = 0;$$

$$f_2(0) = 0, f_2'(0) = 0, f_2'(\infty) = 0 \quad (27)$$

Subsequently, equations (22) to (27) are solved analytically and the following results are found. Flow rate (velocity)

$$f'(\eta) = \exp - \eta + \varpi \left(-\eta \exp - \eta + \exp - \eta - \frac{1}{2} \exp - 2\eta - Ht\eta \exp - \eta + Ht \exp - \eta - \frac{G_t(2+P_0)}{P_0^2(1+P_0)} \exp - (2+P_0)\eta - \frac{1}{2} \exp - \eta - Ht \exp - \eta + \frac{G_t(2+P_0)}{P^2(1+P_0)} \exp - \eta \right) \quad (28)$$

Temperature

$$h(\eta) = \exp - P_0\eta + \varpi \left(-P_0\eta \exp - P_0\eta - \frac{(P_0)^2}{1+P_0} \exp - (1+p_0)\eta + \frac{E_0}{P_0} \eta \exp - P_0\eta + \frac{P_0^2}{1+P_0} \exp - P_0\eta \right) \quad (29)$$

Concentration specie

$$\varphi(\eta) = \exp - Sc\eta + \varpi \left(-Sc\eta \exp - Sc\eta - \frac{(Sc)^2}{1+Sc} \exp - (1+Sc)\eta + \frac{(Sc)^2}{1+Sc} \exp - Sc\eta \right) \quad (30)$$

3.3. Physical Quantities

Of utmost importance to the engineering, thermal, and material sciences are skin friction and wall local thermal transfer rate which are defined below.

$$Cf_x = \frac{\tau_w}{\rho U_w^2} = \frac{f''(0)}{\sqrt{2Re_x}} \quad f''(0) = -1 + \varpi \left(-\frac{1}{2} - Ht + \frac{G_t(2+P_0)^2}{P_0^2(1+P_0)} - \frac{G_t(2+P_0)}{P_0^2(1+P_0)} \right) \quad (31)$$

$$q_w = -P_0 W'(\eta)_{\eta=0} \quad N_{ux} = -k(T_w - T_\infty) \sqrt{\frac{a}{2\nu c}} e^{\frac{x}{2c}} h'(0) \quad h'(\eta) = -P_0 + \varepsilon \left(-p_0 + p_0^2 + \frac{E_0}{P_0} - \frac{P_0^3}{1+P_0} \right) \quad (32)$$

4. Results and Discussion

The analytical solutions are presented in equations (28), (29), (30), (31), and (32) respectively while their numerical solutions are shown in Figs. 2 to 10. However, the effect of pertinent parameters on the velocity, temperature, and concentration distributions are presented in graphical forms with legends followed by detailed analysis. The dimensionless velocity f' , temperature h , and concentration φ appear on the vertical axis while the independent variable η is on the horizontal axis of the graphs. The Hartmann number (Ht) quantifies the influence of the strength of a magnetic field on a conducting fluid. An increase in the Hartmann number signifies a stronger magnetic field which enhances the Lorentz force acting on the charged particles in the fluid. This force opposes the fluid motion and creates a damping effect that reduces the velocity of the fluid [3,5] as shown in Fig. 2. This phenomenon is central in the study of MHD since it revolves around the dynamics of electrically conducting fluids in the presence of magnetic fields. A significant application of the parameter is in the design and optimization of cooling systems for nuclear reactors in which liquid metal coolants are subjected to a strong magnetic field for controlling and stabilizing the flow, ensuring efficient heat transmission, and safe operation. Physically, it is primarily associated with MHDs and signifies the relative significance of magnetic forces compared to viscous forces in a conducting fluid. It indicates that the magnetic forces dominate the viscous forces thereby leading to a more streamlined flow that is less influenced by viscosity. Conversely, a low Hartmann number implies that viscous effects are more significant and this causes a more chaotic flow regime. The real-world applications of the Ht are as follows.

- **Electromagnetic Flow Control:** In industries where electrically conductive liquids (such as molten metals) are used, the Hartmann number helps to guide the effectiveness of magnetic fields in controlling the flow and enhancing mixing or stabilizing processes.
- **MHD Power Generation:** In MHD generators, the parameter is crucial for evaluating the effectiveness of the magnetic fields in extracting energy from the conducting fluids. A higher Ht often means a better conversion efficiency.
- **Nuclear Fusion Reactors:** In fusion plasma physics, understanding the behavior of conducting fluids under the influence of a magnetic field is vital for predicting the stability of plasma and confinement conditions.

- Material Processing: The use of magnetic fields in processes such as continuous casting or metal processing could be helpful from the analysis of the Hartmann number, Ht by stabilizing the flow and controlling the temperature distributions.

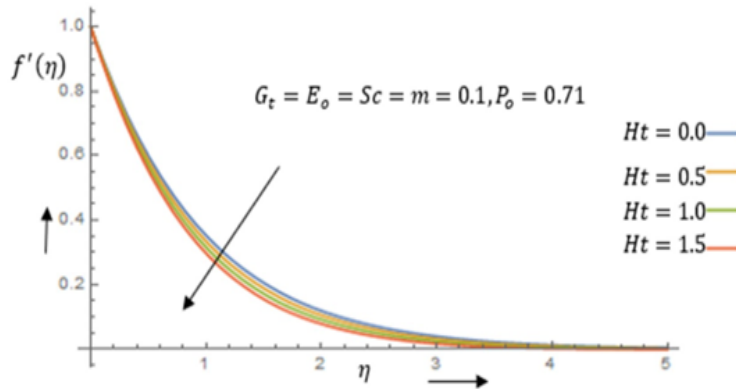


Figure 2. Velocity profile for Ht

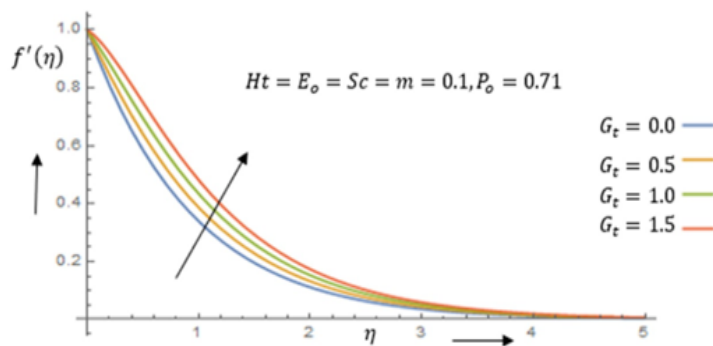


Figure 3. Velocity profile for G_t

Figure 3 displays the effect of the threshold thermal Grashoff number, G_t on the velocity distribution. This parameter (G_t) measures the impact of buoyancy forces resulting from the temperature gradients within a fluid. Its enhancement is an indication of a higher temperature differential between regions of the fluid which in turn amplifies buoyancy forces. These forces induce stronger convective currents and accelerate the fluid's motion and turbulence near the surface thereby increasing its velocity. Thus, this turbulent motion increases skin friction because the turbulent flow has higher energy dissipation and shear stress at the surface which causes more drag [29]. Therefore, by optimizing the value of this parameter, the efficiency of heat dissipation can be enhanced through convective cooling. This phenomenon aids electronic components to maintain safe operating temperatures even under high power loads [30]. Figure 4 interprets the velocity field as a result of variations in the suction parameter (m). An increase in this parameter suppresses the velocity due to the principles of fluid

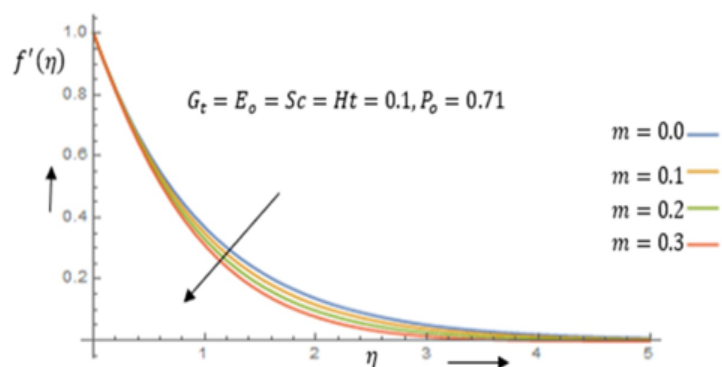


Figure 4. Velocity profile for m

dynamics particularly the Bernoulli equation which states that an increase in the pressure difference (caused by suction) results in a decrease in the fluid velocity. When suction is applied, a higher-pressure gradient across the fluid is created. This gradient causes the fluid to accelerate towards the lower pressure region. However, as the fluid particles are drawn into the suction area, there is a drop in the kinetic energy due to the wall friction and it leads to a decrease in the overall velocity as evident in Fig. 4. This phenomenon is commonly observed in various applications such as the functioning of vacuum pumps and suction devices [31]. The decrease in the kinetic energy of the fluid particles especially in the context of a flow system (such as a pump or an airflow system) can be attributed to several interconnected factors primarily related to the viscous effects, wall friction, and energy transformations within the fluid system.

1. Viscous Drag and Wall Friction

When the fluid particles move through a conduit or any other physical boundary they are subjected to viscous forces. Meanwhile, viscosity measures a fluid's resistance to deformation and flow. As the fluid comes into contact with the walls of the area of the suction, the following occurs.

- **Velocity Gradient:** Fluid particles in direct contact with the wall adhere to it (due to the no-slip condition). This means that they have zero velocity relative to the wall. As they move away from the wall, the velocity increases so as to match the flow. This creates a velocity gradient which leads to a shear stress in the fluid [32].
- **Energy Dissipation:** The shear stress induces frictional forces between the successive layers of the fluid (viscous drag). As the fluid layers interact, energy is transferred and also lost to heat due to the frictional interactions which leads to energy dissipation. This energy loss manifests as a decrease in the kinetic energy of the fluid particles as they approach the wall [33].

2. Flow Constriction and Acceleration Changes

As the fluid is drawn into the area of the suction, the geometry often changes and can impact flow velocity in the following ways:

- **Converging Flow:** If the suction area has a narrowing section (for example, in a venturi effect or the throat of a nozzle), the fluid must accelerate to pass through the constricted area. Initially, as the fluid enters the suction area, it may slow down due to the resistance from the surrounding walls and create the required velocity only after some acceleration. This initial slowing down can lead to a momentary decrease in the kinetic energy [34].
- **Bernoulli's Principle:** According to Bernoulli's principle, an increase in the fluid velocity creates a decrease in the pressure and kinetic energy of a streamlined flow. When particles enter a region of higher resistance (like a suction area) the pressure can increase momentarily to cause energy redistribution where part of the kinetic energy may be converted into potential energy thereby leading to a decreased kinetic energy [35].

3. Turbulence and Flow Separation

As the fluid moves toward the suction area, it may encounter obstacles or changes in the flow conditions that induce turbulence.

- **Turbulent Flow:** In turbulent flow, the formation of eddies and vortices can lead to chaotic changes in the energy distribution. Due to these turbulent interactions, some kinetic energy is transformed into thermal energy which also produces losses in the kinetic energy of the fluid particles [36].
- **Flow Separation:** If the geometry of the suction area is such that it causes flow separation, then it can lead to an adverse pressure gradient which will further detract from the kinetic energy of the fluid particles.

In summary, the decrease in the kinetic energy of the fluid particles being drawn into the suction area is primarily caused by the:

- viscous drag and wall friction that dissipate energy into heat.

- changes in the velocity due to the flow constriction which leads to an initial acceleration and overall energy loss.
- turbulent interactions that transform kinetic energy into thermal energy.
- flow separation and adverse pressure gradients that further hinder the kinetic energy of the approaching fluid particles [37].

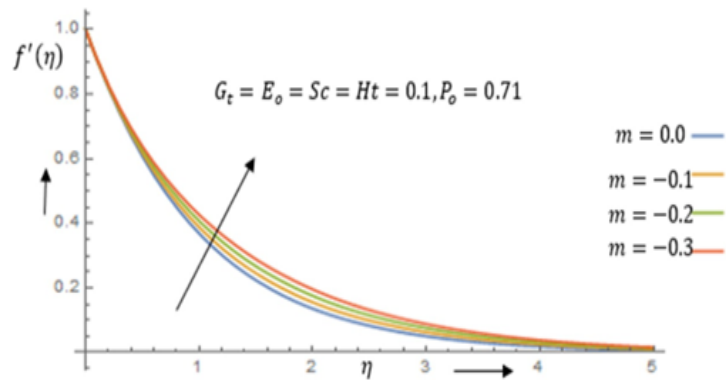


Figure 5. Velocity profile for $-m$

However, in fluid dynamics, a decrease in suction leads to an increase in velocity because of the inverse relationship between pressure and velocity described by the Bernoulli equation. When suction is reduced, the pressure gradient across the fluid reduces. This produces a lower pressure difference and causes less acceleration of the fluid particles towards the suction area which allows them to retain more of their kinetic energy. As a result of this, the fluid velocity increases because of the lower pressure drop which means that less energy is lost to overcome the pressure difference. Hence, this leads to a faster flow as shown in Fig. 5. This principle is applicable in various scenarios such as airflow in ducts and fluid movement in pipes.

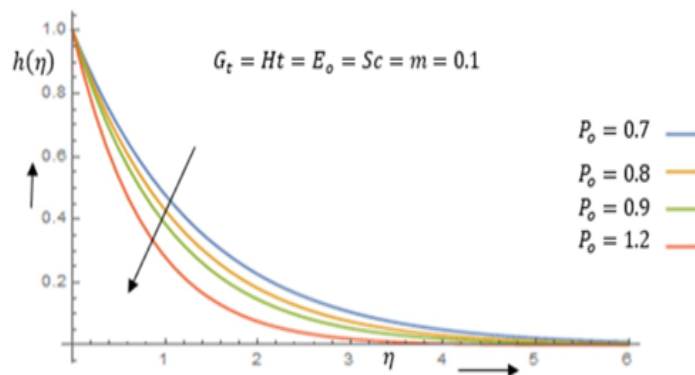


Figure 6. Temperature distribution for P_o

The distribution effect of the Prandtl number (P_o) on the temperature is outlined in Figure 6. An increase in this number signifies that the fluid has greater momentum diffusivity than thermal diffusivity. This means that the fluid's ability to transport momentum (due to viscosity) is more effective than its ability to conduct heat. Consequently, as the Prandtl number increases, the thermal boundary layer (the region where the temperature gradients are significant) becomes thinner relative to the velocity boundary layer where momentum transfer occurs. In practical terms, this implies that as the fluid flows with momentum effectively, its capacity to redistribute the thermal energy is limited. Thus, less heat is transferred away from the hot surfaces, leading to a lower temperature gradient near the surface and ultimately a decrease in the overall temperature of the fluid [17, 44]. From the physical perspective, the implications of a higher Prandtl number on the flow dynamics are significant. The greater resistance to thermal changes can lead to a more stable thermal profile, meaning the fluid retains its heat for longer while flowing. This behavior can create regions of localized heating as the energy supplied to the fluid is not dissipated rapidly resulting in a more uniform temperature distribution throughout the fluid. In applications to thermal management and engineering systems, the choice of fluids with high Prandtl numbers can be advantageous for achieving stable temperature profiles and reducing heat loss thereby enhancing the efficiency

of cooling or heating processes. Understanding the interplay between the Prandtl number, temperature distribution, and flow characteristics is essential for optimizing thermal performance in various industrial applications. Scientifically, this phenomenon is essential for the heat transfer processes in various applications such as the cooling of electronic components where a high Prandtl number would slow down the thermal dissipation required for different cooling strategies. From the physical perspective, engineers leverage this knowledge to optimize the designing of heat exchangers, HVAC systems, and thermal insulation to efficiently manage heat transfer rates and maintain the desired operating temperatures in industrial processes and technological applications [38].

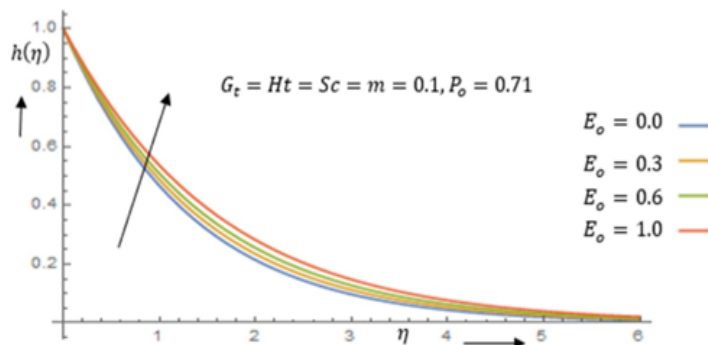


Figure 7. Temperature distribution for E_o

In terms of the physical meaning, the Brinkman number (E_o) is a dimensionless number that characterizes the relative importance of viscous heating to conduction in a fluid flow. An increase in the parameter indicates that the viscous dissipation or conversion of mechanical energy into thermal energy due to the viscosity of the fluid becomes more significant relative to heat conduction. As the viscous forces in the fluid generate more heat as the fluid flows, the overall temperature of the fluid increases [26] as portrayed in Figure 7. This effect is particularly pronounced in areas where the viscous heating is substantial such as in high-temperature applications or flows with high shear rates that lead to a warmer fluid temperature as the energy input from the mechanical work is transformed into thermal energy. Practically, this knowledge is important for enhancing the performance of renewable energy systems such as solar thermal collectors by leveraging a higher Brinkman number (E_o) to achieve higher thermal efficiencies [39]. From a physical perspective, the implications of increasing E_o are critical for understanding the flow behavior in various engineering applications. For instance, in processes involving high shear rates such as those found in polymer processing or certain chemical reactions, enhanced viscous heating can lead to a localized hot spot within the fluid. This leads to a spatially non-uniform temperature distribution which can affect the reaction rates, material properties, and overall system efficiency. Moreover, the increase in temperature can alter the properties of the fluid such as viscosity which impacts the flow dynamics. Therefore, when designing systems where viscous heating is a concern such as in heat exchangers or reactors, it is essential to consider the Brinkman number to ensure optimal thermal management and flow stability. Thus, understanding the balance between viscous heating and heat dissipation is crucial for achieving the desired thermal performance in several applications. Thus, the Brinkman number is applied to the following areas.

- **Heat Exchangers:** In systems where fluids experience significant viscous heating such as in high-speed heat exchangers, the Brinkman number (E_o) helps in its design to optimize heat transfer and thermal performance.
- **Polymer Processing:** During the processing of polymers, the viscosity and flow characteristics can lead to significant heating. Understanding this parameter (E_o) can help to control overheating to avoid the thermal degradation of materials.
- **Geothermal Systems:** In geothermal energy extraction, this parameter (E_o) helps in the assessment of heat transfer efficiency in high-viscosity fluids impacting the design and performance of geothermal systems.
- **Chemical Reactions:** Processes that involve exothermic reactions in viscous fluids indicate the importance of viscous heating which aids in the designing of reactors to ensure safety.

Figure 8 shows the effect of the suction parameter on the temperature field. An increase in suction leads to a decrease in temperature due to the principles of thermodynamics particularly the adiabatic cooling process [5]. When suction is applied, it causes a rapid decrease in pressure within the fluid. As the fluid expands into the lower

pressure area created by the suction, it does so without the addition of external heat (adiabatically). This expansion causes the fluid molecules to spread out thereby opposing the surrounding pressure which later reduces their kinetic energy.

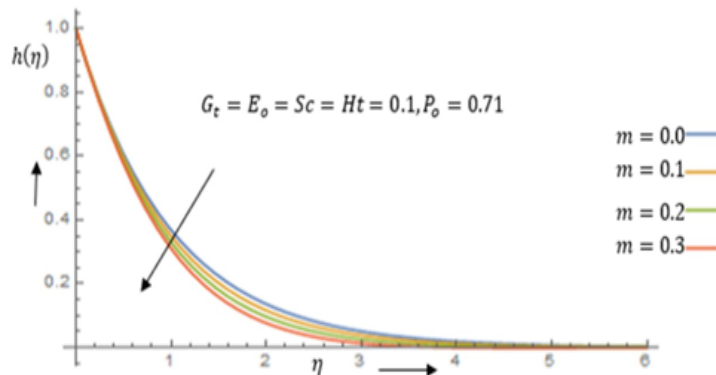


Figure 8. Temperature distribution for m

Since temperature is a measure of the average kinetic energy of the molecules, this decrease in kinetic energy causes a corresponding drop in the temperature. This effect is commonly observed in devices such as refrigerators and air conditioners where increased suction is used to cool the refrigerant.

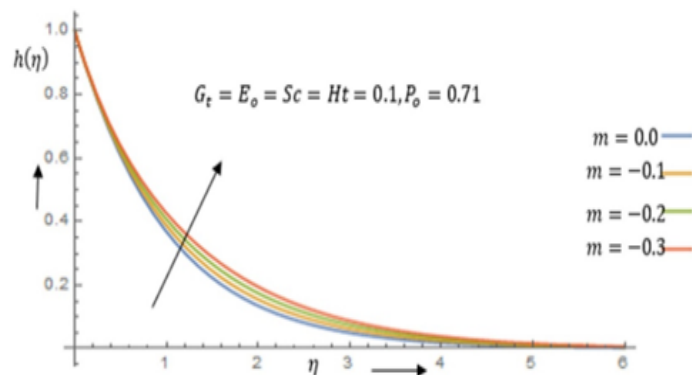


Figure 9. Temperature distribution for $-m$

A decrease in suction leads to an increase in temperature due to the principles of thermodynamics and the behavior of gases under compression. When suction is reduced, the pressure within the fluid increases. As the fluid is compressed, the molecules are brought closer thereby increasing their collisions and kinetic energy. Thus, this increase in the kinetic energy produces a temperature rise which is illustrated in Fig. 9. This process is known as adiabatic heating. It refers to a situation where the work done on the fluid during compression translates into increased thermal energy. This principle is utilized in various applications such as heat pumps and compressors where decreasing suction (or increasing pressure) raises the temperature of the working fluid.

An upsurge in the Schmidt number (Sc) indicates that the diffusivity of momentum (viscosity) relative to the diffusivity of mass (concentration) is higher. This means that momentum is transferred more readily than mass within the fluid. Consequently, when Sc appreciates, the mass transfer rate decreases because viscous forces dominate over molecular diffusion thereby resulting in a slower mixing and dispersion of the concentration field which is shown in Figure 10. Thus, the concentration decreases as the Schmidt number rises [40]. This effect is significant in some areas of applications such as the chemical engineering processes, environmental fluid dynamics, and biological systems where transporting substances such as pollutants, nutrients, or chemical reactants is key. With the knowledge of this relationship, scientists and engineers can optimize the mixing strategies to design efficient reactors and model pollutant dispersion in natural water bodies or industrial effluents. Practical applications include wastewater treatment whereby controlling the Schmidt number influences the efficiency of processes such as biological nutrient removal or chemical oxidation by adjusting the mixing regimes or reactor configurations to enhance mass transfer rates. However, due to the importance of this study, the effects of some pertinent parameters such as the threshold thermal Grashoff (G_t) and Brinkmann numbers (E_o)

on skin friction and Prandtl number P_o on the wall heat transfer have been tabulated and shown in Tables 1 and 2, respectively. Both tables contain the numerical values of some thermophysical parameters that have been varied to find their effect on skin friction and Nusselt number. However, understanding the trends in both tables would be helpful in the energy optimization, thermal management, and polymer extrusion processes.

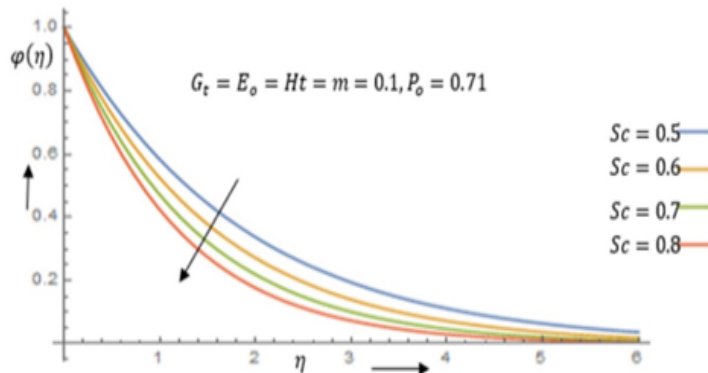


Figure 10. Concentration distribution for Sc

Table 1. The Influence of G_t and Ht on Skin Friction.

Threshold thermal Grashoff Number G_t	Hartmann Number, Ht	Prandtl Number, P_o	Brinkman Number, E_o	Akhar et al. [41]RK $-f''(0)$	Akhar et al. [41]NFD $-f''(0)$	Skin Friction, $-f''(0)$ Present Result
0.5	0.0	0.71	0.0	0.80274	0.80275	0.78120
1.0	0.0	0.71	0.5	0.61617	0.61612	0.51241
0.5	1.0	0.71	0.0	1.22381	1.22388	1.10000
1.0	1.0	0.71	0.5	1.04349	1.04352	1.15000

The threshold thermal Grashoff number (G_t) signifies the ratio of buoyancy forces to viscous forces in a fluid flow affected by temperature gradients. An increase in this number indicates a stronger buoyancy relative to viscous forces thus leading to an enhanced fluid motion and turbulence near a wall surface. This turbulent motion increases skin friction because turbulent flow has higher energy dissipation and shear stress at the surface and causes greater drag. Conversely, the Hartmann number Ht represents the ratio of electromagnetic forces (Lorentz forces) to viscous forces in MHD flows which are influenced by a magnetic field. An improvement in this parameter (Ht) strengthens the Lorentz forces and suppresses the fluid motion and turbulence near the surface due to the magnetic damping effect. This suppression reduces the velocity gradients and turbulence intensity at the surface and causes a decline in skin friction [3]. Meanwhile, skin friction is crucial for aerospace, production processes, automobiles, and geophysical science. With this understanding, controlling aerodynamics becomes essential for optimizing aircraft and vehicle designs to reduce drag and improve efficiency. In geophysics, it affects the behavior of fluids in geological formations and oceans and influences natural processes including convection and climate dynamics.

Table 2. The Influence of Prandtl, P_o and Brinkman numbers, E_o on the wall heat transmission, $h'(0)$.

Hartmann Number, Ht	Stretching Sheet parametric Condition, m	Prandtl Number, P_o	Brinkman Number, E_o	Bidin and Nazar [42]	Ishak [43]	Nusselt Number, $-h'(0)$
0.0	0.1	1.00	3.0	0.9547	0.9548	0.7500
0.0	0.1	2.00	3.0	1.4714	1.4715	1.9167
0.0	0.1	3.00	3.0	1.8691	1.8691	2.3750

An increase in the Prandtl number corresponds to a higher ratio of momentum diffusivity (kinematic viscosity) to thermal diffusivity in a fluid and it's indicative of the fact that the thermal conduction occurs more readily than momentum diffusion. This characteristic enhances the efficiency of convective heat transfer processes since the thermal energy can move more effectively through the fluid. Understanding and controlling convective heat transfer via the Nusselt number is essential for achieving efficient energy utilization, reducing operational costs,

and improving the performance and durability of machinery and equipment. Scientifically, the rate of heat transport provides a quantitative measure of convective heat transfer efficiency, aiding in developing advanced heat transfer models, climate control systems, and thermal insulation materials.

4. Conclusions

The examination of the boundary layer thickness and temperature transfer effects in a viscous fluid flow with different Hartmann and thermal nonequilibrium effects over an exponentially stretching/shrinking plate has been analyzed in the present study. Thus, the following points are significant:

1. An increase in the suction parameter m leads to a decline in the velocity and temperature while a decrease in the parameter shows a reversed trend in the velocity and temperature distributions.
2. The enhancement of the Hartman number H_t initiate a fall in the velocity and skin friction.
3. As the Brinkman number E_o improves, the thermal boundary layer and Nusselt number $h'(0)$ are enhanced.
4. An increase in the Schmidt number Sc suppresses the concentration distribution.
5. An increase in the Prandtl number P_o reduces the thermal boundary layer thickness and improves the rate of heat transfer $h'(0)$.

The novel findings of the present study stand out due to the incorporation of the effects of thermal non-equilibrium and viscous heating simultaneously within the context of fluid flow over an exponentially stretching/attenuating sheet. Unlike many previous works that focus solely on thermal equilibrium conditions or simplified geometries, this research provides a comprehensive exploration of how the aforementioned pertinent parameters influence the boundary layer dynamics, velocity, temperature, and concentration distributions.

Table 3. A Comparison highlighting the similarities with existing studies.

Author(s)	Parameters	Similarities	Present Study
1. Shuguang et al., [47].	Hartmann Number, H_t .	As the Lorentz forces become stronger for higher Hartmann numbers, the velocity decreases.	The enhancement of the Hartman number, H_t leads to a reduction in the velocity.
2. Shuguang et al., [47].	Schmidt Number, Sc .	An upsurge in the value of the Schmidt number creates a decline in the concentration field.	An increase in the Schmidt number, Sc improves the concentration distribution.
3. Y. Dharmendar Reddy et al., [45].	Prandtl Number, P_o .	An increase in the Prandtl number P_o creates a diminution in the thermal boundary layer, which outcomes in a decrease in the temperature profile.	As the Prandtl number rises, the temperature decreases.
4. Akhar et al., [41]	Thermal Grashoff Number, G_t .	Increasing the thermal Grashoff number G_t significantly lowers skin friction.	Skin friction is significantly reduced by raising the thermal Grashoff number. G_t .
5. Krishnamurthy et al., [46].	Hartmann Number, H_t .	The strength of the magnetic field similarly increases with a higher Hartmann number M . In the stretched nanofluid sheet, it increases the thickness of the momentum boundary layer thereby preventing the flow.	The strength of the magnetic field increases as the Hartmann number H_t rises. In addition to the obstruction of the flow, it thickens the momentum barrier layer in the stretching nanofluid sheet.

A notable finding is an observation that the distributions of skin friction for the effects of thermal Grashoff number at two different values of the Hartmann (MHD) number, i.e., $H_t = 0.0$ which indicates an electrically non-conducting case and $H_t = 1.0$ meaning an electrically conducting case which is shown in Table 1 indicated that the magnitude of skin friction is significantly elevated with the increasing magnetic field at different values of the thermal Grashoff number i.e., $G_t = 0.5$ and 1.0 . Furthermore, the work uniquely demonstrates that the thermal

non-equilibrium parameter enhances temperature while an increased thermal Grashoff number leads to improved skin friction. This highlights the intricate dependencies that are often overlooked in conventional analyses.

Another novel aspect is the dual-method approach of solution involving the combination of the analytical series technique and a robust numerical scheme via the MATHEMATICA, with a detailed analysis of the results obtained. In comparison to the literature, the results of the present study in the graphical and tabular presentations of varying parametric values are exceptionally detailed. By bridging the gaps in understanding the interplay between thermal and magnetic effects, this research contributes to a richer, and multi-dimensional perspective to the field of boundary layer theory.

However, in terms of this study's differences compared to similar parameters in the literature, it was noted that:

1. an increase in the Prandtl number reduces the diminution of the thermal boundary layer which brings about a decrease in the temperature [45]. Thus, it improves the rate of heat transfer.
2. the Brinkmann number is an increasing function of the temperature distribution while in [40], it is a decreasing function of the velocity field.
3. the fluid velocity decreases with increasing values of the Hartmann number H_t (magnetic effect), while [44] reported an increase in the velocity.

Also, a comparison of the similarities of the results in the present study with existing studies in the literature has been tabulated and shown in Table 3. It would be beneficial to explore the effects of varying fluid properties such as non-Newtonian fluid characteristics on the boundary layer dynamics and thermal distributions in similar flow configurations.

Acknowledgments

The authors express their appreciation to Professor Emeka Amos for his constructive input towards the success of this work.

Authors' Contributions

UU conceived and designed the research study. UU, EE, and OI contribute to the theoretical framework of the research through the provision of critical intellectual input throughout the research process. UU obtained the solution of the transformed mathematical model. UU, EE, and OI carried out the result analysis, and interpretation of results, and participated in the revision and formatting of the research manuscript. UU, EE, and OI re-checked the article not only for spelling and grammatical errors but also for intellectual content. All the authors read and approved the final manuscript.

Competing Interests

The authors state that no competing interests are in existence.

References

- [1] B. C. Sakiadis, "Boundary layer behavior on continuous solid surfaces: I. Boundary layer equations for two-dimensional and axisymmetric flow", *American Institute of Chemical Engineers (AIChE J.)*, vol. 7, pp. 26-28, 1961. <https://doi:10.1002/aic.690070108>
- [2] V. Poply, P. Singh, and A. K. Yadav, "A study of Temperature-dependent fluid properties on MHD free stream flow and heat transfer over a non-linearly stretching sheet", *Proc Eng*, vol. 127, pp. 391-397, 2015. <https://doi:10.1016/j.proeng.2015.11.386>
- [3] K. V. Prasad, K. Vajravelu, and P. S. Datti, "The effects of variable fluid properties on the hydro-magnetic flow and heat transfer over a non-linearly stretching sheet", *International journal of thermal science*, 49(3): 603-610, (2010). <https://doi:10.1016/j.ijthermalsci.2009.08.005>
- [4] R. L. V. D. Renuka, T. Poornima, R. N. Bhaskar, and S. Venkataraman, "Radiation and mass transfer effects on MHD boundary layer flow due to an exponentially stretching sheet with a heat source", *International Journal of Engineering Innovative Technology*, vol. 3, pp. 33-39, 2014.

- [5] S. Mukhopadhyay, "Slip effects on MHD boundary layer flow over an exponentially stretching sheet with suction/blowing and thermal radiation", *Ain Shams Engineering Journal*, vol. 4, pp. 485-491, 2012. [https://doi: 10.1016/j.jasej.2012.10.007](https://doi.org/10.1016/j.jasej.2012.10.007)
- [6] E. Mabood, W. A. Khan, and A. I. Md Ismail, "MHD flow over exponential radiating stretching sheet using Homotopy Analysis Method" *Journal of King Saud University Engineering Science*, vol. 29, pp. 68-74, 2017.
- [7] T. Poornima, and R. N. Bhask, "Radiation effects on MHD free convective boundary layer flow of nanofluids over a nonlinear stretching sheet", *Advances in Applied Science Research*, vol. 4, pp. 190-202, 2013.
- [8] W. A. Khan, O. D. Makinde, and Z. H. Khan, "Non-aligned MHD stagnation point flow of variable viscosity nanofluids past a stretching sheet with radiative heat", *International Journal of Heat and Mass Transfer*, vol. 96, pp. 525-534, 2016. [https://doi: 10.1016/j.ijheatmasstransfer.2016.01.052](https://doi.org/10.1016/j.ijheatmasstransfer.2016.01.052).
- [9] N. Bachok, A. Ishak, and I. Pop, "Boundary layer stagnation-point flow and heat transfer over an exponentially stretching/shrinking sheet in a nanofluid", *International Journal of Heat and Mass Transfer*, vol. 55, pp. 8122-8128, 2012. [https://doi: 10.1016/j.ijheatmasstransfer.2012.08.051](https://doi.org/10.1016/j.ijheatmasstransfer.2012.08.051)
- [10] M. Y. Malik, M. Naseer, S. Nadeem, and A. Rehman, "The boundary layer flow of Casson nanofluid over a vertical exponentially stretching cylinder", *Applied Nanoscience*, vol. 4, pp. 869-873, 2014. [https://doi: 10.1007/s13204-013-0267.0](https://doi.org/10.1007/s13204-013-0267.0).
- [11] M. R. Eid, "Chemical reaction effect on MHD boundary-layer flow of two-phase nanofluid model over an exponentially stretching sheet with a heat generation", *Journal of Molecular Liquids*, vol. 220, pp. 718-725, 2016. [https://doi: 10.1016/j.molliq.2016.05.005](https://doi.org/10.1016/j.molliq.2016.05.005).
- [12] T. Gangaiah, N. Saidulu, and L. A. Venkata, "Magnetohydrodynamic flow of nanofluid over an exponentially stretching sheet in the presence of viscous dissipation and chemical reaction", *Journal of Nanofluids*, vol. 7, pp. 439-4448, 2018. [https://doi: 10.1166/jon.2018.1465](https://doi.org/10.1166/jon.2018.1465).
- [13] M. Abel, S. Mahantesh, M. Nandeppanavar, and V. Basanagouda, "Effects of variable viscosity, buoyancy, and variable thermal conductivity on mixed convection heat transfer due to an exponentially stretching surface with magnetic field", *Proceedings of the National Academy of Sciences, India Section A: Physical Sciences*, vol. 87, pp. 247-256, 2017. [https://doi: 10.1007/s40010-016-0338-1](https://doi.org/10.1007/s40010-016-0338-1).
- [14] M. A. Yousif, I. H. Farhan, T. Abbas, and R. Ellahi, "Numerical study of momentum and heat transfer of MHD Carreau nanofluid over an exponentially stretched plate with internal heat source/sink and radiation", *Heat Transfer Research*, vol. 50(7), pp. 649-658, 2019. [https://doi: 10.1615/HeattransRes.208025568](https://doi.org/10.1615/HeattransRes.208025568)
- [15] R. Ellahi, A. Zeeshan, F. Hussain, and T. Abbas, "Thermally charged MHD Bi-phase flow coatings with non-Newtonian nanofluid and Hafnium particles along slippery walls", *Coatings*, vol. 9, No. 5, pp. 300, 2019. [https://doi: 10.3390/coatings9050300](https://doi.org/10.3390/coatings9050300).
- [16] Z. Ahmed, S. Nadeem, S. Saleem, and R. Ellahi, "Numerical study of unsteady flow and heat transfer CNT-based MHD nanofluid with variable viscosity over a permeable shrinking surface", *International Journal of Numerical Methods for heat and fluid flow*, vol. 29(12), pp. 4607-4623, 2019. [https://doi: 10.1108/HFF-04-2019-0346](https://doi.org/10.1108/HFF-04-2019-0346).
- [17] M. Naseer, M. Y. Malik, S. Nadeem, and A. Rehman, "The boundary layer flow of hyperbolic tangent fluid over a vertical exponentially stretching cylinder", *Alexandra Engineering Journal*, vol. 53, pp. 747-750, 2014.
- [18] R. R. Rangi, and N. Ahmad, "Boundary layer flow past over the stretching cylinder with variable thermal conductivity", *Applied Mathematics*, vol. 3, p. 205-209, 2012.
- [19] M. S. Abel, and N. Mathesha, "Heat transfer in MHD viscoelastic fluid flow over a stretching sheet with variable thermal conductivity and non-uniform heat source", *Applied Mathematical Modeling*, vol. 32, pp. 1965-1983, 1997.
- [20] A. Öztürk, F. Sönme, and A. Kabakuş, "Determination of optimum parameters using different nanofluids in heat pipe heat exchangers with response surface method", *Chemical Engineering Communications*, vol. 211, No. 5, pp. 725-735, 2023. <https://doi.org/10.1080/00986445.2023.2289146>
- [21] A. Öztürk, F. Sönme, and A. Kabakuş, "Optimization of Parameters Affecting the Thermal Efficiency in Heat Pipes Using Different Nanofluids with Taguchi Method", *Yüzüncü Yıl University Institute of Science and Technology Journal*, vol. 28, No. 3, pp. 1081-1090, 2023. <https://doi.org/10.1053433/yyufbed.1242697>
- [22] S. Mukhopadhyay, "Analysis of boundary layer flow over a porous nonlinearly stretching sheet with partial slip at the boundary", *Alexandria Engineering Journal*, vol. 52, pp. 563-569, 2013. <http://dx.doi.org/10.1016/j.aej.2013.07.004>

- [23] Ul. H. Rizwan, Z. Zeeshan, S. S. Syed, "Existence of dual solution for MHD boundary layer flow over a stretching/shrinking surface in the presence of thermal radiation and porous media: KKL nanofluid model", *Heliyon*, vol. 9(11), e20923, 2023.
- [24] B. Nagaraju, N. Kishan, J. V. Tawade, P. Meenapandi, B. Abdullaeva, M. Waqas, M. Gupta, N. Batool, and F. Ahmad, "Analysis of boundary layer flow of a Jeffrey fluid over a stretching or shrinking sheet immersed in a porous medium", *Partial Differential Equations in Applied Mathematics*, vol. 12, 100951, 2024. <https://doi.org/10.1016/j.padiff.2024.100951>
- [25] R. S. Vidya, P. B. Mallikarjun, and A. J. Chamkha, "Analysis of MHD boundary layer flow of a viscous fluid past a stretching sheet employing the Legendre wavelet method", *International Journal of Ambient Energy*, vol. 45(1). Article: 2310629, 2024. <https://doi.org/10.1080/01430750.2024.2310629>
- [26] M. K. Joseph, P. Ayuba, and A. S. Magaj, "Effect of Brinkman number and magnetic field on laminar convection in a vertical plate channel", *Science World Journal*, vol. 12(4), pp. 58-62, 2017.
- [27] I. Buongiorno, "Convective transport in nanofluids", *Journal of Heat Transfer*, vol. 128, pp. 240-250, 2006.
- [28] A. R. Bestman, "The boundary layer flow past a semi-infinite heated porous plate for two-components plasma", *Astrophysics and Space Science*, vol. 173, pp. 93-100, 1990.
- [29] F. P. Incropera, and D. P. DeWitt, *Fundamentals of Heat and Mass Transfer*, 7th Edition., Wiley, 2017.
- [30] A. Bejan, *Convection Heat Transfer*, 4th edition, John Wiley & Sons, 2013.
- [31] B. R. Munson, A. T. Rothmayer, and T. H. Okiishi, *Fundamentals of Fluid Mechanics*, 7th Edition, John Wiley & Sons, 2013.
- [32] S. B. Pope, *Turbulent Flows*, Cambridge University Press, 2000.
- [33] T F. Laadhari, "Reynolds number effect on the dissipation function in wall-bounded flows", *Physics of Fluids*, vol. 19(3), 038101, 2007. <https://doi.org/10.1063/1.2711480>
- [34] J. P. Monty, N. Hutchins, H. C. H. NG, I. Marusic and M. S. Chong, "A comparison of turbulent pipe, channel, and boundary layer flows", *Journal of Fluid Mechanics*, vol. 632, pp 431-442, 2009. <https://doi:10.1017/S0022112009007423>
- [35] S. B. Pope, *Turbulent Flows*, Cambridge University Press, (Cornell University), 2000.
- [36] D. Modesti, and S. Pirozzoli, "Reynolds and Mach number effects in compressible turbulent channel flow", *International Journal of Heat and Fluid flows*, vol. 39. Pp. 33-49, 2016. <https://doi:10.1016/j.ijheatfluidflow.2016.01.007>
- [37] H. Schlichting, and K. Gersten, *Boundary-Layer Theory*, 8th Revised and Enlarged edition, Springer, McGraw Hill, 2000. DOI 10.1007/978-3-642-85829-1
- [38] Y. A. Çengel, and A. J. Ghajar, *Heat and Mass Transfer: Fundamentals and Applications*, 5th Edition, McGraw-Hill, 2019.
- [39] F. P. Incropera, and D. P. DeWitt, *Fundamentals of Heat and Mass Transfer*, 7th edition, Wiley, 2017.
- [40] M. Ramzan, Z. Un Nisa, M. Ahmad, and M. Nazar, "Flow of Brinkman fluid with heat generation and chemical reaction", *Hindawi Complexity*, vol. 2021, pp. 1-11, Article ID 5757991, 11 pages <https://doi.org/10.1155/2021/5757991>
- [41] N. S. Akhar, D. Tripathi, Z. H. Khan, and O. A. Beg, "A numerical study of magnetohydrodynamic transport of nanofluids over a vertical stretching sheet with exponential temperature-dependent viscosity and buoyancy effects", *Chemical Physics Letters*, 2016, <https://doi.org/10.1016/j.cplett.2016.08.043>
- [42] B. Bidin, and R. Nazar, "Numerical solution of the boundary layer flow over an exponentially stretching sheet with thermal radiation", *European Journal of Scientific Research*, vol 33(4), pp. 710-717, 2009.
- [43] A. Ishak, "MHD boundary layer flow due to an exponentially stretching sheet with radiation effect", *Sain Malaysiana*, vol. 40, pp. 391-395, 2011.
- [44] S. R. Sheri, A. K. Suram, and P. Modulgua, "Heat and Mass Transfer Effects On MHD Natural Convection Flow Past An Infinite Inclined Plate With Ramped Temperature", *J. KSIAM*, Vol. 20(4), pp. 355-374, 2016. <http://dx.doi.org/10.12941/jksiam.2016.20.355>
- [45] Y. Dharmendar Reddy, B. Shankar Goud, Kottakkaran Soopy Nisar, B. Alshahrani, M. Mahmoud, C. Park, "Heat absorption/generation effect on MHD heat transfer fluid flow along a stretching cylinder with a porous medium", *Alexandria Engineering Journal*, Vol. 64, pp. 659-666, 2023. <https://doi.org/10.1016/j.aej.2022.08.049>
- [46] M. R. Krishnamurthy, B. C. Prasannakumara, B. J. Giresha, and R. S. R. Gorla, R, "Effect of viscous dissipation on hydromagnetic fluid flow and heat transfer of nanofluid over an exponentially stretching sheet with fluid-particle suspension", *Cogent Mathematics*, Vol. 2(1), pp. 1-18, 2015. <https://doi.org/10.1080/23311835.2015.1050973>

- [47] L. Shuguang, K. Raghunath, A. Alfaleh, A. et al. "Effects of activation energy and chemical reaction on unsteady MHD dissipative Darcy–Forchheimer squeezed flow of Casson fluid over horizontal channel", Sci Rep, Vo. 13, 2666, 2023. <https://doi.org/10.1038/s41598-023-29702-w>

Research Article

Optimizing Access Point Allocation Based on Genetic Algorithm with Channel Conflict Detection

Ramazan Kocağolu^{1a}, M. Hanefi Calp^{1b}, M. Ali Akcayol^{1c}

¹Computer Engineering, Faculty of Engineering, Ostim Technical University, Ankara, Türkiye

²Management Information Systems, Ankara Hacı Bayram Veli University, Ankara, Türkiye

³Computer Engineering, Faculty of Engineering, Gazi University, Ankara, Türkiye

ramazan.kocaoglu@ostimteknik.edu.tr

DOI : 10.31202/ecjse.1529228

Received: 07.08.2024 Accepted: 28.03.2025

How to cite this article:

Ramazan Kocağolu, M. Hanefi Calp, M. Ali Akcayol, "Optimizing Access Point Allocation Based on Genetic Algorithm with Channel Conflict Detection", El-Cezeri Journal of Science and Engineering, Vol: 12, Iss: 2, (2025), pp.(153-166).

ORCID: ^a0000-0002-6554-3335; ^b0000-0001-7991-438X. ^c0000-0002-6615-1237.

Abstract : In recent years, high-bandwidth and cost-effective wireless network technologies have emerged as a competition factor in the process of forming its own infrastructure. On the other hand, today's challenges of designing an effective layout have become an important problem for public institutions and private companies with increasing requests. There are some methods to solve this problem. In this study, a new approach based on a genetic algorithm is proposed to solve the mentioned problem. A simulation is developed to test the success of the algorithm. The most effective layout design of the access points is constituted by the distance between the access points and the communication channels used in the developed simulation. The experimental results obtained showed that the proposed algorithm successfully achieved the challenge of designing an access point layout in terms of total coverage area and average bandwidth per user. We have obtained experimental results that the maximum coverage area is 1181.1 m, 1183.6 m and 1148 m, and bandwidth usage is 11, 54 and 248 mbps for 802.11b, 802.11g and 802.11n standards, respectively.

Keywords : Access Point Allocation, Genetic Algorithms, Optimization, Channel Conflict

1 Introduction

Wireless network technologies such as IEEE 802.16 (WiMAX) and IEEE 802.11 (Wifi) are used commonly in almost every field of life such as home, office, airport, and other open public spaces. These technologies are more popular than cabled technologies in open public spaces [1]–[7]. Effective usage of wireless networks depends on the quality of a given network service. One of the most important factors that affect the service quality is a layout of access points to an area in which network service will be given. While mentioned layouts are relatively easy in case of less access points, the most effective layouts are considerable difficult where there is a need of many access points like corporations and institutions. For this reason, today's complex and difficult conditions cause new solution methods that give fast and easy solutions for the problems.

In literature, genetic algorithms have been used in many studies to solve problems in wired and wireless network technologies. Lee et al. studied access point allocation optimization for smart home systems by using a genetic algorithm [1], [8]. They have revealed the impact of access point allocation on overall wireless system performance regardless of channel conflict challenge. However, the issue is quite a component which impacts on the quality of wireless services. Yoshino and Ohtomo [9] conducted a study about effective channel assignment methods for mobile communication systems by using genetic algorithms whereas we focus on wireless network systems and their issues. Therefore, their study cannot directly adapt to wireless infrastructure because of different technologies.

Funabiki et al. [10] studied the subject that allocates an optimal access point for a wireless infrastructure mesh network. Turgut et al. [11] studied clustering algorithm optimization on mobile Ad Hoc networks by using a genetic algorithm approach. Singh and Bhukya suggested a solution based on a hybrid genetic algorithm that can be a candidate to solve the problem of the minimum energy usage on wireless ad-hoc networks. The suggested hybrid approach was compared with the known intuitional approaches to solve this problem [12]. These studies attempt to solve issues about the allocation of access points for mesh networks, mobile ad-hoc networks, and energy efficiency problems for ad-hoc networks, respectively. Our study differs from them in terms of using wireless technology. Agustin-Blas et al. suggested a hybrid genetic algorithm application to solve the problem regarding the determination of access points places needed to be distributed for constituting wireless networks. The

Table 1: The Comparison of the related studies

Related Studies	Network Type	Optimization Problem	Optimization Algorithm
T. Scully and K.N. Brown [2]	Wireless	Load Balancing	GA
W. Yan et al. [3]	Wireless	Bandwidth	GA
J. H. Lee et al. [8]	Wireless	Location	GA
J. Yoshino and I. Ohtomo [9]	GSM	Channel Assignment	Hybrid
Funabiki et al. [10]	Mesh	Location	GA
Turgut et al. [11]	Ad Hoc	Clustering	Hybrid
Singh and Bhukya [12]	Ad Hoc	Energy Consumption	Hybrid
Agustin-Blas et al. [13]	Wireless	Load Balancing	Hybrid
El-Alfy [14]	MPLS	Minimum Cost	GA
Calvo et al. [15]	Ethernet	Dividing	GA
Zhang and Zhang [16]	Ethernet	Dividing	GA
Sanz et al. [17]	Ethernet	Switch Layout	Hybrid
Singh et al. [18]	WSN	Sink Location	GA
Quyang et al. [19]	Wireless	AP Location	Hybrid
Hanh et al. [20]	WSN	Coverage	Hybrid
V. Bertolini et al. [22]	Wireless Charging	Energy Consumption	Hybrid
Y. E. M. Hamouda [23]	WSN	Sink Location	Hybrid
L. V. Quan [24]	WSN	Sink Location	GA
D. J. Bahadur et al. [26]	WSN	Energy Consumption	Hybrid
X. Gong et al. [27]	WSN	Energy Consumption	GA

proposed algorithm aimed to determine a cost-effective network topology for this problem. Performance and effectiveness of the algorithm were tested by constituting a topology determined by two different 1000 and 2000 users randomly [13]. They focus on the load balancing problem while we consider the channel conflict issue.

El-Alfy suggested a design method based on a genetic algorithm to find the topological structure of networks based on MPLS which supplies the minimum cost. With this technology, designing an ISP backbone with the most effective and minimum cost emerged as a problem. An approach based on a genetic algorithm was suggested to solve this problem [14]. Calvo et al. suggested a new genetic algorithm to solve the problem of dividing traditional ethernet networks into parts. The performance of the suggested genetic algorithm was tested in various simulations. When it is compared with previous genetic algorithm approaches, it can be said that the suggested approach can produce faster and more productive solutions [15]. Zhang and Zhang analyzed the problem of dividing the network into parts in industrial key ethernet technology. The genetic algorithm was suggested to solve the problem of dividing networks into parts [16]. Sanz et al. suggested a model based on hybrid genetic algorithm that supplies switches to place into the optimum points in a network to achieve the most efficient performance. They tested the approach that suggested a switch layout problem on network architecture in Madrid, Spain. Obtained experimental results showed that the hybrid genetic algorithm method obtained the best performance in solving the switch layout problem [17]. These studies are related to some challenges of wired technology such as MPLS, switches, and ISP infrastructure whereas our study attempts to cope with challenges such as efficiency access point allocation and channel conflict for traditional wireless networks.

Singh et al. suggested a Genetic Algorithm (GA) based sink mobility technique for WSN. The GA process determines the optimal sink locations on the trajectory for each cluster. In addition, a network energy consumption model is proposed that implements the fitness evaluation operator of the GA process. Obtained experimental results showed that GA based sink mobility provides increase in network lifetime than other protocols [18]. Ouyang et al. suggested a model adaptive genetic algorithm (IAGA) to handle the localization problem of wireless networks and a modified evaluation function to reduce the error of distance measurement in a topological structure [19]. Hanh et al. proposed a novel and efficient metaheuristic in the form of a genetic algorithm. The proposed genetic algorithm includes a heuristic population initialization procedure and the proposed exact integral area calculation for the fitness function. Obtained experimental results showed that the algorithm delivers the best performance in terms of solution quality and stability on a majority of the tested instances [20].

In this study, a genetic algorithm, which makes access point layout optimization regarding problem of crossing channels between access points, is proposed. The rest of the paper is prepared as follows. In section 2, the problem is defined, and limits in the real world are mentioned that need to be taken into consideration in the solution of the problem. In section 3, the design of the developed algorithm is mentioned in detail. Tests and obtained experimental results are presented in section 4. Section 5 concludes the paper with some further discussions.

2 Problem Definition

Some challenges should be solved to use wireless networks in a more effective way after these networks have become widespread. While the institutional wireless network is taken into consideration, there are some problems that affect the overall performance of the network. The design, which is made by regarding these problems, is important because of achieving real-like results. Developed methods and algorithms need to solve these problems within the existing limits. The problems and limits considered by GA design in this article are as below:

- Each access point serving from 2.4 GHz frequency uses a wireless channel between 1 and 13 to give service. Channel

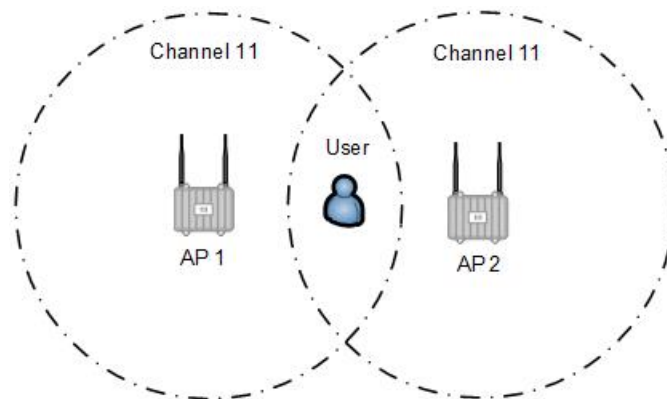


Figure 1: Channel conflict problem

conflict means that access points, which have the same SSID and the same channel, are neighbors that they enter into each other's coverage area. The users of wireless service expose to channel conflict have a serious lack of many services. A channel conflict, which can occur with two access points, as shown in Figure 1. The wireless user is at the junction point of coverage areas of two access points that use the same channel. In this situation, critical problems in the user's connection can be encountered. As a conclusion, the neighbor access points should not use the same channel. In other words, access points which use the same channel should not be near to each other. Suggested GA design determines the place of access points by regarding this problem. This means that it appoints different channels to neighbor access points.

- One of the most important elements that affect the efficiency and coverage area of wireless communication in a building is walls. The proposed algorithm places access points regarding this situation.
- Making optimization considering 802.11 b/g/n wireless network standards is an acceptable solution that is similar to the real world's problem. Accordingly, the designing of access point allocation is made based on network standards determined by the user while specifying the most suitable place for them.
- It makes layouts to the specific places such as corners and edges of the walls while locating the places of access points. It means that access point cannot be placed any desired area in order to approximate the real environment.
- The proposed algorithm determines optimal places of access points considering the 3D environment.

3 A Genetic Algorithm for Access Point Layout with Channel Conflict Detection

A genetic algorithm is an algorithm that can successfully solve critical problems like the deployment of devices on communication networks in urban planning. It is a technique that codes feasible solutions to solve an existing problem inspiring an evolutionary process. The most important point should be taken into consideration in GA design is that coding the problem and defining the fitness function that impact on directly solution of the problem. While the coding of the problem draws limits of search space GA works on, the fitness function determines the suitability of achieved solutions [12], [13], [14], [15], [16], [17], [18], [19], [20], [21], [22], [23], [24], [25], [26], [27].

Nowadays, there are different wireless network standards to be used for wireless communication. Although there are some distinctions that separate these standards, the most remarkable difference is the distance of coverage area technology provides. In this paper, a genetic algorithm has been designed to place access points to the most efficient places inside buildings so that it can achieve overall coverage area at the top level, and prevent channel conflict by considering 802,11b, 802,11g, and 802,11n wireless network standards.

3.1 Problem Encoding

GA is a selection algorithm based on natural selection and the evolution mind. Generally, there are four fundamental steps in the GA optimization procedure. These are selection, crossing, mutation, and evaluation. GA optimization procedure practices repeated selection strategy applies crossing and mutation, and then evaluates the suitability of chromosomes. The structure of a chromosome in the proposed GA is seen in Figure 2. Each access point is represented as a chromosome and a set of chromosomes is represented as a population. In other words, population is expressed as a candidate solution that contains a set of access points. An access point consists of some units such as X, Y, and Z coordinates, channel, and cost calculated according to the position of other access points in the population. Each unit is called a gene in the chromosome as shown in Figure 2.

Figure 3 shows structure of population in the proposed algorithm and possible layout in the real world.

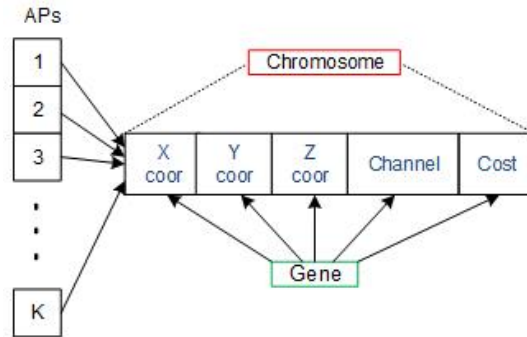


Figure 2: Structure of the AP encoding in GA

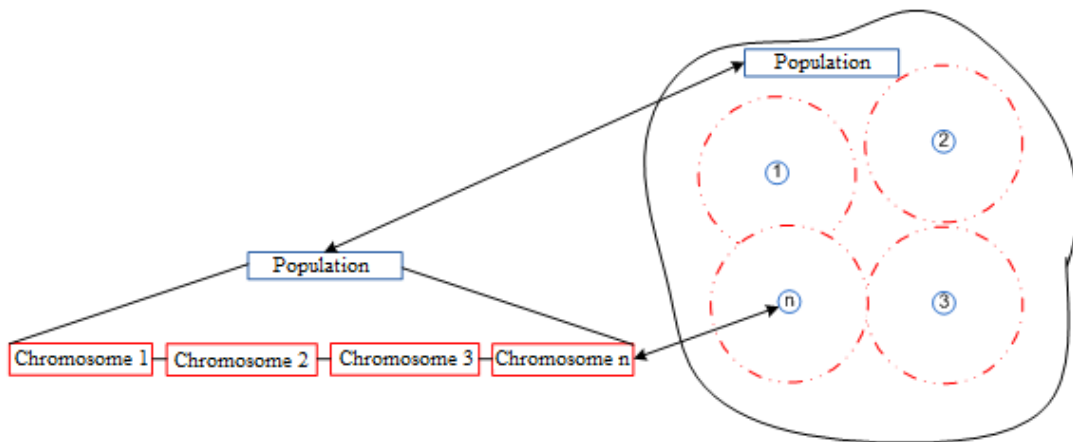


Figure 3: Population and its Allocation in a Reel Network Environment

Consequently, each population is a candidate solution that represents the allocation of access point in real environment as shown in Figure 3. The most important challenge is to discover the optimal allocation of access points by considering used channel of them. The population can include inefficient layout the distance between access points is either too close or too far.

3.2 Initialization of the Algorithm

Each chromosome in the population is randomly generated at the beginning of algorithm as following.

- Firstly, all coordinates where access points can be placed are discovered. Specific points where access points will be placed are randomly selected between these coordinates. These selected coordinates are transferred to genes that constitute the x, y, and z coordinates of chromosomes.
- Each access point serving from 2.4 GHz frequency selects randomly a wireless channel between 1 and 13 to serve network services for wireless users. Channel conflict is not taken into consideration at this state and is not make any operation to detect it. Besides, each access point serving from the 5 GHz frequency wireless standard selects randomly an available wireless channel.
- While generating the initial population, a 0 value is appointed to cost the gene of all chromosomes.

The process of generating the initial population continues to reach a determined iteration number. All state of the proposed optimization procedure is shown in Figure 4.

3.3 Selection Operator

In this section, a rank-based wheel selection mechanism, as described in [9] is used. Therefore, the individuals are sorted in a list based on their efficiency. The position of the individuals within the list is sorted by comparing cost which is a gene defined in our study. Efficiency of fitness function, the most important section of genetic algorithm, impacts directly on efficiency of the algorithm. The fitness function considers the distance between access points and channel conflict. It gives a point that implies the possibility of passing the next generation to individuals according to the distance between two access points and the used channel. The point is the saved cost gene in each chromosome. The total of these points is used to determine whether the individuals in the population pass to the next generation or not.

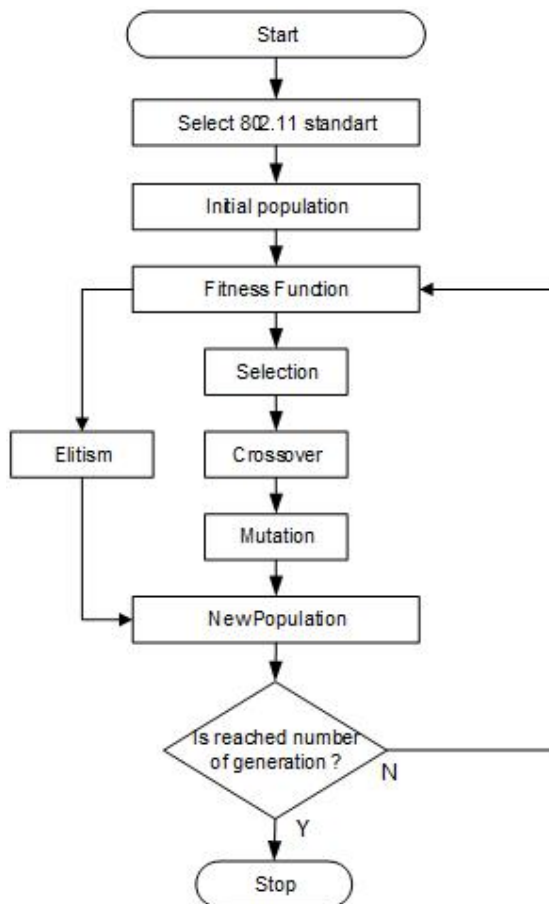


Figure 4: The General Flow Diagram of the Algorithm

We suggest that the coverage areas of neighbor access points should overlap at the rate of % 25 because a wireless user to pass between access points without interrupt of any services. Figure 5 shows the optimum layout of access points in space. Consequently, if the radius of the access point’s coverage area is r , the distance between two access points (1) is calculated as below:

$$D_S = 2r - \frac{r}{4} = \frac{7r}{4} \tag{1}$$

$$W = \text{Number of Wall} \times \beta \tag{2}$$

$$D_W = D_S - W = \frac{7r}{4} - W \tag{3}$$

The optimum distance (3) between two access points can be found by subtracting the loss of (2) because of the existing walls in (1) distance. (2) is calculated by multiplying the number of walls the in-coverage area and the β constant. β represents the loss of signal noise because of the existing wall in the area. It is assumed 1,5 meters. (3) distance between each neighbor area is the optimal location where the access point can be placed. Let AP_1 and AP_2 be neighbor access points. We denote that AP_{1C} and AP_{2C} are channels used by AP_1 and AP_2 , respectively. α is the fitness function of the proposed GA. Let χ be the distance between AP_1 and AP_2 . The fitness value is calculated as below.

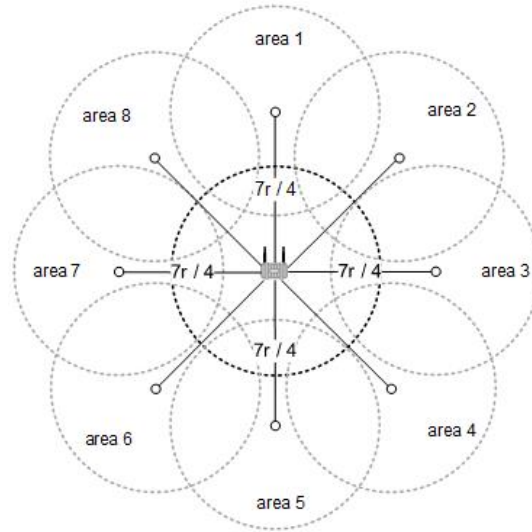


Figure 5: Optimal Allocation Between Neighbor Access Points

Algorithm 1 Fitness function

```

if  $AP_{1C} == AP_{2C}$  then
 $\alpha \leftarrow -500$ 
else
  if  $\chi < 20$  then
     $\alpha \leftarrow -100$ 
  end if
  if  $20 - (2) \leq \chi \leq 30 - (2)$  then
     $\alpha \leftarrow 0$ 
  else if  $30 - (2) < \chi \leq 40 - (2)$  then
     $\alpha \leftarrow -20$ 
  else if  $40 - (2) < \chi \leq 50 - (2)$  then
     $\alpha \leftarrow -50$ 
  else if  $50 - (2) < \chi \leq 55 - (2)$  then
     $\alpha \leftarrow -70$ 
  else if  $55 - (2) < \chi \leq 59 - (2)$  then
     $\alpha \leftarrow -90$ 
  else if  $59 - (2) < \chi \leq 62 - (2)$  then
     $\alpha \leftarrow -100$ 
  else if  $62 - (2) < \chi \leq 66 - (2)$  then
     $\alpha \leftarrow -90$ 
  else if  $66 - (2) < \chi \leq 70 - (2)$  then
     $\alpha \leftarrow -70$ 
  else if  $70 - (2) < \chi \leq 80 - (2)$  then
     $\alpha \leftarrow -50$ 
  else if  $80 - (2) < \chi \leq 90 - (2)$  then
     $\alpha \leftarrow -20$ 
  else if  $90 - (2) < \chi \leq 100 - (2)$  then
     $\alpha \leftarrow -10$ 
  else
     $\alpha \leftarrow -100$ 
  end if
end if=0

```

The fitness value is equal to 0 at the start of the process. A chromosome with the maximum fitness value means that it is the optimal solution for the problem. Initially, this value will be decremented by 500 for each neighbor APs that uses the same channel in order to prevent channel conflict. Additionally, fitness value will be increase or decrease by distance between

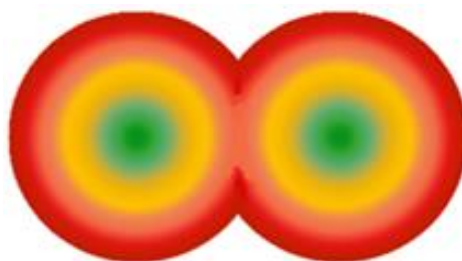


Figure 6: Position of Neighbor Access Points With Each Other

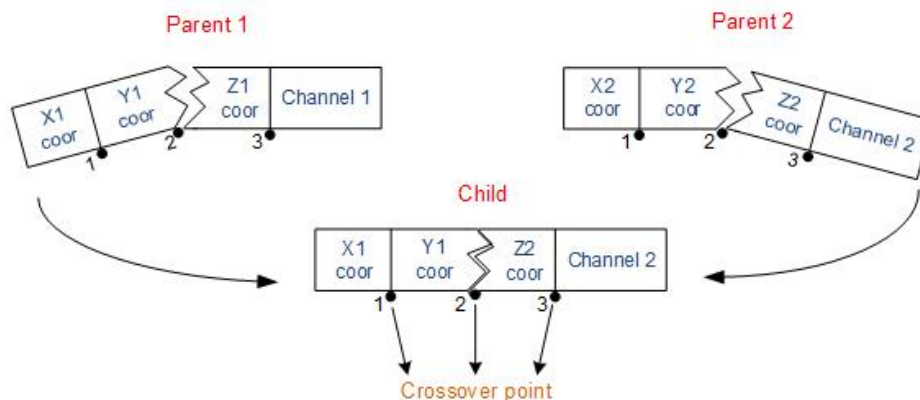


Figure 7: Example of Crossover Process in GA

neighbor access points. While the fitness value is 100 for the optimum distance between neighbor APs, it is decremented far or near this distance. The fitness function catches the best value by considering the distance according to 802.11 standards and then sends it to the next population. Figure 6 shows the position of two access points is how to influence each other. The optimum position of neighbor access points is the green field. Consequently, being far from or too near each other of access points are unsuited solution. In addition, access points can be placed only at the edge, or corners of walls. Other places apart from these points are not accepted as solutions.

After arraying of individuals in each population according to the cost gene in chromosome, % 30 of individuals which have the best location of access point pass directly to the next generation by elitism. As a result of tests, when the rate of elitism is % 30, the best result is achieved. Therefore, the rate of elitism is selected as % 30. Other individuals are transferred to the next generation after selecting randomly from the population and applying crossing and mutation.

3.4 Crossover and Mutation Operators

The crossover and mutation operators implemented in the proposed algorithm are based on those used in [9], [12]. The process for performing the crossover is the following: We consider a special crossover operator in which two parents produce one child. Two individuals are selected; one will be named father, and the other mother. Only one offspring individual will be generated from these two individuals. The parents are randomly chosen among the individuals in the population that have not been discarded. The two parents are coupled and a crossover point is randomly selected. Figure 7 shows the process of producing a new individual from the two parents. There are three crossover points in each individual. These points are used for the crossover operator. For example, point 2 is randomly selected by a proposed genetic algorithm in order to produce a new child. After this operation, population diversity is ensured by producing new individuals.

After the crossover operator, a mutation operator is applied so as to generate more diversity in the population. A swap-type operator is used. Two parents are coupled at random, and two genes of each parent are swapped to generate two mutated individuals. The mutation is used to avoid that the algorithm remains stuck in the local minimums of the fitness function. Figure 8 shows an example of the process of mutation for coordinate genes. If the channel gene is selected for mutation, the swap-type operator is not used. See Figure 9 as an example. A number is randomly produced between 1 and 13. This number is swapped to the existing channel number. Therefore, a new individual with a different channel number is produced after the mutation operator.

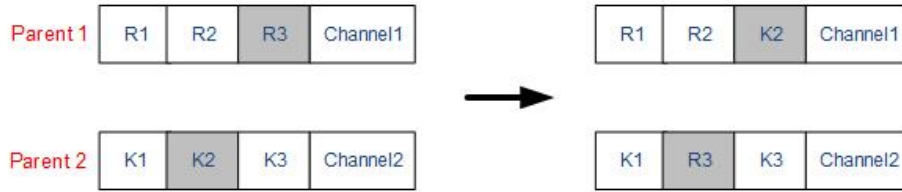


Figure 8: Example of Crossover Process for Coordination in GA

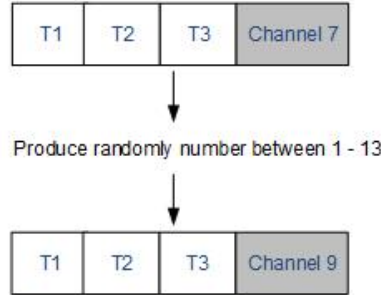


Figure 9: Example of Crossover Process for Channel in GA

4 Simulation

In this section, we have simulated the proposed GA optimization model in Visual Studio with the parameter lists in Table 2. The simulation has been performed on an Intel Core 2 Duo CPU 2.53 GHz with 4 GB RAM. The proposed GA attempts to discover optimal places of access points on the used building in the simulation taking into consideration the wireless standards and channel conflict.

4.1 Assumptions and Parameters

In Turkey, city hospitals have begun to be built in various cities of Turkey within the scope of public-private partnerships. Kayseri City Hospital is one of these hospitals and was opened in 2018. It has a bed capacity of 1583 and a closed area of 300,000 m². It consists of 4 blocks that are architecturally similar to each other, a central hospital connecting these blocks, and 1 physical therapy rehabilitation center. It will serve approximately 5,000 wireless network users daily. Determining where access points will be positioned in such large structures is a very difficult process. Access points must use appropriate channels so as not to cause channel conflict. In addition, the number of access points must be at an optimal level. Using too many access points increases both the cost and the possibility of channel conflict. The building architecture of Kayseri City Hospital is shown in Figure 10.

One of the buildings with the same architecture is a cardiovascular hospital. Therefore, the developed algorithm was applied

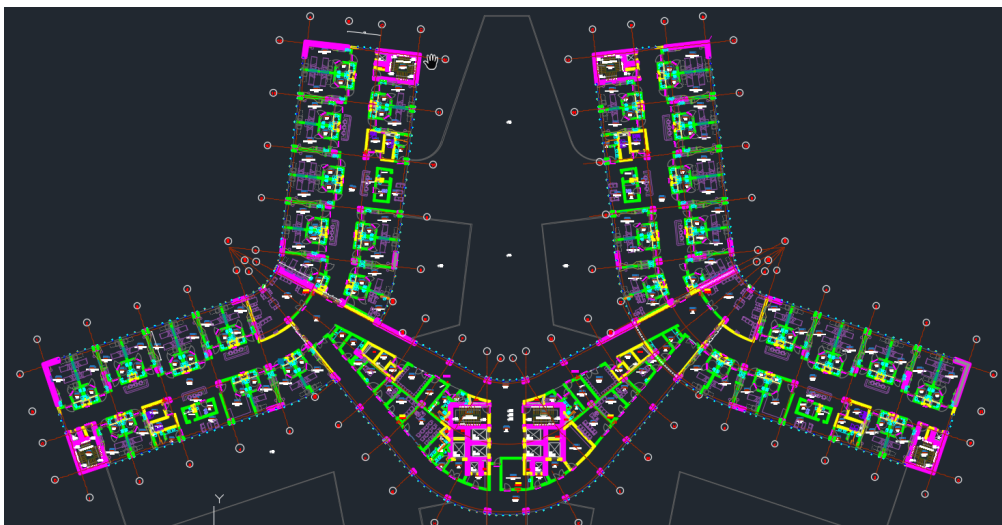


Figure 10: Kayseri City Hospital Building Plan

Table 2: Simulation Parameters

Parameters	Values
The signalling range of access point with 802.11.b	35(m)
The signalling range of access point with 802.11.g	35(m)
The signalling range of access point with 802.11.n	70(m)
The number of access points with 802.11b	55
The number of access points with 802.11g	55
The number of access points with 802.11n	33
The number of wireless users	800

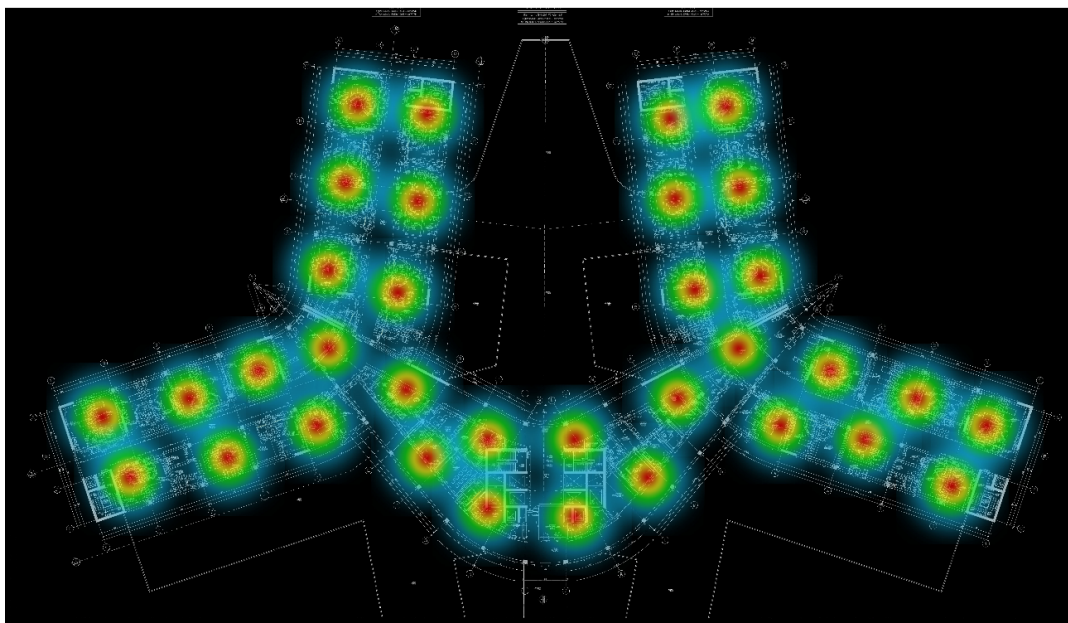


Figure 11: Kayseri City Hospital Used in the Simulation

in the cardiovascular hospital. In addition, it was tested in a physical therapy rehabilitation center.

4.2 Simulation Results

In this section, we present the impact of the proposed GA scheme on the maximum coverage area and average bandwidth per user.

4.2.1 Maximum Coverage Area

Firstly, we examine the maximum coverage area. 802.11 standards have different signaling range. For example, in the building, 802.11b, 802.11g, and 802.11n wireless standards cover the area about 35, 35, and 70 meter diameter area, respectively [15]. We employ 25, 25 and 50 access points for 802.11b, 802.11g and 802.11n standards, respectively. Therefore, we can simply calculate maximum coverage area for space environment as multiplying number of access point and signaling range of wireless standard. Thus, maximum coverage area is 1750 m for all wireless standards in the simulation. However, it is expected the maximum coverage area is considerably shorter than 1750 m in simulation because existing walls in the building causes signal noise. We have obtained experimental results that maximum coverage area is 1181.1 m, 1183.6 m and 1148 m and average coverage area of each access point is 23.62 m, 23.67 m and 45.92 m for 802.11b, 802.11g and 802.11n standards, respectively. X, Y, Z coordinates, channels, and coverage area of each access point are detail shown in Table 3. Figure 12, 13 and 14 depict that proposed GA allocates access points on building shown figure 11 according to 802.11b, 802.11g and 802.11n, respectively.

We calculate the fitness function as mentioned in section 3.3. When the optimal distance between access points is obtained, the fitness function achieves 100 award points. Obviously, the optimal layout for 50 access points should have 5000 points according to proposed algorithm. Similarly, it should have 2500 points for 25 access points. Figure 15 shows that the algorithm reached a maximum point after 5000 iterations according to 802.11b and 802.11g standards, and after 3000 iterations according to 802.11n standards. The population size is determined as $p_s=200$, the rate of crossing was $p_c=0,7$, and the rate of mutation was $p_m=0,1$, and the rate of elitism was $p_e= \%30$ in the simulation. 802.11b and 802.11g standards have the same signaling range of access points. The curve of the two technologies in the graphic overlaps because the fitness function makes optimization by considering the distance between access points.

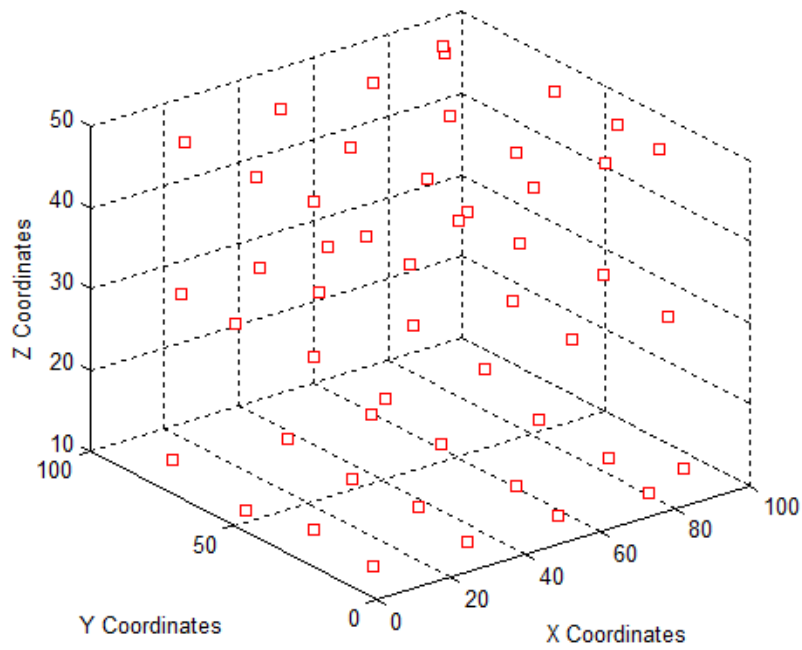


Figure 12: Access Point Allocation According to 802.11b Standard

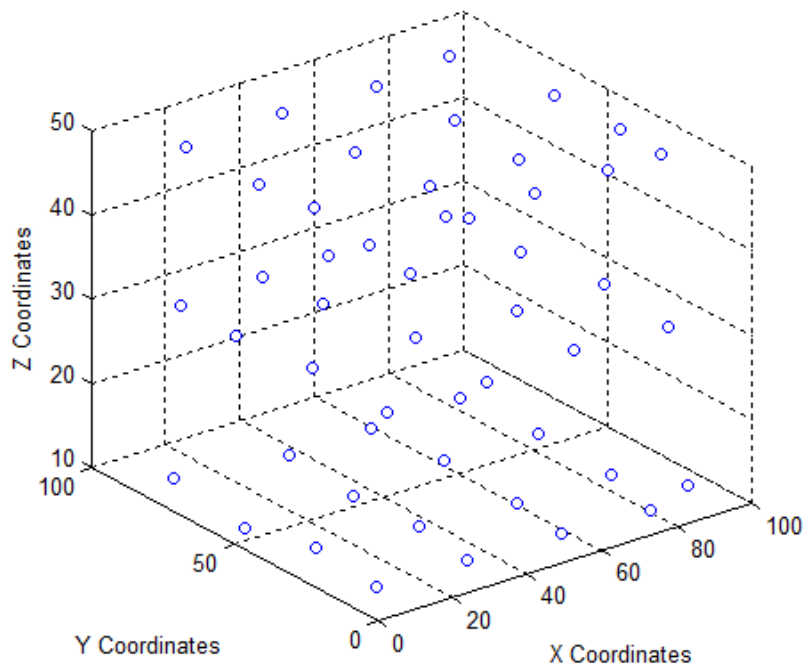


Figure 13: Access Point Allocation According to 802.11g Standard

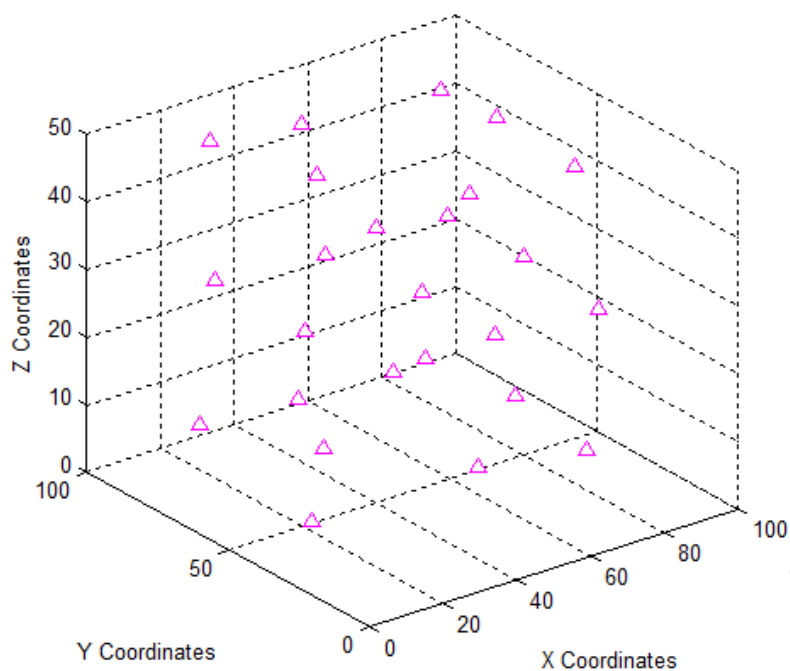


Figure 14: Access Point Allocation According to 802.11n Standard

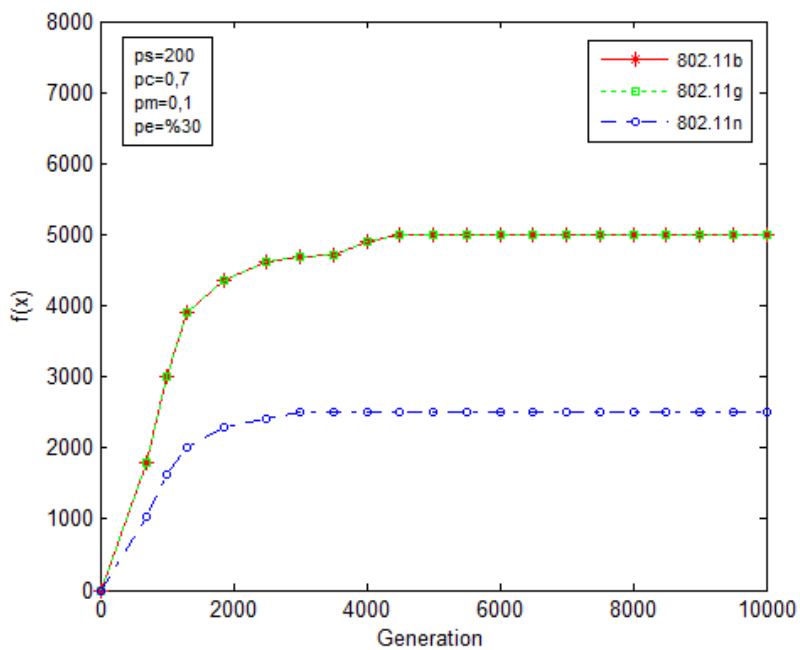


Figure 15: The Curve of Fitness Function According to Number of Generations

Table 3: Coordinate, Channels and Coverage Area of Access Points in the Building

AP	802.11b					802.11g					802.11n				
	X	Y	Z	Ch	Cvr	X	Y	Z	Ch	Cvr	X	Y	Z	Ch	Cvr
1	10,3	14,4	10	10	20,8	10,5	14,1	10	11	20,8	24,1	23,5	10	13	43,8
2	34,2	12,9	10	2	21,3	34,1	13,3	10	4	21,3	47,3	23,3	10	4	45
3	58,4	12,5	10	6	21,5	58,7	12,3	10	6	21,5	71,1	16,3	10	7	47,5
4	80,7	10,1	10	12	21,3	80,9	10,1	10	9	21,3	26,9	51,5	10	9	43,8
5	94,3	15,6	10	1	22,5	94,7	15,3	10	10	21,3	75,9	47,5	10	1	45
6	12,5	38,1	10	5	26,5	12,7	38,3	10	8	26,5	13,1	77,3	10	5	46,3
7	37,3	33,9	10	13	23,8	37,1	33,7	10	3	23,8	37,9	74,7	10	12	47,5
8	60,9	30,2	10	9	21,3	60,7	30,7	10	12	21,3	78,7	74,7	10	3	50
9	85,1	29,8	10	4	25	85,5	29,7	10	5	25	20,7	18,7	30	10	42,5
10	7,3	55,2	10	3	20	7,1	55,5	10	2	21,3	49,5	20,3	30	2	43,8
11	35,6	54,4	10	10	26,3	35,3	54,7	10	7	26,3	75,1	16,9	30	8	47,5
12	61,8	57,7	10	1	22,5	61,9	57,3	10	1	22,5	18,1	46,3	30	4	41,3
13	86,3	55,4	10	12	25,8	86,1	55,9	10	4	25,8	50,3	47,3	30	11	43,8
14	10,9	85,5	10	8	26,8	10,7	85,3	10	9	26,8	78,9	48,1	30	5	45
15	37,5	79,6	10	11	25	37,3	79,5	10	11	26,3	18,9	79,3	30	7	46,3
16	59,7	79,1	10	3	25	59,3	79,3	10	3	25	45,5	75,1	30	13	47,5
17	84,4	80,9	10	7	26,3	84	80,7	10	6	26,3	78,7	74,9	30	1	48,8
18	14,4	15,4	30	9	21,3	14,5	15,3	30	1	21,3	20,5	24,3	50	9	43,8
19	40,9	15,2	30	3	23,8	40,7	15,1	30	8	23,8	47,1	26,3	50	3	45
20	65,1	16,6	30	5	23,8	65,5	16,5	30	4	23,8	73,5	23,3	50	12	50
21	88,6	13,7	30	13	25	88,3	13,9	30	7	25	26,7	53,3	50	4	43,8
22	15,9	42,5	30	6	23,8	15,7	42,9	30	2	22,5	75,7	53,9	50	6	45
23	42,9	42,8	30	8	23,8	42,9	42,7	30	6	23,8	19,1	81,5	50	2	47,5
24	67,7	40,3	30	10	25	67,9	40,1	30	13	25	40,3	76,5	50	8	47,5
25	91,5	39,8	30	2	23,3	91,1	39,9	30	11	23,3	74,5	71,9	50	10	50
26	13,4	66,6	30	12	20	13,1	66,5	30	1	20	-	-	-	-	-
27	37,4	68,5	30	1	23,8	37,5	68,1	30	5	22,5	-	-	-	-	-
28	61,9	68,8	30	11	21,3	61,7	68,9	30	9	21,3	-	-	-	-	-
29	87,5	63,7	30	5	25	87,5	63,9	30	4	25	-	-	-	-	-
30	13,7	85,8	30	7	26,3	13,3	85,7	30	12	26,3	-	-	-	-	-
31	35,5	86,7	30	4	23,8	35,7	86,9	30	3	23,8	-	-	-	-	-
32	53,9	86,9	30	13	23,8	53,9	87,1	30	8	25	-	-	-	-	-
33	85,4	87,9	30	2	26,3	85,5	87,7	30	5	26,3	-	-	-	-	-
34	10,7	17,5	50	11	20,8	10,9	17,3	50	10	20,8	-	-	-	-	-
35	36,1	15,2	50	4	21,3	36,1	15,1	50	2	21,3	-	-	-	-	-
36	55,1	16,6	50	6	20,3	55,1	16,7	50	6	20,3	-	-	-	-	-
37	74,9	17,3	50	9	21,3	74,7	17,1	50	12	21,3	-	-	-	-	-
38	88,4	16,4	50	10	22,5	88,5	16,5	50	1	23,8	-	-	-	-	-
39	13,6	39,6	50	8	26,5	13,3	39,5	50	5	26,5	-	-	-	-	-
40	39,9	33,8	50	3	23,8	39,7	33,7	50	13	23,8	-	-	-	-	-
41	63,2	33,4	50	12	21,3	63,1	33,1	50	9	21,3	-	-	-	-	-
42	89,9	32,7	50	5	23,8	89,7	32,5	50	4	23,8	-	-	-	-	-
43	11,6	56,7	50	2	21,3	11,3	56,1	50	3	22,5	-	-	-	-	-
44	37,2	57,3	50	7	26,3	37,7	57,1	50	10	26,3	-	-	-	-	-
45	64,1	57,6	50	1	22,5	64,7	57,3	50	1	22,5	-	-	-	-	-
46	89,8	54,8	50	4	25,8	89,5	54,9	50	12	25,8	-	-	-	-	-
47	10,7	80,9	50	9	28	10,9	80,7	50	8	28	-	-	-	-	-
48	37,8	82,6	50	11	23,8	37,9	82,9	50	11	23,8	-	-	-	-	-
49	61,8	81,4	50	3	25	61,9	81,3	50	3	25	-	-	-	-	-
50	83,5	84,7	50	6	25	83,9	84,3	50	7	25	-	-	-	-	-

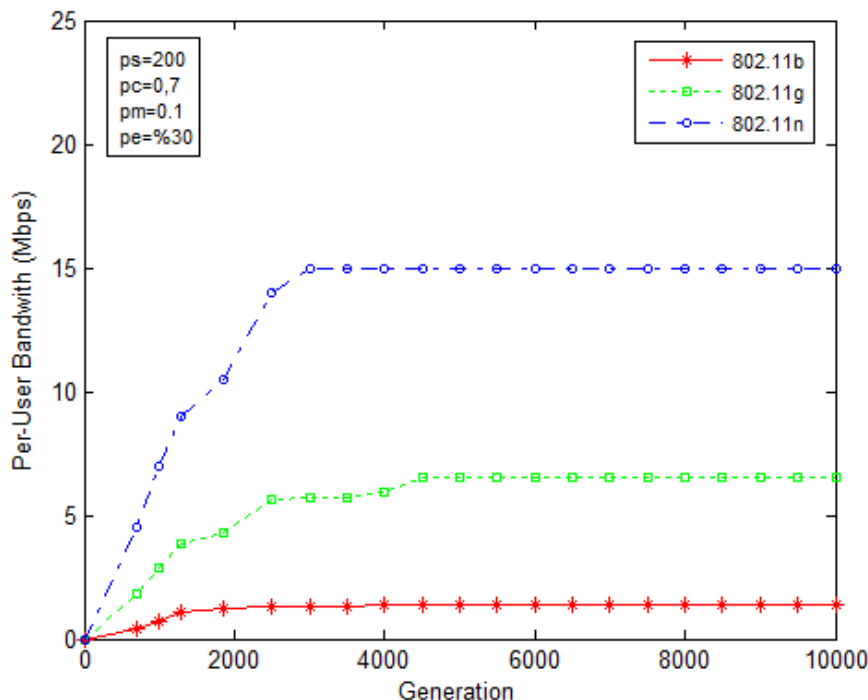


Figure 16: Average Bandwidth Per User with Generation Number

4.2.2 Average bandwidth per user

We investigate the sharing of bandwidth to wireless users. They are randomly located in the simulation to show how to effect on amount of bandwidth. 802.11b, 802.11g, and 802.11n network standards have 11, 54 and 248 mbps bandwidth respectively [15]. The bandwidth per user changes according to the number of users because wireless network architecture is the sharing network. In addition, the distance between a user and the access point affects directly on the amount of bandwidth. In other words, if the distance between the user and the access point increases, the bandwidth per user decreases. Consequently, the position of access points is a milestone for service quality. The bandwidth per user according to the optimal access point is calculated according to network standards. Figure 16 show the amount of average bandwidth per user according to generation number.

The bandwidth per user reached the top level after 5000 generations for 802.11b and 802.11g, and 3000 generations for 802.11n as in Figure 2. As it is seen from these two graphics, there is a parallel between the layout of access points and the average bandwidth per user. Optimal allocation of access points provides the best service quality because of average bandwidth apart from the maximum coverage area. Finally, the experimental results obtained show that the proposed algorithm successfully discovered the optimal layout of the access point on the building in simulation.

5 Conclusion and Future Work

In this paper, we have presented an optimal access point layout based on GA with channel conflict detection. The proposed algorithm optimizes parameters such as coverage area and channel conflict to provide service quality for wireless users in building environments. We have implemented the proposed GA method and then simulated it to demonstrate the impact of the proposed algorithm on overall system performance in terms of maximum coverage area and average bandwidth per user. Based on simulation results, the proposed GA method provides an acceptable solution and stable performance. In the future, we would like to improve the GA code implemented for real-world conditions such as the types of materials used for walls in the building due to the effect on signal quality. We also consider conducting field tests to validate the simulation results and explore the adaptability of the algorithm to different wireless standards and environments. The finding of optimal AP location will also be evaluated with other optimization algorithms in the future.

Acknowledgments

The authors greatly thank Kayseri City Hospital for their support in conducting the simulation.

Authors' Contributions

Ramazan KOCAOĞLU: Conceptualization, Methodology, Writing, and Visualization. M. Hanefi CALP: Conceptualization, Methodology, Writing, and Visualization. M. Ali AKCAYOL: Validation, Formal analysis, and review & editing. All authors

have read and approved the final manuscript.

Competing Interests

The authors declare that they have no conflict of interest.

References

- [1] J. Lee, B. Han, H. J. Lim, Y. D. Kim, N. Saxena, and T. M. Chung, "Optimizing access point allocation using genetic algorithmic approach for smart home environments," *The Computer Journal*, vol. 52, pp. 938–949, 2009.
- [2] T. Scully and K. Brown, "Wireless lan load-balancing with genetic algorithms," *Knowledge-Based Systems*, vol. 22, pp. 529–534, 2009.
- [3] W. Yan, S. Xin-xin, and S. Yan-ming, "Study on application of genetic algorithms in the optimization of wireless network," *Procedia Engineering*, vol. 16, pp. 348–355, 2011.
- [4] D. Pandey, R. Dhara, S. Bhunia, and S. Kundu, "Design and analysis of a compact millimeter-wave pentaband antenna for 5g fr-2 band wireless technologies," *International Journal of Electronics and Communications*, vol. 184, 2024.
- [5] E. Oughton, G. Geraci, P. M., V. Shah, B. D., and S. Blue, "Reviewing wireless broadband technologies in the peak smartphone era: 6g versus wi-fi 7 and 8," *Telecommunications Policy*, vol. 48, no. 6, 2024.
- [6] K. Guan, X. Guo, D. He, P. Svoboda, M. Berbineau, S. Wang, B. Ai, Z. Zhong, and M. Rupp, "Key technologies for wireless network digital twin towards smart railways," *High-speed Railway*, vol. 2, no. 1, pp. 1–10, 2024.
- [7] H. J. Madi, "A review of new developments in reliability and connectivity of wireless sensor technology over recent years." in *Comprehensive Materials Processing (Second Edition)*. Elsevier, 2024, p. 5700.
- [8] J. H. Lee, B. J. Han, H. K. Bang, and C. T-M., "An optimal access points allocation scheme based on genetic algorithm," *In Proceedings of IEEE Future Generation Communication and Networking*, vol. 2, pp. 55–29, 2007.
- [9] J. Yoshino and I. Ohtomo, "Study on efficient channel assignment method using the genetic algorithm for mobile communication systems," *Soft Computing*, vol. 9, no. 2, pp. 143–148, 2005.
- [10] N. Funabiki, T. Nakanishi, Y. Nomura, T. Farag, S. Tajima, and T. Higashino, "An optimal access-point allocation for wireless infrastructure mesh networks," *In Proceedings of IEEE International Conference on Computer Theory and Applications*, vol. 9, no. 2, pp. 143–148, 2006.
- [11] D. Turgut, S. K. Das, R. Elmasri, and B. Turgut, "Optimizing clustering algorithm in mobile ad hoc networks using genetic algorithmic approach," *In Proceedings of IEEE Global Telecommunications Conference*, vol. 1, pp. 62–66, 2002.
- [12] A. Singh and W. N. Bhukya, "A hybrid genetic algorithm for the minimum energy broadcast problem in wireless ad hoc networks," *Applied Soft Computing*, vol. 11, no. 1, pp. 667–674, 2011.
- [13] L. E. Agustín-Blas, S. Salcedo-Sanz, P. Vidales, G. Urueta, and J. A. Portilla-Figueras, "Near optimal citywide wífi network deployment using a hybrid grouping genetic algorithm," *Expert Systems with Applications*, vol. 38, no. 8, pp. 9543–9556, 2011.
- [14] E.-S. M. El-Alfy, "Applications of genetic algorithms to optimal multilevel design of mpls-based networks," *Expert Systems with Applications*, vol. 30, no. 9, pp. 2010–2020, 2007.
- [15] L. Calvo-Carro, S. Sanz-Salcedo, J. A. Figueras-Portilla, and E. G. Ortiz-García, "A genetic algorithm with switch-device encoding for optimal partition of switched industrial ethernet networks," *Journal of Network and Computer Applications*, vol. 33, pp. 375–382, 2010.
- [16] Q. Zhang and W. Zhang, "Network partition for switched industrial ethernet using genetic algorithm," *Engineering Applications of Artificial Intelligence*, vol. 20, pp. 79–88, 2007.
- [17] S. S. Sanz, J. A. P. Figueras, E. G. O. Garcia, A. M. P. Bellido, C. Thraves, A. F. Anta, and X. Yao, "Optimal switch location in mobile communication networks using hybrid genetic algorithms," *Applied Soft Computing*, vol. 8, pp. 1486–1497, 2008.
- [18] M. K. Singh, S. I. Amin, and A. Choudhary, "Genetic algorithm based sink mobility for energy efficient data routing in wireless sensor networks," *International Journal of Electronics and Communications*, vol. 131, 2021.
- [19] A. Ouyang, Y. Lu, Y. Liu, M. Wu, and X. Peng, "An improved adaptive genetic algorithm based on dv-hop for locating nodes in wireless sensor networks," *Neurocomputing*, vol. 458, pp. 500–510, 2021.
- [20] N. T. Hanh, H. T. T. Binh, N. X. Hoai, and M. S. Palaniswami, "An efficient genetic algorithm for maximizing area coverage in wireless sensor networks," *Information Sciences*, vol. 488, pp. 58–75, 2019.
- [21] M. H. Calp, "A hybrid anfis-ga approach for estimation of regional rainfall amount," *Gazi University Journal of Science*, vol. 31, no. 1, pp. 145–162, 2019.
- [22] V. Bertolini, F. Corti, M. Intravaia, A. Reatti, and Cardelli, "Optimizing power transfer in selective wireless charging systems: A genetic algorithm-based approach," *Journal of Magnetism and Magnetic Materials*, vol. 587, 2023.
- [23] Y. E. M. Hamouda, "Optimally sensors nodes selection for adaptive heterogeneous precision agriculture using wireless sensor networks based on genetic algorithm and extended kalman filter," *Physical Communication*, vol. 63, 2024.
- [24] L. V. Quan, N. T. Hanh, H. T. T. Binh, V. D. Toan, D. T. Ngoc, and B. T. Lam, "Optimally sensors nodes selection for adaptive heterogeneous precision agriculture using wireless sensor networks based on genetic algorithm and extended kalman filter," *Expert Systems with Applications*, vol. 217, 2023.
- [25] M. H. Calp and A. M. A., "Optimization of project scheduling activities in dynamic cpm and pert networks using genetic algorithms," *Süleyman Demirel Üniversitesi Fen Bilimleri Enstitüsü Dergisi*, vol. 22, no. 2, pp. 615–627, 2018.
- [26] D. J. Bahadur and L. Lakshmanan, "A novel method for optimizing energy consumption in wireless sensor network using genetic algorithm," *Microprocessors and Microsystems*, vol. 96, 2023.
- [27] X. Gong, D. Plets, E. Tanghe, T. D. Pessemer, L. Martens, and W. Joseph, "An efficient genetic algorithm for large-scale transmit power control of dense and robust wireless networks in harsh industrial environments," *Microprocessors and Microsystems*, vol. 65, pp. 243–259, 2018.

Research Article

Antibacterial Amphiphilic Composites of Poly(Diethylaminoethyl Methacrylate-co-Ethyl Methacrylate)/Polyindole Controlling Biofilm Adhesion for Antifouling Investigations

Cengiz Soykan^{1a}, Burak Tüfekçi^{1b}

¹Department of Material Science & Nanotechnology, Faculty of Engineering & Natural Sciences, Uşak University, 64200 Uşak, Türkiye

cengizsoykan@usak.edu.tr

DOI : 10.31202/ecjse.1557919

Received: 29.09.2024 Accepted: 29.03.2025

How to cite this article:

Cengiz Soykan, Burak Tüfekçi, " Antibacterial Amphiphilic Composites of Poly(Diethylaminoethyl Methacrylate-co-Ethyl Methacrylate)/Polyindole Controlling Biofilm Adhesion for Antifouling Investigations", El-Cezeri Journal of Science and Engineering, Vol: 12, Iss: 2, (2025), pp.(167-175).

ORCID: ^a0000-0002-5802-5097; ^b0000-0001-8695-8604.

Abstract : Amphiphilic and conductive composites are considered notable biomaterials and used as antibacterial agents because they effectively inhibit bacterial growth. In the current study; In the first stage, amphiphilic poly(DEAEMA-co-EMA) copolymers were synthesized from the hydrophilic monomer 2-diethylamino ethylmethacrylate (DEAEMA) and the hydrophobic monomer ethyl methacrylate (EMA) using free radical polymerization. In the second stage, five series composites were prepared at different concentrations using indole conductive monomer in the presence of iron(III) chloride (FeCl₃) using the in situ oxidative polymerization technique in poly(DEAEMA-co-EMA) copolymer. The structures of the polymer composites (PCs) were elucidated using FTIR, TGA, SEM, AFM characterization techniques. PCs exhibited significant performance on bacterial biofilm adhesion tested using the Streptococcus mutans by the test tube method (TM). In this study, the 0.006 mg/ml concentration of PC1 reduced the biofilm formation of Streptococcus mutans by 83.199%; PC5, 89.218%; PC3 inhibited 86.078%. 0.003 mg/ml concentration of PC1 prevented S. mutans from forming biofilm by 47.055%; PC5, 71.285%; PC3 was found to inhibit +68.139%. As the concentration and amount of poly(indole) in the CPs increases, the % antibiofilm effect also increases. From these results, it can be said that PCs as biofilms may be useful materials in antifouling research.

Keywords : Diethylamino Ethyl Methacrylate-co-Ethyl Methacrylate, Polyindole, Antifouling, Streptococcus Mutans, Biofilm.

1 Introduction

Conducting polymers (CPs) constitute a class of organic compounds that are included in a large group of important commercial polymers [1]. CPs constitute a vital type of functional materials that find many comprehensive applications in science and technology [2]. Owing to their biocompatibility, the areas of use of CPs include tissue engineering [3], [4], regenerative medicine [5], [6], targeted drug delivery systems [7], [8], and cell cultivation [9]. CPs and their composites are ideal materials for the conjugation of biological equipment and electrodes in bioelectrochemical fields, because of their high conductivity [10]–[12]. CPs also serve as effective matrices in the immobilization of biological materials, realize free diffusion of substrates and substances formed in the reaction, and create a biocompatible space for microorganisms and enzymes. CPs can be prepared in different ways. One of the most suitable methods for CP production is the chemical polymerization process. The formation of polymerization is explained by three stages: The 1st stage is oxidation step, the 2nd stage is coupling and the last stage is deprotonation. With this method, very expensive experimental setups are not required for CP preparation, and at the same time, this method is scalable, so it is economical. Since there are fewer internal cross-links between polymer macromolecules, which are generally obtained by chemical synthesis, they dissolve much better in suitable solvents. Moreover, this technique is the most ideal for covalent modification of CPs. This method is the most ideal for the modification of CPs [13]. In chemical polymerization method, various oxidizing agents such as ammonium persulfate ((NH₄)₂S₂O₈), sodium vanadate (NaVO₃), cerium sulfate (Ce(SO₄)₂), hydrogen peroxide (H₂O₂), potassium iodate (KIO₃), potassium dichromate (K₂Cr₂O₇) and iron (III) chloride (FeCl₃) are used [14]–[17]. Since the usage area of pure polymers is limited, their composites formed with feature conductive polymers have very widespread usage areas. Composites can be created: in situ (sequentially), ex situ (separately) and in one pot (simultaneously) [13], [18], [19]. When all techniques for the synthesis of CPs and their composites are compared, it can be seen that a wide variety of possibilities exist for the preparation of CPs and composites. Developed strategies to integrate

Table 1: Composition of the poly(DEAEMA-co-EMA) composites with varying indole content.

Indole content of the composite (% , m/m)	Amount of used poly(DEAEMA-co-EMA) (g)	Amount of used FeCl ₃		Amount of used indole		Code of Composite
		(g)	(mol × 10 ²)	(g)	(mol × 10 ²)	
10	3.6	1.45	0.90	0.53	0.45	PC1
30	2.8	4.37	2.70	1.58	1.35	PC2
50	2.0	7.25	4.48	2.62	2.24	PC3
70	1.20	10.20	6.30	3.68	3.15	PC4
90	0.40	13.05	8.06	4.72	4.03	PC5

CPs into a polymer matrix with effective interfacial interactions have advance developed this unique class of materials to find unlimited application. In addition, synthesis opportunities may develop towards the emergence of new composites with higher conductivity. A controlled architecture will influence the synthesis process and quality of composites in the future by tuning their structures and properties with high accuracy. It seems that polymer composite syntheses are becoming more environmentally friendly by using biological templates and using methods that place less burden on the environment. These advances in the synthesis of conducting polymers and their composites will make it possible to produce more effective and functional materials in a broad spectrum of capabilities in different fields, especially electronics, energy, and medicine.

The most used antimicrobial reagents in biomedical applications are examined in four specific groups: positive active compounds such as silver, quaternary ammonium salts and chlorhexidine, oxidants containing chlorine and peroxides, organic substances such as isothiazolones and formaldehyde, and electrophilic substances such as mercury and copper [20], [21]. In biomedical applications, the use of antimicrobial polymers with various superlatives such as chemical stability, skin impermeability and volatility is becoming more important day by day [22], [23]. Different and important antifouling functional groups such as fluoro group, quaternary ammonium group, and sulfobetaine then pave the way to make new arrangements in the molecular structure of the polymer and composite for certain end applications [24]. Amphiphilic polymers have a important superiority over cationic polymers owing to their enhanced biocidal effect opposite Gram-positive and Gram-negative bacteria [25], [26]. Microorganisms adhere to living or inanimate surfaces by creating biofilm, a polymeric substance they produce. Microbial biofilms cause serious health problems worldwide due to their ability to not affected by antibiotics, countering the host's immune response and cope with extreme environmental impact, and their relationship with established infections [27]. The development of tooth decay is relevant with biofilm formation, affecting large audiences around the world. Bacteria belonging to the *Streptococcus mutans* species are believed to be the priority etiological agent involved in this important situation. *Streptococcus mutans* plays a serious role in the formation of complex structure and multidimensional in the tooth enamel and oral mucosa [28]. It gets some cariogenic features, such as adhesion to solid surfaces, colonize the oral cavity, and they can survive in acidic conditions in the oral cavity [29]. Additionally, *S. mutans* uses acidic metabolites that produce carbohydrates, which causes acid formation and demineralization, and as a result, tooth decay occurs as a result of the removal of mineral substances [30].

In this study; for the first time, we report a facile approach to increase the antimicrobial activity against bacteria of amphiphilic and conductive composites prepared with varying amounts of hydrophilic and hydrophobic polymers. These amphiphilic composites were synthesized by in situ polymerization method. The desired antimicrobial properties were achieved thanks to the presence of the t-amine functional group in DEAEMA, which has a biofilm adhesion.

2 Experimental Methods

2.1 Materials

2-diethylamino ethylmethacrylate (DEAEMA, 99%), ethylmethacrylate (EMA, 99%), Indole (IN, 99%), Iron(III) chloride (FeCl₃, 98%), ammonium persulfate (APS), Chloroform (CHCl₃, 99%) (Sigma-Aldrich, St. Louis, MO, USA) was used in copolymer and polymer composite synthesis reaction.

2.2 Synthesis of Polymer Composites

In this study, firstly, a 50% - 50% mass ratio copolymer of DEAEMA and EMA was prepared by free radical polymerization technique in 1,4-dioxane solution with APS initiator. This prepared copolymer was used in composite preparation. Poly(DEAEMA-co-EMA)/PIN conductive composites with PIN content of 10, 30, 50, 70 and 90% by mass were prepared as stated in the method in the literature [31], and they are named with the codes PC1, PC2, PC3, PC4, and PC5, respectively. The preparation ratio of PCs are given in Table 1.

In the synthesis of PCs, firstly, FeCl₃ was dissolved in 25 ml of CHCl₃ in a three-mouthed 250 ml reaction bubble in the proportions given in Table 1. The reaction bubble was cooled to 0 °C with ice. Meanwhile, nitrogen gas was introduced into the reaction flask. Then, poly(DEAEMA-co-EMA) polymer dissolved in 25 ml of chloroform were added to this solution and mixed. In the last step, indole monomer dissolved in 25 ml of chloroform was added dropwise to the reaction mixture using a dropping funnel. The reaction was continued for 3 hours. The resulting PCs were washed with distilled water and chloroform.

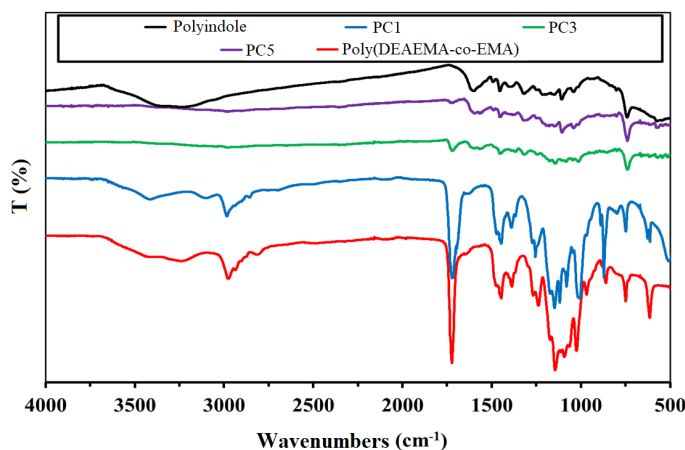


Figure 1: FTIR spectra of PIN, poly(DEAEMA-co-EMA) and PCs

Washing was terminated when the color of the washing solution became clear. The obtained PCs were filtered, dried in a vacuum atmosphere at 40 °C and stored for analysis.

2.3 Characterization Techniques and Measurements

Fourier transform infrared (FTIR) spectra of PCs were analyzed in the wavenumber range of 400–4000 cm^{-1} with a Perkin Elmer Spectrum Two (UATR) IR Spectrometer. TGA analyzes were performed with a Hitachi 7000 TGA/DTA model thermogravimetric analyzer at room temperature – 1000°C, under a nitrogen atmosphere, at a heating rate of 10 °C/minute. Zeiss EVO LS10 model scanning electron microscope (SEM) and VEECO Multimode 8 Atomic Force Microscope (AFM) were used to examine the surface morphology of conducting polymer composites. In AFM analyses, the microscope was operated in contact mode and the force constant of the cantilever was kept at 0.15 N m^{-1} . Surface scans were performed at 1 Hz.

3 Results and Discussion

3.1 FTIR Analysis

The FTIR spectra of PIN, poly(DEAEMA-co-EMA) and PCs are given in Figure 1.

In the poly(DEAEMA-co-EMA) spectrum, the C=O stretching vibration absorption peak of the ester group is seen at 1740 cm^{-1} . The spectrum of poly(indole) exhibited absorption bands at 1600 cm^{-1} owing to the stretching vibrations of $-C=C-$ aromatic groups. In the spectra of PCs, absorption bands are seen at 2920 cm^{-1} due to the stretching vibrations of $-CH_2-$ and $-CH_3$ groups [28]. PCs, the C=O stretching vibrations of the ester group of DEAEMA and EMA units exhibited bands at 1740 cm^{-1} [32]. The peak at 2842 cm^{-1} can be attributed to the C-H stretching vibration of the $N(\text{CH}_3)_2$ group of DEAEMA unit [33], [34]. We can understand the stretching vibration of C-O-C of both methacrylate units from the peaks at 1150–1250 cm^{-1} [35]. In each spectrum, the peak at 1020 cm^{-1} indicates the C-N stretching vibration of the tertiary amine group, confirming the presence of the DEAEMA segment in the composites. The two peaks at 1380 cm^{-1} and 755 cm^{-1} can be attributed to the methyl group in poly(DEAEMA-co-EMA) of polymer composites. Localized signals from the C-N groups of the DEAEMA unit in the composites are seen in the other part of the spectrum at 800–730 cm^{-1} . The peak at 985 cm^{-1} together with the peaks at 1060 cm^{-1} and 840 cm^{-1} , constitutes the characteristic absorption vibration of poly(DEAEMA-co-EMA) in composites. Since there are no similar groups in the PIN unit, no intense peaks were observed in the region below 1000 cm^{-1} . Based on the above discussions, it can be concluded that the prepared polymer composite is indeed macromolecular poly(DEAEMA-co-EMA)/PIN [36].

From the FTIR spectra of PCs, we can say that when the PIN ratio in the composites increases (from the PC1 to the PC5), the absorption intensity of the NH peak belonging to the PIN at 3390 cm^{-1} increases. Also, In composites PC1 to PC5 concentration of poly(DEAEMA-co-EMA) decreases and accordingly the band intensity of C=O and C-N groups also decreases. DEAEMA has a hydrophilic structure and the composites retain a little moisture. This is why the broad O-H group band seen in the 3000–3500 cm^{-1} region in Figure 1 is due to this. In PC5, -OH band disappeared due to very low concentration of poly(DEAEMA-co-EMA) and higher content of PIN.

3.2 Thermogravimetric Studies

The TGA curves of PIN, poly(DEAEMA-co-EMA) and PCs are shown in Figure 2. The results of thermogravimetric analysis (TG) is summarized in Table 2. In thermograms, the decomposition has a two-stage character; the first stage is related to the degradation of the side groups and the second is related to the degradation of the main chain. Adding different proportions

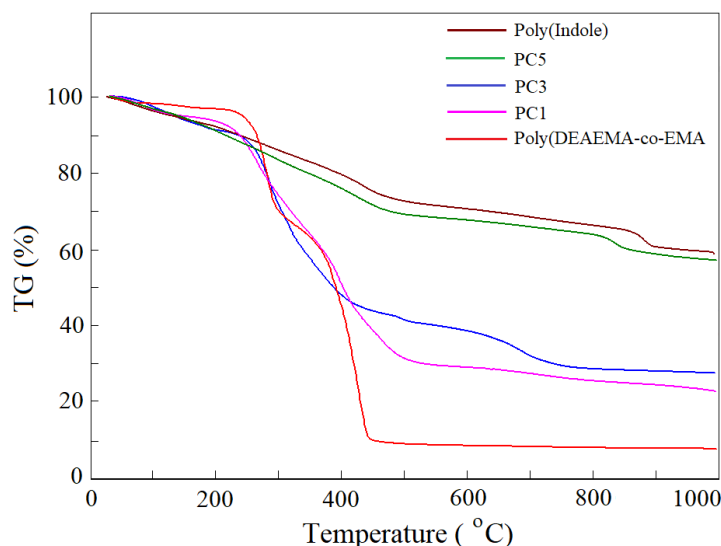


Figure 2: TGA curve of PIN, poly(DEAEMA-co-EMA) and PCs.

Table 2: Thermal analysis results of investigated compounds.

Sample name	Maximum de- composition temperature (°C)	Temperature of 40% weight loss (°C)	% Weight loss at 400 °C	% Weight loss at 700 °C	% Residue at 1000 °C
Poly(DEAEMA-co-EMA)	430	416	51	90	9
PC1	468	420	44	71	24
PC3	642	394	48	64	32
PC5	805	872	23	30	65
Poly(Indole)	830	908	16	27	67

of DEAEMA, EMA and Indole to composites can significantly reduce or improve thermal resistance [37]. In order to obtain complete information about the course of thermal degradation, polymer composite samples were heated at various temperature ranges. The most in-depth studies of the thermal properties of PDEAEMA were published in [38]. This decomposition occurred in two steps. It was confirmed that in the first phase of the first stage of decomposition, the amino groups undergo thermal destruction, and in the second phase, the disappearance of side groups can be observed. The first stage occurred in the 290–400°C range; and the second is located between 390–550°C.

Different proportions of DEAEMA-EMA copolymer and Indole were used in the composites we prepared. Since the order of DEAEMA and EMA units and the order of Indole units in the composites may be different, the thermogram curves of the composites may differ even though they are similar to the thermograms of their homopolymers. For this reason, the 40% weight loss temperature and the % mass loss values at 400°C of the PC3 sample did not show a similar degradation curve with the other composites. It is likely that the order and amount of DEAEMA-co-EMA units in PC3 in the composite composition differed slightly from other composites.

It can be seen from the TG curves that when the PIN ratio in PCs increases, the residue release rate of the composites also increases. It is observed that PCs with high poly(DEAEMA-co-EMA) ratios have 40% mass loss around 400°C and show more stable behavior. It is seen that PCs are stable at higher temperatures (700-1000°C) as the PIN ratio increases and leave residue at rates of 40-47%. It can be said that this is caused by the 6-ring and 5-ring groups in PIN. It is reported in the literature that the decomposition temperature of PIN is higher than the values reported for conductive polymers such as polyaniline, polythiophene, and polypyrrole [39].

3.3 Morphological Analysis

It is an emphasized fact that the features of materials depend largely on their morphological structures. In terms of physicochemical and biological properties, the distribution of components in polymer composites is extremely important. FESEM images of PC4 has been seen in Figure 3(a). As can be seen FESEM image, we can said that, PC4 has a ununiform, unhomogenous and sponge-like structure. The surfaces on which FESEM EDX field spectra and EDX analysis was performed in the PC4 is seen in Figure 3(b). The peaks of C, N and O elements were viewed 0.275; 0,410 and 0,530 keV, respectively.

At the same time, a microscopic examination of PC4 was also examined using AFM. Examination was performed with the surface using contact mode. In the study, the typical force constant of the console was kept constant at 0.15 Nm⁻¹. The surface

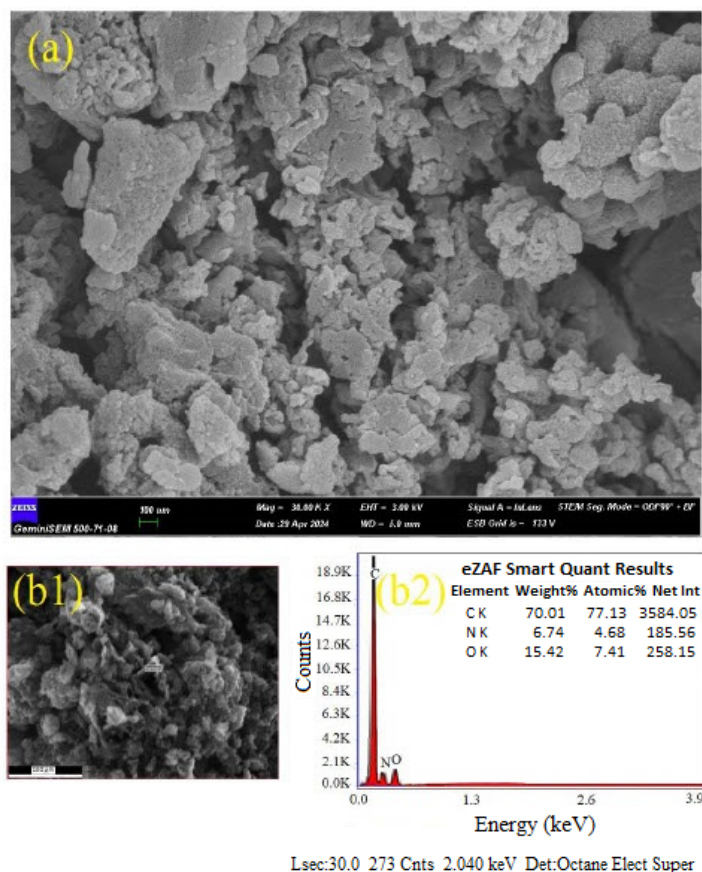


Figure 3: (a) FESEM and (b1-b2) EDX field analysis of prepared PC4.

morphology examination of PC4 was carried out at a scan rate of 1.00 Hz [Figure 4(a)]. A typical three-dimensional (3D) image and light colors are seen at elevations in Figure 4(a)'s AFM images, dark colors are seen at depths of PC4 in AFM are shown in Figure 4(b). It can be seen that PC4 has a cloudy form in the AFM image. By selecting a horizontal section as the profile, a 2D AFM image ($5 \mu\text{m} \times 5 \mu\text{m}$) cross-section of PC4 were obtained. In Figure 4(d) indicates its RMS values are (22.615 nm), (40.084 nm) distance from this data; we say that distance: (2.119 μm) vertical distance: (4048 nm) out-of-plane Distance : (276 nm), horizontal distance: ($5 \mu\text{m}$), and patchy and unhomogeneous structure on the bare glass surface.

3.4 Detection of Antibiofilm Effect

Polymer/polyindole conductive polymer composites are gaining attention owing to their potential applications in different fields, including biomedical and antibacterial coatings. The surface properties of the composite play a crucial role in preventing bacterial adhesion and subsequent biofilm formation. Biofilms are colonization of living or non-living surfaces by adhering to them through the exopolysaccharides they produce. Properties such as surface roughness or smoothness, hydrophobicity, chemical composition and surface charge determine the extent of adhesion. Positively charged and hydrophilic surfaces were more selective towards electroactive microbes and more conducive to electroactive biofilm formation [40]. Amphiphilic copolymer of poly(DEAEMA-co-EMA) are partially soluble in water, poly(DEAEMA) is water soluble and poly(EMA) is water insoluble due to hydrophilic and hydrophobic nature. These amphiphilic copolymers played profound effect on the antibacterial activity. Amphiphilic composites of poly(DEAEMA-co-EMA)/PIN have shown different zones of inhibitions along side Gram-positive bacteria *Streptococcus mutans*. PC1 has more concentration of poly(DEAEMA-co-EMA); hence it is prevented higher activity against bacteria owing to it had higher charge density owing to amino groups [41]. Because, the Gram-positive bacteria have cell wall that made up of only peptidoglycan the diffusion for the cationic polyelectrolytes with hydrophobic group are easier [42]. The presence of polyindole in the composite can change the surface energy and topography, making it suitable for bacterial attachment. Polyindole, a conducting polymer, can exhibit electrochemical activity. The composite can be designed to incorporate antimicrobial agents or drugs into its matrix. Poly(diethylaminoethylmethacrylate-co-ethylmethacrylate), a polymer with diethylamino groups, can serve as a matrix for the controlled release of these substances. This sustained release inhibits

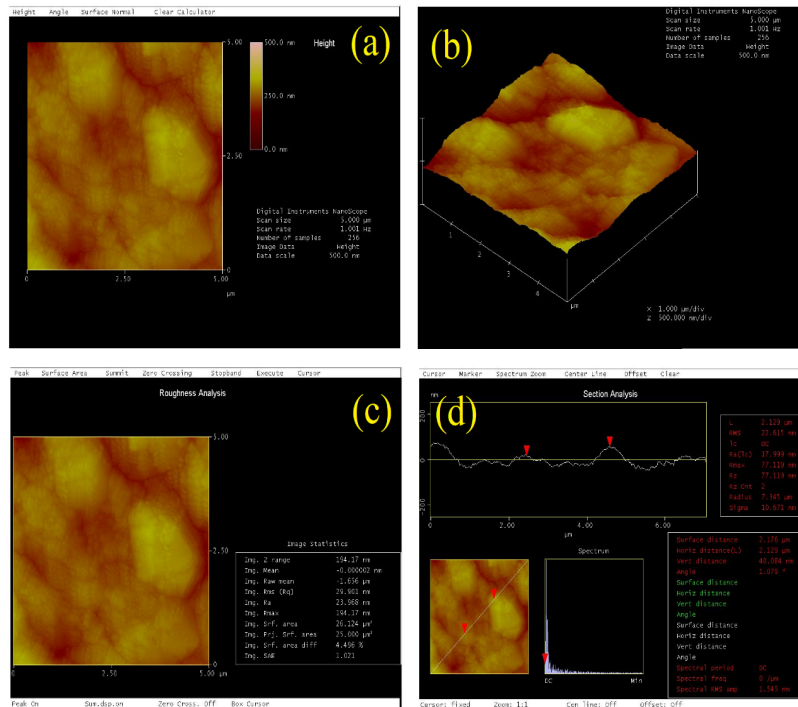


Figure 4: (a) 2D AFM image (b) 3D AFM image (c) Roughness analysis (d) Cross section analysis of the PC4 coated glass. (The scan size is 5 μm x 5 μm).

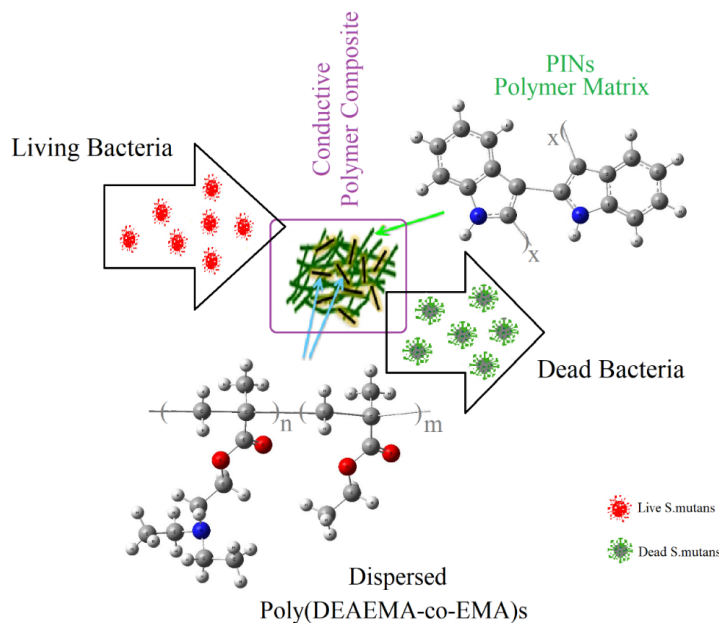


Figure 5: Schematic illustration of composites that control bacterial adhesion.

bacterial growth and biofilm formation. Due to the antifouling property of DEAEMA, it has the ability to repel and destroy microorganisms, and EMA has the antibacterial property [43]. Polyindole can exhibit pH-sensitive behavior such as swelling or shrinkage in response to changes in pH. This property can be exploited to create surfaces that undergo structural changes in response to bacterial colonization and inhibit biofilm formation. Schematic illustration of composites that control bacterial adhesion is given in Figure 5.

Pathogens were planted in Nutrient Broth medium and incubated at 37 °C for 24 hours. After incubation, cultures were adjusted to 0.5 McFarland turbidity (10^6 CFU mL⁻¹). 200 μg of Streptococcus mutans was inoculated into the previously

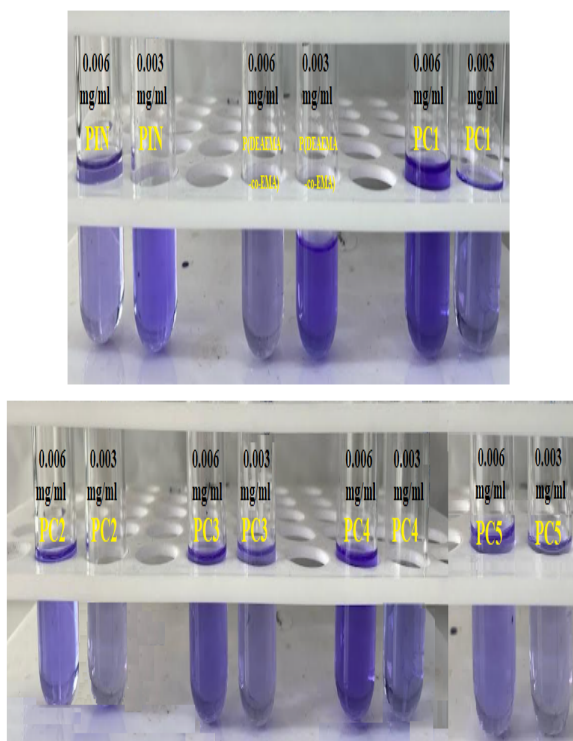


Figure 6: Crystal Violet color developed by some Streptococcus mutans isolates showing different dyeing process of their formed biofilms as determined by test tube method.

Table 3: Inhibition of biofilm formation (%).

Tested polymers and composites	30 mg/ml	60 mg/ml
	concentration	concentration
Poly(Indole)	73,695	90,495
Poly(DEAEMA-co-EMA)	42,838	81,058
PC1	47,055	83,199
PC2	63,253	85,743
PC3	68,139	86,078
PC4	68,495	86,546
PC5	71,285	89,218

prepared Nutrient Broth medium containing test material at 30 and 60 μg concentrations. 0.5 McFarland was added to these tubes and then were incubated at 37 $^{\circ}\text{C}$ for 24 hours. After incubation, the liquid medium was poured out and the tubes were washed 3 times with distilled water. First, ethanol: acetic acid (95:5) was added to the dried tubes and fixed for 10 minutes, and at the end of the period, the tubes were emptied and left to dry. Then, 0.1% crystal violet was added to the dried tubes and the dyeing process was performed. The results are seen in Figure 6. After the dyeing process, the crystal violet in the tubes was emptied, washed 2-3 times with distilled water, and then dried. To remove the stained and attached bacteria in the drying tubes, ethanol: acetic acid (95:5) was added to the wells and incubated for 10 minutes. The dye was allowed to dissolve by waiting for a while. At the end of the period, the optical density value of the microplate was measured at 570 nm in a spectrophotometer and the biofilm percentages were calculated compared to the positive control [44]. Inhibition of biofilm formation (%) was calculated from the equation below, and the results are given in Table 3.

$$\text{Inhibition \%} = \left(\frac{A \text{ control} - A \text{ sample}}{A \text{ control}} \right) \times 100 \quad (1)$$

where:

- A control: Absorbance value containing only the bacterial strain
- A sample: Absorbance value with added test material

Antibacterial activities of all composites with different concentrations of poly(DEAEMA-co-EMA) were assessed against Gram-positive bacteria which commonly cause biofilm on materials [21]. Biofouling resistance of synthesized composite materials against *Streptococcus mutans* biofilm formation was studied. Antibacterial activity also influenced by the spacer length owing to conformation charge density on the composites [24]. As well as DEAEMA monomer had positive charge because ammonia group copolymerized and EMA monomer had no charge with hydrophobic in nature. The increase in antibacterial activity increase with charge density by polymerization and assumed more adhesion owing to negative charged bacterial cell surface, increase dispersal through the cell wall. These cationic polymers fix to the cytoplasmic membrane, interruption the cytoplasmic membrane, discharge of intracellular elements and bacterial cells mortality [45]. Composites antibacterial action mechanism occurred by (a) bacterial cell surface adsorption, (b) cell Wall diffusion, (c) cytoplasmic membrane adsorption, (d) cytoplasmic disruption, (e) leakage of cellular components, and (f) cell death [46]. Here more positive charge present on composites PC1 and PC2 that caused interactions between composites and bacteria. So it is a critical factor, and further action disrupted the cell wall, fluid leaked, cell ruptured and death occurred [47].

4 Conclusion

Biofilms are considered microbial cells in an unusual structure. Proliferation of microbial cells occurs within the polymeric matrix, which acts as a protective coating. Biofilms contribute to the character of antimicrobial resistance. The fact that the behavioral mechanism of biofilms under different environmental conditions has not been sufficiently elucidated in research shows that there are inconsistencies between in vitro analysis results and in vivo studies. In this study, we aimed to prepare a polymer composite with biofilm-forming properties that can be used to remove harmful dyes. For this purpose, we obtained a series composite by polymerizing the indole conductive polymer with the in situ polymerization method in the poly(DEAEMA-co-EMA) polymer we prepared. We elucidated the chemical structure of this molecule using spectroscopic methods and characterized its surface morphology. *Streptococcus mutans* is a gram-positive, facultative anaerobic bacterium mostly found in the human oral cavity and is an important factor in the formation of dental caries. Here, we observed for the first time that the polymer composite we prepared created a protective biofilm effect against this bacteria.

Authors' Contributions

CS: Sources, Research, Formal analysis, Validation, Methodology, Visualization, Writing – Original Draft. BT: Sources, Research, Formal analysis, Validation, Methodology, Visualization, Writing – Original Draft.

Competing Interests

The authors have no conflicts of interest to declare regarding the content of this article.

References

- [1] T. Pal, S. Banerjee, P. Manna, and K. K. Kar, "Characteristics of conducting polymers," *Handbook of Nanocomposite Supercapacitor Materials I: Characteristics*, pp. 247–268, 2020.
- [2] K. Namsheer and C. S. Rout, "Conducting polymers: a comprehensive review on recent advances in synthesis, properties and applications," *RSC advances*, vol. 11, no. 10, pp. 5659–5697, 2021.
- [3] B. Guo and P. X. Ma, "Conducting polymers for tissue engineering," *Biomacromolecules*, vol. 19, no. 6, pp. 1764–1782, 2018.
- [4] R. Dong, P. X. Ma, and B. Guo, "Conductive biomaterials for muscle tissue engineering," *Biomaterials*, vol. 229, p. 119584, 2020.
- [5] Y. Park, J. Jung, and M. Chang, "Research progress on conducting polymer-based biomedical applications," *Applied Sciences*, vol. 9, no. 6, p. 1070, 2019.
- [6] S. S. Nair, S. K. Mishra, and D. Kumar, "Recent progress in conductive polymeric materials for biomedical applications," *Polymers for Advanced Technologies*, vol. 30, no. 12, pp. 2932–2953, 2019.
- [7] K. Krukiewicz, B. Bednarczyk-Cwynar, R. Turczyn, and J. K. Zak, "Eqcm verification of the concept of drug immobilization and release from conducting polymer matrix," *Electrochimica Acta*, vol. 212, pp. 694–700, 2016.
- [8] C. Boehler, F. Oberueber, and M. Asplund, "Tuning drug delivery from conducting polymer films for accurately controlled release of charged molecules," *Journal of Controlled Release*, vol. 304, pp. 173–180, 2019.
- [9] S. Lakard, N. Morrand-Villeneuve, E. Lesniewska, B. Lakard, G. Michel, G. Herlem, T. Gharbi, and B. Fahys, "Synthesis of polymer materials for use as cell culture substrates," *Electrochimica Acta*, vol. 53, no. 3, pp. 1114–1126, 2007.
- [10] P. Humpolíček, V. Kašpárková, J. Pacherník, J. Stejskal, P. Bober, Z. Capáková, K. A. Radaszkiewicz, I. Junkar, and M. Lehocký, "The biocompatibility of polyaniline and polypyrrole: A comparative study of their cytotoxicity, embryotoxicity and impurity profile," *Materials Science and Engineering: C*, vol. 91, pp. 303–310, 2018.
- [11] S. Ramanavicius and A. Ramanavicius, "Charge transfer and biocompatibility aspects in conducting polymer-based enzymatic biosensors and biofuel cells," *Nanomaterials*, vol. 11, no. 2, p. 371, 2021.
- [12] H. He, L. Zhang, X. Guan, H. Cheng, X. Liu, S. Yu, J. Wei, and J. Ouyang, "Biocompatible conductive polymers with high conductivity and high stretchability," *ACS applied materials & interfaces*, vol. 11, no. 29, pp. 26 185–26 193, 2019.
- [13] D. N. Nguyen and H. Yoon, "Recent advances in nanostructured conducting polymers: from synthesis to practical applications," *Polymers*, vol. 8, no. 4, p. 118, 2016.
- [14] Y. Fan, W. Bai, P. Mu, Y. Su, Z. Zhu, H. Sun, W. Liang, and A. Li, "Conductively monolithic polypyrrole 3-d porous architecture with micron-sized channels as superior salt-resistant solar steam generators," *Solar Energy Materials and Solar Cells*, vol. 206, p. 110347, 2020.
- [15] S. Nie, Z. Li, Y. Yao, and Y. Jin, "Progress in synthesis of conductive polymer poly (3, 4-ethylenedioxythiophene)," *Frontiers in chemistry*, vol. 9, p. 803509, 2021.
- [16] M. Fadel, D. A. Fadel, M. Ibrahim, R. M. Hathout, and A. I. El-Kholly, "One-step synthesis of polypyrrole-coated gold nanoparticles for use as a photothermally active nano-system," *International Journal of Nanomedicine*, pp. 2605–2615, 2020.

- [17] N. K. Jangid, S. Jadoun, and N. Kaur, "Retracted: A review on high-throughput synthesis, deposition of thin films and properties of polyaniline," 2020.
- [18] R. B. Choudhary, S. Ansari, and M. Majumder, "Recent advances on redox active composites of metal-organic framework and conducting polymers as pseudocapacitor electrode material," *Renewable and Sustainable Energy Reviews*, vol. 145, p. 110854, 2021.
- [19] C. I. Idumah, E. Ezeani, and I. Nwuzor, "A review: advancements in conductive polymers nanocomposites," *Polymer-Plastics Technology and Materials*, vol. 60, no. 7, pp. 756–783, 2021.
- [20] J. Chapman, "The development of novel antifouling materials-a multi-disciplinary approach," Ph.D. dissertation, Dublin City University, 2011.
- [21] G. Lu, D. Wu, and R. Fu, "Studies on the synthesis and antibacterial activities of polymeric quaternary ammonium salts from dimethylaminoethyl methacrylate," *Reactive and Functional Polymers*, vol. 67, no. 4, pp. 355–366, 2007.
- [22] K.-S. Huang, C.-H. Yang, S.-L. Huang, C.-Y. Chen, Y.-Y. Lu, and Y.-S. Lin, "Recent advances in antimicrobial polymers: a mini-review," *International journal of molecular sciences*, vol. 17, no. 9, p. 1578, 2016.
- [23] P. Elena and K. Miri, "Formation of contact active antimicrobial surfaces by covalent grafting of quaternary ammonium compounds," *Colloids and Surfaces B: Biointerfaces*, vol. 169, pp. 195–205, 2018.
- [24] E.-R. Kenawy, S. Worley, and R. Broughton, "The chemistry and applications of antimicrobial polymers: a state-of-the-art review," *Biomacromolecules*, vol. 8, no. 5, pp. 1359–1384, 2007.
- [25] A. M. Carmona-Ribeiro and L. D. de Melo Carrasco, "Cationic antimicrobial polymers and their assemblies," *International journal of molecular sciences*, vol. 14, no. 5, pp. 9906–9946, 2013.
- [26] Z. Zhou, D. R. Calabrese, W. Taylor, J. A. Finlay, M. E. Callow, J. A. Callow, D. Fischer, E. J. Kramer, and C. K. Ober, "Amphiphilic triblock copolymers with pegylated hydrocarbon structures as environmentally friendly marine antifouling and fouling-release coatings," *Biofouling*, vol. 30, no. 5, pp. 589–604, 2014.
- [27] R. Vasudevan, "Biofilms: microbial cities of scientific significance," *J Microbiol Exp*, vol. 1, no. 3, p. 00014, 2014.
- [28] Y. Wang, X. Shen, S. Ma, Q. Guo, W. Zhang, L. Cheng, L. Ding, Z. Xu, J. Jiang, and L. Gao, "Oral biofilm elimination by combining iron-based nanozymes and hydrogen peroxide-producing bacteria," *Biomaterials science*, vol. 8, no. 9, pp. 2447–2458, 2020.
- [29] W. Krzyściak, A. Jurczak, D. Kościelniak, B. Bystrowska, and A. Skalniak, "The virulence of streptococcus mutans and the ability to form biofilms," *European Journal of Clinical Microbiology & Infectious Diseases*, vol. 33, pp. 499–515, 2014.
- [30] S. M. Zayed, M. M. Aboulwafa, A. M. Hashem, and S. E. Saleh, "Biofilm formation by streptococcus mutans and its inhibition by green tea extracts," *AMB Express*, vol. 11, no. 1, p. 73, 2021.
- [31] D. Billaud, E. Maarouf, and E. Hannecart, "Chemical oxidation and polymerization of indole," *Synthetic Metals*, vol. 69, no. 1-3, pp. 571–572, 1995.
- [32] M. Degirmenci, "Synthesis and characterization of novel well-defined end-functional macrophotoinitiator of poly (mma) by atp," *Journal of Macromolecular Science, Part A*, vol. 42, no. 1, pp. 21–30, 2005.
- [33] D. Zielińska, D. Stawski, and A. Komisarzyk, "Producing a poly (n, n-dimethylaminoethyl methacrylate) nonwoven by using the blowing out method," *Textile Research Journal*, vol. 86, no. 17, pp. 1837–1846, 2016.
- [34] N. S. Okten, C. C. Canakci, and N. Orakdogan, "Hertzian elasticity and triggered swelling kinetics of poly (amino ester)-based gel beads with controlled hydrophilicity and functionality: A mild and convenient synthesis via dropwise freezing into cryogenic liquid," *European Polymer Journal*, vol. 114, pp. 176–188, 2019.
- [35] J. Li, T.-T. Jiang, J.-n. Shen, and H.-M. Ruan, "Preparation and characterization of pmma and its derivative via raft technique in the presence of disulfide as a source of chain transfer agent," *Journal of Membrane and Separation Technology*, vol. 1, no. 2, p. 117, 2012.
- [36] Z. Lin, "Analysis and identification of infrared spectrum of the polymer," 1989.
- [37] M. T. Hunley, J. P. England, and T. E. Long, "Influence of counteranion on the thermal and solution behavior of poly (2-(dimethylamino) ethyl methacrylate)-based polyelectrolytes," *Macromolecules*, vol. 43, no. 23, pp. 9998–10005, 2010.
- [38] D. Stawski and A. Nowak, "Thermal properties of poly (n, n-dimethylaminoethyl methacrylate)," *PLoS One*, vol. 14, no. 6, p. e0217441, 2019.
- [39] P. S. Abthagir, K. Dhanalakshmi, and R. Saraswathi, "Thermal studies on polyindole and polycarbazole," *Synthetic metals*, vol. 93, no. 1, pp. 1–7, 1998.
- [40] K. Guo, S. Freguia, P. G. Dennis, X. Chen, B. C. Donose, J. Keller, J. J. Gooding, and K. Rabaey, "Effects of surface charge and hydrophobicity on anodic biofilm formation, community composition, and current generation in bioelectrochemical systems," *Environmental science & technology*, vol. 47, no. 13, pp. 7563–7570, 2013.
- [41] D. Raafat and H.-G. Sahl, "Chitosan and its antimicrobial potential—a critical literature survey," *Microbial biotechnology*, vol. 2, no. 2, pp. 186–201, 2009.
- [42] L.-A. B. Rawlinson, S. M. Ryan, G. Mantovani, J. A. Syrett, D. M. Haddleton, and D. J. Brayden, "Antibacterial effects of poly (2-(dimethylamino ethyl) methacrylate) against selected gram-positive and gram-negative bacteria," *Biomacromolecules*, vol. 11, no. 2, pp. 443–453, 2010.
- [43] S. Mushtaq, N. M. Ahmad, A. Mahmood, and M. Iqbal, "Antibacterial amphiphilic copolymers of dimethylamino ethyl methacrylate and methyl methacrylate to control biofilm adhesion for antifouling applications," *Polymers*, vol. 13, no. 2, p. 216, 2021.
- [44] M. Sandberg, A. Määttänen, J. Peltonen, P. M. Vuorela, and A. Fallarero, "Automating a 96-well microtitre plate model for staphylococcus aureus biofilms: an approach to screening of natural antimicrobial compounds," *International journal of antimicrobial agents*, vol. 32, no. 3, pp. 233–240, 2008.
- [45] H. Takahashi, E. F. Palermo, K. Yasuhara, G. A. Caputo, and K. Kuroda, "Molecular design, structures, and activity of antimicrobial peptide-mimetic polymers," *Macromolecular bioscience*, vol. 13, no. 10, pp. 1285–1299, 2013.
- [46] W. Ren, W. Cheng, G. Wang, and Y. Liu, "Developments in antimicrobial polymers," *Journal of Polymer Science Part A: Polymer Chemistry*, vol. 55, no. 4, pp. 632–639, 2017.
- [47] W. Yandi, S. Mieszkin, M. E. Callow, J. A. Callow, J. A. Finlay, B. Liedberg, and T. Ederth, "Antialgal activity of poly (2-(dimethylamino) ethyl methacrylate)(pdmaema) brushes against the marine alga ulva," *Biofouling*, vol. 33, no. 2, pp. 169–183, 2017.

Research Article

Ultrasonic Characterization of the Mechanical Behavior of Epoxy/Date Kernel Powder Biocomposites: A Feasibility Study of the Powder Size Effect

Fares Mohammed Laid Rekbi^{1,2a}, Rafik Halimi^{1b}, Mabrouka Oustani^{3c}, Imran Oral^{4d}, Wahiba Djerir^{1e}, Fethi Remli^{5f}, Hicham Henna^{6g}

¹Research Center in Industrial Technologies CRTI, P.O. Box 64, Cheraga 16014, Algeria

²Scientific and Technical Research Center in Physico-Chemical Analysis (CRAPC), BouIsmaïl, Algeria

³Laboratory of Saharan bio-resources: Preservation and Development, Kasdi Merbah University, Ouargla, 30000, Algeria

⁴Department of Physics Education, Ahmet Kelesoglu Faculty of Education, Necmettin Erbakan University, 42090 Konya, Türkiye

⁵Center for the Development of Advanced Technologies CDTA, City 20 August 1956, P.O.Box Baba Hassen, 16303, Algeria

⁶Electrical Engineering Laboratory LAGE, Kasdi Merbah University, Ouargla, 30000, Algeria

oralimran@erbakan.edu.tr

DOI : 10.31202/ecjse.1572805

Received: 27.10.2024 Accepted: 07.04.2025

How to cite this article:

F.M.L. Rekbi, R. Halimi, M. Oustani, I. Oral, W. Djerir, F. Remli, H. Henna " Ultrasonic Characterization of the Mechanical Behavior of Epoxy/Date Kernel Powder Biocomposites: A Feasibility Study of the Powder Size Effect", El-Cezeri Journal of Science and Engineering, Vol: 12, Iss: 2, (2025), pp.(176-190).

ORCID: ^a0000-0001-7079-3462, ^b0000-0001-6601-6505, ^c0000-0003-0209-6010, ^d0000-0002-5299-5068, ^e0000-0002-7362-2316,

^f0000-0003-3597-9952, ^g0000-0002-2096-7425.

Abstract : This study aims to address the effect of date kernel powder (DKP) as reinforcement obtained from Touggourt oasis, Algeria, on the elastic properties of biocomposites based on two prepared DKPs with grain size 300 μm and 500 μm mixed on epoxy (ER) matrix. The weight percentage of powders with 5%, 10%, and 15% was used to obtain epoxy matrix (ER)/date kernel powder (DKP) biocomposites. The effects of DKP size on the elastic properties of ER/DKP biocomposites, such as ultrasonic wave velocities (longitudinal and shear), longitudinal modulus, shear modulus, bulk modulus, Young's modulus of elasticity, ultrasonic microhardness, Poisson's ratio, and acoustic impedance, were determined using the ultrasonic through-transmission method. In addition, the two biocomposites prepared to analyze the chemical changes in the functional groups and their morphology were studied using X-ray diffraction and optical microscopy, respectively. The results of ultrasonic characterization of the ER/DKP biocomposites showed that there is a significant relationship between the sizes of DKP and elastic constant values. In addition, the experimental results illustrated that the optimum weight percent of DKP reinforcement in neat ER for excellent mechanical behavior of ER/DKP biocomposites is 5% and 10% for 300 μm and 500 μm , respectively.

Keywords : Date kernel powder (DKP), Bio-sourced materials, Ecofriendly materials, Ultrasonic characterization, Elastic constants.

1 Introduction

To reduce the use of synthetic materials in numerous industries, such as composite materials, engineering uses natural fibers as reinforcement in advanced composite materials for specific behavior. Date palm tree (DPT) is a natural fiber. It can be turned into a value added manufacturing process through the production of new eco-friendly composites based on several thermoplastic or thermoset materials replacing synthetic fibers [1]–[3]. It represents abundant lignocellulose and a renewable source in all Afro-Asiatic dry bands from Saharan countries in northern North Africa to the Middle East [4], [5], with approximately two-thirds of the date palm trees cultivated in Arab countries such as the Algerian oasis for exploitation of date fruits [3], [6], with 15941.4 tons of kernel waste in Algeria [7]. The palm date is divided into several parts such as mesh, leaflet, fronds, kernel, petiole, midrib, and rachis. Generally, the reinforcements from the date palm can be extracted from all parts of them as fibers [8]. In addition, particles and powder can be produced by milling the date palm fruit seeds [9]. Furthermore, for example, the kernel derived from date palm fruit is largely available in the Saharan countries in northern Africa [10], and it can be regarded as waste material during the use of whole fruits processing.

The use of date kernel waste is a research topic for many applications such as engineering, including composite materials [11]. Where, Nasser et al. [12] reported that this kind of palm part has constituted a significant alternative to using a potential new renewable energy. In the past few years, several studies have used the parts of date palms as reinforcement in polymeric

materials for various applications [5], [13]–[15]. In addition, these natural by-products could be used with or without chemical treatment [5]. Date palm fibers with longitudinal architecture (0° , 45° , and 90°) were used in the study by AlZebdeh et al. [9] to develop a new eco-friendly composite. After chemical treatment of fibers with 1 wt.% of NaOH for 2 h, biocomposite sheet samples were fabricated. The results of the tensile tests (Young's modulus, tensile strength, and elongation break) show that date palm fibers can be used for low-strength applications as reinforcement materials. Short date palm fibers with diameters of 200-400, 400-600, and 600-800 μm and 10 mm of length were used as natural reinforcement on DPF/Epoxy composites by Abdal-Hay et al. [16]. This study investigated the effect of chemical modification of fibers on the tensile and morphological properties of composites.

The authors found that the fibers are amenable to chemical modification, leading to improved adhesion fiber/matrix, tensile strength, and Young's modulus. In another study, date palm fiber in the form of powder was used as reinforcement for polymeric composites by Ibrahim [33]. The effect of a volumetric ratio of up to 25% of powder on the tribological behavior of the studied composites was investigated. The experimental results show the effect of different parameters on the coefficient of friction, rate of wear, and resistance of wear of the proposed materials according to the amount of powder. Cellulosic seed particles of palm date used as reinforcement for unsaturated polyester by Ameh et al. [34]. Composites with particle sizes of 0.5, 2.0, and 2.8 mm and particle loadings of 5–25 wt.% were obtained for traditional destructive characterization, such as tensile strength, water absorption, and hardness. The results indicated that date palm seed particles can be used as reinforcement to enhance the behavior of composites. The authors also, declared that the 15 wt.% and 10 wt.% are the optimum loadings for tensile strength and elastic modulus, respectively, using 0.5 mm size. On the other hand, the better hardness at a particle size of 2 mm at 25 wt%. Masri et al. [35] fabricated and characterized new date palm leaflets/Polystyrene composites, and three sizes of leaflet reinforcements were selected. The authors found that the composites exhibit good thermal insulation and can be recycled after their useful life. Sh. Al-Otaibi et al. [3] investigated the effect of 5%, 10%, and 15% loadings of date palm fiber (DPF) with lengths (8-12 mm and less than 2 mm) on morphological, mechanical, and thermal properties of a composite base on recycled polypropylene (RPP), impact copolymer (ICP), and homopolymer (HPP) reinforced by the treated DPF. Initially, the fiber was treated with 1% NaOH for 1 h at 100°C . Subsequently, the composite samples for morphological, mechanical, and thermal tests were prepared. Among the most important experimental results are that the RPP can be used as an alternative to HPP with DPF treated to improve the tensile strength of the polypropylene (PP) matrix. In addition, the increase in fiber loading increased the modulus and decreased the tensile property. Date palm fiber mesh waste was used as reinforcement on composites in the study of Boumhaout et al. [36]. Mortar/DPF composites for thermal insulation of buildings were examined under thermomechanical tests with a volume percentage of DPF ranging from 0% to 51%. The composites used in the study by Benaniba et al. [37] were formed with DPF and cement. The 7 mm length of fiber was used with 6, 12, 18, 24, and 30% of weight. The results show that the effect of increasing the weight amount of DPF led to a reduction in thermal conductivity, compressive strength, and flexural. Also, the addition of DPF increases the thermomechanical properties of the mortar. Recently, Abd Mohammed [38] studied the hardness properties and wear rates of olive seeds (OS) and date seeds (DS) by destructive investigation. Effect of weight fraction and grain size on the wear and hardness behavior of epoxy resin reinforced with OS and DS. It was found that the weight fraction of powder has a higher effect than particle size on the properties of the studied materials. The effect of date stone flour (DSF) on the mechanical, thermal, and morphological properties of SDF/Polypropylene (PP) composites with ethylene-butyl acrylate-glycidyl methacrylate (EBAGMA) as the compatibility was studied by Hamma et al. [10]. Fixed the amount of compatibility to half of the DSF and varied the loading rate of DSF between 10 and 40 wt%. The results show that the addition of EBAGMA improved the characteristics of the SDP/PP composites, such as the dispersion of SDF and the ductility due to the elastomeric. Debabeche et al. [39] prepared a destructive study that analyzed the effect of three types of treatment (hydrogen peroxide, NaOH, and acetic anhydride) on the surface of palm petiole fiber. We evaluated the Petiole/linear low-density polyethylene (LLDPE) composite with loading 15 wt% of fiber. The mechanical, dynamic mechanical, and morphological properties confirmed the effect of the treatments on the fiber surface. Palm kernels can be used not only to make new materials, but also to clean wastewater with a cheap and simple method. For example, in the research conducted by Ozelik [40], it was stated that heavy metal ions can be removed from wastewater with an easy and cheap method by adsorbing Cu (II) ions on palm kernels. Many methods have been applied and developed to overcome the behavior of composite materials, including the nondestructive method. From an economical and technical point of view, the use and development of nondestructive test (NDT) methods such as ultrasound measurements for the measurement of elastic constants is important to predict the behavior of materials. Ultrasonic waves have been used for many years both in material characterization and in the characterization of defects in materials [41]. Because this method is accurate, faster, and more sensitive, it is the preferred method compared with destructive methods such as tensile testing [42], [43]. Recently, many studies have been conducted using ultrasonic NDT methods (Table 1).

An important research by Rabhi et al. [18] has been conducted to investigate the effect of the chemical treatment of date stone flour (DSF) on the elastic constants of DSF mixed with green epoxy resin (GER) for biocomposite materials. A nondestructive characterization via the ultrasonic transmission method was applied to the samples. They observed an increase in the elastic constants of treated filler biocomposites compared with pure GER. Also, they were found to be the most suitable treatment of filler via the permanganate chemical treatment compared to other treatments (alkaline and benzoyl chloride).

Table 1: Report of an example of research on the nondestructive NDT characterization of materials.

Material	Parameters	NDT Test	Key findings	Refs
Epoxy/Polyaniline composite (PANI)	weight percentages of 5%,10% and 15% of PANI	Ultrasonic pulse-echo-overlap method (PEOM)	Effects of PANI amount on the mechanical properties of composite	[17]
Epoxy/Date Stone Flour composite	<ul style="list-style-type: none"> 30wt% of filler, Soda(alkaline), potassium permanganate and benzoyl-chloride chemical treatments. 	Ultrasonic through-transmission method	Effect of filler chemical treatment on elastics constant of bio-composites	[18]
Epoxy/Polyvinyl alcohol (PVA) nanocomposite	5,10 and 15 layers of PVA nanofiber mats	Ultrasonic wave velocity method	Effect of the number of PVA layers on the elastic properties of nanocomposite	[19]
Modified Epoxy/Andesite Waste composite	<ul style="list-style-type: none"> 10-30wt% of andesite waste (aw) filler, 5wt% of polyaniline to modify the resin. 	Ultrasonic pulse-echo method	Examine the effect of filler amount on the ultrasonic and electrical properties of the composites	[20]
Epoxy/Coconut and Epoxy/fique	/	Ultrasonic through-transmission method	Effect of natural fiber on stiffness of composites	[21]
Al/SiC nanocomposites	0,5 and 10 vol.% of nano size SiC particle	Ultrasonic pulse-echo-overlap method (PEOM)	Effect of SiC content on mechanical properties of nanocomposites	[22]
Epoxy/China Poplar Char (CPC) and Epoxy/Pine Cone Chare (PCC) composites	Weight percentage of 10, 20 and 30% of biochars	Ultrasonic pulse-echo-overlap method(PEOM)	Effect of biochars amounts on ultrasonic properties	[23]
Epoxy/Marble Waste Powder (MWP) composite	Weight percentage of 20 of Marble Waste Powder	Ultrasonic pulse-echo method	Effect of marble powder, dosage and coagulant type on elastic properties	[24]
Modified Polystyrenes (MPS)/Pure Polystyrenes (PS) composites	<ul style="list-style-type: none"> Molecular weights(350×10^3 and 500×10^3) of (PS), Molecular weights (230×10^3) of Modified Polystyrenes (MPS), Weight ratio (%) of 90:10, 20:80 and 70:30 of composites. 	Ultrasonic pulse-echo method	Effect of molecular weight and weight ratio (%) on elastic properties	[25]
Epoxy/ Polyethylene Terephthalate (PET) chare powder composites	Weight percentage of 10%, 20% and 30% of chars	Ultrasonic pulse-echo method	Effect of chars powder on the elastic constants	[26]
Epoxy3419/Carbon T700	/	Backwall reflection method (BRM)	Comparison between BRM measured and theoretically calculated ultrasonic travel time for determining the elastic constants	[27]
Polymethyl methacrylate (PMMA)/ Date Stone Flour (DSF) composite and Green Epoxy Resin (GER)/ Date Stone Flour (DSF) composite	<ul style="list-style-type: none"> Filler content of 10, 20, and 30wt%, Potassium permanganate treatment. 	Ultrasonic through-transmission method	Examine the effect of matrix and the Potassium permanganate treatment	[28]
Polypropylene (PP)/ Olive Wood Flour (OWF) composite	Weight percentage of 10, 20, and 30wt% of reinforcement	Ultrasonic immersion in water method	Effect of reinforcement weight ratio (%) on elastic properties	[29]
Grafted Marble (M)/Epoxy composite and Granite Powder (G)/Epoxy composite	Weight percentage of 20, 60, and 100wt% of fillers	Ultrasonic pulse-echo method	Effect of fillers weight ratio (%) on elastic properties	[30]
Rigid Polyurethane Foam	Foam density	Ultrasonic wave propagation methods	Effect of density of foam on elastic moduli	[31]
Polymethyl methacrylate (PMMA), Polystyrene (PS), and Polyvinyl-chloride (PVC)	/	Immersion sing-around method and ultrasonic pulse-echo method	To determine of elastic properties of thermoplastic resin	[32]

Table 2: Chemical compositions of the date kernel.([12], [44])

Cellulose (%)	Lignin (%)	Hemicellulose (%)	Ash (%)	Carbon (%)	Oxygen (%)	Hydrogen (%)
32.77	37.03	12.64	1.4	44.1-45.3	47.2-48.3	5.6-6.1



Figure 1: Reinforcement type used: (a) Date kernel (DK), (b) Raw date kernel powder (DKP) 300 μm and (c) Raw date kernel powder (DKP) 500 μm.

Investigations related to the use of natural powders of different sizes, such as date kernel powder (DKP) with epoxy resin (ER) matrix, and to the non-destructive characterization of these composites are very limited and have not been reported in the open scientific literature. The current study predicts the potential of date kernel powder (DKP) incorporation into epoxy resin (ER) to improve its mechanical properties. To this end, the elastic properties of the ER/DKP bio composites based on the size effect of date kernel powder (DKP) will be considered using the ultrasonic wave velocity measurement method.

2 Materials and Methods

2.1 Raw Materials

In this research, the natural reinforcement as kernel of date palm of Deglat Nour (DPDN) cultivar from Oasis agriculture in Touggourt, Algeria (Latitude 33° 06' 18.97'' N and Longitude 6° 03' 28.66'' E) was used as natural reinforcement material of biocomposites. This bio-waste kernel was isolated from date palm fruit collected after full ripeness. Two types of Date Kernel Powder (DKP) were obtained after kernels were cleaned with water to remove impurities and after being naturally dried for two days to reduce water content. The kernels were ground to powder using a mill and sieved to size 300 μm and 500 μm (Figure 1). In this study, we used date palm kernel powder without any treatment. The average values of the chemical composition of the date kernel are shown in Table 2.

2.2 Preparation of the Biocomposites Samples

The matrix used in this investigation was a MEDA-EPOXY INJECT 812 matrix composed of resin and hardener. The preparation of the composite samples took two stages, with the first step manually mixing the powder and matrix for 15-20 min. The second step fabricating the sample composite in the mold, as shown in Figure 2.

Epoxy resin was used in this study because it is commonly used for engineering applications, has good stiffness, better dimensional stability, and is cheaper [45]. The abbreviations and detailed information of the obtained biocomposites are given in Table 3.

2.3 Density Measurement

According to ASTM D792, the density measurements (ρ) with an analytical balance (KERN DBS Germany, readability 10-3mg, and weight capacity 60g) at a room temperature of 25°C were carried out.

Table 3: Contents of epoxy resin ER and date kernel powder (DKP).

Samples' ID	Composition ratio of ER/DKP (wt.%)
ER	100:0
COM305	95:5
COM310	90:10
COM315	85:15
COM505	95:5
COM510	90:10
COM515	85:15



Figure 2: Illustration of the process followed for ER/DKP biocomposites preparation.

2.4 Ultrasonic wave velocity (V_L and V_S) Measurements

Ultrasonic wave velocity measurements were performed using the contact-through transmission method. This method is based on the set of time (t) of flight of the sound through the sample thickness (d). In the first step, the thickness of the specimens was measured. Then, transmitting and receiving transducers type (OLYMPUS) placed on opposite sides of the specimens were used to detect the ultrasonic wave traveling via the thickness of specimens. Ultrasound lubricant was used for coupling through the device of generator (OLYMPUS 35MHz-5800PR) to apply a power supply with a pulse duration of $1 \mu s$. The ultrasonic waves were amplified and transferred to a digital TELEDYNE Locroy oscilloscope with a frequency of 1 GHz. Two longitudinal contact probes with a frequency of 5 MHz and a diameter of 9.5 mm and two shear contact probes with a frequency of 2.25 MHz and a diameter of 12.5 mm. Ultimately, the data were managed on a computer (Figure 3).

The determination of the time of flight (t) led to the calculation of the wave velocities (V) of the transmitted pulse along the sample by applying Equation 1

$$V = \frac{d}{t} \tag{1}$$

where $t(s)$, $d(m)$, and $V(m/s)$ are the time of flight, specimen thickness, and velocity of sound through the specimen, respectively.

2.5 Evaluation of the Elastic Constants

Because the measurement of the density and ultrasonic wave velocities of a material is acceptable for the ultrasonic characterization of isotropic materials, the other elastic constants can be determined depending on these two physical properties [46]. Considering the ER/DKP biocomposite samples as isotropic materials, the elastic properties of the biocomposites are calculated according to the following equations:

$$L = \rho V_L^2 \tag{2}$$

$$G = \rho V_S^2 \tag{3}$$

$$K = L - \frac{4}{3}G \tag{4}$$

$$\mu = \frac{L - 2G}{2(L - G)} \tag{5}$$

$$E = 2G(1 + \mu) \tag{6}$$

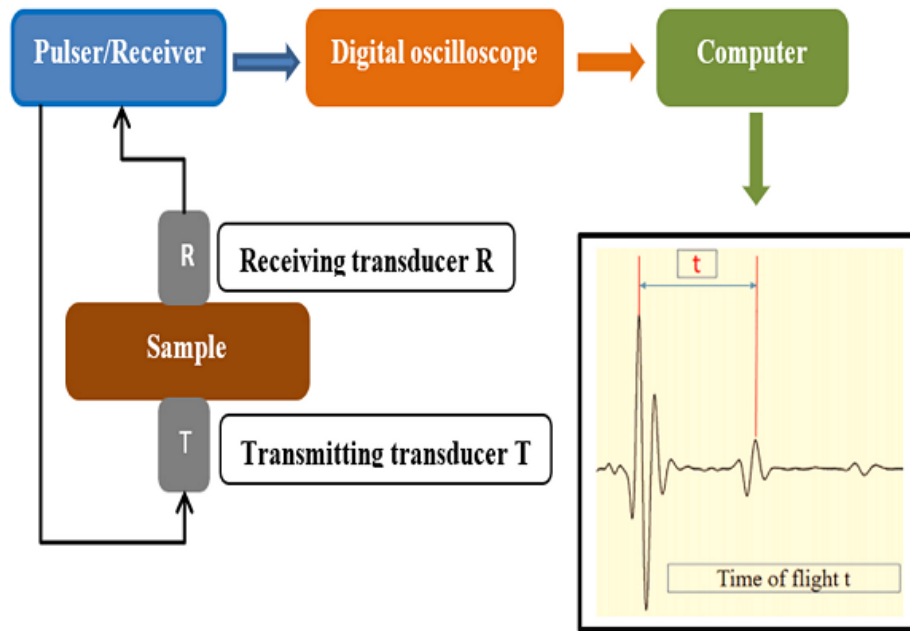


Figure 3: Diagram of the ultrasonic measurement setup used in this study.

$$H = \frac{(1 - 2\mu)E}{6(L + \mu)} \tag{7}$$

$$Z = \rho V_L \tag{8}$$

where L, G, K, μ , E, H, and Z are the longitudinal modulus, shear modulus, bulk modulus, Poisson’s ratio, Young’s modulus of elasticity, ultrasonic microhardness, and acoustic impedance, respectively. It is worth noting that these equations are valid for isotropic materials [47].

2.6 Morphological Measurements

The XRD analysis of the pure ER matrix and ER/DKP biocomposites was conducted using a D2 Phaser Bruker diffractometer, Germany, with operating conditions Cu-k α source ($\lambda = 1.54184\text{\AA}$, power source= 30KV and 10mA) and Bragg angle 2θ ($10^\circ - 90^\circ$), with a step speed of $1^\circ/\text{min}$. From the obtained XRD curves, the values of the crystalline index of the biocomposites samples were determined using the Ruland-Vonk method [48] and the application of Equation 9.

$$\text{Crystallinity (\%)} = \frac{\text{Crystalline area} \times 100}{\text{Total area under curve}} \tag{9}$$

In addition, the morphological structure of biocomposites was determined using an optical microscope (OM) tool.

3 Results and Discussion

3.1 Density and Wave Velocity

The density values of epoxy resin and ER/DKP composites are reported in Table 4, and it is clear that there is a remarkable change in their values.

Table 4: The density (ρ) and ultrasonic wave velocities (V_L and V_S) of the ER matrix and ER/DKP biocomposites.

Sample ID	Density ρ (kg/m^3)	Longitudinal Wave Velocity V_L (m/s)	Shear Wave Velocity V_S (m/s)
ER	1138.08 (± 7.85)	2200.05 (± 3.75)	1058.27 (± 23.53)
COM305	1151.25 (± 2.58)	1841.25 (± 31.31)	1081.61 (± 16.37)
COM310	1158.10 (± 3.31)	1366.89 (± 6.60)	962.23 (± 48.55)
COM315	1165.14 (± 5.65)	1277.55 (± 67.59)	896.16 (± 21.15)
COM505	1147.02 (± 0.57)	1723.66 (± 14.98)	1080.71 (± 41.00)
COM510	1155.31 (± 1.41)	1995.93 (± 21.13)	1139.26 (± 17.15)
COM515	1151.14 (± 1.82)	1650.47 (± 28.25)	1016.86 (± 32.19)

The obtained experimental density ranged between 1138.08 kg/m^3 and 1165.14 kg/m^3 . The density values of biocomposites are higher than those of ER and are increased by approximately 1.16%, 1.76%, 2.38%, 0.79%, 1.51%, and 1.15% for COM305, COM310, COM315, COM505, COM510, and COM515 biocomposites, respectively, compared to the ER matrix. The highest density value was recorded for COM315. This is the reason for better interfacial adhesion between pure ER and DKP [49]. Also, according to the variation in density values given in Figure 4, ρ values of the ER/DKP biocomposites increase with an increase

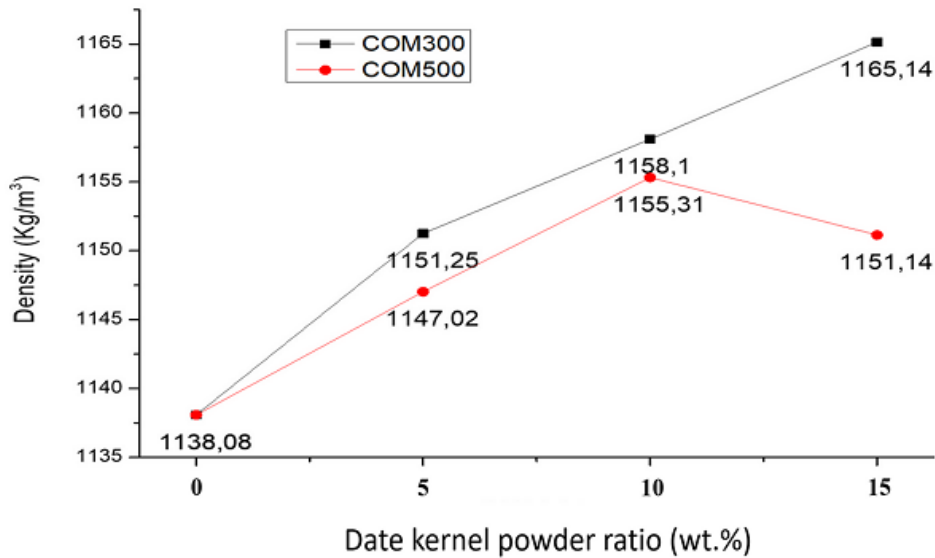


Figure 4: Variation in density (ρ) for ER matrix and ER/DKP biocomposites.

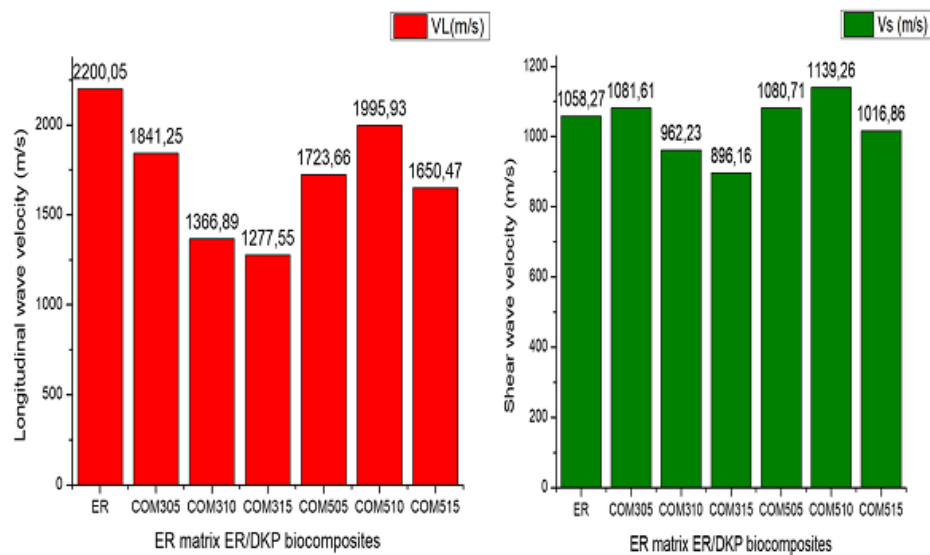


Figure 5: Variation in longitudinal wave velocity (V_L) and shear wave velocity (V_S) for the ER matrix and ER/DKP biocomposites.

in the DKP size 300 μm as compared with the unreinforced ER matrix. However, in the case of powder size 500 μm the density values of the ER/DKP biocomposites increase with an increase in the weight of DKP up to 10 wt% but decrease slightly when the weight of DKP is increased up to 15 wt%. This decrease may be due to an insufficient epoxy matrix to blend with the DKP. As seen also in Table 4 and Figure 4, the density values of the ER/DKP biocomposites with powder size 300 μm are higher than the density values of the ER/DKP biocomposites with powder size 500 μm in the same loading. This can be attributed to the role of reinforcement density and high volume of DKP, where good bond was found in the case of smaller DKP, unlike the presence of voids between the large DKP [50], [51].

The relationship between the ultrasonic wave velocities and the elastic constants of materials provides important information about the elastic and mechanical properties of materials [18].

As shown in Table 4, the values of longitudinal wave velocities V_L of the studied materials ranged from 1277.55 m/s to 2200.05 m/s. Also, V_L values of ER/DKP biocomposites are less than that of neat ER. The velocity values V_L of the COM305, COM310, and COM315 composites decreased by approximately 16.31%, 37.87%, and 41.93%, respectively.

In addition, the COM505, COM510, and COM515 composites decreased by approximately 21.65%, 9.28%, and 24.98%, respectively, compared to the ER matrix. On the other hand, the shear wave velocity values V_S of the ER/DKP biocomposites of the studied materials ranged from 902 m/s to 1139 m/s. In addition, the V_S values of the ER/DKP biocomposites were higher than that of ER, except for the COM310, COM315, and COM515 samples, which had the minimum values. The shear velocity

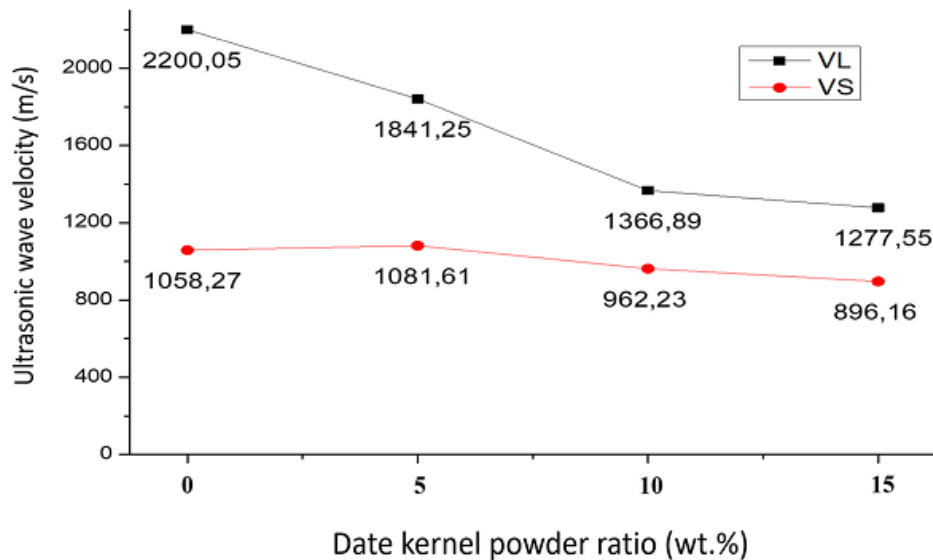


Figure 6: Variation in ultrasonic wave velocities (V_L and V_S) for the ER matrix and ER/DKP biocomposites with a powder size of 300 μm .

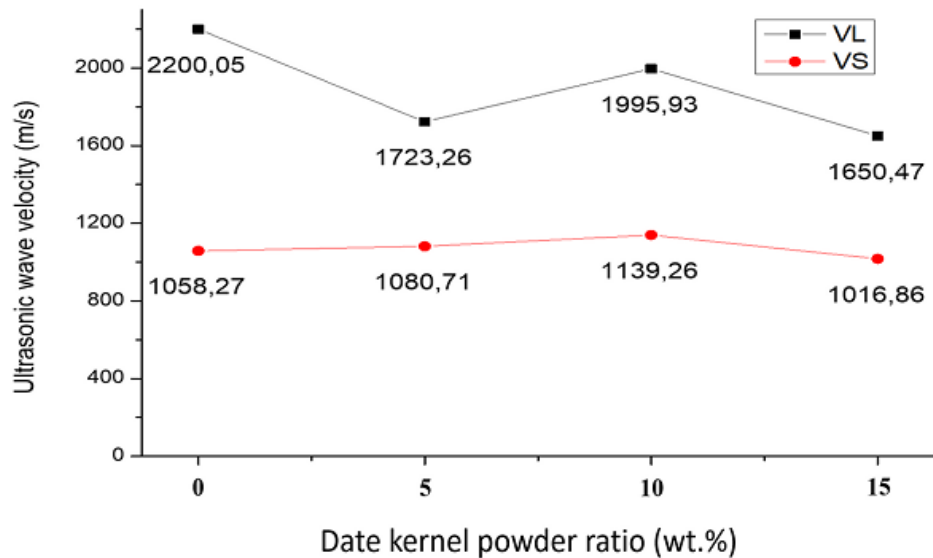


Figure 7: Variation in ultrasonic wave velocities (V_L and V_S) for the ER matrix and ER/DKP biocomposites with a powder size of 500 μm .

values V_S of COM305, COM505, and COM510 increased by approximately 2.21%, 2.12%, and 7.65%, respectively, whereas those of COM310, COM315, and COM515 decreased by approximately 9.08%, 15.32%, and 3.91%, respectively, compared to the ER. The same morphology of evolution of wave velocities V_L and V_S as a function of the loading ratio of powder in the two-configuration biocomposites studied was observed (Figure 5). The highest values for V_L and V_S were seen for COM300 and COM500 biocomposites in the 95:5wt% and 90:10wt%, respectively.

3.2 Elastic Moduli

The experimental values of the elastic moduli (L, G, K, and E) of the ER matrix and ER/DKP obtained by different DKP incorporation contents are reported in Table 4. The variation of these elastic moduli is illustrated in Figure 8. As observed from Table 4, the longitudinal modulus L values range between 3.84 and 9.26 GPa, the shear modulus G values range between 0.95 and 1.50 GPa, the bulk modulus values K range between 2.57 and 7.26 GPa, and the Young's modulus E values range between 2.54 and 4.22 GPa for pure ER and ER/DKP biocomposites. It is consistent with the results of the study [23]. Also, from Table 5, it can be noticed that the values of the elastic moduli (L, G, K, and E) of ER/DKP in the case of powder size 300 μm are lower than pure ER, except for COM305 composite, which have the maximum values, by increasing about 29.77%, 5.18%, 37.12%, and 8.73% for L, G, K, and E, respectively. But on another hand, in the case of powder size 500 μm the values of the elastic

Table 5: Elastic constants of the ER matrix and ER/DKP biocomposites.

Samples ID	Longitudinal Modulus L(GPa)	Shear Modulus G(GPa)	Bulk Modulus K(GPa)	Young's Modulus E(GPa)
ER	5.52(±0.01)	1.28(±0.05)	3.81 (±0.04)	3.45 (±0.07)
COM305	7.86(±0.13)	1.35(±0.04)	6.06(±0.03)	3.78(±0.09)
COM310	4.39(±0.02)	1.08(±0.10)	2.94(±0.07)	2.90(±0.10)
COM315	3.84(±0.20)	0.95(±0.04)	2.57(±0.03)	2.54(±0.08)
COM505	6.91(±0.22)	1.34(±0.10)	5.12(±0.08)	3.70(±0.02)
COM510	9.26(±0.09)	1.50(±0.05)	7.26(±0.07)	4.22(±0.11)
COM515	6.34(±0.10)	1.19(±0.07)	4.75(±0.09)	3.30(±0.07)

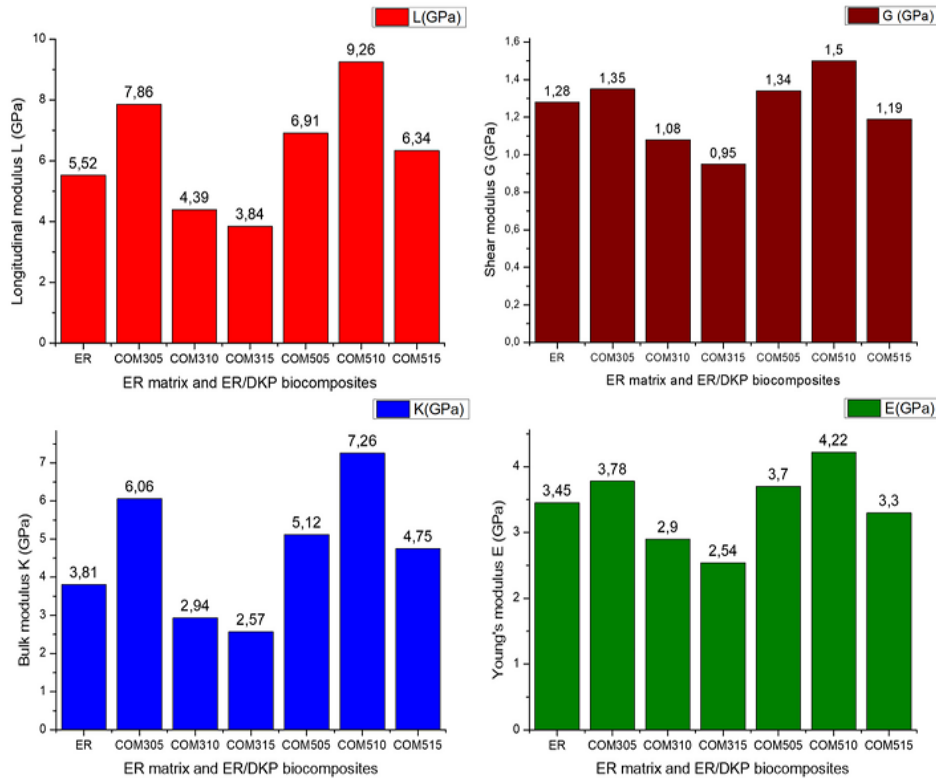


Figure 8: Variation in elastic moduli (L, G, K, and E) for the ER matrix and ER/DKP biocomposites.

moduli (G and E) of ER/DKP are higher than pure ER, except for COM515 composite, which has the minimum value, by decreasing about 7.56% and 4.54% for G and E, respectively.

The value of Young’s modulus of elasticity (E) of the ER matrix increased from 3.45 to 3.70 and 4.22 GPa after the incorporation of 5 wt% and 10 wt% of DKP for size 500 μm of powder, respectively, by approximately 6.75% and 18.24% for 5 wt% and 10 wt% of powder, respectively. In addition, these results show that in the case of powder size 500 μm the values of the elastic moduli (L and K) of ER/DKP are higher than those of pure ER. As an example, in the case of powder size 500 μm the value of longitudinal modulus (L) of the ER matrix increased from 5.52 GPa to 6.34 and 6.91GPa for 15wt.% and 5wt.% of powder, respectively, until the maximum value 9.26GPa for 10wt.% of DKP, by about 20.11%, 25.37%, and 12.93% for 5 wt.%, 10 wt.%, and 15 wt.% of powder.

In the case of powder size 500μm, the bulk modulus (K) value of the ER matrix increased from 3.81 GPa to 5.12 and 4.75GPa for 5wt.% and 15wt.% of powder, respectively, until the maximum value 7.26GPa for 10wt.% of DKP, by about 25.58%, 47.52%, and 19.78% for 5 wt.%, 10 wt.%, and 15 wt.% of DKP. These results show the improvement of all elastic moduli (L, G, K, and E) by the incorporation of 5% and 10% of kernel powder with 300 μm and 500μm, respectively, which can be considered as the optimum value of the weight of the reinforcement in these sizes of powder. This result explained that the strong bonding formed between the ER matrix and the reinforcement DKP in these weights, which explained the decrease in the movement of the polymer chains, led to material characteristics strength [49], [52].

Data from Table 5 and Figure 8 show that the values of elastic moduli L, G, K, and E have the same behavior as a function of powder size. We find that in the case of 300 μm powder size, these values decrease when the weight of the powder increases from 5 to 15 wt.%. On the other hand, in the case of 500 μm powder size, the values of elastic constants moduli increase when the powder weight is from 5% to 10% and slightly decrease when the powder weight increases up to 15%. The decrease in these values may be due to insufficient adhesion between the natural powder and epoxy matrix upon further increasing the powder

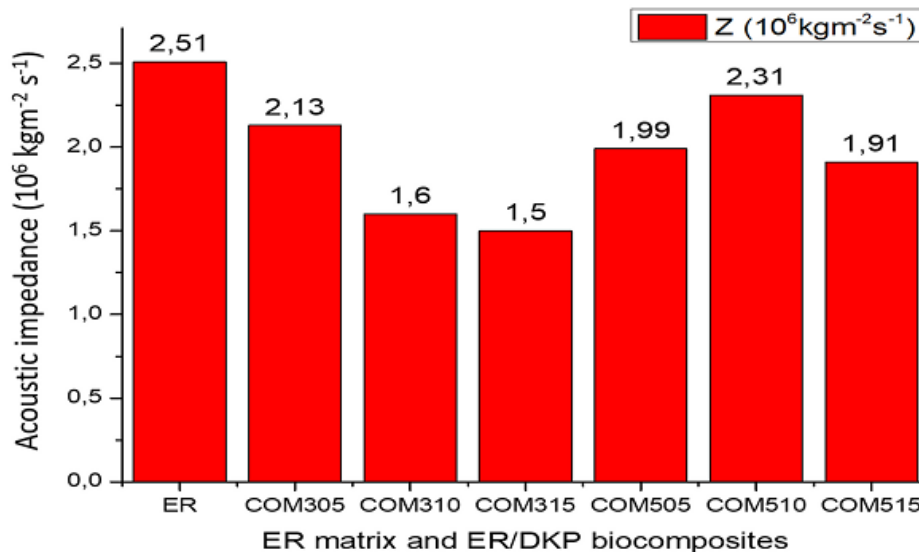


Figure 9: Variation in acoustic impedance Z for the ER matrix and ER/DKP biocomposites.

percentage. This also leads us to predict the optimum and maximum powder loading values.

3.3 Acoustic Impedance, Poisson’s Ratio, and Ultrasonic Microhardness

According to Figure 9 and Table 7, a pattern of change in Z values through the change in powder weight was detected. The ultrasonic impedance Z ranged from 1.5 to 2.51 × 10⁶ kgm⁻² s⁻¹ (Figure 9).

Table 6: Variation of Z, H, and μ of the pure matrix ER and ER/DKP biocomposites.

Sample ID	Acoustic Impedance Z (10 ⁶ kg·m ⁻² ·s ⁻¹)	Ultrasonic Micro-Hardness H (GPa)	Poisson’s Ratio μ
ER	2.51 (± 0.02)	0.131 (± 0.005)	0.349 (± 0.003)
COM305	2.13 (± 0.02)	0.094 (± 0.003)	0.396 (± 0.004)
COM310	1.60 (± 0.07)	0.119 (± 0.006)	0.335 (± 0.001)
COM315	1.50 (± 0.03)	0.105 (± 0.005)	0.335 (± 0.001)
COM505	1.99 (± 0.01)	0.107 (± 0.001)	0.379 (± 0.004)
COM510	2.32 (± 0.02)	0.097 (± 0.006)	0.403 (± 0.004)
COM515	1.91 (± 0.01)	0.092 (± 0.005)	0.384 (± 0.003)

Z decreased from 2.51 to maximum value 2.13 × 10⁶ kgm⁻² s⁻¹, when neat matrix reinforced with 5 wt%, and also decreased to 1.6 and 1.5 × 10⁶ kgm⁻² s⁻¹ when neat matrix reinforced with the 10wt.%, and 15wt.% respectively, in the case of powder size 300 μm (Table 7). Also, Z decreased from 2.51 to 1.99 and 1.91 × 10⁶ kgm⁻² s⁻¹ when neat matrix reinforced with 5wt.% and 15wt.% of powder, respectively, in the case of 500 μm of powder, until the case of 10wt.% weight when the value of the Z decreases to 2.32 × 10⁶ kgm⁻² s⁻¹ by about 8.62%.

This parameter is considered an indicator of a material’s resistance when wave propagates in it [24]. Therefore, COM305 and COM510 are the most desirable biocomposites and have higher durability against propagation sound waves by their 2.13 and 2.32 × 10⁶ kgm⁻² s⁻¹ values of Z, respectively (Figure 9). The obtained results for ultrasonic impedance Z agree with the ultrasonic wave velocities.

The Poisson’s ratio μ values were calculated using Eq. (6). μ values ranged from 0.335 to 0.403 (Table 7). These results are consistent with the study of Oral et al. [53], who mentioned that the Poisson’s ratio of most materials ranges between 0.0 and 0.5. μ decrease from 0.349 to 0.335 when neat matrix reinforced with the 10wt% and 15wt.% in the case of powder size 300 μm, except for the loading weight 5wt.% the value of the Poisson’s ratio increases up to a maximum value of 0.396 (Figure 10). On another hand, in the case of 500 μm of powder size, μ increased from 0.349 to 0.379 and 0.384 when neat matrix reinforced with 5 wt.% and 15 wt.% of powder, until it reached a maximum value of 0.403 in the case of 10 wt.% weight. Oral et al. [53] declared that in their contribution, the assumption of an inverse relationship between Poisson’s ratio and elastic constants is not true every time. As shown in Figure 11, the microhardness H values ranged from 0.092 to 0.119 GPa. The highest values of microhardness were observed for 10 wt.% in the case of 300 μm of powder and 5 wt.% in the case of 500 μm of powder with values of 0.119 GPa and 0.107 GPa, respectively. The increase and decrease in microhardness justify the role of powder on the biocomposite. For example, in the case of powder size 300 μm, the optimum weight is 10 wt.% of powder and 5 wt.% of powder in the case of 500 μm. Then, H of ER/DKP biocomposites decreased slightly to 0.092 GPa by increasing DKP weight from 5 wt.% to 15 wt.% in the case of powder size 500 μm.

On the other hand, in the case of powder size 300 μm, the microhardness increased from 0.094 to the maximum value of 0.119 GPa by DKP addition ratio 5 wt.% to 10 wt.% and decreased to 0.105 GPa by increasing DKP weight from 10 wt.% to

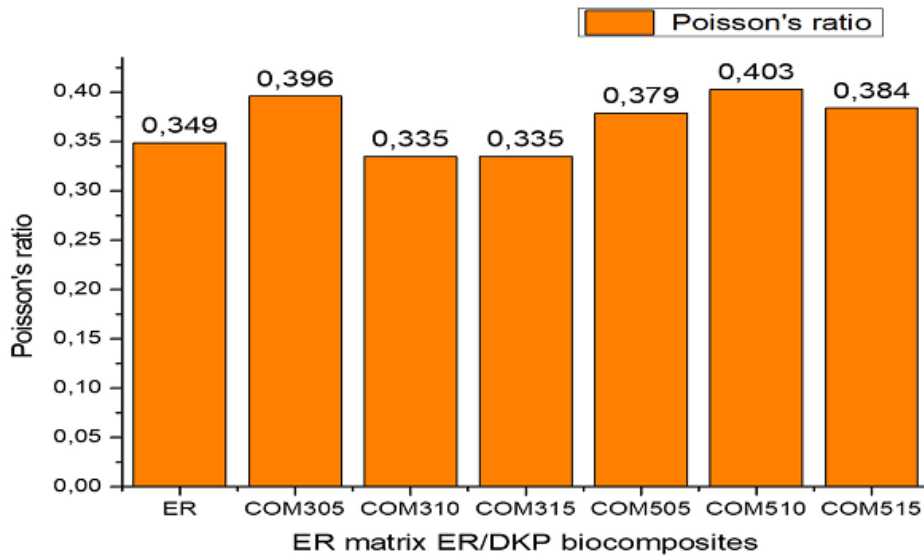


Figure 10: Variation in Poisson's ratio μ for ER matrix and ER/DKP biocomposites.

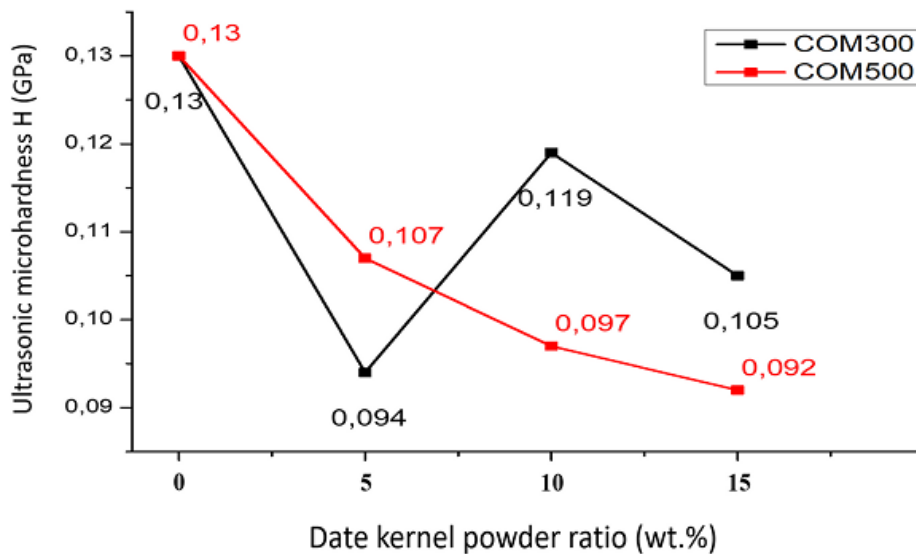


Figure 11: Variation in ultrasonic microhardness H for the ER matrix and ER/DKP biocomposites.

15 wt.% in the case of powder size 300 μm . Table 8 summarizes some ultrasonic investigations on the mechanical behavior of the obtained biocomposite materials.

3.4 XRD Analysis Results for the ER and ER/DKP Biocomposites

Figure 12 represents the XRD patterns of the ER matrix and ER/DKP biocomposites. This shows that the XRD peaks of both the samples of size 300 μm and 500 μm were shaped in the same way as the ER matrix. On the other hand, XRD peaks show the amorphous type of the biocomposites and have a higher intensity than the ER matrix, which increased with increasing powder loading in the case of 300 μm . All these results confirmed the good dispersion of the biopowder of date kernel powder in the

Table 7: Comparison of the ultrasonic properties of ER/DKP biocomposites with those of other powder-based composites.

Material	Fiber sizes (μm)	L, G, K, E maximum values	μ and Z values	Treatment condition	Refs
DKP/Epoxy	300	7.86, 1.35, 6.06, 3.78	0.396, 2.13	fiber not treated	This study
	500	9.26, 1.50, 7.26, 4.22	0.403, 2.32		
DPS/Epoxy	200	8.89, 1.45, 6.96, 4.06	0.411, 3.33	treated fiber	[18]
Polyaniline/Epoxy	< 63	9.02, 1.51, 7.00, 4.24	0.400, 3.26	fiber not treated	[17]
Marble/Epoxy	/	7.37, 1.20, 5.89, 3.14	0.410, 2.78	fiber not treated	[24]
Pine cone char/Epoxy	< 60	9.61, 2.09, 6.83, 5.68	0.374, 3.42	fiber not treated	[23]
Polyaniline/Epoxy	< 63	10.45, 1.98, 8.03, 5.40	0.398, 3.72	modified resin	[20]
Coconut/Epoxy	< 63	10.27, 2.08, 7.83, 5.66	0.393, 3.53	modified resin	[46]

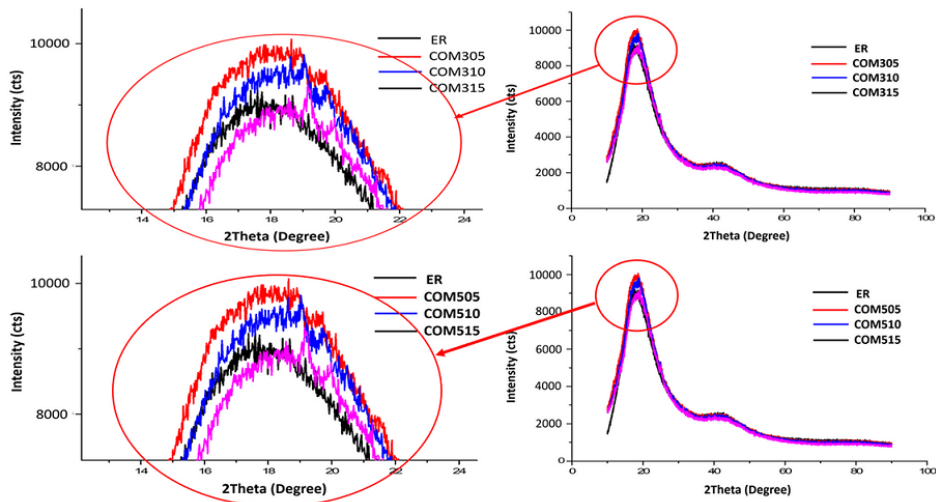


Figure 12: X-ray diffraction curves of the ER matrix and ER/DKP biocomposites.

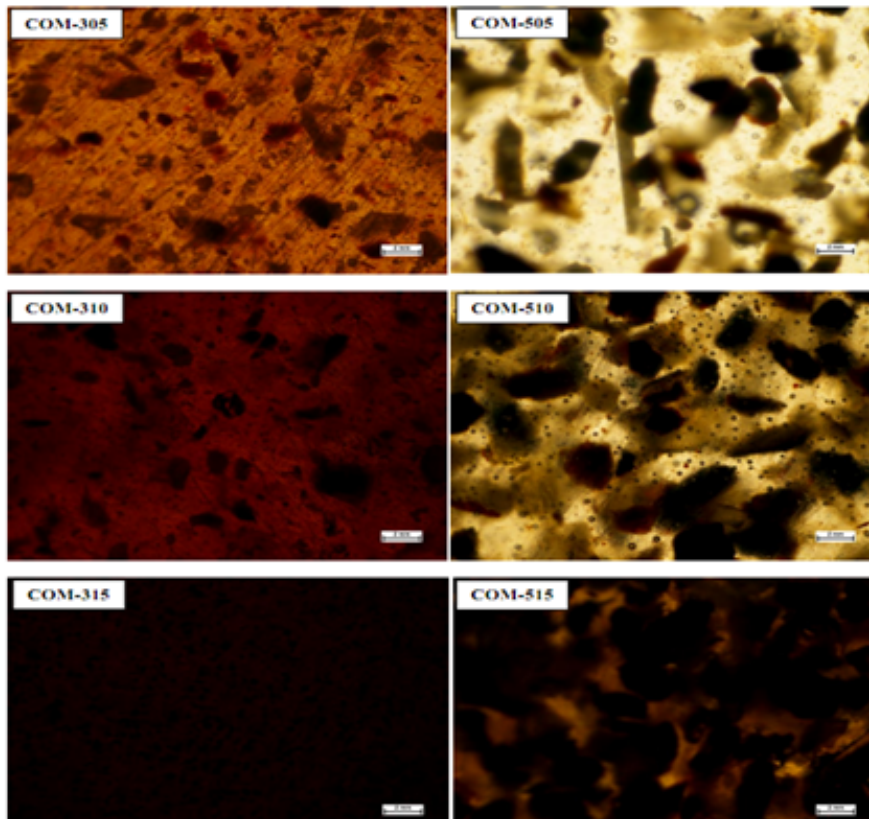


Figure 13: Macroscopic view of the ER/DKP biocomposite samples.

ER matrix [46]. The crystalline index of the biocomposites was measured as 98.10% for the ER matrix, 89.05% for COM305, 80.51% for COM310, 80.38% for COM315, 80.24% for COM505, 78.58% for COM510, and 73.14% for COM515. The same results concerned the increase in the crystalline index in the study of Khosravani et al. [48]. An increase in the crystalline index was observed when the particle size decreased. This high crystallinity index is due to lignin breakage during the grinding process [48], [54].

3.5 Morphological Structure of the ER/DKP Biocomposites

Homogeneity plays an important role in the physical and mechanical properties of filler composites. In addition, the distribution and dispersion of filler in the hydrophilic polymer matrix is a critical issue related to biocomposite manufacturing that needs to be controlled [55], [56]. Therefore, morphological analysis of the ER/DKP biocomposites is essential to explore the effect of DKP loading on adhesion quality.

Figure 13 shows the morphology in terms of size and appearance of the samples prepared with the two powder sizes 300 μm and 500 μm . Figure 13 shows the homogenous distribution of powder with varying loading of DKP, where we found a good distribution of the powder due to the increase in powder concentration. Asyraf et al. [56] reported that biocomposite materials reinforced with low fiber loading exhibited more homogenous dispersion with less fiber aggregation than biocomposites reinforced with high fiber loading. On the other hand, some black spots appear in the form of a few agglomerations, especially in biocomposites with higher loading, such as COM315 and COM515. Powder agglomeration is the main cause of weak part formation in which damage initiates and then propagates [55].

4 Conclusions

Within the scope of this study, date kernels, which are among the most abundant agricultural wastes in Algeria, were produced as environmentally friendly biocomposites as an alternative to synthetic composites that pollute nature. The mechanical properties of these biocomposites were determined by ultrasonic through-transmission, which is a non-destructive test method. The experimental results obtained within the scope of this study can be summarized as follows:

- Following a thorough analysis, the different grain sizes of DKP have a crucial effect on the elastic and mechanical properties of the proposed biocomposite.
- The highest ultrasonic values of wave velocities and elastic constants (L, G, K, E, and Z) were observed for the COM305 and COM510 samples. Therefore, it can be stated that the optimum weight percent of DKP reinforcement in neat ER for excellent mechanical behavior of ER/DKP biocomposites is 5% and 10% for 300 μm and 500 μm , respectively.
- In the case of comparing the results of elastic moduli of the two studied configurations COM300 and COM500 through the weight rate of DKP, the biocomposite with a powder size of 300 μm and a ratio of 5% is better than of 500 μm biocomposites, but in the case of a ratio of 10% and 15% of DKP, the biocomposites 500 μm are better than of biocomposites 300 μm .
- The highest microhardness values (H) were observed for the COM310 and COM505 samples. Therefore, it can be stated that the optimum weight is 10 wt.% and 5 wt.% for the DKP sizes of 300 μm and 500 μm , respectively.
- The results indicate that the ultrasonic through-transmission method is helpful in determining the elastic properties of ER/DKP biocomposites.

Overall, this study might open new avenues for utilizing the proposed DKP reinforcement for different real-life applications. Similar studies can be conducted using treated DKP having different grain sizes. In addition, the ultrasonic method may be considered the best method for determining the mechanical behaviors of biocomposites.

Authors' Contributions

Fares Mohammed Laid Rekbi: Conceptualization, Writing-original draft, Review, and editing, Performing the ultrasonic test, Analyzing the results. Rafik Halimi: Conceptualization, Writing-original draft, Review, and editing, Performing the ultrasonic test, Analyzing the results. Mabrouka Oustani: Review and editing, Analyzing the results. Imran Oral: Visualization, Writing-original draft, Review, and editing, Analyzing the results. Wahiba Djerir: Review and editing, Analyzing the results. Fethi Remli: Review, and editing, Analyzing the results. Hicham Henna: Editing.

Competing Interests

The authors have no relevant financial or non-financial interests to disclose.

References

- [1] F. M. L. Rekbi, "Behavior of materials in the presence of particles additive technique: a review," *ENP Engineering Science Journal*, vol. 3, no. 1, pp. 15–26, 2023.

- [2] F. M. L. Rekki, M. Hecini, and A. Khechai, "Experimental and numerical analysis of mode-I interlaminar fracture of composite pipes," *Journal of the Brazilian Society of Mechanical Sciences and Engineering*, vol. 40, no. 10, p. 502, 2018.
- [3] M. Sh. Al-Otaibi, O. Y. Allothman, M. M. Alrashed, A. Anis, J. Naveen, and M. Jawaid, "Characterization of date palm fiber-reinforced different polypropylene matrices," *Polymers*, vol. 12, no. 3, p. 597, 2020.
- [4] S. Mohammed, A. Meghezzi, Y. Meftah, and S. Maou, "Thermophysical behavior of date palm fiber-reinforced polyvinylchloride/low-density polyethylene/acrylonitrile butadiene rubber copolymer ternary composite," *Polyolefins Journal*, vol. 10, no. 4, pp. 225–233, 2023.
- [5] A. Kriker, G. Debicki, A. Bali, M. Khenfer, and M. Chabannet, "Mechanical properties of date palm fibres and concrete reinforced with date palm fibres in hot-dry climate," *Cement and Concrete Composites*, vol. 27, no. 5, pp. 554–564, 2005.
- [6] C. Belgacem, F. Serra-Parareda, Q. Tarrés, P. Mutjé, M. Delgado-Aguilar, and S. Boufi, "Valorization of date palm waste for plastic reinforcement: Macro and micromechanics of flexural strength," *Polymers*, vol. 13, no. 11, p. 1751, 2021.
- [7] S. Awad, Y. Zhou, E. Katsou, Y. Li, and M. Fan, "A critical review on date palm tree (phoenix dactylifera L.) fibres and their uses in bio-composites," *Waste and Biomass Valorization*, vol. 12, pp. 2853–2887, 2021.
- [8] L. A. Elseify, M. Midani, L. A. Shihata, and H. El-Mously, "Review on cellulosic fibers extracted from date palms (phoenix dactylifera L.) and their applications," *Cellulose*, vol. 26, pp. 2209–2232, 2019.
- [9] K. AlZebdeh, M. Nassar, M. Al-Hadhrami, O. Al-Aamri, S. Al-Defaai, and S. Al-Shuaily, "Characterization of mechanical properties of aligned date palm frond fiber-reinforced low density polyethylene," *The Journal of Engineering Research [TJER]*, vol. 14, no. 2, pp. 115–123, 2017.
- [10] A. Hamma, M. Kaci, and A. Pegoretti, "Polypropylene/date stone flour composites: Effects of filler contents and ebigma compatibilizer on morphology, thermal, and mechanical properties," *Journal of Applied Polymer Science*, vol. 128, no. 6, pp. 4314–4321, 2013.
- [11] K. S. Al-Zahrani, A. A. Faqeeh, Z. R. Abdulghani, and S. P. Thomas, "A review on the physicochemical properties and utilization of date seeds in value-added engineering products," *Polymer Bulletin*, vol. 79, no. 12, pp. 10433–10490, 2022.
- [12] R. A. Nasser, M. Z. Salem, S. Hiziroglu, H. A. Al-Mefarrej, A. S. Mohareb, M. Alam, and I. M. Aref, "Chemical analysis of different parts of date palm (phoenix dactylifera L.) using ultimate, proximate and thermo-gravimetric techniques for energy production," *Energies*, vol. 9, no. 5, p. 374, 2016.
- [13] A. Djoudi, M. M. Khenfer, A. Bali, and T. Bouziani, "Effect of the addition of date palm fibers on thermal properties of plaster concrete: experimental study and modeling," *Journal of Adhesion Science and Technology*, vol. 28, no. 20, pp. 2100–2111, 2014.
- [14] N. Benmansour, B. Agoudjil, A. Gherabli, A. Kareche, and A. Boudenne, "Thermal and mechanical performance of natural mortar reinforced with date palm fibers for use as insulating materials in building," *Energy and Buildings*, vol. 81, pp. 98–104, 2014.
- [15] E. Atiki, A. Khechai, B. Taallah, S. Feia, K. S. Almeasar, A. Guettala, and O. Canpolat, "Assessment of flexural behavior of compressed earth blocks using digital image correlation technique: effect of different types of date palm fibers," *European Journal of Environmental and Civil Engineering*, vol. 28, no. 5, pp. 1208–1229, 2024.
- [16] A. Abdal-Hay, N. P. G. Suardana, D. Y. Jung, K.-S. Choi, and J. K. Lim, "Effect of diameters and alkali treatment on the tensile properties of date palm fiber reinforced epoxy composites," *International Journal of Precision Engineering and Manufacturing*, vol. 13, pp. 1199–1206, 2012.
- [17] I. Oral, "Ultrasonic characterization of conductive epoxy resin/polyaniline composites," *Journal of Applied Polymer Science*, vol. 132, no. 45, 2015.
- [18] S. Rabhi, S. Abdi, R. Halimi, and N. Benghanem, "Green epoxy resin/date stone flour biocomposites: Effect of filler chemical treatments on elastic properties," *Polymer Composites*, vol. 42, no. 9, pp. 4736–4753, 2021.
- [19] I. Oral and M. Ekrem, "Measurement of the elastic properties of epoxy resin/polyvinyl alcohol nanocomposites by ultrasonic wave velocities," *Express Polymer Letters*, vol. 16, no. 6, pp. 591–606, 2022.
- [20] I. Oral, U. Soydal, and M. Bentahar, "Ultrasonic characterization of andesite waste-reinforced composites," *Polymer Bulletin*, vol. 74, no. 5, pp. 1899–1914, 2017.
- [21] C. M. Valencia, J. Pazos-Ospina, E. Franco, J. L. Ealo, D. Collazos-Burbano, and G. C. Garcia, "Ultrasonic determination of the elastic constants of epoxy-natural fiber composites," *Physica Procedia*, vol. 70, pp. 467–470, 2015.
- [22] A. El-Daly, M. Abdelhameed, M. Hashish, and A. Eid, "Synthesis of al/sic nanocomposite and evaluation of its mechanical properties using pulse echo overlap method," *Journal of Alloys and Compounds*, vol. 542, pp. 51–58, 2012.
- [23] I. Oral, "Determination of elastic constants of epoxy resin/biochar composites by ultrasonic pulse echo overlap method," *Polymer Composites*, vol. 37, no. 9, pp. 2907–2915, 2016.
- [24] —, "Ultrasonic properties of epoxy resin/marble waste powder composites," *Polymer Composites*, vol. 36, no. 3, pp. 584–590, 2015.
- [25] I. Oral, H. Guzel, and G. Ahmetli, "Ultrasonic properties of polystyrene-based composites," *Journal of Applied Polymer Science*, vol. 125, no. 2, pp. 1226–1237, 2012.
- [26] I. Oral and G. Ahmetli, "Ultrasonic characterisation of epoxy resin/polyethylene terephthalate (pet) char powder composites," *Materials Science*, vol. 22, no. 4, pp. 553–559, 2016.
- [27] H. Cao, S. Guo, Z. He, Y. Xie, T. Zhang, and W. Feng, "In situ elastic constant determination of unidirectional cfrp composites via backwall reflected multi-mode ultrasonic bulk waves using a linear array probe," *Composites Part B: Engineering*, vol. 238, p. 109953, 2022.
- [28] S. Rabhi, N. Benghanem, and S. Abdi, "Comparative study of two biocomposites: Effect of date stone flour treated with potassium permanganate as a filler on the morphological and elastic properties," *Journal of Composite Materials*, vol. 56, no. 7, pp. 1071–1089, 2022.
- [29] S. Souissi, K. Mezghanni, N. Bouhamed, P. Marechal, M. Benamar, and O. Lenoir, "Comparison between ultrasonic and mechanical young's modulus of a bio-composite reinforced with olive wood flour," in *Advances in Acoustics and Vibration II: Proceedings of the Second International Conference on Acoustics and Vibration (ICAV2018), March 19-21, 2018, Hammamet, Tunisia*. Springer, 2019, pp. 300–309.
- [30] A. A. Yassene, S. Fares, A. Ashour, and M. Abd El-Rahman, "Ultrasonic velocity and attenuation in epoxy resin/granite (marble) powder composite," *Research in Nondestructive Evaluation*, vol. 29, no. 1, pp. 48–60, 2018.
- [31] J. Holt, S. Blackwell, L. Zani, and C. Torres-Sanchez, "Comparison of elastic properties of low-density polymeric foams determined by ultrasonic wave propagation and quasi-static mechanical testing," *Materials Letters*, vol. 263, p. 127243, 2020.
- [32] H. A. Afifi, "Ultrasonic pulse echo studies of the physical properties of pmma, ps, and pvc," *Polymer-Plastics Technology and Engineering*, vol. 42, no. 2, pp. 193–205, 2003.
- [33] R. A. Ibrahim, "Effect of date palm seeds on the tribological behaviour of polyester composites under different testing conditions," *Journal of Material Sciences and Engineering*, vol. 4, no. 6, 2015.
- [34] A. O. Ameh, M. T. Isa, and I. Sanusi, "Effect of particle size and concentration on the mechanical properties of polyester/date palm seed particulate composites," *Leonardo Electronic Journal of Practices and Technologies*, vol. 14, no. 26, pp. 65–78, 2015.
- [35] T. Masri, H. Ounis, L. Sedira, A. Kaci, and A. Benchabane, "Characterization of new composite material based on date palm leaflets and expanded polystyrene wastes," *Construction and Building Materials*, vol. 164, pp. 410–418, 2018.
- [36] M. Boumhaout, L. Boukhatem, H. Hamdi, B. Benhamou, and F. A. Nouh, "Thermomechanical characterization of a bio-composite building material: Mortar reinforced with date palm fibers mesh," *Construction and Building Materials*, vol. 135, pp. 241–250, 2017.
- [37] S. Benaniba, Z. Driss, M. Djendel, E. Raouache, and R. Boubaaya, "Thermo-mechanical characterization of a bio-composite mortar reinforced with date palm fiber," *Journal of Engineered Fibers and Fabrics*, vol. 15, p. 1558925020948234, 2020.
- [38] A. Abd Mohammed, "The experimental study and statistical evaluation of the wear and hardness of epoxy reinforced with natural materials," *Journal of Engineering and Sustainable Development*, vol. 20, no. 3, pp. 14–24, 2016.

- [39] N. Debabeche, O. Kribaa, H. Boussehel, B. Guerira, M. Jawaid, H. Fouad, and M. Azeem, "Effect of fiber surface treatment on the mechanical, morphological, and dynamic mechanical properties of palm petiole fiber/lldpe composites," *Biomass Conversion and Biorefinery*, pp. 1–14, 2023.
- [40] H. Ozcelik, "Nehir sularındaki cu (ii) ağır metal iyonlarının dogal atiklarla uzaklaştırılması," *El-Cezeri Journal of Science and Engineering*, vol. 5, no. 2, pp. 361–366, 2018.
- [41] I. Oral, "Investigation of surface damages in composite materials using ultrasonic lamb waves," *El-Cezeri Journal of Science and Engineering*, vol. 8, no. 2, pp. 652–665, 2021.
- [42] I. Oral, H. Guzel, and G. Ahmetli, "Measuring the young's modulus of polystyrene-based composites by tensile test and pulse-echo method," *Polymer Bulletin*, vol. 67, pp. 1893–1906, 2011.
- [43] F. M. L. Rekbi, A. Khechai, R. Halimi, M. Hecini, and Ö. Özbek, "Crack growth behavior in filament winding composites under mode-i loading test: destructive and non-destructive investigations," *Journal of the Brazilian Society of Mechanical Sciences and Engineering*, vol. 45, no. 2, p. 78, 2023.
- [44] J. B. Niyomukiza, K. C. Nabitaka, M. Kiwanuka, P. Tiboti, and J. Akampulira, "Enhancing properties of unfired clay bricks using palm fronds and palm seeds," *Results in Engineering*, vol. 16, p. 100632, 2022.
- [45] K. R. Rajthilak, S. Ramesh, G. Lokesh, and S. B. Boppana, "Date palm fibre reinforced composite by multiple resin to enhance the properties of a composite-a review," in *IOP Conference Series: Materials Science and Engineering*, vol. 1013, no. 1. IOP Publishing, 2021, p. 012034.
- [46] I. Oral, S. Kocaman, and G. Ahmetli, "Preparation and ultrasonic characterization of modified epoxy resin/coconut shell powder biocomposites," *Journal of Applied Polymer Science*, vol. 139, no. 11, p. 51772, 2022.
- [47] I. Perepechko and G. Leib, *Acoustic methods of investigating polymers*. Mir Publishers, 1975.
- [48] M. R. Khosravani, P. Soltani, K. Weinberg, and T. Reinicke, "Structural integrity of adhesively bonded 3d-printed joints," *Polymer Testing*, vol. 100, p. 107262, 2021.
- [49] I. Oral, S. Kocaman, and G. Ahmetli, "Characterization of unmodified and modified apricot kernel shell/epoxy resin biocomposites by ultrasonic wave velocities," *Polymer Bulletin*, vol. 80, no. 5, pp. 5529–5552, 2023.
- [50] S. Awad, T. Hamouda, M. Midani, E. Katsou, and M. Fan, "Polylactic acid (pla) reinforced with date palm sheath fiber bio-composites: evaluation of fiber density, geometry, and content on the physical and mechanical properties," *Journal of Natural Fibers*, vol. 20, no. 1, p. 2143979, 2023.
- [51] T. Djoudi, H. Djemai, M. Hecini, and A. Ferhat, "Physical, thermal and mechanical characterization of a new material composite based on fibrous wood particles of date palm tree," *Revue des Composites et des Materiaux Avances*, vol. 32, no. 1, p. 45, 2022.
- [52] J. J. Kenned, K. Sankaranarayanan, J. Binoj, and S. K. Chelliah, "Thermo-mechanical and morphological characterization of needle punched non-woven banana fiber reinforced polymer composites," *Composites Science and Technology*, vol. 185, p. 107890, 2020.
- [53] I. Oral, H. Guzel, and G. Ahmetli, "Determining the mechanical properties of epoxy resin (dgeba) composites by ultrasonic velocity measurement," *Journal of Applied Polymer Science*, vol. 127, no. 3, pp. 1667–1675, 2013.
- [54] M. R. Khosravani, S. Rezaei, H. Ruan, and T. Reinicke, "Fracture behavior of anisotropic 3d-printed parts: Experiments and numerical simulations," *Journal of Materials Research and Technology*, vol. 19, pp. 1260–1270, 2022.
- [55] M. M. Nassar, K. I. Alzebeid, T. Pervez, N. Al-Hinai, A. Munam, F. Al-Jahwari, and I. Sider, "Polymer powder and pellets comparative performances as bio-based composites," *Iranian Polymer Journal*, vol. 30, pp. 269–283, 2021.
- [56] M. Asyraf, N. Nurazzi, M. Norrahim, K. Hazrati, A. Ghani, F. Sabaruddin, S. Lee, S. Shazleen, and M. Razman, "Thermal properties of oil palm lignocellulosic fibre reinforced polymer composites: a comprehensive review on thermogravimetry analysis," *Cellulose*, vol. 30, no. 5, pp. 2753–2790, 2023.



Review Article

Analysis of Mooc Data With Educational Data Mining: Systematic Literature Review

Rukiye Orman^{1a}, Nergiz Ercil Çağıltay^{1b}, Hasan Cakır^{1c}

¹Ankara Yıldırım Beyazıt University, Ankara, Türkiye

²Cankaya University, Ankara, Türkiye

³Gazi University, Ankara, Türkiye

rukiyeorman@aybu.edu.tr

DOI : 10.31202/ecjse.1581942

Received: 08.11.2024 Accepted: 07.04.2025

How to cite this article:

Rukiye Orman, Nergiz Ercil Çağıltay, Hasan Cakır, " Analysis of Mooc Data With Educational Data Mining: Systematic Literature Review", El-Cezeri Journal of Science and Engineering, Vol: 12, Iss: 2, (2025), pp.(191-204).

ORCID: "00000-0003-1385-0939"; "00000-0003-0875-9276"; " 00000-0002-4499-9712.

Abstract : Participants' performance is one of the critical factors for the success of the platforms. There is a lot of data in Massive Open Online Course platforms that are free and open to everyone, and due to this large amount of educational data, it is difficult to make accurate predictions and inferences. The primary purpose of this research is to conduct a literature review to discover the existing Educational Data Mining methods and techniques used to analyze Massive Open Online Course data. For this purpose, the focus is on the source from which the data is collected, which Educational Data Mining methods and techniques are used, and which tools are used in the analysis to compare different approaches. A total of 32 articles published between 2013-2024 were included in the scope of the study. According to the findings, there are many algorithms used for Educational Data Mining methods and techniques in the analysis of Massive Open Online Course data. The most preferred algorithm in the studies is "K-Means", followed by "Support Vector Machines", "Decision Trees" and "Random Forest". Coursera and Edx are among the platforms used and preferred worldwide. It is anticipated that making the data available on these platforms public will contribute to further research and guide studies in the education field. Privacy and ethics also come to the fore within the scope of open data publication. In this context, developing some standards and new approaches to share data with researchers in a standard form that does not include privacy violations will significantly contribute to studies conducted in this field.

Keywords : Educational Data Mining (EDM), Machine Learning Algorithms, Massive Open Online Courses (MOOCs).

1 Introduction

Information technologies impact every field, especially education, health, and banking. While economic, political, and health-related change factors bring about new problems, digital technologies and scientific changes help develop new ways to solve these problems. At this point, performing and concretizing data-based operations is essential to better understand the issues experienced and develop solutions. Massive Open Online Courses (MOOCs), which open a new page in education and enable the revision of open and distance education, have opened the doors to taking online courses from world-famous universities. As in university education, opportunities such as badges and certificates are also offered to those who complete the course by accessing all kinds of course resources, participating in exams through the portal, asking questions, receiving answers, and submitting homework. All behaviors of participants registered in these environments on the system are recorded, and data about the students increases daily. Long-term daily data can be used for student and course evaluation [1]. Providing training online and recording detailed data about students' behavior during the training process by the systems significantly contributes to a better understanding of these learning processes. MOOCs and micro-qualifications, which contribute to the digital transformation of education, redefine society's perspective on learning and the roles of institutions/organizations that provide education. The transfer of learning from school desks to lifelong learning brings a new system change in education, as well as time and space independence. This change aims to keep students up to date with technological and economic developments. Micro certificates come to the fore in determining the framework and validity of courses, and valid certificates have an essential place in the sector [2]. While MOOCs were offered free of charge and open to everyone in the early years, later on, as MOOC platforms became independent education companies, there was a need for paid courses to finance the courses and ensure the sustainability of the

platforms. For this reason, in addition to standard paid courses, the production of new content formats that provide financial resources, such as micro certificates and corporate training, has come to the fore. Universities prefer MOOCs because they provide instant data on students' participation in online courses and enable developers to stay up-to-date by developing their courses in line with this data [3]. At the same time, the data obtained from MOOC platforms contributes greatly to online learning research [4].

MOOCs, which contribute to lifelong learning, have attracted attention from many different segments, especially universities, due to the opportunities they offer, they also have disadvantages such as high dropout rates despite the high number of course enrollments, accreditation, high costs of preparation, technical problems, motivation of participants, and measurement and evaluation [5]–[7]. This situation causes the literature's perspective on MOOCs to be questioned again. Despite the high hardware, infrastructure, labor, and time costs, the number of participants who complete MOOCs and receive certificates is very low. Although thousands of participants enroll, the completion rate of most courses is below 13% [8]. In fact, the number of students who continue their courses after the first registration may be less than half [9], [10]. In fact, dropout rates have been a problem in online education even before the emergence of MOOC platforms. However, these two problems differ from each other. When a participant does not complete a course in online education, their self-confidence decreases, and they are discouraged from participating in different online courses. However, the dropout rate in MOOCs prepared with high costs means ineffective courses and cost loss for institutions. For this reason, research is being conducted to increase course completion rates and determine the reasons for dropout.

Studies conducted with data mining (DM) in educational environments are carried out using data collected from traditional classroom environments or online educational environments. [11]. It is more challenging to achieve learning outcomes in face-to-face education environments than in online education environments. For this reason, DM applications are carried out in a more limited way in face-to-face education environments. Educational Data Mining (EDM) applications, which have gained increasing momentum in recent years, mostly use data obtained from online education environments. Models are developed to understand the learning process by applying DM algorithms. These studies are essential in detecting students' interactions and mobility in online environments, modeling student profiles, and predicting their academic success [12]–[14]. EDM is a research area that focuses on applying DM, machine learning, and statistical methods to detect patterns in large-scale educational data. EDM utilizes e-learning platforms such as LMS, Intelligent Tutoring Systems (ITS), and, in recent years, Massive Open Online Courses (MOOCs) to obtain rich and versatile information from student learning interactions in educational environments [11], [15], [16]. These platforms record when and how often students access learning material, whether the answer to an exercise is correct, and how much time they spend reading a text or watching a video. With this recorded information, student performance can be determined, student profiles can be extracted, recommendations can be created, adaptive systems can be developed, and it can be analyzed to address different educational issues such as automatic grading of students' homework. Different EDM methods and techniques have been used to analyze this data. Thus, EDM has significantly influenced recent developments in education and has provided new opportunities for technologically developed learning systems according to the needs of students [17].

All participants' behaviors registered to MOOC are recorded on the system [18]. The instructor using this system can prepare and upload his content according to the system. When the data on these systems is analyzed using EDM methods and techniques, it guides educators and administrators in solving problems by creating participant profiles, personalizing the environment according to the participant, and improving the quality of the educational environment.

When the studies conducted with EDM in the literature are examined, it is seen that studies such as modeling participant/student performances and behaviors, examining participant/student academic success and attendance status, grouping according to participant/student characteristics, evaluation, feedback, pedagogical support, grouping according to participant/student characteristics are carried out [11], [12], [14], [15], [19]–[21]. Studies conducted in recent years focus on different sub-fields of EDMs. New ones were added to the eleven classifications made by Romero and Ventura in the field of EDM in 2010 [11]. With the added classifications, thirteen classification areas have emerged. Studies are being conducted on thirteen different sub-areas, including predicting student performance, detecting undesirable student behaviors, profiling and grouping students, social network analysis, providing reports, creating alerts for stakeholders, planning, and programming, creating course software, developing concept maps, creating recommendations, adaptive systems, evaluation, and scientific research [22].

In the literature, there are generally studies focusing on a single topic or area related to EDM in studies conducted with systematic literature reviews. These are studies using text mining techniques on student-MOOC interactions [23], using predictive video analytics [24], analyzing data obtained from environments such as Facebook and [25], identifying students who dropped out of school and students at risk [26], and measuring self-regulated learning strategies for students [27]. A systematic review was conducted. Studies in the literature on Educational Data Mining (EDM) often focus on a single subfield or a specific data mining method. For example, most studies focus on specific topics, such as student performance prediction or behavior detection, while a systematic review of a wide range of EDM applications is limited.

This study aims to fill an essential gap in the literature by providing a systematic perspective by focusing on the analysis

of Massive Open Online Courses (MOOC) data using Educational Data Mining (EDM) methods and techniques. In particular, unlike the studies focusing on a single EDM field or method in existing research on the analysis of MOOC data, this study provides a broad review covering different subfields of EDM and the methods used. In addition, it offers practical information on the data sources, tools, and techniques used to analyze MOOC data to study large data sets on MOOC platforms. It provides a guide for future research in this field. This study's following research questions were determined to investigate the EDM methods and techniques applied to profiling and grouping students, predicting student performance, identifying student behaviors, and evaluating classifications.

- 1) What are the studies classified according to Educational Data Mining subfields?
- 2) From what sources was MOOC data collected?
- 3) What are the Educational Data Mining methods and techniques used in analyzing data?
- 4) What are the tools used for analysis?

2 Materials And Methods

It is a systematic literature review investigating current approaches to classifying EDM methods and techniques for analyzing MOOC platform data. The Systematic Literature Review approach is used to obtain comprehensive results for analyzing and discussing different published articles [28]. It is an open and repeatable approach based on a search strategy structured according to the publications' predetermined inclusion and exclusion criteria. The results obtained from the articles are analyzed within the framework of the determined research questions. [29], [30]. The search strategy, inclusion and exclusion criteria, and the analyses of the obtained data are explained in the subsections below.

2.1 Design of the Study

The most widely used Web of Science and Education Resources Information Center (EBSCO ERIC) databases were searched to conduct a systematic review. These databases include articles that meet the quality standards of journals of famous publishers such as Elsevier, Springer, IEEE, ACM, etc. Accreditation institutions also prefer them because they meet quality standards [31].

Figure 1 shows the search and selection process used for systematic literature review. Our study used the Preferred Reporting Items for Systematic Reviews and Meta-Analyses (PRISMA) (Boers, 2018; PRISMA, 2020) flow chart, which is the most preferred method for systematic reviews and meta-analyses. A flow chart was used. This flow chart contributed to clearly reporting the work steps and the derivation of meaningful syntheses and conclusions.

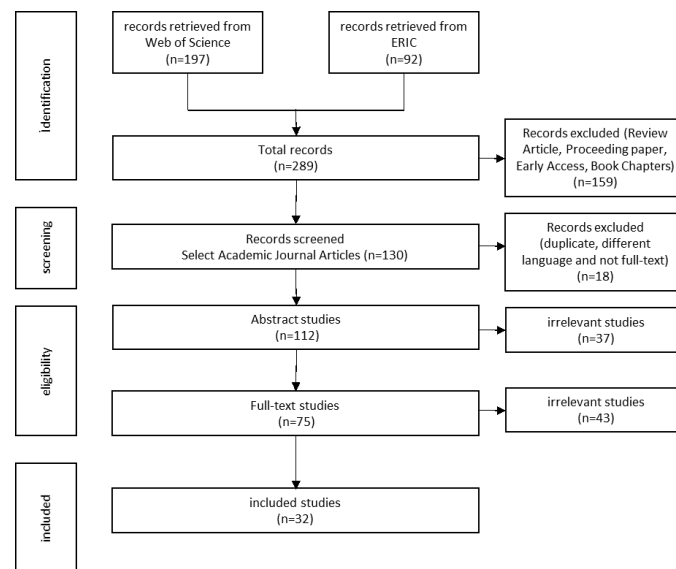


Figure 1: Systematic Search and Selection Process

2.1.1 Search String

First, the Web of Science (WOS) and EBSCO Eric databases followed an automatic search strategy. The search string was built around predefined keywords containing wildcards. The words in the search string were scanned in the title, abstract, and keywords.

Search string: TS= MOOC* AND EDU* AND (“data mining” OR datamining OR “data-mining”)

Indices: CPCI-S, SCI-EXPANDED, SSCI, CPCI-SSH, ESCI, A&HCI, BKCI-SSH.

2.1.2 Inclusion and Exclusion Criteria

The inclusion and exclusion criteria created to access relevant studies and prevent bias in selecting studies are in the table below. Studies were selected by considering general and specific criteria such as the type of study, year of publication, language, and whether it has a complete text and research method.

Table 1: Inclusion and Exclusion Criteria of the Study

Inclusion criteria:	Exclusion criteria:
1. Journal article	1. Literature review, book, book chapter, proceedings
2. Regarding the use of EDM methods in MOOCs	2. Studies outside the field of education
3. Published between 2013 and 2023	3. If the study is not relevant to the research questions
4. Published in English	
5. The full text of the article is available	

2.1.3 Search and Select

For the research to be suitable, it is essential to structure reliable, well-planned data sources and a search and selection strategy. Therefore, a comprehensive and systematic search was conducted to get a proper idea of its usage in the analysis of MOOCs. As a result of the database search, a total of 289 studies, 197 in WOS and 92 in ERIC were published between 2013-2024. A follow-up search was conducted in the databases to check if any new studies were published, and studies published until the first half of 2024 were included. After excluding the remaining articles, such as books, conference proceedings, systematic reviews, and duplicate studies, 130 articles were selected. Since WOS and ERIC index articles meet essential quality factors, this number of articles is anticipated to be suitable for a research pool. Due to the systematic review process, WOS and ERIC search results were included in this study's collection. At this stage, a direct abstract reading activity was performed to create the initial pool studies for filtering.

2.1.4 Summary Reading Activity

After the search and selection process, an abstract reading activity was completed for the remaining 130 articles. The following questions were prepared for the articles that would be excluded from the scope of the study. Exclusion of irrelevant articles is performed based on the following questions:

- Are there any areas of EDM implementation on MOOC platforms to be measured or reviewed?
- Are there any EDM methods used to measure or review?
- If there is a clear answer to either of these two questions, the article is kept; otherwise, the following question applies:
- Are there any EDM evaluation methods and techniques?
- As a final check, the article is excluded if there is no clear answer to this question.

After the summary reading activity, 37 articles that were not related to the field of education, did not contain MOOC data, did not conduct EDM analysis on MOOC data, and did not use any EDM methods and techniques were excluded. At the end of the summary reading activity, 75 articles were included in the study. Since EDM applications are a new application area in education, the number of articles is lower compared to other fields.

2.1.5 Full Reading and Filtering

Each step in this study was systematically addressed, and the first author recorded the process. The process was then comprehensively reviewed by the co-authors. The criteria were considered at each stage of the process. The selected articles (n=32) were read in full text, which required more intensive work than the other steps. In the full reading stage, the relevance of each study to the research questions and the EDM methods and techniques used in the studies was reviewed. Inclusion and exclusion criteria were also applied at this stage. All criteria ensured that the study was conducted according to its purpose.

2.1.6 Analysis of Studies

The studies were classified by focusing on the sub-areas of a) creating and grouping students' profiles, b) estimating student performance, c) determining student behaviors, and d) evaluating within the scope of applying EDM methods to MOOC data. The first research question was determined to identify the data sources in the reviewed articles. Then, the second research question was written to reveal the EDM methods and techniques used in each sub-area. Finally, analyses were conducted within the scope of the third research question in order to identify the tools used in the analyses.

3 Results and Discussion

Our study focused on four sub-areas of EVM in applying EVM methods and techniques to MOOC data. For this purpose, the findings obtained from the analyses were included, including articles published by year, a review of EVM sub-areas, a data

source review, an evaluation of EVM methods and techniques, and tools used to compare different approaches. Four research questions were created for this purpose. The findings obtained according to each research question were discussed in this section, and the results were summarized for stakeholders who could benefit from the study. The analyzed articles are in the table below based on their published years. When the time trends of the publications are examined, it is seen that there is a regular increase from 2014 to 2022, and the publications increase and reach their peak in 2022. Although the number of studies is low in the first years, it increases in the following years. 2022 is the year in which the most studies were conducted, with 20 articles. The year most studies were conducted was 2019, with 17 articles. No articles were published on the subject in 2013. This is because MOOCs are new, and the platforms on which they are published have become popular in the years following. In addition, the fact that the EDM field is new is another effective factor. It is seen that the studies conducted using both EDM and MOOC started to increase after 2017.

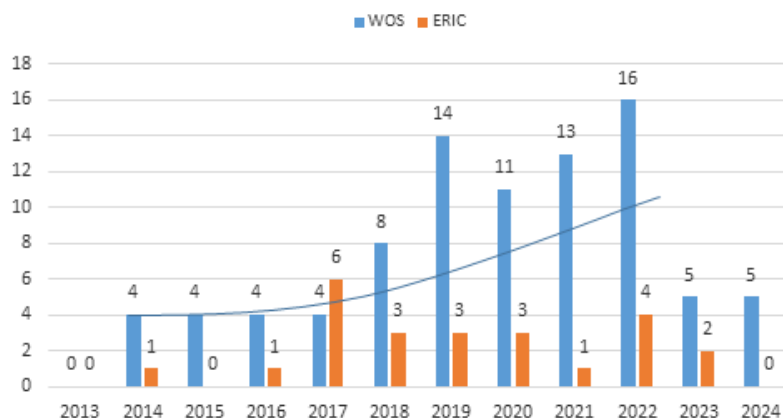


Figure 2: Distribution of publications by year between 2013-2024

When the first pool was created, many studies were conducted. However, when the studies conducted within the scope of education were focused on, the number of studies considered for analysis (n=32) decreased. However, reasons such as the pandemic affected the world in 2020 and later increased the interest in online education. Afterward, online environments gained popularity. Therefore, a large amount of data has been generated in environments such as MOOCs, and a need has arisen for new studies to be conducted in order to interpret this increasing data. It is seen that the studies have gained momentum with the increasing interest in areas such as data science, analytics, artificial intelligence, and machine learning. The number of studies is predicted to increase in the following years. Studies on the application of EVM methods and techniques to MOOC data provide important insights into various educational scenarios. However, the findings of these studies present both opportunities and important limitations in the digital transformation of education systems. Below, the findings from the literature are discussed in detail and in a controversial manner.

3.1 Review of Studies According to EDM Sub-Fields

The articles are examined within the scope of the four areas of EDM; 13 studies were conducted in predicting student performance, 9 in creating and grouping students’ profiles, 9 in determining student behaviors, and 1 in evaluation. The table below includes studies conducted within the scope of the four areas of EDM.

Table 2: EDM Sub-domains and Publications

EDM Subfields	Ref	Number	%
Predicting student performance	(Ahmed, 2024; Alghamdi, 2024; Ani & Khor, 2023; Lemay & Doleck, 2019, 2020; Liang et al., 2014; Monllaó Olivé et al., 2019; Onan, 2020; Pillutla et al., 2020; Swai & Mangowi, 2022; Tomkins & Getoor, 2019; Wan et al., 2019; Youssef et al., 2019)	13	41
Creating profiles and grouping students	(Cohen & Holstein, 2018; Dyulicheva, 2021; Lee, 2018; Li et al., 2022; Nilashi et al., 2022; Rizvi et al., 2019; Saqr et al., 2022; Tang et al., 2018; van den Beemt et al., 2018)	9	28
Determination of student behavior	(Assami et al., 2022; Benoit et al., 2024; Brinton et al., 2014; Geigle & Zhai, 2017; Gupta, 2019; RUIPÉREZ-VALIENTE et al., 2021; Xu et al., 2022; Yang et al., 2016; Zhong et al., 2017)	9	28
Evaluation	(Nie et al., 2020)	1	3

Predicting student performance in this sub-field of EDM, the main goal is to predict the student’s future performance based on their past activities. In the study conducted by Ani and Khor in 2023, machine learning models were used to predict student performance in MOOCs with the interaction of demographic information, academic background, and course materials. Data

were tested in eight supervised machine-learning algorithms (Linear Regression, Logistic Regression, Random Forest, K-nearest neighbors, Support Vector Regression, Linear Discriminant Analysis, Deep Learning, and Decision Trees). It was seen that the data collected from MOOC platforms can be used to predict student performance with over 77% accuracy, and the Random Forest classifier model offers higher accuracy than others in predicting student performance [32]. Students' video interactions, exams, forums, navigation, etc., developed a prediction model to predict students who are at risk of dropping out of the course, those who are likely to fail, and successful students using the data. It was seen that the Random Forest (RF) model provided more accurate predictions than other models, with an average accuracy of 98.6% [33]. In support of this study, a study using the interaction data of school teachers [34] and a model were developed in studies using student, MOOC, and learning activity characteristics [35]. In these models, it was concluded that the RF algorithm produced 96.4% and 95% accurate predictions compared to other algorithms.

In the study conducted in 2024, the K-Means algorithm from the clustering method was used to predict the final result of a student based on gender, region, entryresult, previousattemptnumber, studiedcredits, and disability using various prediction models, and the best prediction model, SVM (96% accuracy), was selected [36]. This study used the clustering method and prediction models to help predict performance. In the other study, classification methods were used to evaluate students' preferences accurately by taking into account the comments on the platform, and the method with the best performance, Support Vector Regression (SVR), produced better results than other algorithms with 80% accuracy [37]. Some studies use the Decision Tree algorithm to find factors that may affect students' participation and performance [38]–[42]. Studies also classify student interactions to determine which students work together and the type of collaboration used [40], [43].

Consequently, predicting student performance involves allowing early prediction and identification of slow student progress and implementing teaching methodologies based on predicted performance. The results of predictive models are essential because they allow instructors to identify low-risk students early and intervene in at-risk students promptly. Timely intervention can enhance the student's learning experience and increase the effectiveness and engagement of the learning process. It can also include providing feedback to the student focused on their progress. Predictive methods can help make accurate recommendations and suggest learning solutions based on many factors. When the above studies are examined, it is seen that DM has a high potential to be a valuable tool for discovering how people learn, predicting learning, and understanding actual learning behavior.

Students' profiles are created and grouped based on daily course data, video viewing, and exam data. This information is used to group students for various purposes. In a study by Li, Du, and Sun in 2022, students' final grades were investigated by statistical analysis, lag sequence analysis, and DM methods to investigate their learning engagement, time organization, content visit sequences, and activity participation patterns. Data were collected from a finance course on the MOOC platform called XuetangX in 2018 (n=535 students). Three groups of students were identified. These were unsuccessful, satisfactory, and excellent [44]. In another study conducted in 2020, a FutureLearn The Educational Process Mining method was used to analyze MOOC (n = 2,086 students). As a result of the analysis, three groups of students were identified and categorized according to the clickstream data. These are markers, partial markers, and non-markers [45]. Another study conducted in 2022 examined the strategies used by teacher candidates in an in-service teacher training MOOC while teaching a programming course. Unsupervised clustering and process mining were applied to analyze MOOC daily data (n=8,547). As a result of the analysis, three groups with different strategies were identified. These are efficient clickers and intermediates [46]. In another study conducted in 2018, clickstream, forum, and exam score data of students (n=607) enrolled in a MOOC on the Canvas Network platform were analyzed. Three groups with different longitudinal participation trajectories were identified using the clustering method from EDM techniques. These are cluster A-infrequent participants, cluster B-gradual dropouts, and cluster C-constant participants [47].

In the above studies, three participant groups were determined using the clustering method of EDM. Data were collected from a single MOOC located on different MOOC platforms in the studies. Only one of the studies included teacher data instead of student data. When teachers were evaluated in terms of learning strategies, it was seen that they were similar to other student groups. There were differences between all three groups determined in the studies in terms of both learning participation and learning patterns. In two of the four studies [45], [47] clickstream data was used rather than daily data. It is seen that the stored daily data does not have any meaning on its own. This is because clicking on the data does not necessarily mean a behavioral interaction, leaving aside cognitive processing or learning. Therefore, it becomes clear that using other data and clickstream data will be important in deriving meaningful results.

In a 2019 study, Lee applied self-organizing map (SOM) and hierarchical clustering algorithms to the log files of MIT's summer 2014 Newtonian mechanics (8.MReVx) physics MOOC to investigate how students solved their weekly homework and exam problems in order to identify clusters of students who exhibited similar problem-solving patterns. Data were collected from the Edx platform (n= 4,337 students). As a result of the hierarchical clustering analysis performed with SOM, four student groups were determined. These are cluster1: those who did not receive a certificate, cluster2: those who received and did not receive a certificate, cluster3: those who struggle, and cluster4: early starters [48]. It was seen that the findings obtained from this study cannot be generalized to MOOCs that emphasize different types of learning activities and pedagogies (social studies,

literature, etc.) where results cannot be obtained with the answer to a single question. As the number of clusters in SOM increases, the students assigned to each cluster become more homogeneous regarding problem-solving patterns. Hierarchical clustering without SOM could not determine the cluster of students who earned a course certificate. Combining SOM and hierarchical clustering algorithms allows a more leisurely exploration of complex, multi-dimensional diary data. In a study conducted in 2018, process mining techniques were applied to the video viewing behavior and exam submission process data of 16,224 students in a MOOC on Coursera. As a result of the analysis, four groups were determined. These are samplers, discriminators, initiators, and achievers. Process mining combined with traditional statistics applied from a personal constructivist perspective shows a fruitful approach to investigating learning behavior and learning processes in MOOCs. Data was collected from a MOOC in both studies, and four student groups were formed due to the analyses.

Cohen & Holstein, in 2018, 3,460 data from 5 different MOOCs from the CourseTalk website were analyzed using content analysis and DM and semantic analysis. The population of the analyzed courses included students from various and different countries. The aim was to reveal the features that contribute to the success of xMOOCs in science and management fields according to students' perceptions and to cluster students with similar preferences. In this study, instead of the commonly analyzed MOOC diary data, the focus was on student comments. As a result of the cluster analysis, five student groups were identified. These are social, no specific preference, cognitive, teaching-teacher, and teaching exam [49]. Although five student profiles were created in the study, the student profile is also related to various features such as previous knowledge, learning style, learning rhythm, etc. A study was conducted on positive student comments about successful courses, but it does not include the comments of all students who attended the courses. It seems that it would be essential to consider all student comments on successful and unsuccessful courses in order to provide a general perspective. In another study conducted in 2021, 38 math MOOCs on Udemy and 1,898 students' definitions of math anxiety were analyzed using text mining techniques (VADER sentiment analysis, k-means, BERT), and five groups were identified [50].

Short videos are the most potent learning objects in online courses and are highly preferred by all students. Badges and micro-credentials are also used in MOOCs. Using them together is anticipated to motivate the participants and encourage them to do the activities. Well-managed discussion forums can replace peer support in a physical classroom and give students a sense of participation. Although there is a significant and robust relationship between students' course completion status and their activity in the forums, it has also been observed that the group of students who did not complete the course actively participated in the forums.

In only one of the reviewed studies, six student groups were identified due to the analysis of MOOC data. The study conducted in 2022 classified different types of participant behavior in MOOCs into clusters using the DM methodology and based on video lectures, discussion forums, and assessment activities. Data were obtained from a MOOC on the Udemy platform. Se cluster analysis identified six participant groups [51]. Adaptive for Prediction Neuro-Fuzzy Inference Systems (ANFIS) were used.

As a result, nine studies were examined within the scope of the subfield of creating profiles and grouping students. Four studies determined three student groups, two that determined four student groups, two that determined five student groups, and 1 study that determined six student groups. The K-means method from cluster analysis was mainly used in the analyses. Determining student groups with the same characteristics can better adapt the course design to the needs and learning styles of the students. As seen in the studies examined, video lectures, discussion forums, and assessments are the primary learning resources in MOOCs. Therefore, analyzing a participant's activity in these components reflects their behavior in the course.

Detection of student behavior: Studies focusing on detecting student behaviors have faced three subtasks: predicting dropout on MOOC platforms, addressing the problem of students' engagement in their learning, and evaluating social functions. In the study by Geigle and Zhai in 2017, a two-layer hidden Markov model (2L-HMM) was used to discover student behavior patterns with click log data obtained from the MOOC platform. Although this study did not extract dropout behaviors, students' positive behaviors were extracted. It was observed that high-performing students tended to have longer [52]. In a different study similar to this study, which aimed to investigate and understand the learning processes and behaviors of students in MOOCs, EDM methodologies (K-means clustering, support vector machine, artificial neural networks) were used [53]. In support of this study, students' navigation traces were extracted to predict student motivation (Assami et al., 2022), and four supervised machine learning algorithms were used. In the study of dropout behavior in online courses, student behavior, perception [38], clickstream [54] and forum data [55] were widely used.

As a result, it can be concluded that most students can be divided into various groups according to their learning styles. Moreover, learning styles can be easily predicted according to the student's learning behaviors. It is seen that students with different learning styles behave differently in MOOCs. It also means that learning style can be a factor that determines the students' learning behaviors and even measures whether a student is suitable for learning through MOOCs. Understanding the behaviors and characteristics of the participants will allow the courses to be better adapted to the needs of different students and thus maximize the impact of MOOCs in providing lifelong learning on a large scale.

Evaluation: The proliferation of MOOCs emphasizes the need to develop accurate and valid evaluation methods to evaluate the quality and effectiveness of courses. A 2021 study by Nie, Luo & Sun proposed a MOOC evaluation (DME) method that combines the Analytical Hierarchy Process algorithm and text mining to integrate expert opinions, standardized rubrics, and

student feedback data into the evaluation process [56]. 30 MOOCs were selected from the Coursera website and evaluated using the DME method, and the results were compared with expert evaluation and student rating scores. The result supports the suitability of the DME method as a low-cost, advanced, and accurate method for MOOC evaluation.

3.2 Data Sources (Platforms)

The studies conducted within the scope of the four areas of EDM, the first of which is the research questions, are examined in terms of data sources and are shown in the table below.

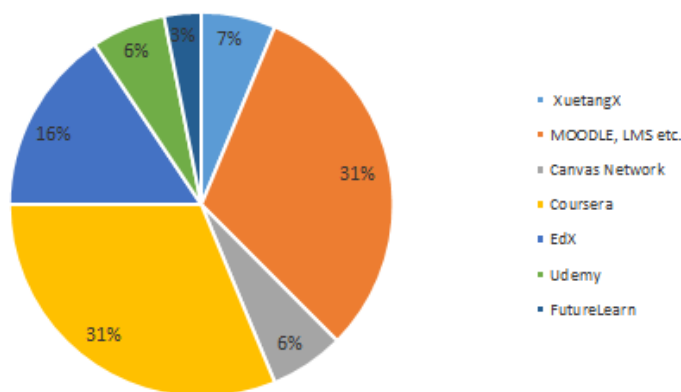


Figure 3: Data Sources

Determining the sources from which data is collected in the studies conducted will help researchers choose appropriate sources and platforms when collecting their data. Data sources in EDM can be online or offline. In the studies examined, data were generally collected from two sources: university courses and MOOC platforms. According to the findings, the most preferred platforms are LMSs such as Moodle (31%). The reason for this is that educational institutions can customize and use such platforms according to their own needs and that higher education institutions are preferred more in studies conducted for educational purposes. Coursera (31%) and EdX (16%) are the other most used platforms. In addition to Coursera and EdX, data was also collected from XuetangX (7%), Canvas Network (6%), Udemy (6%) and FutureLearn (3%) platforms. These platforms are among the platforms used and preferred worldwide. This is because these platforms are provided with MOOC support from universities worldwide, are accessible to a broad audience, and a large amount of data is stored on them. Another reason researchers prefer MOOCs is that they provide educators with a large amount of data that can be used to explain how students interact with the platform based on various factors.

As a result, it is anticipated that making the data available on these platforms public will contribute to further research and guide studies in the education field. Privacy and ethics come to the fore within the scope of open data publication. In this context, developing some standards and new approaches to sharing data with researchers in a standard form that does not include privacy violations will significantly contribute to the studies conducted in this field.

3.3 EDM Methods and Techniques Used

DM is divided into two predictive and descriptive methods. Descriptive methods are divided into classification and regression, predictive methods are divided into clustering and association rules. Algorithms used in the classification method: Decision trees, naive Bayes, k-nearest neighbors, artificial neural networks, support vector machines, time series analysis, and other methods. Linear and logistic regression algorithms are used in the regression method. Algorithms used in descriptive methods are clustering, association analysis, sequential sequence analysis, summarization, descriptive statistics, exception analysis, and other methods.

Massive Open Online Courses (MOOCs) generate a large amount of data that can be used based on various factors to predict and evaluate student performance. Among the machine learning tools used in the existing literature for similar purposes to predict student performance, discriminant analysis, support vector machines, naive Bayes, decision trees, K-nearest neighbors, random forest, linear and logistic regression, bayesian network and community methods [32]. Accuracy, precision, recall, and F-measure are the most commonly used evaluation metrics in MOOCs. Since the prediction models are based on a classifier, many evaluation metrics such as prediction accuracy measurements, confusion matrix, ROC curve, and Area Under the Curve (AUC) are used to measure the prediction quality to evaluate the classification model. Kappa, ROC, AUC, and F evaluation metrics were used in the studies. The primary purpose of presenting the evaluation metrics in the studies is to ensure that the

results that may occur by chance are not reported. The table below shows the features, methods, and accuracy rates used in the studies.

Table 3: EDM Methods Used and Accuracy Results

Method	Ref and Year	Attributes	Accuracy
Support Vector Machine (SVM)	(Ahmed, 2024)	Gender, Region, Entrance Result, Number of Previous Attempts, Studied Credits, Disability, Final result	96%
	(Brinton et al., 2014)	Forum activity data	86%
	(Tomkins & Getoor, 2019)	Forum, assignments, quizzes, and exams data	76%
	(Pillutla et al., 2020)	Discussion board data	79%
	(Alghamdi, 2024)	Comments on the platform	80%
Random Forest (RF)	(Youssef et al., 2019)	Video Interaction, Transcript Interaction, Quiz Interaction, Effort, personal information, Performance, Prerequisites, Forum, Navigation, Weekly Final Test, Supplementary Resources	98%
	(Swai & Mangowi, 2022)	Interaction data: FPF (the frequency of participation in the forum), FDS (the frequency of discussion teaching strategies), KPI (the knowledge level related to PI strategy), KTPS (the knowledge level related to TPS strategy), TSK (the general teaching strategy knowledge level of teacher)	96%
	(Assami et al., 2022)	Learner features, MOOC features, and learning activity features)	95%
	(Ani & Khor, 2023)	studentInfo , studentAssessment and studentVle	77%
Decision Tree (DT)	(Gupta, 2019)	Student Behavior (enrolled, viewed, discovered, certified, gender), Student Perception (number of activities, certified or not, active days, videos played, number of sections), and Student records (course ID, user ID, year of birth, gender, class, and forum post)	98%
	(Liang et al., 2014)	activity completion Reported data (online group meeting, question discussion, reference reading, wiki editing, exam taking, assignment uploading, courseware downloading, and watching videos), learning records, and feedback collected from students ' surveys	80%
	(Wan et al., 2019)	learning learning behaviors (total_duration, total_video_duration, total_courseware_access etc.) habits (avg_start_submission_time, time_first_visit, avg_time_between_problem_submission)	86%
	(Lemay & Doleck, 2020)	Video- Viewing Features	80%
	(Lemay & Doleck, 2019)	Video-Viewing Features (Videos Watched per Week, Avg Frac Spent watching, Total Number of Pauses, Avg Playback Rate, etc.)	70%
Artificial Neural Network (ANN)	(Zhong et al., 2017)	survey data and daily activity data	100%
	(Monllaó Olivé et al., 2019)	student registrations, users, courses	89%
Logistic Regression (LR)	(Xu et al., 2022)	Clickstream data (Access, Discussion, navigate, page_close, problem, video, wiki)	69%
	(Yang et al., 2016)	course content click behavior and course discussion forum data	80%
Naive Bayesian (NB)	(Onan, 2020)	Platform data	79%

When the features used in the studies are examined, the most preferred features are course and forum features, followed by student and exam features. Studies with activity and video diaries follow this. Assignments and word clouds are among the least preferred features in the studies. Analyses are usually performed using data sets belonging to more than one feature in the studies. In cases where high accuracy cannot be achieved using a single feature, analyses are supported using additional features. In addition to these, it is seen that data obtained from survey studies are also used in studies where statistical analysis is performed. There are a limited number of studies on assignments and word clouds. This situation reveals that not enough work has been done on these data sets and that it is essential to include studies in this area.

The clustering method, one of the descriptive models, has been used in studies to create and group students' profiles. Descriptive models allow the identification of patterns in existing data that will guide decision-making instead of prediction. The primary purpose is to find relationships, connections, and behaviors between the data in the data set. The two most commonly used algorithms in the clustering model are K-means and K-medoids.

The reviewed articles use various analysis techniques to analyze MOOC data, including algorithms, evaluations, tools, and statistical methods. Researchers decide which algorithm to use depending on the structure of the data set, the type of problem, and the requirements. Figure 3 shows the methods and techniques used in the studies. The most preferred algorithm in the studies is "K- Means ", followed by "Support Vector Machines", "Decision Trees" and "Random Forest". Then, "Artificial Neural Networks", "Logistic Regression" and " Naive Bayes " is coming. In addition to the Classification and Regression models from predictive models, the "K-means" algorithm used for clustering from descriptive models is included in the studies.

Table 4: EDM Methods Used and Num of Clusters

Method	Ref and Year	Attributes	Number of Clusters
Clustering	(Nilashi et al., 2022)	online reviews and ratings, survey responses	6
	(Ruipérez-Valiente et al., 2021)	Academic engagement (grades and submissions) and behavioral Engagement with the platform (general activity levels, interaction with videos, and Discussion forums).	3
	(Li et al., 2022)	learning engagement, time organization, content Visited sequences, and activity participation patterns	3
	(Cohen & Holstein, 2018)	teaching, social and cognitive, and technological data	5
	(Dyulicheva, 2021)	comments, reviews, social media profiles	5
	(Ahmed, 2024)	Gender, Region, Entrance Result, Number of Previous Attempts, Studied Credits, Disability, Final result	3
	(Saqr et al., 2022)	Daily data ((1) N lessons, (2) N successful lessons, (3) videos, (4) total views, (5) lesson evaluation, (6) interval, (7) duration, and (8) average lesson duration.)	3
	(Tang et al., 2018)	clickstream data, forum data, and Quiz scores	3
	(Benoit et al., 2024)	Activity data, namely, the Exercise ID, the start time and completion time of each exercise for each student, and subscription data, i.e., when the Subscription started and whether they canceled it.	2
	(Lee, 2018)	homework, problems, quizzes, midterm exams, final exam date	4
Process Mining	(van den Beemt et al., 2018)	video viewing and exam data	4
	(Rizvi et al., 2019)	Click behaviors	3

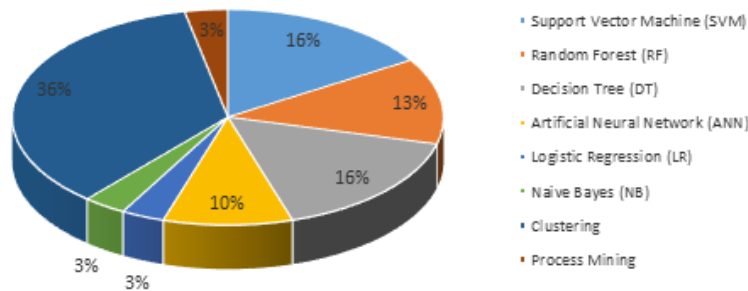


Figure 4: Distribution of Methods Used in Studies

Clustering algorithms have been used to support or direct predictive data. At the same time, statistical analyses used with DM methods are also found in the studies. These algorithms are basic algorithms used by researchers. K-means, Support Vector Machines, Decision Trees, and Random Forests were used the most in the examined studies. This is because more studies have been conducted in creating and grouping students’ profiles and predicting student performance/motivation than in other areas. In addition, Support Vector Machines (SVM) and Decision Trees (DT) are widely used algorithms in the prediction model.

In fact, it is not easy to draw a clear conclusion about which algorithm is used the most in the EDM field because this may vary depending on the data sets used and the requirements of specific projects. However, some studies and application examples show that algorithms such as support vector machines and decision trees are used more. These algorithms offer techniques to extract useful information from training data and improve training processes [57]. However, since each algorithm has its advantages, disadvantages, and suitable usage scenarios, which algorithm to use depends on the characteristics and purpose of the data set. These methods and techniques continue to develop today, and their impact on training is expected to increase.

3.4 Tools Used for Analysis

In most DM applications, Weka, Rapid Miner, and Knime tools provide minimum qualifications for analysis. Keel, Orange, Rapid Miner, and Weka are used in text mining analysis to analyze large amounts of data in video analysis. At the same time, researchers prefer Apache Spark and Apache Hadoop [58]. Among these tools, Rapid Miner and Knime provide an interface for data visualization, and Weka offers a command line interface [59], [60]. The Orange tool, written in Python, allows script writing. Similarly, Knime and Rapid Miner also offer the ability to write snippets in Java and Python. The tools mentioned generally work after installation, but the Keel software can work without an installation requirement. [61]–[63]. Table 6 includes the analysis tools used in the studies.

The studies examined show that essential tools such as Python, Weka, Rstudio, and Discovery are used for analysis. Google Collabs has also been used in a few articles published in recent years. In addition, the name of the tool used for analysis is

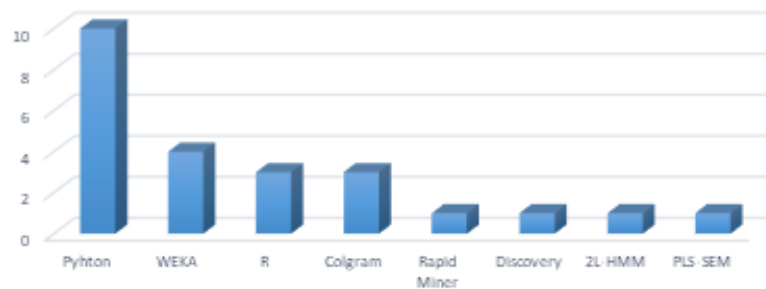


Figure 5: Analysis Tools

not specified in some of the articles examined. When selecting these tools, which have various features that support DM and machine learning processes, it is essential to consider factors such as the type of data to be used, the operating system, the budget, and user requirements.

The findings obtained from the studies can be used in the design of learning systems. These systems can be designed to produce detailed reports for participants, instructors, and administrators. It is envisaged that the reports can be used for participants to see their progress, for instructors to identify at-risk students, to take precautions and update their courses, and for administrators to develop data-based strategies.

4 Strengths and Limitations of the Study

Focusing on studies that apply EDM methods and techniques to MOOC data, the visualization of the findings obtained from data sources, tools used, methods, and techniques reveals the study's strength in providing an easy examination opportunity. Despite this, the study has some limitations. First, the study only examines publications in WOS and ERIC. Examining publications in different databases could have provided more data and awareness about this research. Second, the study only examines academic articles and assumes that they include reliable findings. However, examining various publications, such as announcements, books, book chapters, reports, etc., could have revealed different findings. Third, some sources were excluded because they did not contain sufficient information and did not meet the study's inclusion criteria. The findings of our study provide a general perspective to researchers who will apply EDM methods and techniques to MOOC data, as well as awareness of decision-making processes for educators and administrators.

5 Conclusions and Suggestions

Studies in the literature on Educational Data Mining (EDM) generally focus on a single subfield or a specific data mining method. While most studies focus on specific topics such as student performance prediction or behavior detection, a systematic review of a wide range of EDM applications is limited. Examining MOOC data in a broader context with multiple EDM techniques stands out as a topic that has not yet been fully addressed in the literature and is aimed at filling this gap. This study examines different subfields of EDM (student profiling, performance prediction, etc.) and various data mining methods used in these subfields together. In addition, the sources and tools used in the analysis of MOOC data were evaluated, and suggestions were presented regarding the missing aspects of the literature.

In the findings obtained, the majority of the studies in the literature focus on predicting student performance. For example, algorithms such as Random Forest (RF) and Support Vector Machines (SVM) have been found to be effective in predicting students' failure or success with high accuracy. Such prediction models allow instructors to intervene by identifying students at risk of low success early. In particular, the RF algorithm has attracted attention as one of the most effective prediction models in the literature with an accuracy rate of 98%. Early interventions on student motivation and learning strategies in education can reduce learning losses. Although these results seem positive, the accuracy of these models depends on the homogeneity of the data sets used and the complexity of the algorithms. The same success rate cannot be guaranteed for different demographic groups or students at different educational levels. In addition, incorrect predictions can reduce students' learning motivation and lead to ethical problems. EVM methods are widely used to understand and group students' learning behaviors. Methods such as K-means and Hierarchical Clustering classify student behaviors into three to six different categories. Studies have identified groups of students with different learning strategies. For example, groups such as "Achievers," "Demotivators," and "Insufficient" provide valuable information in understanding student profiles. Analyzing MOOC data in this way enables

personalization of course content and increased participation. However, dividing students into specific groups may ignore individual differences and may not adequately reflect the complexity of the learning process. In addition, the behaviors identified are often based on a limited data set, and the generalizability of these findings is limited. High dropout rates in MOOCs (completion rates below 13%) have been frequently emphasized in the literature. Lack of motivation, content difficulties, and time management problems are prominent reasons for students to drop out of their learning processes. Studies analyzing dropout rates aim to develop motivation-enhancing strategies by predicting students' tendency to leave the platform early. For example, data obtained from forum activities have been correlated with students' participation status. However, strategies aimed at reducing dropout rates may not always yield the expected results. For example, motivation-enhancing elements such as awards or badges are not always effective in the long run. In addition, the methods used to understand the reasons for dropout rates do not take into account students' offline factors (e.g. personal life conditions). EVM studies have focused on classification, clustering and regression models. Decision Trees, Support Vector Machines and Random Forest stand out among the most commonly used methods. Algorithms such as Support Vector Machines and Decision Trees provide effective results in terms of both accuracy and speed. These algorithms are seen as valuable tools in dealing with the wide range of MOOC data. However, the effectiveness of these algorithms depends on the quality and size of the dataset used. In addition, in some cases, the features used (e.g. demographic information) are seen to be ethically sensitive. In the literature, studies comparing the results of different algorithms are limited, which makes it difficult to choose the ideal method. Tools such as Python, Weka and RapidMiner are widely used in EDM analyses. Tools such as Python offer analytical flexibility thanks to their extensive libraries. In addition, cloud-based solutions such as Google Colab make the process of working with large data sets easier. Despite such advantages, the experience level of researchers is an important factor in the use of analysis tools. This may limit the reproducibility of analyses for less experienced researchers. The findings suggest that EVM is a powerful tool for analyzing MOOC data. However, given the limitations of these studies, issues such as generalizability of algorithms, ethical concerns, and applicability of personalized learning strategies remain controversial. Future studies should aim to fill these gaps with larger datasets and more comprehensive methods.

In the studies examined, data was generally collected from two sources: university courses and MOOC platforms. Coursera and Edx are among the platforms used and preferred worldwide. It is anticipated that making the data on these platforms publicly available will contribute to more research and guide the studies to be conducted in the field of education. Privacy and ethics come to the fore within the scope of open data publication. In this context, developing some standards and new approaches for sharing data with researchers in a standard form without privacy violations will significantly contribute to the studies conducted in this field. Stanford University has taken a step on the subject. Datastage: Lagunita, the Stanford example of the NovoEd, Coursera, and OpenEdX platforms, maintains learning research data from courses offered on all three platforms. Access to this data is available upon request. Although access to some data (such as student certification) is limited, making MOOC data publicly available is essential. We hope that researchers can conduct their work on publicly available data in the future. EDM studies and students' privacy should be considered, and appropriate measures should be taken to protect data confidentiality. EDM studies may pose ethical problems. In particular, ethical problems may arise in data collection, data analysis, and interpretation of results. Therefore, it is anticipated that ethical issues will need to be considered in future EDM studies.

In many of the studies examined, the analysis tool is not specified. Specification of the analysis tools is essential to provide ideas for future studies, and it is recommended that researchers pay attention to the analysis tools they use in their future studies.

MOOCs were initially offered free of charge and open to everyone, but later on, as MOOC platforms became independent educational companies, there was a need for paid courses to finance the courses and ensure the sustainability of the platforms. Therefore, in addition to standard paid courses, producing new content formats that provide financial resources, such as micro-certifications and corporate training, has become a current issue. No study was found in the reviewed studies comparing paid and free MOOCs. It is anticipated that it will be essential to include research on whether paid and free MOOCs impact student success, attendance, or certification in future studies.

Authors' Contributions

Rukiye ORMAN: Conceptualization, methodology, formal analysis, research, data curation, visualization, writing-original draft preparation, writing-review and editing; Nergiz Ercil CAGILTAY; supervision, project management, writing – original draft preparation, writing – review and editing; Hasan CAKIR; supervision, project management, writing – original draft preparation, writing – review and editing. All authors have read and accepted the published version of the manuscript.

Competing Interests

The authors have no competing interests to declare.

References

- [1] M. Liu and D. Yu, "Towards intelligent e-learning systems," *Education and Information Technologies*, vol. 28, no. 7, pp. 7845–7876, 2023.
- [2] R. Orman, E. Şimşek, and M. Kozak Çakır, "Micro-credentials and reflections on higher education," *Higher Education Evaluation and Development*, vol. 17, no. 2, pp. 96–112, 2023.

- [3] J. Goopio and C. Cheung, "The mooc dropout phenomenon and retention strategies," *Journal of Teaching in Travel & Tourism*, vol. 21, no. 2, pp. 177–197, 2020.
- [4] P. Diver and I. Martinez, "Moocs as a massive research laboratory: Opportunities and challenges," *Distance Education*, vol. 36, no. 1, pp. 5–25, 2015.
- [5] A. Bozkurt, "Bağlantıcı kitlesel açık çevrimiçi derslerde etkileşim örüntüleri ve öğrenen-öğreten rollerinin belirlenmesi," Ph.D. dissertation, Anadolu University (Turkey), 2015.
- [6] T. Jadin and M. Gaisch, "Extending the moocversity a multi-layered and diversified lens for mooc research," *Proceedings of the European MOOC Stakeholder Summit*, pp. 73–78., 2014.
- [7] K. Jordan, "Massive open online course completion rates revisited: Assessment, length and attrition," *The International Review of Research in Open and Distributed Learning*, vol. 16, no. 3, pp. 341–358., 2015.
- [8] B. Prenkaj, P. Velardi, G. Stilo, D. Distanto, and S. Faralli, "A survey of machine learning approaches for student dropout prediction in online courses," *ACM Computing Surveys*, vol. 53, no. 3, pp. 1–34, 2020.
- [9] N. Çağiltay, K. Çağiltay, and B. Çelik, "An analysis of course characteristics, learner characteristics, and certification rates in mixt moocs," *The International Review of Research in Open and Distributed Learning*, vol. 21, no. 3, pp. 121–139, 2020.
- [10] D. F. Onah, J. Sinclair, and R. Boyatt, "Dropout rates of massive open online courses: behavioural patterns," in *EDULEARN14 proceedings*, 2014, Conference Proceedings, pp. 5825–5834.
- [11] C. Romero and S. Ventura, "Educational data mining: A review of the state of the art," *IEEE Transactions on Systems, Man, and Cybernetics, Part C (Applications and Reviews)*, vol. 40, no. 6, pp. 601–618, 2010.
- [12] R. S. Baker and K. Yacef, "The state of educational data mining in 2009: A review and future visions," *JEDM Journal of Educational Data Mining*, vol. 1, no. 1, pp. 3–17, 2009.
- [13] L. N. M. Bezerra and M. T. Silva, "Educational data mining applied to a massive course," *International Journal Of Distance Education Technologies*, vol. 18, no. 4, pp. 17–30, 2020.
- [14] C. Romero and S. Ventura, "Educational data mining: A survey from 1995 to 2005," *Expert Systems with Applications*, vol. 33, no. 1, pp. 135–146, 2007.
- [15] A. Peña-Ayala, "Educational data mining: A survey and a data mining-based analysis of recent works. expert systems with applications," *Expert systems with applications*, vol. 41, no. 4, pp. 1432–1462, 2014.
- [16] C. Romero and S. Ventura, "Educational data mining: A survey from 1995 to 2005," *Expert Systems with Applications*, pp. 135–146, 2017.
- [17] K. Aulakh, R. K. Roul, and M. Kaushal, "E-learning enhancement through educational data mining with covid-19 outbreak period in backdrop: A review," *International journal of educational development*, vol. 101, p. 102814, 2023.
- [18] J. M. Gallego-Romero, C. Alario-Hoyos, I. Estévez-Ayres, and C. D. Kloos, "Analyzing learners' engagement and behavior in moocs on programming with the codeboard ide," *Etr&D-Educational Technology Research and Development*, vol. 68, no. 5, pp. 2505–2528, 2020.
- [19] N. Bousbia and I. Belamri, "Which contribution does edm provide to computer-based learning environments?" *Educational data mining: Applications and trends*, 2014.
- [20] A. Hicham, A. Jeghal, A. Sabri, and H. Tairi, "A survey on educational data mining [2014-2019]," *IEEE*, 2020.
- [21] R. A. Razak, M. Omar, and M. Ahmad, "A student performance prediction model using data mining technique," *International Journal of Engineering & Technology*, vol. 7, no. 2.15, pp. 61–63, 2018.
- [22] B. Bakhshinategh, O. R. Zaiane, S. ElAtia, and D. Ipperciel, "Educational data mining applications and tasks: A survey of the last 10 years," *Education and Information Technologies*, vol. 23, pp. 537–553, 2018.
- [23] S. Shatnawi, M. M. Gaber, and M. Cocea, "Text stream mining for massive open online courses: review and perspectives," *Systems Science & Control Engineering*, vol. 2, no. 1, pp. 664–676, 2014.
- [24] O. R. Yürüm, T. Taskaya-Temizel, and S. Yildirim, "Predictive video analytics in online courses: A systematic literature review," *Technology Knowledge And Learning*, 2023.
- [25] M. E. Buitrago-Ropero, M. S. Ramírez-Montoya, and A. C. Laverde, "Digital footprints (2005-2019): a systematic mapping of studies in education," *Interactive Learning Environments*, vol. 31, no. 2, pp. 876–889, 2023.
- [26] B. Albreiki, N. Zaki, and H. Alashwal, "A systematic literature review of student' performance prediction using machine learning techniques," *Education Sciences*, vol. 11, no. 9, 2021.
- [27] E. Araka, E. Maina, R. Gitonga, and R. Oboko, "Research trends in measurement and intervention tools for self-regulated learning for e-learning environments-systematic review (2008-2018)," *Research And Practice In Technology Enhanced Learning*, vol. 15, no. 1, 2020.
- [28] M. Bearman, C. D. Smith, A. Carbone, S. Slade, C. Baik, M. Hughes-Warrington, and D. L. Neumann, "Systematic review methodology in higher education," *Higher Education Research & Development*, vol. 31, no. 5, pp. 625–640, 2012.
- [29] B. N. Green, C. D. Johnson, and A. Adams, "Writing narrative literature reviews for peer-reviewed journals: secrets of the trade," *J Chiropr Med*, vol. 5, no. 3, pp. 101–17, 2006.
- [30] M. L. Pan, *Preparing literature reviews: Qualitative and quantitative approaches*. Taylor & Francis., 2016.
- [31] P. M. Moreno-Marcos, C. Alario-Hoyos, P. J. Muñoz-Merino, and C. D. Kloos, "Prediction in moocs: A review and future research directions," *IEEE Transactions on Learning Technologies*, vol. 12, no. 3, pp. 384–401, 2018.
- [32] A. Ani and E. T. Khor, "Development and evaluation of predictive models for predicting students performance in moocs," *Education and Information Technologies*, 2023.
- [33] M. Youssef, S. Mohammed, E. Hamada, and B. Wafaa, "A predictive approach based on efficient feature selection and learning algorithms competition: Case of learners dropout in moocs," *Education and Information Technologies*, vol. 24, no. 6, pp. 3591–3618, 2019.
- [34] C. T. Swai and S. E. Mangowi, "Mining school teachers' mooc training responses to infer their face-to-face teaching strategy preference," *The International Journal of Information and Learning Technology*, vol. 39, no. 1, pp. 82–94, 2022.
- [35] S. Assami, N. Daoudi, and R. Ajhoun, "Implementation of a machine learning-based mooc recommender system using learner motivation prediction," *International Journal of Engineering Pedagogy (iJEP)*, vol. 12, no. 5, pp. 68–85, 2022.
- [36] E. Ahmed, "Student performance prediction using machine learning algorithms," *Applied Computational Intelligence and Soft Computing*, vol. 1, p. 4067721, 2024.
- [37] A. Alghamdi, "Evaluating factors influencing learner satisfaction in massive open online course selection: A data-driven approach using machine learning," *Arabian Journal for Science and Engineering*, vol. 1, no. 26, 2024.
- [38] S. Gupta and A. Sabitha, "Deciphering the attributes of student retention in massive open online courses using data mining techniques," *Education and Information Technologies*, vol. 24, pp. 1973–1994, 2019.
- [39] D. J. Lemay and T. Doleck, "Grade prediction of weekly assignments in moocs: mining "video-viewing behavior," *Education and Information Technologies*, vol. 25, no. 2, pp. 1333–1342, 2019.
- [40] —, "Predicting completion of massive open online course (mooc) assignments from video viewing behavior," *Interactive Learning Environments*, vol. 30, no. 10, pp. 1782–1793, 2022.
- [41] D. Liang, J. Y. Jia, X. M. Wu, J. M. Miao, and A. H. Wang, "Analysis of learners' behaviors and learning outcomes in a massive open online course," *Knowledge Management & E-Learning-An International Journal*, vol. 6, no. 3, pp. 281–298, 2014.
- [42] H. Wan, K. Liu, Q. Yu, and X. Gao, "Pedagogical intervention practices: Improving learning engagement based on early prediction," *IEEE Transactions on Learning Technologies*, vol. 12, no. 2, pp. 278–289, 2019.

- [43] V. S. Pillutla, A. A. Tawfik, and P. J. Giabbanelli, "Detecting the depth and progression of learning in massive open online courses by mining discussion data," *Technology, Knowledge and Learning*, vol. 25, no. 4, pp. 881–898, 2020.
- [44] S. Li, J. Du, and J. Sun, "Unfolding the learning behaviour patterns of mooc learners with different levels of achievement," *International Journal of Educational Technology in Higher Education*, vol. 19, no. 1, 2022.
- [45] S. Rizvi, B. Rienties, J. Rogaten, and R. F. Kizilcec, "Investigating variation in learning processes in a futurelearn mooc," *Journal of Computing in Higher Education*, vol. 32, no. 1, pp. 162–181, 2019.
- [46] M. Saqr, V. Tuominen, T. Valtonen, E. Sointu, S. Väisänen, and L. Hirsto, "Teachers learning profiles in learning programming: The big picture!" *Frontiers in Education*, vol. 7, 2022.
- [47] H. Tang, W. Xing, and B. Pei, "Exploring the temporal dimension of forum participation in moocs," *Distance Education*, vol. 39, no. 3, pp. 353–372, 2018.
- [48] Y. Lee, "Using self-organizing map and clustering to investigate problem-solving patterns in the massive open online course: An exploratory study," *Journal of Educational Computing Research*, vol. 57, no. 2, pp. 471–490, 2018.
- [49] A. Cohen and S. Holstein, "Analysing successful massive open online courses using the community of inquiry model as perceived by students," *Journal Of Computer Assisted Learning*, vol. 34, no. 5, pp. 544–556, 2018.
- [50] Y. Dyulicheva, "Learning analytics in moocs as an instrument for measuring math anxiety," *Voprosy Obrazovaniya / Educational Studies Moscow*, no. 4, pp. 243–265, 2021.
- [51] M. Nilashi, R. A. Abumalloh, M. Zibarzani, S. Samad, W. A. Zogaan, M. Y. Ismail, S. Mohd, and N. A. M. Akib, "What factors influence students satisfaction in massive open online courses? findings from user-generated content using educational data mining," *Education and Information Technologies*, vol. 27, no. 7, pp. 9401–9435, 2022.
- [52] C. Geigle and C. Zhai, "Modeling mooc student behavior with two-layer hidden markov models," *Journal of Educational Data Mining*, vol. 9, no. 1, pp. 1–24, 2017.
- [53] S.-H. Zhong, Y. Li, Y. Liu, and Z. Wang, "A computational investigation of learning behaviors in moocs," *Computer Applications in Engineering Education*, vol. 25, no. 5, pp. 693–705, 2017.
- [54] C. Xu, G. Zhu, J. Ye, and J. Shu, "Educational data mining: Dropout prediction in xuetangx moocs," *Neural Processing Letters*, vol. 54, no. 4, pp. 2885–2900, 2022.
- [55] D. Yang, R. E. Kraut, and C. P. Rose, "Exploring the effect of student confusion in massive open online courses," *Journal of Educational Data Mining*, vol. 8, no. 1, pp. 52–83, 2016.
- [56] Y. Nie, H. Luo, and D. Sun, "Design and validation of a diagnostic mooc evaluation method combining ahp and text mining algorithms," *Interactive Learning Environments*, vol. 29, no. 2, pp. 315–328, 2020.
- [57] S. Batoool, J. Rashid, M. W. Nisar, J. Kim, H. Y. Kwon, and A. Hussain, "Educational data mining to predict students' academic performance: A survey study," *Education and Information Technologies*, vol. 28, no. 1, pp. 905–971, 2023.
- [58] M. M. George and P. S. Rasmi, "Performance comparison of apache hadoop and apache spark for covid-19 data sets." pp. 1659–1665, 2022, January 2022.
- [59] D. M. Dener, Murat and A. Orman, "Açık kaynak kodlu veri madenciliği programları: Weka'da örnek uygulama," *Akademik Bilişim*, vol. 9, pp. 11–13, 2009.
- [60] WEKA, 2024. [Online]. Available: <http://www.cs.waikato.ac.nz/ml/weka/>
- [61] A.-F. J., S. L., G. S., del Jesus M. J., V. S., G. J. M., O. J., R. C., B. J., R. V. M., F. J. C., and H. F., "Keel: A software tool to assess evolutionary algorithms to data min-ing problems," *Soft Computing*, vol. 13, no. 3, pp. 307–318, 2009.
- [62] ORANGE, 2024. [Online]. Available: <http://orange.biolab.si/>, (Erişim Tarihi: 2024).
- [63] R, 2024. [Online]. Available: <http://www.r-project.org/>

Research Paper

Artificial Intelligence Assisted Solar Energy Forecasting by Explainability Approaches with LIME and SHAP

Ali Öter^{1a}, Betül Ersöz^{2b}¹Kahramanmaraş Sütçü İmam University Department of Electronics and Automation, 46030 Kahramanmaraş, Türkiye²Gazi University, Department of Computer and Instructional Technologies Education, 06500 Ankara, Türkiye

alioter@ksu.edu.tr

DOI : 10.31202/ecjse.1591721

Received: 04.12.2024 Accepted: 07.03.2025

How to cite this article:

Ali Öter, Betül Ersöz, "Artificial Intelligence Assisted Solar Energy Forecasting by Explainability Approaches with LIME and SHAP", El-Cezeri Journal of Science and Engineering, Vol: 12, Iss: 2, (2025), pp.(205-212).

ORCID: ^a 0000-0002-9546-0602; ^b0000-0001-6221-1530.

Abstract: Integrating renewable energy sources with new technologies such as artificial intelligence (AI) is important to balance energy supply and demand. The predictability of variable energy sources, such as solar energy, plays an important role in maintaining the stability and efficiency of power grids. This study examines the use of various algorithms in AI applications within renewable energy systems. The study critically evaluates existing methods and proposes an innovative approach for AI prediction in solar energy systems using advanced machine learning techniques. It focuses on the effectiveness of MLP, Ridge, and RF algorithms in forecasting Direct Current (DC). The results showed that the RF algorithm achieved the highest R² value (0.9999) and the lowest error RMSE (0.0024) and MAE (0.0006) measurements to demonstrate the superior ability of the models to explain variance in the data and make accurate predictions. In addition, the model developed with SHAP and LIME explainable AI algorithms is interpreted.

Keywords: Solar energy, Machine learning, Explainable AI, SHAP, LIME, Renewable energy.

1. Introduction

In recent years, there have been many studies on the increasing use of artificial intelligence (AI) methods, namely Deep learning (DL) and machine learning (ML) techniques in the field of solar energy forecasting. These studies address the challenges faced in grid management due to the variable nature of solar energy and utilize AI methods to improve forecasting accuracy. The studies compared deep learning and machine learning models to predict photovoltaic power generation. This study shows that models such as MLP, RNN, and CNN are compelling in accurately predicting power generation levels [1]. Another study examined the use of Deep Learning techniques for solar energy forecasting, namely Recurrent Neural Networks (RNN), Long Short-Term Memory (LSTM), and Gated Recurrent Units (GRU). It reveals that RNN and LSTM perform slightly better than GRU, thanks to their capacity to maintain long-term dependencies in time series data [2]. Similar AI techniques, ANN and Adaptive Neuro-Fuzzy Inference System (ANFIS) for predicting PV energy production, environmental parameters such as solar temperature, radiation, and humidity were analyzed to predict energy production [3]. The study used various ML and DL models, such as Artificial Neural Networks (ANN), Support Vector Machines (SVM), and XGBoost, to predict photovoltaic power generation; the ANN model had the highest accuracy compared to other models [4].

The other study used a hybrid Adaptive Neural Fuzzy Inference System (ANFIS) model to predict global solar radiation. ANFIS models provided more accurate predictions with lower error rates than traditional forecasting models [5]. In another study, solar energy production was estimated using environmental data. Meteorological factors such as temperature, humidity, and wind speed were considered. It strongly confirmed the impact of weather data on solar power generation [6]. In the other study, he examined different regression models for predicting Photovoltaic (PV) power generation. He compared machine learning models like Random Forest, Ridge, and Artificial Neural Networks. ANN showed the best performance in terms of accuracy [7]. ANFIS model was applied to estimate global solar radiation in Nigeria. The study found that despite poor data quality, the model provided accurate results and outperformed conventional methods [8]. In a previous study [9], the ensemble learning model achieved the highest R² value (0.942) and the lowest error metrics MAE (0.040).

In this study, AI-based forecasting is performed for solar power generation. The forecasting is performed using MLP, RF, and Ridge regression algorithms. The accuracy of the models is evaluated using different parameters. Moreover, they were analyzed using Explainable Artificial Intelligence (XAI) techniques such as SHAP and LIME to improve the explainability of the model decisions. In this way, the factors on which the models make predictions are interpreted in detail, and the results are made more visible.

2. Material and Methods Method

2.1. DataSet

The dataset contains comprehensive information on solar power generation and environmental conditions. The dataset is available at <https://www.kaggle.com/datasets/pythonafroz/solar-power>. It consists of 136,472 observations and 12 variables. The dataset is divided into 80% training and 20% testing. To evaluate the performance of solar energy systems, a prediction model was developed using the variables DC_POWER, AC_POWER, DAILY_YIELD, TOTAL_YIELD, AMBIENT_TEMPERATURE, MODULE_TEMPERATURE. These parameters were selected based on their critical role in the solar power generation process. AMBIENT_TEMPERATURE: The ambient temperature around the solar panels is an important factor affecting their efficiency. MODULE_TEMPERATURE: The solar panels' surface temperature determines the cells' operating temperature, which directly affects energy efficiency. IRADIATION: Solar radiation represents the amount of solar energy received by the panels and is an important input for electricity generation. As solar radiation increases, the electrical power generated generally increases.

2.2. Multilayer Perceptron

MLP is a type of ANN that can process data organized in layers. The work presented by Rumelhart et al. in 1986 popularized this method by detailing MLP learning with a backpropagation algorithm [10]. ANN are structures inspired by the functioning of nerve cells in the human brain and information processing technology. These neural networks are an important artificial intelligence component, especially machine learning. They are used to model complex relationships between input and output values. A neural network contains interconnected units organized in layers. These units are called neurons. Each neuron receives input signals, processes these signals through an activation function, and produces an output signal transmitted to other neurons in the network. MLPs often perform strongly on nonlinear problems because they can perform nonlinear mappings with the help of hidden layers. Moreover, thanks to integrating various optimization algorithms and regularization techniques, modern MLPs can be successfully used on high-dimensional and complex datasets [11, 12]. The basic structure of a neural network is the neuron (Figure 1); the input variables (x_i) are connected to the neuron through weighted connections (w_i) that mimic dendrites, while the sum (Σ), bias (b), and activation function (h) play the role of the cell body. The propagation of the output is similar to the axon in a biological neuron. The behavior of the neural network is defined by the shape of the connections of its neurons or nodes and the weight values of these connections. These weights are automatically adjusted during training according to a learning algorithm until the network correctly performs the desired task [13].

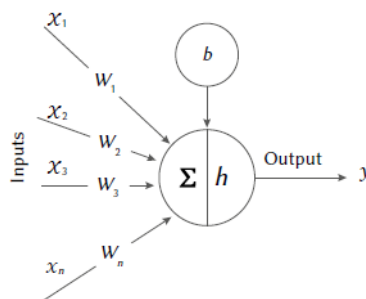


Figure 1. Neuron Model [13]

The weighted sum of the weights of a neuron input is called activation. Therefore, for neuron j of layer a^{ll} , activation is given as follows:

$$a_j^l == \sum_{k=0}^{n_i-1} w_j^l x_i^{l-1} \quad (1)$$

The purpose of the MLP structure can be defined as learning the fundamental relationship between the input data and output variables in the training set and making accurate predictions. For training the MLP, the desired output values are determined for the desired input values. The MLP output is calculated for the desired input values. The difference between the desired output and the calculated output is used to update the weights of the MLP using the backpropagation algorithm. This process is called training or optimizing the MLP. Updating the weights is continued until the desired success value is achieved.

2.3. Random Forests

RF is a machine learning technique that combines multiple decision trees to create a more robust and generalizable model. The data set is randomly partitioned into small pieces to form decision trees. Overfitting is a major challenge in machine learning. RF method uses randomization with bootstrap sampling and random feature selection. The RF model is a machine-learning method that can be used for both classification and regression problems. In the forecasting stage, the forecasts of the decision trees formed from the data set are averaged. The reason for using the Random Forest Regression model in this study is that it largely avoids the problem of overfitting the historical data used during training; the data type is time series and is a method that gives successful results [14-16].

$$y = \text{mod}(y_1, y_2, \dots, y_m) \quad (2)$$

where y is the final predicted value, and m is the total number of trees in the forest.

2.4. Ridge

Ridge among the basic hyperparameters of regression is alpha (the regularization parameter). This parameter controls how much the model will adjust. The larger the Alpha value, the higher the amount of adjustment. There are also hyperparameters `fit_intercept`, which determines whether to add bias to the prediction; `normalize`, which sets True or False to scale the data; and `solver`, which is the algorithm that determines how the model is solved [16, 17].

2.5. Explainable AI

SHAP, one of the most widely used XAI techniques, is based on game theory and aims to fairly distribute the contribution of each feature to the model's output. It offers new approximation methods based on improved computational performance and predictions that show better consistency with human intuition. It has been shown that machine learning and deep learning models make decision-making processes transparent and make it easier for users to understand model insights. It ensures that descriptions are consistent and provide a singular importance value for each attribute. LIME is another well-known XAI technique [18]. The LIME method interprets individual model predictions based on estimating the model locally around a given prediction. As a result, for a fair comparison, we chose MLP, RF, and Ridge regression for explainability using SHAP and LIME explainers [19-21].

2.6. Performance Metrics

Using metrics to assess model performance allows us to understand and improve the predictive power of a model before deploying it for production on new data.

Mean Absolute Error (MAE): Predicting a numerical value in order to assess and report on the performance of a predictive regression model, the mean absolute error (MAE) is a frequently used error measure. MAE calculates the deviation between the predicted and actual values of a model. It evaluates how well a model generalizes and

how well its predictions match the actual values. This study used MAE to find the closest predictive modeling to our experimental results, see the deviations from the experimental values, and capture the relationships between the dependent and independent variables [22].

$$MAE = \frac{1}{n} \sum_{i=1}^n |Y_i - Y_{mean}| \quad (3)$$

n number of data values, Y_i data values in the set, Y_{mean} the mean value of the data set

R-Squared (R^2): It measures the proportion of variation in the dependent variable explained by the model's independent variables. It is calculated by squaring the Correlation Coefficient. R-squared does not account for overfitting. A regression model with too many independent variables may fit the training data well but not the test data. It is why adjusted R-squared is used. Adjusted R-squared addresses the problem of overfitting. It takes into account additional independent variables added to the model. The R-squared value, which expresses the relationship between actual and predicted values, varies between 0 and 1. The closer the R^2 value is to 1, the more the model is more successful [23-25].

$$R^2 = 1 - \frac{\sum_i^N (Y - Y_i)^2}{\sum_i^N (Y_{mean} - Y_i)^2} \quad (4)$$

where N is the number of data points, Y_i data values in the set, Y_{pred} is the predicted values, and Y_{mean} is the mean value.

Mean Squared Error (MSE): provides an absolute number that shows how much your predicted results differ from the actual number. It gives a real number to compare with other model results and helps to choose the best regression model [22, 26].

$$MSE = \frac{1}{N} \sum_i^N (Y_i - Y_{pred})^2 \quad (5)$$

N is the number of data Y_i data values in the set, and Y_{pred} is the predicted values.

3. Results

The repeatability of the models used in the study conducted with AI is critical. The study determined the best parameters in Table 1 by selecting cross-validation k-fold = 5. The parameters used in training are given in detail in Table 1.

Table 1. Hyperparameters

Models	Parameters	Best parameters
RF	n_estimators: [100, 200, 300], max_depth: [None, 5, 10, 15], min_samples_split: [2, 5, 10], min_samples_leaf: [1, 2, 4], max_features: [auto, sqrt, log2]	n_estimators=300, max_depth=None, max_features=sqrt, min_samples_leaf=1, min_samples_split=2, random_state=42
MLP	hidden_layer_size: [(50,), (100,), (50, 50), (100, 50), (100, 100)], activation: [tanh, relu], solver: [adam, sgd], alpha: [0.0001, 0.001, 0.01], learning_rate: [constant, adaptive]	activation=relu, alpha=0.001, hidden_layer_sizes=(100, 50), learning_rate=constant, solver=adam, max_iter=1000, random_state=42
Ridge	alpha: [0.1, 1.0, 10.0, 100.0, 1000.0]	alpha=0.1

The results compare the performance of different models with AI and machine learning methods for solar energy forecasting. MAE, RMSE, and R^2 metrics help us understand each model's accuracy and error level. According to the analysis results in Table 2, MLP: MAE = 0.0187, RMSE = 0.0479, R^2 = 0.9541. The MLP model performs quite well with relatively low error rates (MAE and RMSE). The R^2 value = 0.9541 indicates that the model explains the

data well and accurately predicts. However, the error values of the MLP remain slightly higher than the other models. RF: MAE = 0.0006, RMSE = 0.0024, R² = 0.9999. The RF model shows the best performance. With the lowest MAE and RMSE values, this model minimizes the bias in its predictions. The R² value of 0.995504 indicates that the model provides almost perfect accuracy, and its predictions are very accurate. Ridge Regression: MAE = 0.0824, RMSE = 0.1182, R² = 0.7204. The Ridge regression model has higher error rates compared to the other models. Since MAE and RMSE values are higher, the predictions of this model are considered less accurate. Although the R² value is also lower than the other models, it performs well with 0.959601. Overall, the RF model outperforms the other two models by having the lowest values in terms of error rates and achieving the highest R² value. The MLP provides better results than the Ridge regression but is slightly inferior to the RF. The Ridge regression model has the lowest performance among the three models.

Table 2. Model Performances

Models	MAE	RMSE	R ²
MLP	0.0187	0.0479	0.9541
RF	0.0006	0.0024	0.9999
Ridge	0.0824	0.1182	0.7204

Comparing the three models, MLP Model: The MAE and RMSE values are moderate, indicating that the model's errors are relatively balanced. The RMSE value is higher than the MAE, meaning the model penalizes significant errors more. Ridge Regression: This model has the highest MAE and RMSE, making more errors than the other models. Ridge regression usually performs well with high linear dependencies, but it was not as effective in this case as the other models. RF Model: The model with the lowest MAE and RMSE values, which means it performs the best. Random Forest is generally known to be a model that balances the margins of error well, so the errors are minor than in other models.

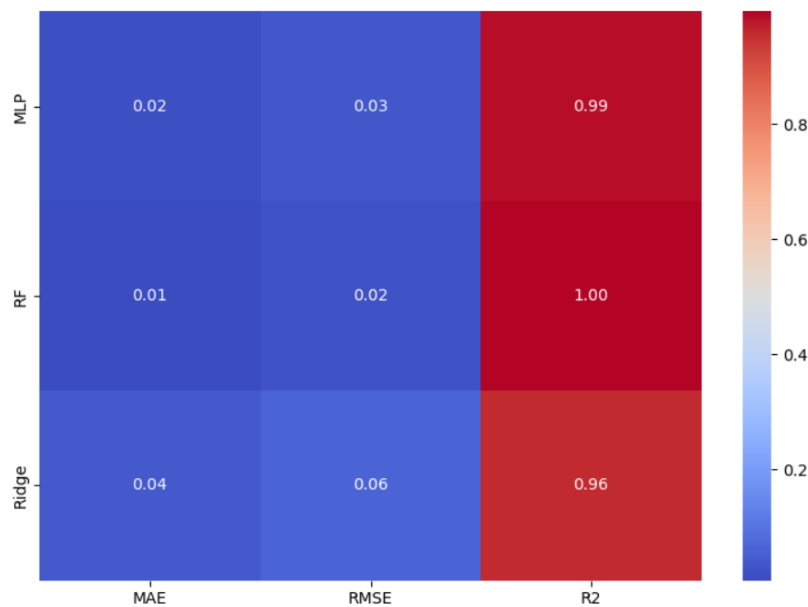


Figure 2. Performance Metrics

In the heatmap graph shown in Figure 2, the Random Forest (RF) model performed the best, while Ridge Regression performed the worst. The MLP model performed moderately well. These results show that RF is superior in accuracy and minimizes error rates. In addition, the model performances of the study were interpreted with XAI. The visualization of the RF model with LIME shows the prediction output and the importance of the relevant features in Figure 3. On the left side, a horizontal bar graph shows the predicted value ranging from -0.00 to 0.70. The predicted value of 0.03 on the bar indicates that the model's prediction lies between these minimum and maximum limits and is a production. In the middle section, the effects of the features on the forecast are divided into "positive" and "negative." IRRADIATION MODULE_TEMPERATURE shows a positive impact on the

model. The values of the variables the model uses as inputs are shown on the right side. TOTAL_YIELD 0.54, IRRADIATION 0.77, MODULE_TEMPERATURE 0.65, AC_POWER 0.29, AMBIENT_TEMPERATURE 0.56, DAILY_YIELD 0.17. DC_POWER is 0.03, indicating that energy is generated.

Solar irradiation and module temperature have the most significant impacts on model predictions. These features are the most important inputs in energy production prediction models. The negative impact of Total Yield suggests that historical production data may sometimes limit the prediction. In the future, the effects of this feature in different scenarios can be analyzed in detail. LIME outputs have effectively explained which features the model predicts and the relationships between these features, which have helped us better understand the prediction process.

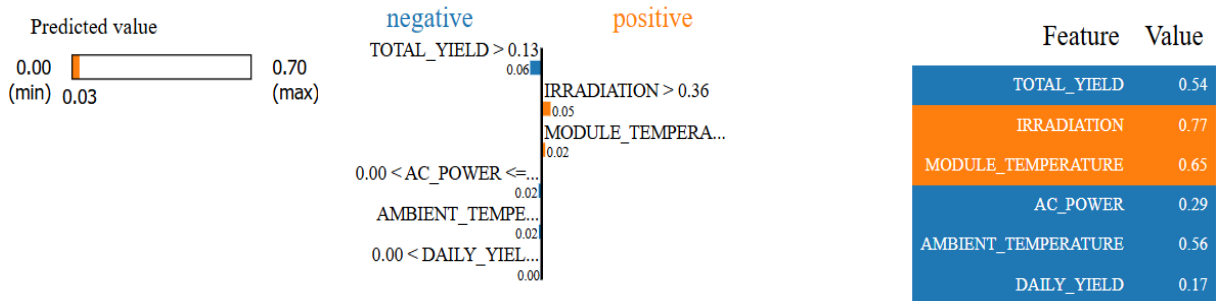


Figure 3. Demonstration of instantaneous energy generation using the LIME Model by a single instance

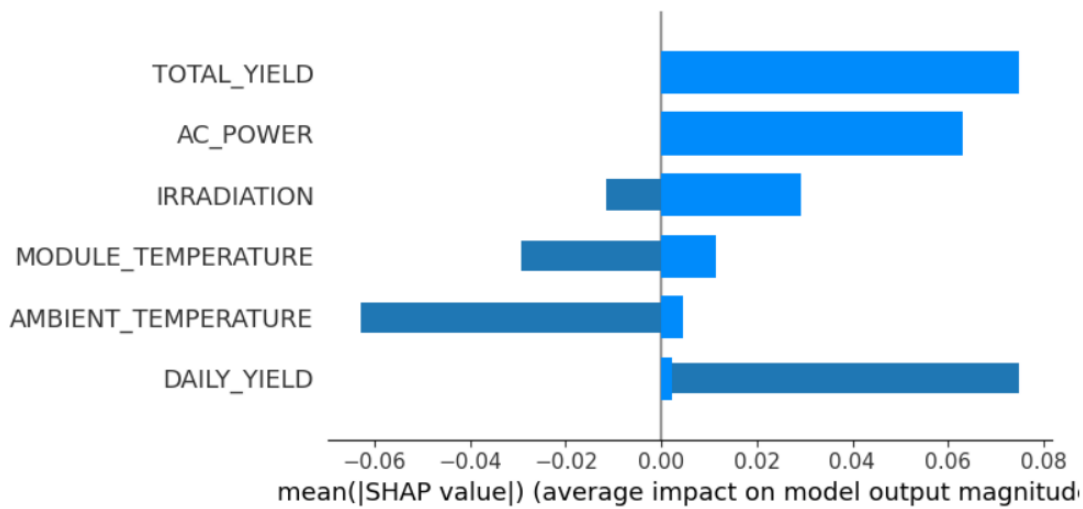


Figure 4. SHAP shows the global feature importance of the RF

As shown in Figure 4, SHAP was used to evaluate the performance of solar PV systems with XAI. In Figure 4, the horizontal axis shows the magnitude of the average effect of each input in the data set used on the model output. DAILY_YIELD and AC_POWER inputs stand out as having the highest impact. It is also observed that both of these two inputs make positive contributions. TOTAL_YIELD has a moderate impact. AMBIENT_TEMP, MODULE_TEMP, and DC_POWER are ranked with smaller effect sizes but are still significant in model performance.

4. Discussion and Conclusion

The predictability of solar electricity is critical for the balanced operation and efficiency of electricity grids. In this study, we focus on the role of AI algorithms in energy forecasting and optimization. In particular, the performance of algorithms such as MLP, Ridge Regression, and RF in Direct Current (DC) forecasting is compared. The study's findings show that the RF algorithm performs superior energy prediction, achieving high accuracy with

an R^2 value of 0.9999 and the lowest error rates (RMSE: 0.0024, MAE: 0.0006). These results show that the RF algorithm can better model complex and variable energy data. While the performance of other models, such as MLP and Ridge Regression, is also noteworthy, the predictability of RF and its ability to explain the variance in the data provide a more suitable alternative for solar energy forecasting. However, each algorithm has different advantages and disadvantages based on data structure, training time, and computational cost. Therefore, each model needs to be tailored to specific application areas. In addition, the LIME and SHAP methods are used in this study to provide the proposed model with a more transparent and comprehensible explanation, thus making the forecast results more transparent and understandable. It increases the credibility of energy managers and policymakers in decision-making processes based on forecast results. In conclusion, this research presents an innovative approach based on explainable AI methods that can provide more accurate forecasts for solar energy systems. Going forward, combining different AI algorithms with hybrid models may further improve the forecast performance.

Although the RF algorithm has proven to be a powerful tool in combination with explainable artificial intelligence approaches, evaluating the model's performance on different datasets and improving its adaptability to real-world applications is an important research area for future work. SHAP and LIME analyses are used to explain the decision mechanisms of the model. In addition to feature importance levels, interactions between features are also examined and inferences are made in the context of solar energy forecasting. These analyses contribute to a better understanding of solar energy forecasting models and the development of more robust forecasting systems.

Authors' Contributions

All the authors read and approved the final manuscript.

Competing Interests

The authors state that no competing interests are in existence.

References

- [1] J. Yu, X. Li, L. Yang, L. Li, Z. Huang, K. Shen, X. Yang, X. Yang, Z. Xu, D. Zhang, and S. Du, "Deep Learning Models for PV Power Forecasting: Review," *Energies*, vol. 17, no. 16, pp. 3973, 2024.
- [2] I. Jebli, F.-Z. Belouadha, M. I. Kabbaj, and A. Tilioua, "Deep learning based models for solar energy prediction," *Advances in Science, Technology and Engineering Systems Journal*, vol. 6, no. 1, pp. 349-355, 2021.
- [3] K. R. Kumar, and M. S. Kalavathi, "Artificial intelligence based forecast models for predicting solar power generation," *Materials today: proceedings*, vol. 5, no. 1, pp. 796-802, 2018.
- [4] S. Cantillo-Luna, R. Moreno-Chuquen, D. Celeita, and G. Anders, "Deep and Machine Learning Models to Forecast Photovoltaic Power Generation," *Energies*, vol. 16, no. 10, pp. 4097, 2023.
- [5] L. M. Halabi, S. Mekhilef, and M. Hossain, "Performance evaluation of hybrid adaptive neuro-fuzzy inference system models for predicting monthly global solar radiation," *Applied Energy*, vol. 213, pp. 247-261, 2018/03/01/, 2018.
- [6] G. Zhang, X. Wang, and Z. Du, "Research on the prediction of solar energy generation based on measured environmental data," *International Journal of u-and e-Service, Science and Technology*, vol. 8, no. 5, pp. 385-402, 2015.
- [7] A. R. Kaushik, S. Padmavathi, K. S. Gurucharan, and S. C. Raja, "Performance Analysis of Regression Models in Solar PV Forecasting." pp. 1-5.
- [8] S. Salisu, M. Mustafa, and M. Mustapha, "Predicting global solar radiation in Nigeria using adaptive neuro-fuzzy approach." pp. 513-521.
- [9] B. Ersöz, M. C. Taşdelen, S. Eren, S. Sagirolu, and A. Öter, "Solar Energy Forecasting Using Ensemble Learning Method." pp. 283-287.
- [10] D. E. Rumelhart, G. E. Hinton, and R. J. Williams, "Learning representations by back-propagating errors," *nature*, vol. 323, no. 6088, pp. 533-536, 1986.

- [11] I. Goodfellow, Y. Bengio, and A. Courville, "Regularization for deep learning," *Deep learning*, pp. 216-261, 2016.
- [12] Y. LeCun, Y. Bengio, and G. Hinton, "Deep learning," *nature*, vol. 521, no. 7553, pp. 436-444, 2015.
- [13] R. Touza, J. Martínez Torres, M. Álvarez, and J. Roca, "Obtaining anti-missile decoy launch solution from a ship using machine learning techniques," 2022.
- [14] L. Breiman, "Random forests," *Machine learning*, vol. 45, pp. 5-32, 2001.
- [15] A. Liaw, "Classification and regression by randomForest," *R news*, 2002.
- [16] T. Hastie, R. Tibshirani, J. H. Friedman, and J. H. Friedman, *The elements of statistical learning: data mining, inference, and prediction*: Springer, 2009.
- [17] A. E. Hoerl, and R. W. Kennard, "Ridge regression: Biased estimation for nonorthogonal problems," *Technometrics*, vol. 12, no. 1, pp. 55-67, 1970.
- [18] S. Sezer, A. Oter, B. Ersoz, C. Topcuoglu, H. i. Bulbul, S. Sagiroglu, M. Akin, and G. Yilmaz, "Explainable artificial intelligence for LDL cholesterol prediction and classification," *Clinical Biochemistry*, pp. 110791, 2024.
- [19] S. Lundberg, "A unified approach to interpreting model predictions," *arXiv preprint arXiv:1705.07874*, 2017.
- [20] C. Molnar, *Interpretable machine learning*: Lulu. com, 2020.
- [21] A. Vırit, and A. Öter, "Kardiyovasküler Hastalıkların Derin Öğrenme Algoritmaları ile Tanısı," *Gazi Üniversitesi Fen Bilimleri Dergisi Part C: Tasarım ve Teknoloji*, vol. 12, no. 4, pp. 902-912, 2024.
- [22] C. J. Willmott, and K. Matsuura, "Advantages of the mean absolute error (MAE) over the root mean square error (RMSE) in assessing average model performance," *Climate research*, vol. 30, no. 1, pp. 79-82, 2005.
- [23] A. C. Cameron, and F. A. Windmeijer, "An R-squared measure of goodness of fit for some common nonlinear regression models," *Journal of econometrics*, vol. 77, no. 2, pp. 329-342, 1997.
- [24] J. Neter, M. H. Kutner, C. J. Nachtsheim, and W. Wasserman, "Applied linear statistical models," 1996.
- [25] A. Öter, "Automatic Detection of Epileptic Seizures from EEG Signals Using Artificial Intelligence Methods," *Gazi University Journal of Science Part C: Design and Technology*, pp. 1-1, 2024.
- [26] A. Öter, B. Ersöz, Z. Berktaş, H. i. Bülbül, E. Orhan, and Ş. Sağıroğlu, "An artificial intelligence model estimation for functionalized graphene quantum dot-based diode characteristics," *Physica Scripta*, vol. 99, no. 5, pp. 056001, 2024.

Research Article

A Comprehensive Study of the Relationships between Hardenability and Heat Transfer in a Jominy Test Sample

Mehmet Çakır^{1a}

¹Yıldız Technical University, Department of Marine Engineering Operations, 34160 Beşiktaş, İstanbul, Türkiye

mecakir@yildiz.edu.tr

DOI : 10.31202/ecjse.1597001

Received: 05.12.2024 Accepted: 24.04.2025

How to cite this article:

Mehmet Çakır, "A Comprehensive Study of the Relationships between Hardenability and Heat Transfer in a Jominy Test Sample", El-Cezeri

Journal of Science and Engineering, Vol: 12, Iss: 2, (2025), pp.(213-217).

ORCID: "0000-0001-5939-951X".

Abstract : Quenching is that the steel is quickly cooled in a quenching medium from the austenitising temperature, typically in between 845 and 870 °C. Jominy end quench test is a standard test used to characterize hardenability of steels. In this study, 1050 steel is quenched with Jominy end quenched test. Thermocouples were placed on the sample to determine the cooling rate in Jominy sample quenched end, and is investigated the relationship between heat transfer and hardenability. The relations among critical cooling rate, heat transfer and hardness is determined in Jominy sample for 1050 steel. At the point where the maximum hardness was observed that the maximum cooling rate. Heat transfer quantitative is fastest in 790 °C. This point of temperature is determined that critical a value for hardenability of 1050 steel.

Keywords : Jominy quenched end test, Hardenability, Hardness and heat transfer.

1 Introduction

The Jominy quenching method is a standard test used to determine the hardenability of steels. In this method, a cylindrical sample, 100 mm in length and 25 mm in diameter, is heated to the austenitizing temperature and cooled by applying pressurized water to the end of the sample [1].

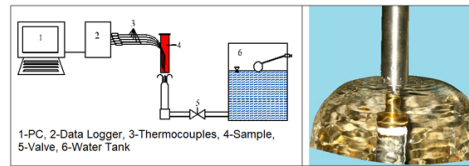
Quenching refers to the process of rapidly cooling steel from the austenitizing temperature, which is typically between 845–870 °C, in a quenching medium. This process prevents the formation of ferrite or pearlite during phase transformation and aims for the formation of bainite or martensite instead, [2]- [3]. The tendency of a steel to form martensite, leading to an increase in hardness, is referred to as its hardenability. Carbon content and the cooling rate are critical factors for achieving the maximum attainable hardness under normal conditions [4]. Numerous studies have focused on the relationship between the characteristics of the quenching medium [5]- [6]- [7], the specimen [8]- [9], and the heat transfer during the quenching process [10], [11], [12], [13], [14].

In addition to the Jominy test, numerical prediction methods for hardenability are also found in the literature. Even a rough estimate of the cooling intensity can be highly beneficial, as it can be used to determine the quenching response of various types of steel with different compositions and sizes [15]. Numerous studies have particularly focused on the prediction of hardness through numerical calculations in the Jominy quenching test.

The hardenability of a steel sample can be predicted using numerical heat transfer models, provided that the thermal properties of the sample are known [16] , [?]. A cylindrical Jominy specimen, 100 mm in length and 25 mm in diameter, was heated to 900 °C and subjected to water jet quenching using the Iterative Regularization Method (IRM) and Function Specification Method (FSM) to investigate the hardness change as a function of heat transfer coefficient variation. In this process, the relationship between heat transfer and the boiling and evaporation stages of water was examined, along with the microstructural changes in the material [17]. In another study, where two thermocouples were placed at depths of 1.3 mm from the surface, 10 mm, and 50 mm from the end of the specimen, cooling rates were measured. The effect of cooling rate on the material's microstructure at critical temperatures was analyzed, exploring how the quenching conditions affected the formation of microstructures [11]. For examining the effects of variations in the Jominy quenching conditions on hardenability, a mixture of air and water was used for quenching, and it was observed that hardness values at the first 10 mm distance were higher than those obtained with normal pressurized water [18]. There is an inevitable relationship between the quenching medium and heat transfer coefficient in terms of hardenability [17]. Specifically, during the Jominy test, the specimen is cooled from only one

Table 1: Chemical Composition of AISI 1050 Steel (%)

C	Mn	Si	P	S	Cr	Mo	Ni	Al	Cu	Sn	Fe
0.50	0.64	0.24	0.010	0.005	0.12	0.01	0.07	0.014	0.16	0.011	98.22

**Figure 1: Jominy Quenching Test and Cooling System**

end, and the relationship between heat transfer at that end and hardenability is significant. These relationships can be explored through both numerical calculations and experimental studies.

In this study, the Jominy quenching test was applied to 1050 steel. Thermocouples were placed on the specimen to determine the cooling rate at the quenched end, and the relationship between hardenability and heat transfer at the quenching end was investigated. The variation of the heat transfer coefficient with temperature and time was determined, and the effects of heat transfer events at the quenching end on hardenability were analyzed.

2 Experimental Study

The specimens, prepared in accordance with the TS 1381 EN ISO 642 standard (100 mm in length and 25 mm in diameter), were heated to 840 °C in a heat treatment furnace and quenched in water at a pressure of 65 mmSS using the cooling system shown in Figure 1. The temperature data, recorded over time from thermocouples placed at 1 mm from the quenching end and at distances of 5 mm and 10 mm, were transferred to a data acquisition card [19].

After being ground to a thickness of 0.4 mm axially, the Rockwell C hardness values were measured to determine the hardness depth of the specimens.

For optical microscopy, the samples were sequentially polished with SiC abrasive papers of 400, 600, and 1200 grit, followed by polishing with 0.25–1 μm diamond paste. After polishing, the samples were washed with ethyl alcohol and dried. To reveal the microstructure, the specimens were etched using a mixture of 3% nitric acid and 97% ethyl alcohol.

3 Results and Discussion

The experimental results showed the time-dependent cooling curves, as measured by K-type thermocouples at the quenched end, 5 mm, and 10 mm from the quenching surface, which are presented in Figure 2. Continuous cooling curves for the Jominy sample were measured using these thermocouples.

In Figure 2, as the cooling proceeds from the quenched end towards the interior of the sample, the cooling rate decreases over time. Notably, at 10 mm, the transformation to ferrite and bainite is observed. In contrast, at the quenched end, a lower cooling rate than the critical cooling curve was achieved, and the structure was fully martensitic. This difference is evident in the hardness values as well. At 5 mm, the structure contains a mix of bainite and a small amount of ferrite, with a hardness value of 53 HRC, which indicates that the majority of the structure is martensitic. The microhardness value at this point is much closer to the hardness at the quenched end, which is 61 HRC, than to the hardness at 10 mm, which is 30 HRC.

In the Jominy quenching test, heat loss occurs at the quenched end. The time-dependent variation of the heat transfer coefficient (h) at a pressure of 65 mmSS is shown in Figure 3, and its variation with temperature is shown in Figure 4.

At 65 mmSS pressure during the Jominy test, the heat transfer coefficient at the quenched end continuously increased until 2 seconds, reaching 11200 W/m²°C. From 2 to 5 seconds, a continuous decrease was observed, reaching 2300 W/m²°C at 5 seconds. After this point, the heat transfer coefficient showed little change, following a downward trend over time.

A study examining the variation of the heat transfer coefficient with time and distance from the quenched end found that the heat transfer rate was maximum in the first 2 seconds, after which it decreased linearly [10]. This finding is consistent with the result in this study, where the heat transfer coefficient reached its maximum at 2 seconds.

The specimen reached 11200 W/m²°C at 790 °C. Figure 4 shows that during cooling, the heat transfer coefficient rapidly increased to 11200 W/m²°C at 790 °C. As cooling continued to 430 °C, the heat transfer coefficient decreased linearly to 2300 W/m²°C. An increase was observed up to 385 °C, reaching 3000 W/m²°C, after which a continuous decrease occurred until the cooling medium temperature was reached. These temperature points correspond to critical temperature points during cooling and can be associated with hardenability. Particularly, temperatures between 700–800 °C, corresponding to the 2nd second of quenching, are directly related to hardenability [11].

As expected, the amount of heat transferred is inversely proportional to the variation of the heat transfer coefficient. The changes in the amount of transferred heat over time and with temperature are shown in Figures 5 and 6, respectively.

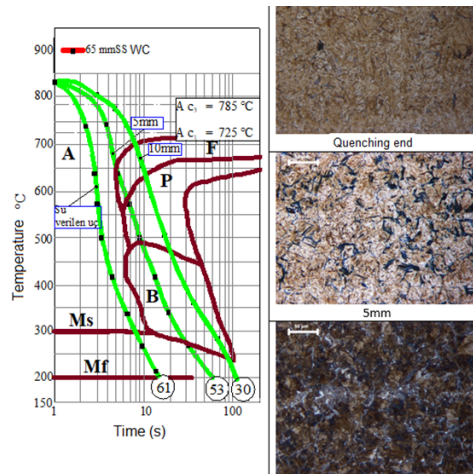


Figure 2: Jominy quenching end, cooling curves, hardness values and microstructure photographs at 5mm and 10mm distances.

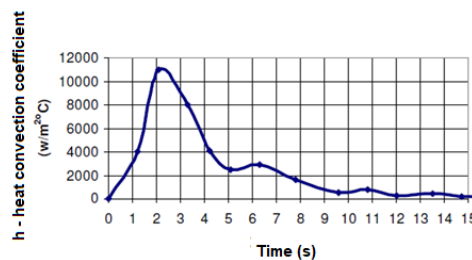


Figure 3: Time-dependent variation of the heat transfer coefficient at the quenching end.

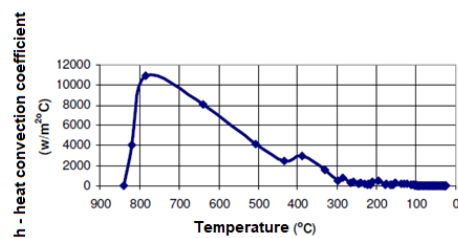


Figure 4: Variation of the heat transfer coefficient with temperature at the quenching end.

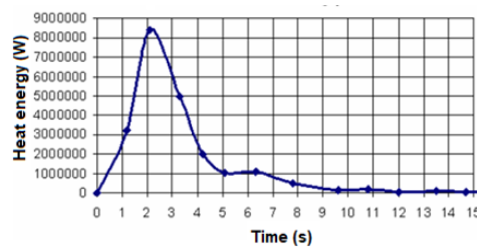


Figure 5: Time-dependent change in energy transferred from the quenching end.

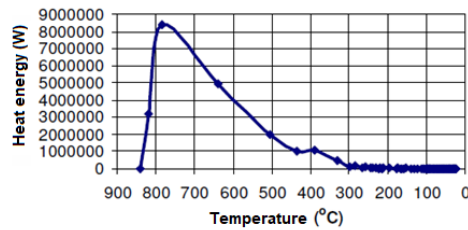


Figure 6: Temperature-dependent change in energy transferred from the quenching end.

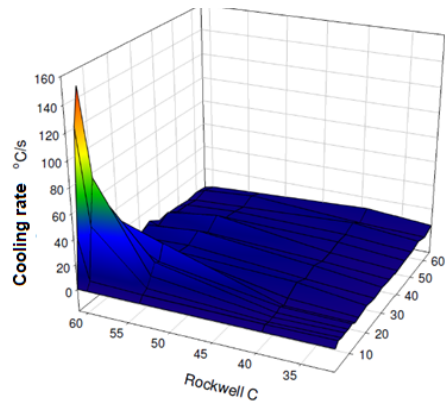


Figure 7: Change of hardness and cooling rate with distance from the end at 65 mmSS Pressure.

In Figure 5, the change in transferred heat over time shows a rapid increase in the first 2 seconds, reaching a value of 8×10^6 W. After this point, a decrease is observed until 5 seconds, and the transferred heat energy dropped to 10^6 W.

As for the temperature-dependent heat transfer, energy was mainly transferred at temperatures above 800°C during the initial stages. The highest heat transfer occurred at 790°C , after which the amount of energy transferred began to decrease as the cooling continued. Thus, the maximum energy transfer occurred at the highest temperature range, which also relates to the hardenability of the steel. Lower transfer rates below 500°C led to lower martensitic phase formation at the interior points of the specimen, which explains the difference in hardness measured from the quenched end to the interior.

The Figure 7 is given so that the cooling rate and hardness relationship of the Jominy test sample, especially at the tip, at 5 mm and 10 mm distance can be shown in more detail in 3D.

The maximum cooling rate is 145°C/s versus 61 HRC hardness the end surface of sample. The cooling rates at 5 mm and 10 mm distances are 80°C/s and 40°C/s , respectively, and the efficiency values are 53 HRC and 30 HRC. As can be seen from the figure, the efficiency values are not change a lot after 10 mm, and in the same way, the cooling rate of the experimental result does not change much after 10 mm.

4 Conclusion

The results of this study show a clear correlation between the cooling rate, heat transfer coefficient, and hardenability of AISI 1050 steel during the Jominy quenching test.

The cooling rate is highest at the quenched end, resulting in a fully martensitic microstructure and the highest hardness. As the distance from the quenched end increases, the cooling rate decreases, leading to the formation of bainite and ferrite, which corresponds to a decrease in hardness. The heat transfer coefficient was found to be temperature-dependent, with higher values observed in the initial cooling stages. The critical cooling rate for hardenability corresponds with temperatures in the range of $700\text{--}800^\circ\text{C}$, where the highest heat transfer rates are observed. Therefore, controlling quenching conditions and understanding the heat transfer behavior are essential for optimizing the hardenability of steels.

Acknowledgments

This study was supported by SDU-BAPK with Grant Number: 1571-YL-07.

Authors' Contributions

In this study, MÇ performed this work and wrote up the article.

Competing Interests

The authors declare that they have no conflict of interest.

References

- [1] Anonymous, *Celik Ucuna Su Verilerek Sertleşebilirlik Deneyi (Jominy Deneyi)*. Ankara: TSE, 2001, tS 1381 EN ISO 642 (ICS 77.040.99).
- [2] P. Fernandes and K. N. Prabhu, "Effect of section size and agitation on heat transfer during quenching of aisi 1040 steel," *Journal of Materials Processing Technology*, vol. 183, pp. 1–5, 2007.
- [3] N. S. Köksal, M. Uzku, and B. S. Ünlü, "Farklı karbon İçerikli Çeliklerin mekanik Özelliklerinin ısı işlemlerle değişimi," *DEÜ Mühendislik Fakültesi, Fen ve Mühendislik Dergisi*, vol. 6, no. 2, pp. 95–100, 2004.
- [4] N. Tükel, *Demir – Karbon Alaşımları*, 2nd ed. İstanbul: Arpac Matbaacılık Tesisleri, 1981.
- [5] M. Cigdemoglu and Z. Cigdemoglu, "Su verme uygulamalarında metal-ortam ısı transferi ve ana değişkenlerin İncelenmesi," *Mühendis ve Makine Dergisi*, vol. 24, no. 283, pp. 3–10, 1983.
- [6] S. Karaca, "Jominy deneyi ve deney parametrelerinin deney üzerindeki etkileri," Master's thesis, Y.T.Ü. Fen Bilimleri Enstitüsü, İstanbul, 1999.
- [7] I. Karagöz, "Hardness change due to carburization time and material thickness during heat treatment of sae 8620 (21nicrmo2) plates," *El Cezeri Journal of Science and Engineering*, vol. 6, no. 3, pp. 748–754, 2019.
- [8] P. L. Masson, T. Loulou, and E. Artioukhine, "Comparison between two methods for estimating the convection heat transfer coefficient during a metallurgical jominy end-quench test," in *4th International Conference on Inverse Problems in Engineering*, Rio de Janeiro, Brezilya, 2002.
- [9] C. Heming, H. Xieqing, and X. Jianbin, "Comparison of surface heat-transfer coefficients between various diameter cylinders during rapid cooling," *Journal of Material Processing Technology*, vol. 138, pp. 399–402, 2003.
- [10] P. L. Masson, T. Loulou, and E. Artioukhine, "Estimations of a 2d convection heat transfer coefficient during a metallurgical "jominy end-quench" test: Comparison between two methods and experimental validation," *Inverse Problems in Science and Engineering*, vol. 12, no. 6, pp. 595–617, 2003.
- [11] R. Mihaly, V. Balazs, C. Zsolt, and P. Jiansheng, "Modeling of intercritical heat treatment of dp and trip steels," *Transactions of Materials and Heat Treatment*, vol. 25, no. 5, pp. 710–715, 2004.
- [12] B. Smoljan, "Prediction of mechanical properties and microstructure distribution of quenched and tempered steel shaft," *Journal of Materials Processing Technology*, vol. 175, pp. 393–397, 2006.
- [13] A. Z. Yazdi, S. A. Sajjadi, S. M. Zebarjad, and S. M. M. Nezhad, "Prediction of hardness at different points of jominy specimen using quench factor analysis method," *Journal of Materials Processing Technology*, vol. 11134, pp. 1–6, 2007.
- [14] G. S. Sarmiento, J. F. Bugna, L. C. F. Canale, G. M. M. Riofano, R. A. Mesquita, G. E. Totten, and A. C. Canale, "Modeling quenching performance by the kuyucak method," *Materials Science and Engineering A*, vol. 459, pp. 383–389, 2007.
- [15] N. İzar, *Çelik Seçimi ve Sertleşebilme*. Ankara: Makine Mühendisleri Odası, 1971, yayın No: 58.
- [16] M. Çakır and A. Özsoy, "Investigation theoretically and empirically of correlation between hardenability and heat transfer for jominy sample," *Journal of the Faculty of Engineering and Architecture of Gazi University*, 2013.
- [17] B. Smoljan, N. Tomasic, D. Iljkic, I. Felde, and T. Reti, "Application of jm-test in 3d simulation of quenching," *Journal of Achievements in Materials and Manufacturing Engineering*, vol. 17, no. 1–2, pp. 281–284, 2006.
- [18] M. Cakir and A. Özsoy, "Investigation of the correlation between thermal properties and hardenability of jominy bars quenched with air–water mixture for aisi 1050 steel," *Materials and Design*, vol. 32, no. 5, pp. 3099–3105, 2011.
- [19] M. Çakır, "Su verme ısı İşleminde Çelik-ortam arasındaki ısı transferinin İncelenmesi," Master's thesis, Süleyman Demirel Üniversitesi, Fen Bilimleri Enstitüsü, Isparta, 2008.

Research Article

Detection of Pufferfish Using Computer Vision and Deep Learning Methods

Hüseyin Umut Yüksel^{1a}, Güray Tonguç^{2b}¹Department of Computer Programming, Vocational School, Alanya University, Alanya, Antalya, 07400, Türkiye²Department of Management Information Systems, Faculty of Applied Sciences, Akdeniz University, Konyaaltı, Antalya, 07070, Türkiye

guraytonguc@akdeniz.edu.tr

DOI : 10.31202/ecjse.1628790

Received: 29.01.2025 Accepted: 24.03.2025

How to cite this article:

Hüseyin Umut Yüksel, Güray Tonguç, "Detection of Pufferfish Using Computer Vision and Deep Learning Methods", El-Cezeri Journal of Science and Engineering, Vol: 12, Iss: 2, (2025), pp.(218-234).

ORCID: ^a0000-0003-1891-3644; ^b0000-0002-5476-7114.

Abstract: The opening of the Suez Canal and the construction of the Aswan Dam have significantly impacted the Mediterranean ecosystem. These changes increased species migration from the Red Sea to the Mediterranean, leading to the spread of new species, causing economic losses and threats to human health. Among these, the pufferfish is a toxic species with no natural predators and wide distribution. This study focuses on training an object detection model to identify pufferfish (*Lagocephalus sceleratus*) using computer vision and deep learning techniques. YOLO (You Only Look Once), a leading algorithm, was used. Training data was gathered from diving schools and instructors in the Mediterranean. Frames extracted from underwater videos were labeled to create a dataset of 2,473 images. The YOLOv8m version achieved the best result with a mAP (Mean Average Precision) of 96.90%. The model was better at detecting pufferfish from head and side angles. However, challenges in manual labeling, particularly with tails and fins, slightly affected the model's focus. This study's findings could help control pufferfish populations using underwater robots and automated systems, contributing to ecological balance.

Keywords: Information Systems, Computer Vision, YOLO, Pufferfish, Object Detection

I. Introduction

The Suez Canal, completed in 1869, connected the Mediterranean Sea and Indian Ocean, sparking a significant migration of species from the Red Sea [1]-[4]. Zenetos et al. [5] documented 903 migrant species, with alien species along Turkish coasts increasing from 400 in 2010 to 539 by 2020 [6], [7]. Among these, the pufferfish *Lagocephalus sceleratus*, identified in the Gulf of Gökova in 2003 [8], stands out due to its tetrodotoxin (TTX) content [9]. With no natural predators, it preys on shrimp, crabs, and small fish, disrupting ecosystems, damaging fishing nets, and causing economic losses [10]. Fatalities from human consumption have also been reported [11]. Traditional overfishing methods are in use [12], but advanced solutions like computer vision and deep learning remain underexplored for pufferfish detection [13]-[16]. This study applies the YOLO algorithm to detect *L. sceleratus*, aiming to enhance sustainable marine management with underwater robots.

Artificial intelligence (AI), evolving since the mid-20th century [17], has advanced with artificial neural networks (ANNs) [18] and deep learning [19], driven by increased computational power [20]. AI now supports applications in mobile devices [21], healthcare [22], finance [23], and beyond [24]. ANNs, inspired by the human brain [25], model complex data relationships for tasks like image and speech recognition [26]. Deep learning, a subset of machine learning, uses multi-layered networks to extract high-level features from data [27], enabling object and face recognition [28], [29]. Computer vision, a key AI domain, interprets digital imagery [30] and is vital for underwater applications where optical challenges like refraction hinder traditional observation [31]-[33]. The YOLO (You Only Look Once) algorithm, introduced in 2016 [34], excels in real-time object detection with a single-stage approach [35]. Trained on datasets like Pascal VOC [36], it predicts object classes and locations efficiently [37].

Evolving through versions like YOLOv10 [38], developed by communities [39] and companies [40], it offers enhanced accuracy and speed [41].

Underwater studies leverage these technologies effectively. Deep learning models address detection, tracking, and classification challenges in marine environments [42], with various algorithms applied [43]. Li et al. [44] achieved an 81.4% Mean Average Precision (mAP) using Fast R-CNN on 24,277 fish images, outperforming prior studies by 80% in speed. Villon et al. [45] reported a 94.9% accuracy with CNNs, surpassing human performance (89.3%), especially for obscured fish. Hridayami et al. [46] used VGG16 with transfer learning, achieving a 96.4% acceptance rate on mixed RGB datasets. Allken et al. [47] reached 94% accuracy with synthetic data for species classification, addressing data scarcity. Jalal et al. [48] combined YOLO with optical flow, yielding a 95.47% F-score for moving and camouflaged fish. Salman et al. [49] achieved 87.44% accuracy with R-CNN using movement-based regions. Hussain et al. [50] modified AlexNet for 90.48% accuracy, improving on the original 86.65% with dropout layers. Wang et al. [51] enhanced YOLOv5 with SiamRPN++, achieving 99.4% AP50 for abnormal fish behavior detection, with 76.7% tracking accuracy. Patro et al. [52] used YOLOv5-CNN for 86% precision in adverse conditions, aiding fish farm monitoring.

These studies highlight computer vision's role in fish detection [30], disease identification [32], and net monitoring [33], yet pufferfish-specific applications are scarce [12]-[16]. Li et al. [44] and Villon et al. [45] focused on broad species recognition, while Hridayami et al. [46] and Allken et al. [47] tackled diverse datasets. Jalal et al. [48] and Salman et al. [49] improved detection in complex scenes, and Hussain et al. [50] optimized model efficiency. Wang et al. [51] and Patro et al. [52] addressed real-time challenges, but none specifically targeted *L. sceleratus*. This gap motivates our study, building on YOLO's proven capabilities [34]-[41] to address ecological and economic impacts [1]-[11] through precise, automated detection.

II. Materials And Methods

In underwater environments, light refraction, water turbidity, and intense background noise make fish detection and tracking challenging. Observing fish and tracking their movements through human observation in such conditions is difficult. To address this issue and focus on detecting pufferfish in underwater environments, our study initially collected video footage containing pufferfish. The collected video footage was divided into frames, the pufferfish in the images were labeled, and a dataset was created for training the object detection model using these labeled frames. YOLOv8 and YOLOv5 models were trained using the labeled frames from the videos, and their training performance was compared based on precision, recall, and average precision values.

A. Dataset

In this study, videos used for detecting pufferfish were obtained from some diving schools and professional diving instructors operating in the Mediterranean region. The acquired videos were divided into frames for training the YOLO model. The code required to convert the videos into frames was written using the Python programming language in the PyCharm IDE, with the help of the OpenCV library.

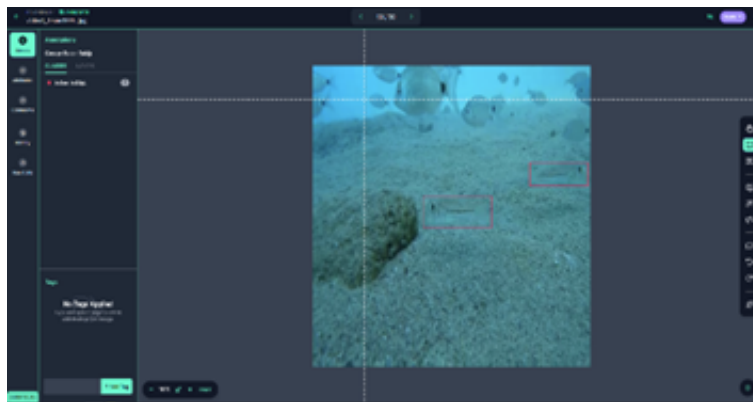


Figure 1: Roboflow image annotation tool

The frames need to be labeled for use in the training process of the dataset. For labeling the images, the annotation interface provided by the Roboflow platform was used (Figure 1). Roboflow is an online platform that facilitates the

creation and management of computer vision projects, available for both paid and free use. Through its API (Application Programming Interface), the dataset containing labeled images in YOLO format can be used in model training within the Google Colab environment. Google Colab was chosen as the training environment for this study. Google Colab is a cloud-based Jupyter Notebook service provided by Google, accessible through a web interface, offering integration with Google Drive, and free GPU and TPU support.

Since YOLOv8 and YOLOv5 models can use images of size 640×640 for training, the images were resized to 640×640 dimensions. Data augmentation operations, including horizontal flip, vertical flip, and rotations by 90 degrees clockwise and counterclockwise, were performed on the data. After augmentation, the dataset consisted of a total of 2473 images, including 1773 for training, 450 for validation, and 250 for testing (approximately 70:20:10). These values align with similar studies [53]. The data processing script used OpenCV's `cv2.VideoCapture` to extract frames at 1-second intervals, followed by resizing with `cv2.resize` and augmentation via Roboflow's built-in tools.



Figure 2: Examples of annotated images used during training

As seen in Figure 2, care was taken to ensure that the selected pufferfish images for annotation included examples from different angles. In the bounding box process, emphasis was placed on the fish's body, while the fins and tails of the fish were given less consideration in the annotations. The reasons for this are explained in the subsequent sections.

B. Training Process

In the study conducted for pufferfish detection, the dataset containing 2473 images was trained in the Google Colab environment. Ultralytics YOLOv8.0.134 and YOLOv5 v7.0-72 versions were used for training the model in the Colab environment. Python 3.10.12 and torch 2.0.1+cu118 libraries were utilized. The training code adapted from Ultralytics' repositories is publicly available at github.com/username/pufferfish-detection. Key hyperparameters included a learning rate of 0.01, batch size of 16, momentum of 0.937, and weight decay of 0.0005, optimized for convergence over 300 epochs. The patience parameter was set to 100 to halt training if validation loss did not improve, preventing overfitting.

Before training, a compute unit was purchased on Google Colab, and A100 and V100 graphics processing units were used during the study. The system specifications used during the study on Google Colab were a 12-core processor, 83.5 GB RAM, 166.8 GB disk space, and either a 40GB Nvidia A100 SXM graphics processing unit or a 16GB Nvidia V100 graphics processing unit. The driver version of the graphics processing unit was 525.105.17, and the CUDA version was 12.0.

After preparing the dataset, it was uploaded to the Colab environment, and the YOLO algorithms' codes were run step-by-step with a value of 300 epochs to perform the training, validation, and testing processes. The entire process can be summarized as shown in Figure 3. Training involved the following steps: (1) loading the dataset in YOLO format, (2) initializing pre-trained weights (e.g., yolov8m.pt), (3) running the train.py script with specified hyperparameters, and (4) saving the best model weights based on validation mAP.

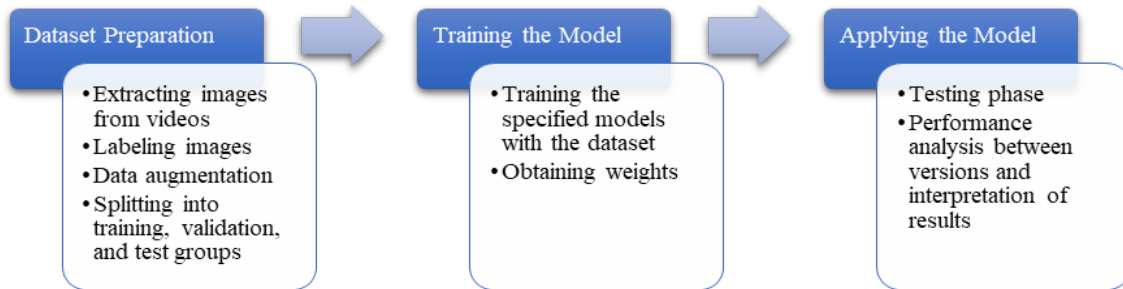


Figure 3: Stages of the study

C. Evaluation Methods (Metrics)

After model training is completed, the model is evaluated from various perspectives. The confusion matrix is one of the fundamental tools used to assess the performance of classification models. Typically presented as a two-dimensional table, this matrix shows the relationships between the classes predicted by the model and the actual classes. This matrix and its values are provided in Table 1.

Table 1: Confusion Matrix Structure

		Predicted Values	
		TP	FN
Actual Values		FP	TN

TP (True Positives): These are the examples correctly predicted as positive by the model. In our study, it represents the number of images correctly identified as pufferfish.

TN (True Negatives): These are the examples correctly predicted as negative by the model. In our study, it represents the number of images correctly identified as not containing pufferfish.

FP (False Positives): These are the examples predicted as positive by the model but are actually negative. In our study, it represents the number of images where pufferfish is not present but the model incorrectly identified them as containing pufferfish.

FN (False Negatives): These are the examples predicted as negative by the model but are actually positive. In our study, it represents the number of images where pufferfish is present but the model incorrectly identified them as not containing pufferfish.

Precision indicates how many of the positive predictions are actually correct, which is particularly important in cases of imbalanced classes. Recall, also known as sensitivity or true positive rate, shows how many of the actual positive examples are correctly predicted. Accuracy represents the ratio of correct predictions to the total number of predictions and is often used with balanced datasets. The F1 Score balances precision and recall by calculating their harmonic mean. Additionally, Average Precision (AP) and mean Average Precision (mAP), which summarize the model's performance in terms of precision and recall across different classes into a single metric, are used to characterize the model's precision and evaluate its accuracy.

$$Precision = \frac{TP}{TP+FP} \quad (1)$$

$$Recall = \frac{TP}{TP+FN} \quad (2)$$

$$Accuracy = \frac{True\ Predictions\ (TP+TN)}{All\ Predictions\ (TP+TN+FP+FN)} \quad (3)$$

$$F1 = \frac{2 \times Precision \times Recall}{Precision+Recall} \quad (4)$$

$$AP = \int_0^1 P(R) dR \quad (5)$$

$$mAP = \frac{1}{k} \sum_{k=1}^K AP_k \quad (6)$$

Additionally, the PR curve (precision and recall curve) shows the trade-off between precision and recall at different thresholds. By calculating the area under the precision-recall curve, average precision (AP) is obtained for each class, and the mean of these values provides the mean Average Precision (mAP). mAP is a critical metric for assessing the overall performance of the model and the balance across classes. It is calculated by averaging the AP values for each class using a 0.5 IoU threshold [54].

D. Performance Parameter

For deep learning models like YOLO, performance parameters provide information about the model's efficiency and applicability. Measurements under this category include processing speed (in milliseconds or seconds), frame rate (frames per second), model size, memory usage, training time, computational complexity, and energy consumption [55].

E. Loss Functions

In addition to the metrics mentioned above, the loss functions used during model training include Box Loss, Classification Loss (cls loss), and Distribution Focal Loss (dfl loss). These functions are used to improve the training performance of the model and measure how much the predictions deviate from the actual values. Loss functions are fundamental tools for optimizing model performance.

Box Loss measures how well the predicted bounding boxes overlap with the actual bounding boxes. It consists of components such as box localization loss and box size loss. Classification Loss measures how well the predicted class labels match the actual class labels; a lower classification loss indicates better alignment between the predicted and actual class labels. DFL Loss assesses how well the predicted boxes overlap with the actual bounding boxes, similar to box localization loss, but uses different methods for calculation [56], [57].

III. Results And Discussion

Detecting the invasive pufferfish, which is increasingly populating the Mediterranean and causing various economic and social impacts, is an important step in mitigating the damage they cause and may cause in the future. In the study, the epoch value for each model was set to 300, and the patience value was set to 100. An epoch represents a single pass of the entire training data through the model. The patience value monitors consecutive epochs and terminates the training if no better values are achieved within the specified number of epochs, without waiting for all epochs to complete. This value was set to 100 to avoid wasting resources when the model is no longer learning effectively. If the patience value equals the number of epochs, training will continue until all epochs are completed; if set to 0, training will continue until all epochs are completed. The training results for the YOLOv5 and YOLOv8 models included in the study are provided in Table 2.

Table 2: Training Results of the Models

Model	Precision	Recall	Average Precision	GPU	Duration
YOLOv5n	%97,20	%88,70	%92,40	V100	1 hour 06 min 53 sec
YOLOv5m	%95,10	%89,70	%93,40	V100	2 hour 45 min 50 sec
YOLOv8n	%93,90	%93,90	%95,80	V100	1 hour 06 min 18 sec
YOLOv8m	%97,60	%92,70	%96,90	V100	1 hour 55 min 02 sec
YOLOv8l	%97,40	%92,30	%96,70	A100	1 hour 47 min 13 sec

The values in Table 2 were automatically generated at the end of training based on the precision and recall formulas applied to the error matrices of the validation dataset. The average precision values were obtained using the area under the precision-recall curve, which was also automatically calculated after training. In the Google Colab environment, the A100 GPU was selected for the image processing unit. However, Colab provided the V100 GPU instead of the A100. Colab's resource allocation may provide alternatives to the requested GPU based on availability. The difference in GPUs used during training affects the training duration.

An examination of the data in Table 2 reveals that the YOLOv8n model achieved better average precision and training duration compared to the YOLOv5n model. Additionally, when comparing the average precision and training duration of the YOLOv5m model with the YOLOv8m model, the YOLOv8m model delivered superior results. There was also an approximate 51-minute difference in training completion time between the two trainings conducted with the same GPUs.

A. Loss Functions

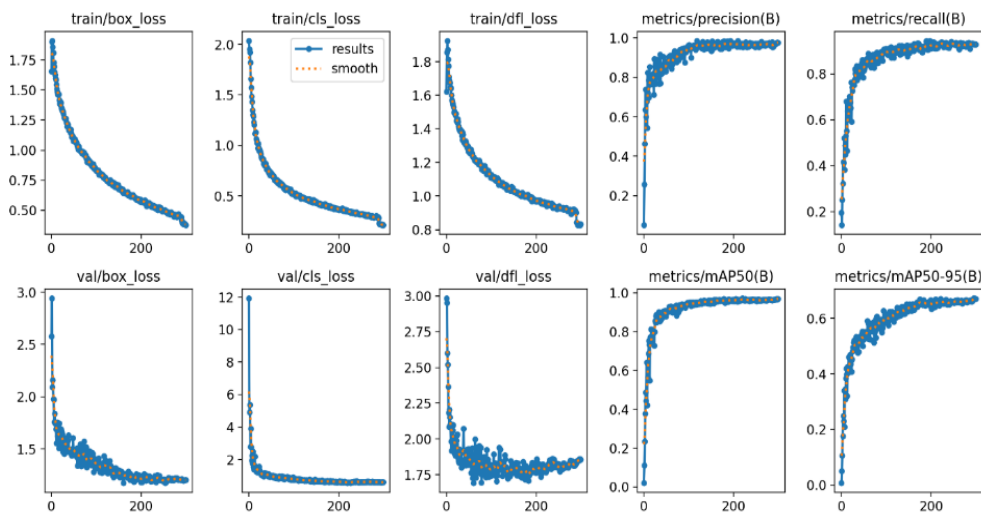


Figure 4: YOLOv8m Training Charts

Examining the training results for the YOLOv8m model presented in Figure 4, it is observed that after 200 epochs, the model's recall, precision, and average precision values stabilized. Between 250 and 300 epochs, the model exhibited stable performance in average precision. In the validation (val) graphs, an increase in the DFL loss value was noted after 250 epochs. In the Google Colab environment, training with 300 epochs for the YOLOv8m model was completed in approximately 1 hour and 55 minutes, while the average precision and completion times for other models are listed in Table 2. The highest average precision value was observed with the YOLOv8m model.

Figure 5. displays the training results for the YOLOv8n model. The graphs show the variations in values throughout the training process conducted over 300 epochs. An increase in the validation box loss and DFL loss values is observed between 200 and 300 epochs.

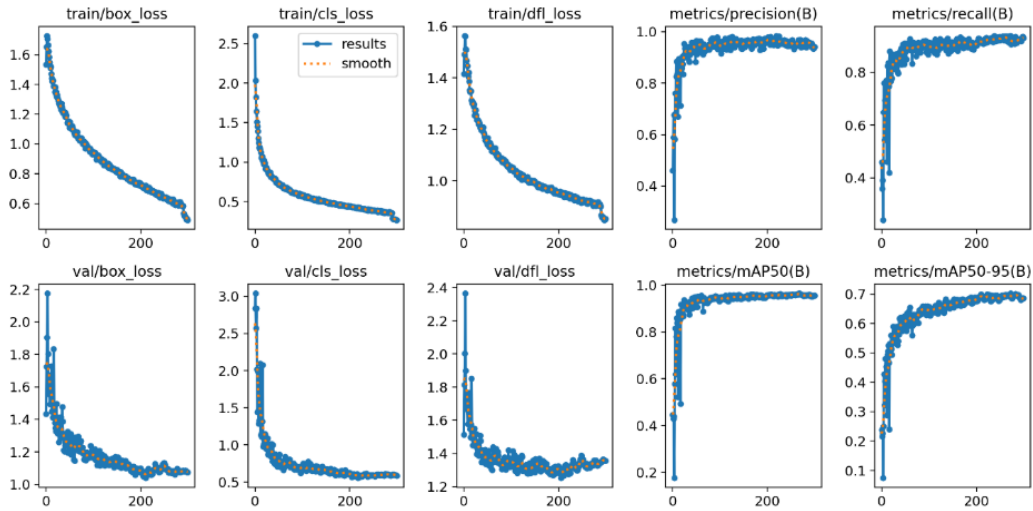


Figure 5: YOLOv8n Training Charts

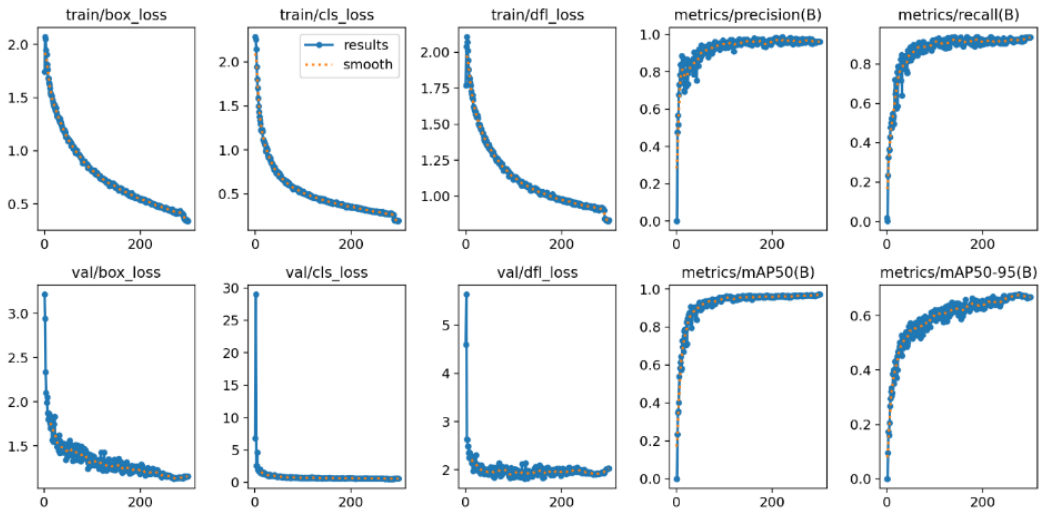


Figure 6: YOLOv8l Training Charts

Figure 6. shows the training results for the YOLOv8l model. The analysis of the training results indicates that the validation (val) box loss and DFL loss values remained higher compared to the YOLOv8n and YOLOv8m models. Additionally, it was observed that the DFL values increased after 250 epochs.

Figure 7. presents the training results for the YOLOv5n model. Due to differences between YOLOv5 and YOLOv8 models, the YOLOv5 model calculated the classification loss as 0 for single-class examples. It was observed that the validation (val) objective loss values increased after 200 epochs.

Figure 8. shows the training results for the YOLOv5m model. It was observed that the validation (val) objective loss exhibited an increasing trend after 200 epochs.

B. Metrics

Figure 9. presents the error matrices for the models used in the study. In the YOLOv8 models, for single-class tasks, the confusion matrices produced by YOLO do not display the true negative values. Overall, it was observed that all

three models performed quite well in detecting pufferfish. However, some errors were noted, such as misidentifying backgrounds as pufferfish and failing to detect some pufferfish. Generally, the YOLOv8m model demonstrated the best performance during the validation and testing phases.

The Precision-Recall curves for the YOLOv8n, YOLOv8m, and YOLOv8l models during validation and testing at a 0.50 threshold are presented in Figure 10. In these PR graphs, the closer the curve is to the top corner of the graph, the better the model's performance, indicating high precision and recall. The area under the curve (AUC-PR) value summarizes the model's overall performance, and a high AUC-PR value is indicative of good performance. According to this:

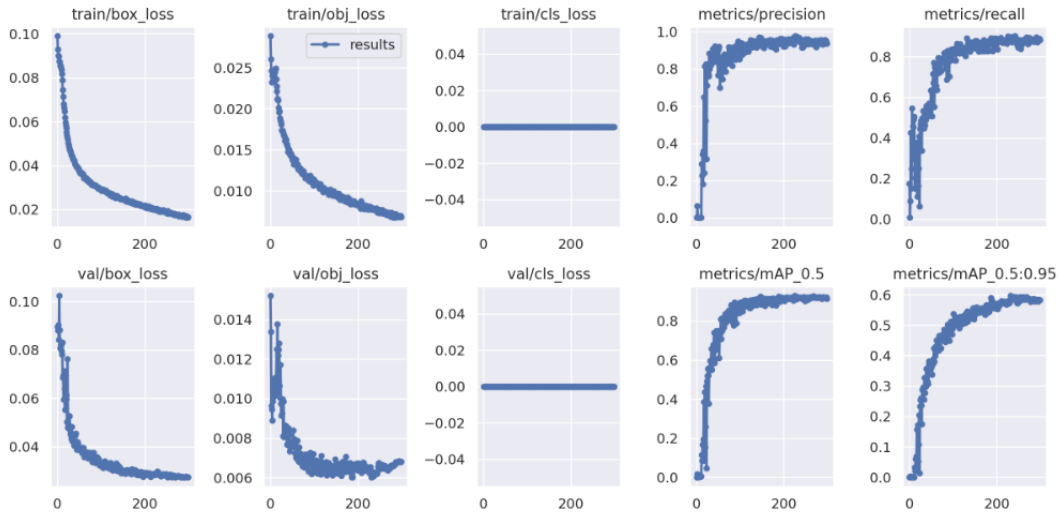


Figure 7: YOLOv5n Training Charts

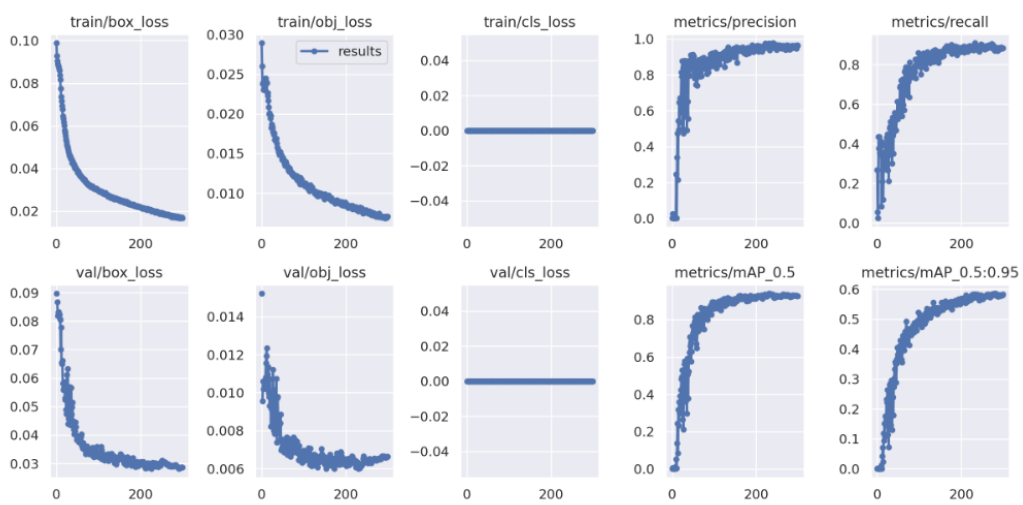


Figure 8: YOLOv5m Training Charts

The YOLOv8n model's average precision during validation was found to be 96.10%. These high precision and recall values indicate that the model accurately identifies a high proportion of true positives and that a large portion of the positive predictions are correct. The average precision on the test set was found to be 98%. Similarly, high precision and recall values were observed on the test set, demonstrating that the model's generalization capability is quite strong.

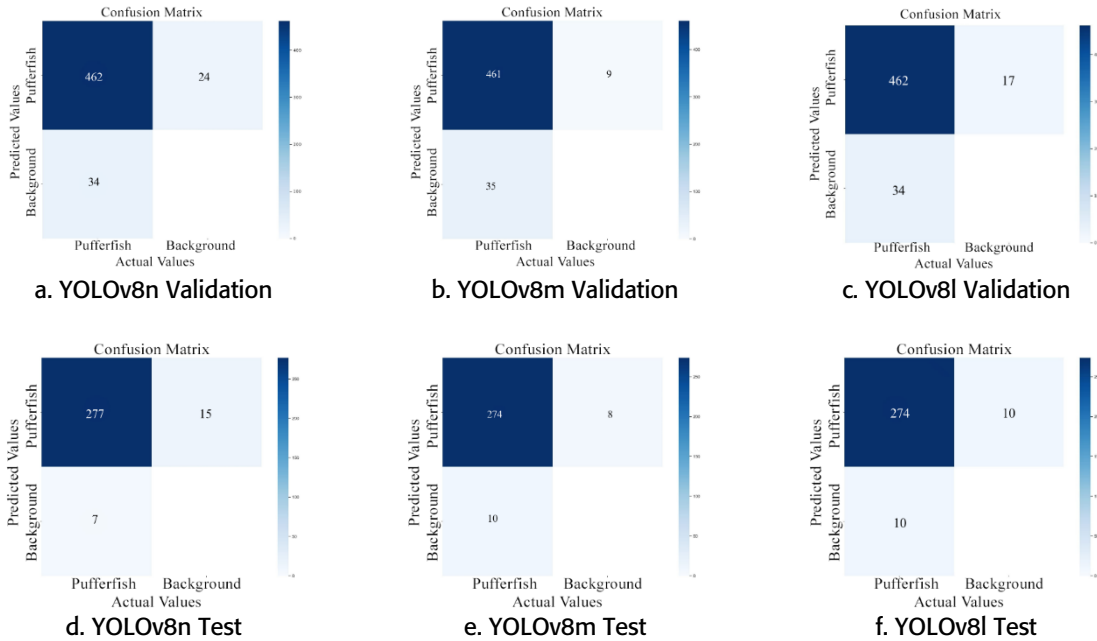


Figure 9: Error Matrices of the Models in the Study

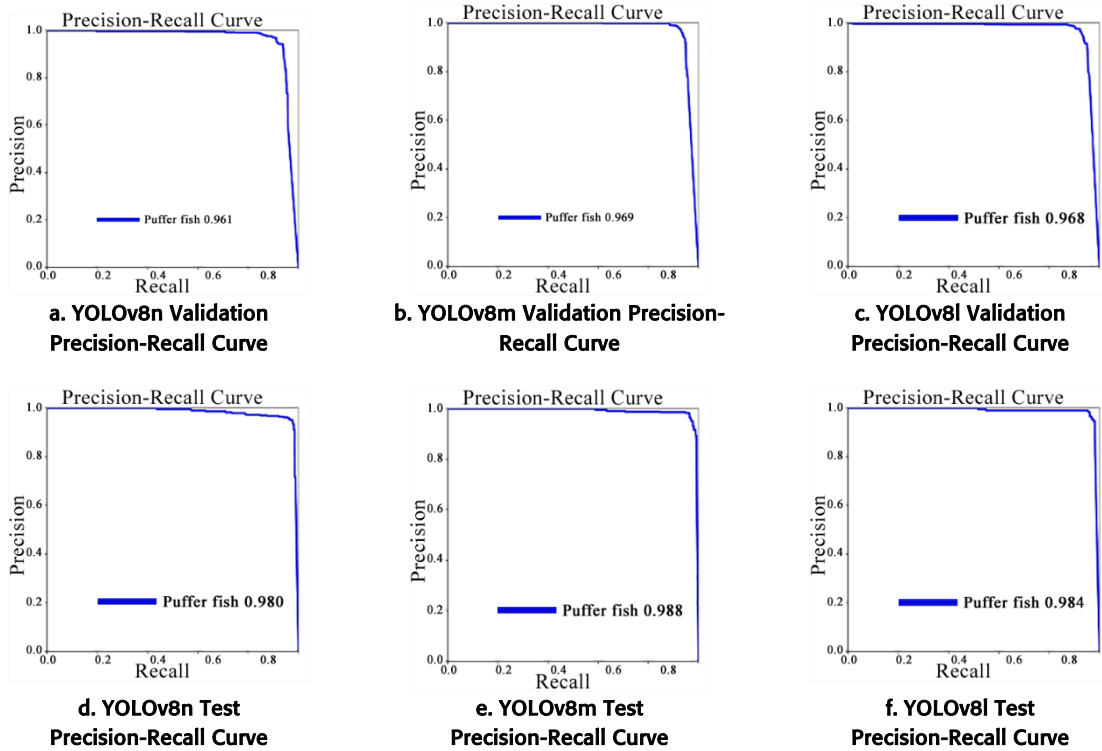


Figure 10: Precision-Recall (PR) Curves of the Models in the Study

The YOLOv8m model's average precision during validation was found to be 96.90%. The model's high precision and recall values indicate a high accuracy rate and strong detection capability. The average precision during testing was found to be 98.80%. The model's performance on the test set was similar to the validation set, demonstrating that the model could generalize well from the training data to the test set.

The YOLOv8l model's average precision during validation was found to be 96.80%. The high precision and recall values during validation show the model's ability to accurately predict positive classes. The average precision on the test set was found to be 98.40%. The model's performance on the test set was very close to that on the validation set, indicating good generalization ability.

Both the YOLOv8m and YOLOv8l models exhibit high consistency and performance on both the validation and test sets. Their PR curves indicate that these models have high positive classification abilities with low false negative and false positive rates. While the YOLOv8m model shows the best performance with an excellent PR curve, a slight performance drop was observed in the YOLOv8n model.

C. Test Phase Examples



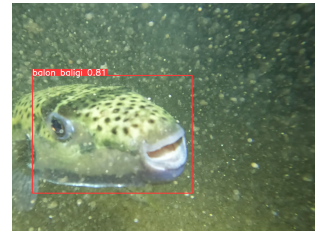
a. Pufferfish detected using the trained model weights



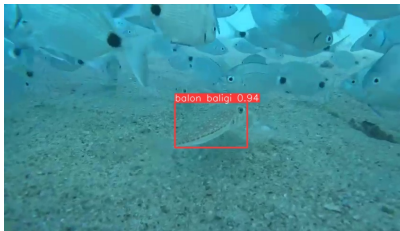
b. Pufferfish detected using the YOLOv8m model in low-light nighttime conditions



c. Pufferfish detected using the YOLOv8m model in well-lit nighttime conditions



d. Pufferfish detected using the YOLOv8m model in a high-noise nighttime environment



e. Pufferfish detected using the YOLOv8m model in daylight conditions with normal lighting



f. Pufferfish detected using the YOLOv8m model in daylight conditions with normal lighting



g. Pufferfish detected using the YOLOv8m model in a noisy environment

Figure 11: Pufferfish Detection Under Various Lighting and Noise Conditions

Figures 11.a to 11.g shows the YOLOv8m model's performance in detecting pufferfish under various lighting and noise conditions. Figures 11.a through 11.g showcase the performance of the YOLOv8m model in detecting pufferfish under various lighting and noise conditions. Figure 11.a: The model achieved a 90% accuracy in detecting the pufferfish in a noisy environment with artificial lighting. This demonstrates the model's ability to perform with high accuracy even under complex lighting conditions. Figure 11.b: During a low-light nighttime shoot, the model achieved a 79% accuracy. This result highlights the model's capability to make reliable predictions even in low-light conditions. Figure 11.c: The model attained a 69% accuracy in a nighttime shoot with high artificial lighting. This indicates that the model can operate with reasonable accuracy even in highly illuminated environments. Figure 11.d: In a high-noise environment, the model achieved 81% accuracy. This shows that the model can accurately detect pufferfish in noisy conditions. Figure 11.e: Under daylight and natural lighting conditions, the model achieved a 94% accuracy, indicating high performance under ideal lighting conditions. Figure 11.f: In daylight with normal lighting, the model achieved an 89% accuracy, suggesting consistent high accuracy under natural lighting conditions. Figure 11.g: The model detected pufferfish with a 54% accuracy from a rear dorsal view in a noisy environment. This finding shows that while the model performs reasonably well in challenging conditions, performance can drop in such atypical scenarios. Overall, the YOLOv8m model demonstrates high accuracy in detecting pufferfish across various lighting

and noise conditions. The results suggest that the model can be effectively used in a range of real-world scenarios and has strong generalization capabilities.

D. Challenges Encountered In Underwater Environments

In training a deep learning model for high-accuracy pufferfish detection in underwater environments, obtaining a sufficient number of correctly labeled examples is crucial. However, accessing the data needed to train the model and achieve accurate results is a challenging process. Underwater images are often taken under low light conditions or are blurred, making it difficult to detect fish species, including pufferfish. Low image quality can hinder labeling accuracy and affect the model's ability to accurately detect pufferfish examples. Additionally, pufferfish may be viewed from various perspectives and sizes underwater. Some pufferfish are captured up close, while others are seen from a distance. This variability necessitates additional data for the model to recognize different perspectives and sizes effectively.

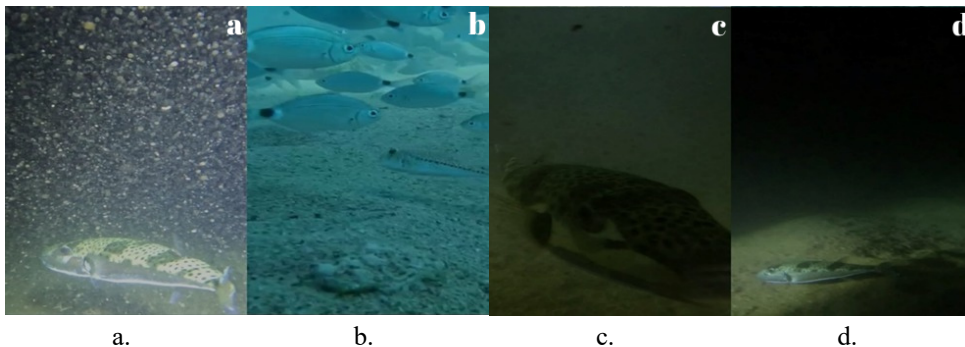


Figure 12: Representative Examples of Challenging Underwater Environments

The underwater environment is complex and challenging. Objects such as algae, rocks, and corals can complicate pufferfish detection and hinder the model's ability to produce accurate results. Figure 12 illustrates these challenging environments. Figure 12.a Shows an underwater scene captured at night with high noise. The low light and high noise levels make it difficult to detect pufferfish. Figure 12.b displays an environment where other fish are present, and the pufferfish blends with the sandy sea floor. As the fish gets closer to the sand, distinguishing it from its surroundings becomes challenging. Figure 12.c Depicts an environment with insufficient lighting, which further complicates accurate pufferfish detection. Figure 12.d Features a dark underwater scene captured with artificial lighting. Even under these artificial light conditions, detecting pufferfish can be difficult. In such environments, the model's ability to produce accurate results depends on its effectiveness in filtering out noise and distinguishing the pufferfish from its surroundings.

Figure 13. shows labeled pufferfish images from the dataset, sourced from the Roboflow platform, captured in various underwater environments. Figure 13.a Illustrates a scene where pufferfish are found alongside other fish species, highlighting the complexity of detection in mixed environments. Figure 13.b Features a night-time shot with low lighting, where the pufferfish is clearly visible, demonstrating detection capabilities under low-light conditions. Figure 13.c shows a pufferfish close to the camera, with visible noise in the recording environment, emphasizing challenges in high-noise settings. Figure 13.d displays a scene where the pufferfish is near the sandy sea floor and camouflaged with the sand, illustrating the fish's natural camouflaging ability and the difficulty in detection. These images provide crucial reference points for evaluating the model's performance in various underwater scenarios.

In this study, the potential of the YOLO deep learning algorithm was explored for developing an automatic pufferfish detection system capable of accurately identifying pufferfish samples in real-time. Initially, a unique dataset consisting of 2473 images was created, with 1773 images for training, 450 images for validation, and 250 images for testing. YOLOv5 and YOLOv8 versions, including n, m, and l packages, were trained using this dataset, and the weights of the models were obtained upon completion of the training process.

In the training conducted with 300 epochs, it was observed that pufferfish could be better detected from the head and side views. This outcome can be attributed to the effectiveness of the manual labeling process of the images. During the manual labeling process, some images were attempted to be annotated with bounding boxes around the areas covered by the pufferfish. However, due to the unclear appearance of the tail and fins, only the more visible part, the body, could be included within the bounding boxes. Challenges encountered during manual labeling included images with excessive noise (e.g., Figures 11.d, g), very high or low lighting (e.g., Figures 11.b, c), and pufferfish camouflaged among other objects and fish in the environment. In such problematic images, bounding boxes were included only if the fish's fins and tail could be clearly distinguished. This situation naturally influenced the model's performance as well (e.g., Figures 11.e, f) [58].

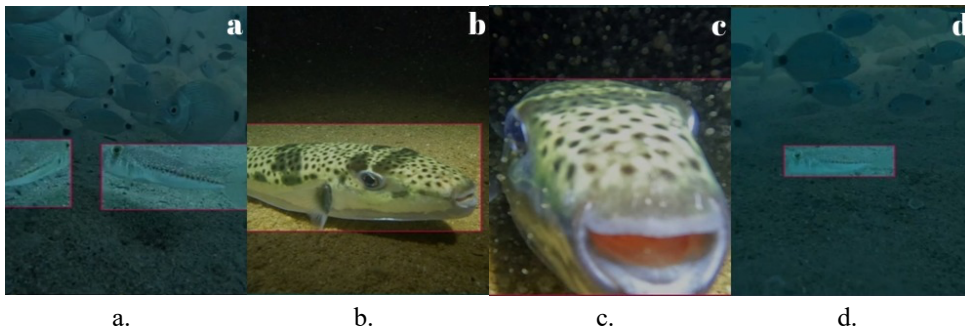


Figure 13: Labeled Pufferfish Images from the Dataset

At the end of the training, the YOLOv8 model achieved the expected success, and the performance of YOLOv5 was compared with YOLOv8. YOLOv8 models demonstrated better average precision performance compared to YOLOv5 models. The success of the YOLOv8 model compared to YOLOv5 aligns with the success comparisons of YOLO versions published by Ultralytics [59]. Both YOLO versions were trained for pufferfish detection, and the results, including precision, recall, and average precision values shown in Table 2, indicate that the model provides acceptable results regarding its performance [60]-[63].

Figures 4, 5, and 6, which display the training results for YOLOv8 models, show an increase in dfl loss values after 250 epochs. Similarly, Figures 7 and 8, which depict the training results for YOLOv5 models, reveal an increase in objective loss values after 250 epochs. Overfitting is a phenomenon where a model performs well on the training data but poorly on new, unseen test data [64], [65]. This indicates that overfitting problems emerged in the models after 250 epochs of training. During the training of the models, the patience value was set to 100. Generally, the patience value is used to manage the training process in a balanced way and control overfitting. If a lower patience value is applied, the training might be concluded before completing 300 epochs. Setting the patience value too low can lead to prematurely halting the training, which may reduce the model's chances of learning generalization and showing its true potential [66], [67]. Carefully adjusting the patience value is important to ensure the model trains for a sufficient duration, allowing it to adapt to the training data while also learning generalization [68]. Properly setting this value provides flexibility while monitoring the model's performance on validation data and reduces the likelihood of overfitting. Selecting a lower patience value to complete the training within 250 epochs or less could potentially enhance the models' performance.

Box loss, classification loss, and dfl values can vary depending on the model's complexity, the dataset, and the training process [69], [70]. Lower dfl loss values indicate better object detection performance by the model [71], [72]. The results obtained show that the model is able to correctly classify pufferfish in images taken from the head and side angles but struggles with accurately determining their locations. The higher dfl loss compared to other values suggests that the model makes errors, particularly in bounding box predictions, indicating that the predicted bounding boxes are not well-aligned with or overlapping with the ground truth bounding boxes. It appears that the model has difficulties dealing with rare classes or challenging examples and requires more data to accurately classify these objects and predict their bounding boxes [73], [74]. Although the high DFL loss causes some inconsistencies in the model's bounding box estimates, it was observed that this loss did not seriously reduce the overall accuracy rate of the model. This shows that the model has the ability to successfully detect pufferfish from various angles. However, since there may be possible inconsistencies in the bounding box estimates, it is very important to create a

data set that includes more image diversity and especially views of the fish from different angles to avoid this problem.

IV. Conclusion

In this study, a model for detecting pufferfish using computer vision and deep learning was trained with ESA-based YOLOv8 and YOLOv5 models, including some of their subversions (n, m, l). The videos used in the study were recorded in the Mediterranean Sea. An original dataset consisting of 2473 images was created from frames extracted from videos containing pufferfish obtained from various diving schools. For model training, the images were divided into training, validation, and test sets in a 70-20-10 ratio. The models were compared based on precision, recall, and average precision metrics, with the best performance achieved by the YOLOv8m model, which obtained an average precision of 96.90%.

In this study, YOLOv8 models have been demonstrated to be effective for detecting specialized species like pufferfish in underwater environments, achieving successful detection. Given the unique challenges of underwater environments and the specific issues posed by classifying fish, such as whether to include features like fins and tails in labeling, it would be beneficial to repeat the study with datasets containing more data. Although the precision, recall, and average precision values obtained throughout the study are high, different optimization strategies and hyperparameter tuning could be explored to reduce the dfl loss. To address the issue of image blurriness affecting focus on the body, clearer images can be used, and higher resolution images could be incorporated into training using methods like "patch-based training" [75] or "sliding window approach" [76]. The model developed in this study can serve as a foundation for future work, enabling the use of underwater robots or drones for unmanned detection and monitoring of pufferfish. However, this study has limitations, including the relatively small dataset size, which may not fully represent the variability of *Lagocephalus sceleratus* across different conditions and regions. Manual labeling difficulties, particularly in low-light or noisy underwater images, also impacted detection accuracy for certain angles. Furthermore, the focus on Mediterranean data limits its geographic applicability, and the use of only YOLOv5 and YOLOv8 excludes other potentially effective algorithms. For further improvement, future studies could expand the dataset with diverse environmental samples, employ automated labeling tools to enhance consistency, using transfer learning methods and test additional deep learning models to optimize performance.

This study could be integrated into unmanned underwater vehicles (UUVs) to monitor and control pufferfish populations in real-time, reducing ecological damage in the Mediterranean. Fishermen could use this technology via mobile apps or onboard systems to avoid catching pufferfish, minimizing net damage and economic losses. In aquaculture, the model could identify pufferfish intrusions in fish farms, protecting native species and improving yield. Environmental agencies might deploy it to track invasive species spread, informing policy decisions. For public health, coastal authorities could use it to issue warnings about pufferfish presence, preventing consumption-related incidents. These applications extend beyond detection, offering actionable insights for sustainability and safety. Expanding these application examples, the model could support biodiversity studies by mapping pufferfish distribution, assist in automated culling systems to curb overpopulation, or integrate with drone-based surveillance for large-scale monitoring. Such implementations could amplify its impact on marine conservation, fishing efficiency, and public safety.

Acknowledgments

This study was produced from the master's thesis with the same title prepared by the first author at Akdeniz University, Department of Management Information Systems. We would like to extend our gratitude to Professor Dr. Mehmet GÖKOĞLU, Associate Professor Dr. Ahmet BALCI, Star Diving Academy, Poseidon Kemer Diving, and Diving Instructor Orkun TEKİN for their support during this study.

Authors' Contributions

All authors contributed equally to the conceptualization, methodology, software development, validation, formal analysis, resources, and data curation. They also shared equal responsibility for writing the original draft, reviewing and editing the manuscript, and creating visualizations. Both authors equally supervised the project, managed its administration.

Competing Interests

The authors of this study declare that they have no financial, commercial, legal, or professional relationships or conflicts of interest with any organizations or individuals that could be perceived as influencing the outcomes of this research.

Ethics Committee Approval

This study received ethical approval from the Scientific Research and Publication Ethics Committee of Akdeniz University, with the decision dated September 5, 2023, under reference number 370.

References

- [1] M. El-Raey, "Impacts and implications of climate change for the coastal zones of Egypt," *Coastal Zones Climate Change*, vol. 7, pp. 31–50, 2010. [Online]. Available: https://www.stimson.org/wp-content/files/file-attachments/Mohamed_1.pdf Accessed on: May.5, 2023
- [2] S. Mavruk and D. Avsar, "Non-native fishes in the Mediterranean from the Red Sea, by way of the Suez Canal," *Rev. Fish Biol. Fish.*, vol. 18, no. 3, pp. 251–262, 2008, DOI: 10.1007/s11160-007-9073-7.
- [3] J. P. Rodrigue, *The Geography of Transport Systems*, 5th ed. New York, NY, USA: Routledge, 2020.
- [4] D. Golani, "Impact of Red Sea fish migrants through the Suez Canal on the aquatic environment of the eastern Mediterranean," *Yale F&ES Bull.*, vol. 103, pp. 375–387, 1998.
- [5] A. Zenetos, S. Gofas, C. Morri, A. Rosso, D. Violanti, J. E. García-Raso, and N. Streftaris, "Additions to the marine alien fauna of Greek waters (2007 update)," *Mediterr. Mar. Sci.*, vol. 9, no. 1, pp. 119–165, 2008.
- [6] M. E. Çınar, M. Bilecenoğlu, B. Öztürk, T. Katağan, M. B. Yokeş, V. Aysel, and E. Dağlı, "An updated review of alien species on the coasts of Turkey," *Mediterr. Mar. Sci.*, vol. 12, no. 2, pp. 1–19, 2011.
- [7] M. E. Çınar, M. Bilecenoğlu, M. B. Yokeş, B. Öztürk, E. Taşkın, K. Bakır, and S. Açıık, "Current status (as of end of 2020) of marine alien species in Turkey," *PLoS ONE*, vol. 16, no. 5, p. e0251086, 2021, DOI: 10.1371/journal.pone.0251086.
- [8] O. Akyol, V. Ünal, T. Ceyhan, and M. Bilecenoğlu, "First confirmed record of the lionfish *Pterois volitans* (Linnaeus, 1758) in the Mediterranean Sea," *J. Fish Biol.*, vol. 66, no. 4, pp. 1183–1186, 2005.
- [9] A. Zenetos, S. Gofas, M. Verlaque, M. E. Çınar, J. E. García Raso, C. N. Bianchi, and N. Streftaris, "Alien species in the Mediterranean Sea by 2010. A contribution to the application of European Union's Marine Strategy Framework Directive (MSFD). Part I. Spatial distribution," *Mediterr. Mar. Sci.*, vol. 11, no. 2, pp. 381–493, 2010.
- [10] M. Kulbicki, Y. M. Bozec, P. Labrosse, Y. Letourneur, G. Mou-Tham, and L. Wantiez, "Diet composition of carnivorous fishes from coral reef lagoons of New Caledonia," *Aquat. Living Resour.*, vol. 18, no. 3, pp. 231–250, 2005.
- [11] S. Tüzün, *Yapay Zeka ve Uygulamaları*. İstanbul, Türkiye: Papatya Yayıncılık Eğitim, 2012.
- [12] V. Arvind, A. Ranjan, and D. Saha, "Machine learning techniques for fish detection and classification: A survey," *Aquaculture*, vol. 504, pp. 331–345, 2019.
- [13] M. Chuang, J. N. Hwang, K. Williams, and A. Das, "Fish species recognition from video using neural networks," *J. Vis. Commun. Image Represent.*, vol. 42, pp. 140–148, 2017.
- [14] L. Kezebou, I. Zennouhi, Z. Bousalem, and A. Said, "Deep learning approaches for fish species recognition in underwater videos: Performance comparison," *Proc. Comput. Sci.*, vol. 151, pp. 113–120, 2019.
- [15] C. Spampinato, J. Chen-Burger, R. B. Fisher, G. Nadarajan, and D. Giordano, "Detecting, tracking and counting fish in low quality unconstrained underwater videos," in *Proc. VISAPP*, Madeira, Portugal, 2008, pp. 514–519.
- [16] B. Xu and Z. Cheng, "Fish detection and tracking in real-life underwater environment," *Multimedia Tools Appl.*, vol. 76, no. 20, pp. 21171–21187, 2017.
- [17] M. Ahmad, M. A. Khatkhat, and S. Ali, "The impact of AI on modern industry," *J. Innov. Manage.*, vol. 9, no. 4, pp. 78–95, 2021.
- [18] P. Bharadiya, "Advanced AI techniques in financial markets: A review," *Financial Innov.*, vol. 9, no. 2, pp. 155–170, 2023.
- [19] K. Crawford, *The Atlas of AI: Power, Politics, and the Planetary Costs of Artificial Intelligence*. New Haven, CT, USA: Yale Univ. Press, 2021.

- [20] Y. Duan, J. S. Edwards, and Y. K. Dwivedi, "Artificial intelligence for decision making in the era of Big Data—evolution, challenges and research agenda," *Int. J. Inf. Manage.*, vol. 48, pp. 63–71, 2019.
- [21] T. Hwang, "Computational power and the social impact of artificial intelligence," arXiv preprint, 2018. [Online]. Available: <https://arxiv.org/abs/1803.08971> Accessed on: Oct.12, 2022
- [22] Y. Lu, "Artificial intelligence: A survey on evolution, models, applications and future trends," *J. Manage. Anal.*, vol. 6, no. 1, pp. 1–29, 2019.
- [23] C. Zhang and Y. Lu, "Study on image recognition of fish behavior based on machine learning," *Sci. Rep.*, vol. 11, no. 1, pp. 1–10, 2021.
- [24] S. B. Maind and P. Wankar, "Research paper on basic of artificial neural network," *Int. J. Recent Innov. Trends Comput. Commun.*, vol. 2, no. 1, pp. 96–100, 2014.
- [25] Y. Bengio, A. Courville, and P. Vincent, "Representation learning: A review and new perspectives," *IEEE Trans. Pattern Anal. Mach. Intell.*, vol. 35, no. 8, pp. 1798–1828, 2013.
- [26] W. Liu, Z. Wang, X. Liu, N. Zeng, Y. Liu, and F. E. Alsaadi, "A survey of deep neural network architectures and their applications," *Neurocomputing*, vol. 234, pp. 11–26, 2017.
- [27] Y. Guo, Y. Liu, A. Oerlemans, S. Lao, S. Wu, and M. S. Lew, "Deep learning for visual understanding: A review," *Neurocomputing*, vol. 187, pp. 27–48, 2016.
- [28] Y. LeCun, Y. Bengio, and G. Hinton, "Deep learning," *Nature*, vol. 521, no. 7553, pp. 436–444, 2015.
- [29] S. Pouyanfar, S. Sadiq, Y. Yan, H. Tian, Y. Tao, M. P. Reyes, and S. S. Iyengar, "A survey on deep learning: Algorithms, techniques, and applications," *ACM Comput. Surv.*, vol. 51, no. 5, pp. 1–36, 2018.
- [30] C. Beyan and H. I. Browman, "Fish recognition and species classification in underwater videos: A survey," *Fish. Res.*, vol. 226, p. 105521, 2020.
- [31] W. Zhao, Y. Zhang, L. Yu, and S. Du, "Automatic fish classification system using deep learning," *Comput. Electron. Agric.*, vol. 170, p. 105254, 2019.
- [32] D. Li, Y. Yang, Z. Yin, D. Luo, and S. Ma, "A novel deep learning approach for fish detection in real-life underwater environments," *Ocean Eng.*, vol. 250, p. 110867, 2022.
- [33] H. Cui, Y. Zhang, X. Chen, and L. Wei, "Real-time fish tracking and classification in underwater videos using deep learning," *Pattern Recognit. Lett.*, vol. 140, pp. 1–8, 2020.
- [34] H. Wang, L. Zhang, and J. Li, "End-to-end neural network for real-time detection and tracking of abnormal fish behavior," *Neurocomputing*, vol. 494, pp. 375–385, 2022.
- [35] J. Redmon, S. Divvala, R. Girshick, and A. Farhadi, "You only look once: Unified, real-time object detection," in *Proc. IEEE Conf. Comput. Vis. Pattern Recognit.*, Las Vegas, NV, USA, 2016, pp. 779–788.
- [36] X. Zhou, D. Wang, and P. Krähenbühl, "Deep learning for automatic fish species classification," *Fish. Res.*, vol. 204, pp. 1–10, 2017.
- [37] J. Redmon and A. Farhadi, "YOLOv3: An incremental improvement," arXiv preprint, 2018. [Online]. Available: <https://arxiv.org/abs/1804.02767> Accessed on: Jun.8, 2023
- [38] K. Kim, K. Kim, and S. Jeong, "Application of YOLO v5 and v8 for recognition of safety risk factors at construction sites," *Sustainability*, vol. 15, no. 20, p. 15179, 2023.
- [39] A. Bochkovskiy, C.-Y. Wang, and H.-Y. M. Liao, "YOLOv4: Optimal speed and accuracy of object detection," arXiv preprint, 2020. [Online]. Available: <https://arxiv.org/abs/2004.10934> Accessed on: Jan.20, 2023
- [40] Ultralytics, "YOLOv5," GitHub Repository, 2020. [Online]. Available: <https://github.com/ultralytics/yolov5> Accessed on: Feb.5, 2023
- [41] Thu-Mig, "YOLOv10," GitHub Repository, 2024. [Online]. Available: <https://github.com/THU-MIG/yolov10> Accessed on: May.10, 2024
- [42] E. M. Diritia, S. Lopez-Marcano, M. Sievers, E. L. Jinks, and R. M. Connolly, "Deep learning for underwater fish detection: Accuracy and efficiency of human and automated methods," *Ecol. Inform.*, vol. 55, p. 101019, 2020.
- [43] N. Wang, Y. Zhang, and J. Han, "Fish detection and classification in complex underwater environments using deep learning," *Inf. Sci.*, vol. 578, pp. 298–314, 2022.
- [44] X. Li, Y. You, J. Wu, and H. Zhou, "Fish species recognition in underwater video based on deep convolutional neural networks," *J. Comput. Sci.*, vol. 10, pp. 124–133, 2015.
- [45] S. Villon, D. Mouillot, M. Chaumont, and T. Claverie, "Automatic underwater fish species classification with limited data using deep learning," *Ecol. Inform.*, vol. 48, pp. 124–131, 2018.
- [46] D. Hridayami, Y. Tjahyadi, and W. Widhiarso, "Deep learning-based fish classification system for real-time underwater fish monitoring," *Procedia Comput. Sci.*, vol. 157, pp. 447–453, 2019.

- [47] V. Allken, N. O. Handegard, S. Rosen, T. Schreyeck, T. Mahiout, and K. Malde, "Fish species identification using a convolutional neural network trained on synthetic data," *ICES J. Mar. Sci.*, vol. 76, no. 1, pp. 342–349, 2019.
- [48] A. Jalal, M. Nasir, and K. Kim, "Fish detection and species classification in underwater environments using deep learning with temporal information," *Sensors*, vol. 20, no. 12, p. 3452, 2020.
- [49] A. Salman, A. Jalal, and K. Kim, "Region-based convolutional neural network for fish detection in underwater environments," *Sensors*, vol. 20, no. 5, p. 1400, 2020.
- [50] M. Hussain, A. Jalal, and K. Kim, "Modified AlexNet for fish classification in underwater environments," *Comput. Electr. Eng.*, vol. 93, p. 107231, 2021.
- [51] H. Wang, S. Zhu, M. Wang, and J. Ye, "Advances in deep learning: Applications in the healthcare sector," *J. Healthcare Eng.*, vol. 2022, no. 1, pp. 1–14, 2022.
- [52] B. Patro, S. Mukhopadhyay, and P. P. Roy, "Real-time object detection using YOLOv5 for fish monitoring in adverse environments," *J. Ocean Technol.*, vol. 18, no. 2, pp. 61–73, 2023.
- [53] Y. Eği, "YOLO v7 and computer vision-based mask-wearing warning system for congested public areas," *J. Inst. Sci. Technol.*, vol. 13, no. 1, pp. 22–32, 2023.
- [54] Z. Yücel and D. Çetintaş, "Yolov9 ile kan hücrelerinin otomatik tanımlanması: Optimizasyon ve öğrenme oranı etkileri," *Adıyaman Üniv. Müh. Bilim. Derg.*, vol. 11, no. 22, pp. 125–135, 2024.
- [55] D.-J. Shin and J.-J. Kim, "A deep learning framework performance evaluation to use YOLO in Nvidia Jetson platform," *Appl. Sci.*, vol. 12, no. 8, p. 3734, 2022.
- [56] C. Li, Y. Zhang, X. Wu, and Y. Yang, "Deep learning-based fish behavior analysis in underwater videos," *Inf. Sci.*, vol. 579, pp. 92–105, 2022.
- [57] T. Y. Lin, P. Goyal, R. Girshick, K. He, and P. Dollár, "Focal loss for dense object detection," *IEEE Trans. Pattern Anal. Mach. Intell.*, vol. 42, no. 2, pp. 318–327, 2020.
- [58] J. Terven and D. Cordova-Esparza, "A comprehensive review of YOLO architectures in computer vision: From YOLOv1 to YOLOv8 and YOLO-NAS," *arXiv preprint*, 2023. [Online]. Available: <https://arxiv.org/abs/2304.00501> Accessed on: Mar.15, 2024
- [59] G. Jocher and M. R. Munawar, "Ultralytics YOLOv8," *GitHub Repository*, 2023. [Online]. Available: <https://github.com/ultralytics/yolov8> Accessed on: Mar.15, 2024
- [60] V. Viswanatha, R. K. Chandana, and A. C. Ramachandra, "Real time object detection system with YOLO and CNN models: A review," *arXiv preprint*, 2022. [Online]. Available: <https://arxiv.org/abs/2208.00773> Accessed on: Mar.12, 2023
- [61] P. Jiang, D. Ergu, F. Liu, Y. Cai, and B. Ma, "A review of Yolo algorithm developments," *Procedia Comput. Sci.*, vol. 199, pp. 1066–1073, 2022.
- [62] M. Hussain, "YOLOv1 to v8: Unveiling each variant—A comprehensive review of YOLO," *IEEE Access*, vol. 12, pp. 42816–42833, 2024.
- [63] A. Vijayakumar and S. Vairavasundaram, "YOLO-based object detection models: A review and its applications," *Multimedia Tools Appl.*, vol. 83, no. 35, pp. 83535–83574, 2024, DOI: 10.1007/s11042-024-18872-y.
- [64] C. F. G. D. Santos and J. P. Papa, "Avoiding overfitting: A survey on regularization methods for convolutional neural networks," *ACM Comput. Surv.*, vol. 54, no. 10, pp. 1–25, 2022.
- [65] S. Aburass, "Quantifying overfitting: Introducing the overfitting index," *arXiv preprint*, 2023. [Online]. Available: <https://arxiv.org/abs/2308.08682> Accessed on: Oct.15, 2023
- [66] L. Prechelt, "Early stopping – But when?," in *Neural Networks: Tricks of the Trade*. Berlin, Germany: Springer, 2012.
- [67] J. Brownlee, "A gentle introduction to early stopping to avoid overtraining neural networks," *Machine Learning Mastery*, 2019. [Online]. Available: <https://machinelearningmastery.com/how-to-stop-training-deep-neural-networks-at-the-right-time-using-early-stopping/>, Accessed on: Apr. 1, 2024.
- [68] S. Paguada, L. Batina, I. Buhan, and I. Armendariz, "Being patient and persistent: Optimizing an early stopping strategy for deep learning in profiled attacks," *IEEE Trans. Comput.*, vol. 74, no. 3, pp. 1–12, 2024.
- [69] C. Zhu, Y. Zheng, K. Luu, and M. Savvides, "CMS-RCNN: Contextual multi-scale region-based CNN for unconstrained face detection," in *Deep Learning for Biometrics*. Cham, Switzerland: Springer, 2017.
- [70] T. Y. Lin, P. Goyal, R. Girshick, K. He, and P. Dollár, "Focal loss for dense object detection," *IEEE Trans. Pattern Anal. Mach. Intell.*, vol. 42, no. 2, pp. 318–327, 2020.
- [71] K. Su, L. Cao, B. Zhao, N. Li, D. Wu, and X. Han, "N-IoU: Better IoU-based bounding box regression loss for object detection," *Neural Comput. Appl.*, vol. 36, no. 6, pp. 3049–3063, 2024.

- [72] P. Liu, G. Zhang, B. Wang, H. Xu, X. Liang, Y. Jiang, and Z. Li, "Loss function discovery for object detection via convergence-simulation driven search," arXiv preprint, 2021. [Online]. Available: <https://arxiv.org/abs/2102.04700> Accessed on: Apr.8, 2023
- [73] P. Jayanthi, "Machine learning and deep learning algorithms in disease prediction: Future trends for the healthcare system," in *Deep Learning for Medical Applications with Unique Data*. Cambridge, MA, USA: Academic Press, 2022.
- [74] P. D. K. Reddy, M. Margala, S. S. Shankar, and P. Chakrabarti, "Early fire danger monitoring system in smart cities using optimization-based deep learning techniques with artificial intelligence," *J. Reliable Intell. Environ.*, vol. 10, no. 2, pp. 197–210, 2024.
- [75] Z. Ding, L. Sun, X. Mao, L. Dai, and B. Xu, "Location-independent adversarial patch generation for object detection," *J. Electron. Imaging*, vol. 32, no. 4, p. 043035, 2023.
- [76] V. Kshirsagar, R. H. Bhalerao, and M. Chaturvedi, "Modified YOLO module for efficient object tracking in a video," *IEEE Latin Amer. Trans.*, vol. 21, no. 3, pp. 389–398, 2023.